CONTRACTOR REPORT

SAND88—7035
Unlimited Release
UC—237

Development of a Stretched Membrane Dish – Phase I

Solar Kinetics, Inc.
10635 King William Drive
Dallas, Texas

Prepared by Sandia National Laboratories Albuquerque, New Mexico 87185
and Livermore, California 94550 for the United States Department of Energy
under Contract DE-AC04-76DP00789

Printed March 1989

Issued by Sandia National Laboratories, operated for the United States Department of Energy by Sandia Corporation.

Printed in the United States of America
Available from
National Technical Information Service
U.S. Department of Commerce
5285 Port Royal Road
Springfield, VA 22161

NTIS price codes
Printed copy: A11
Microfiche copy: A01

DEVELOPMENT OF A STRETCHED MEMBRANE DISH - PHASE I

Solar Kinetics, Inc.
10635 King William Drive
Dallas, Texas

Sandia Contract #53-9663

ABSTRACT

A stretched-membrane dish concentrator design was developed in Phase I of a contract directed by Sandia National Laboratories, Albuquerque. The concentrating optical element was investigated in detail, and conceptual designs were provided for the collector support system. The optical element was defined by a monolithic, single-facet, parabolic design with an f/D ratio of 0.6. The conceptual support system was a hub and spoke structure similar to a bicycle wheel. The estimated optical element weight was 2.3 lb/ft^2 (11 kg/m^2), and 6.6 lb/ft^2 (32 kg/m^2) for the entire collector. A 0.010" (0.25-mm) thick aluminum diaphragm was plastically deformed without the use of a mold or mandrel to create the optical membrane. This free-form yield process was demonstrated with 1.4-m and 3.7-m diameter tests. The one-sigma slope error of these test membranes, based on a peak flux bound, was less than 2 mrad at the smaller scale, and less than 4 mrad at the larger scale. The aluminum membrane defined the concentrator shape for a separate, reflective polymer film membrane. Contact between the two membranes was maintained with a vacuum. The stretched-membrane dish technology, applied to a parabolic dish, demonstrated the potential for high performance with low weight.

CONTENTS

LIST OF FIGURES

APPENDIX A

Figure (a) Ideal and Actual Displacement vs. Radial Position
(b) Slope Error vs. Radial Position

APPENDIX B

LIST OF TABLES

Appendix A

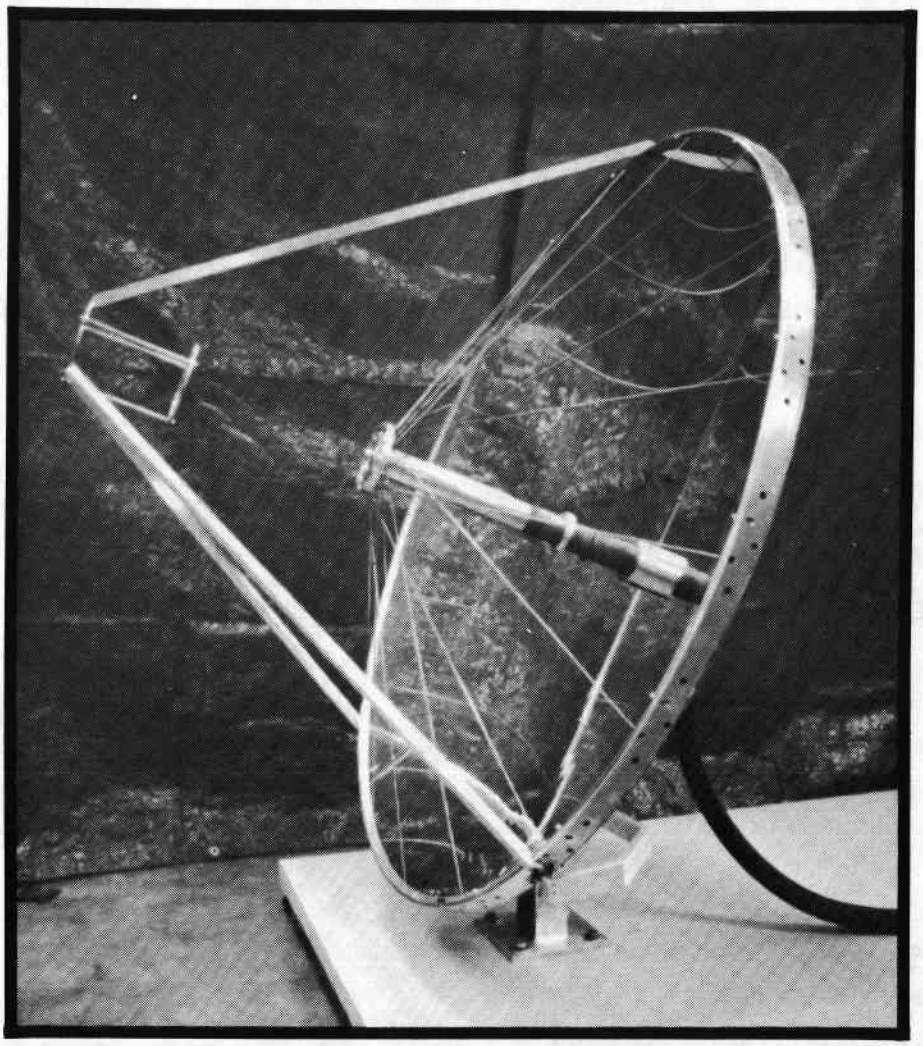

Model of Stretched-Membrane Dish Collector Constructed in Phase I, 1.4 m Diameter

1.0 Introduction

This report summarizes the first phase of research and development on stretched-membrane technology applied to a parabolic dish. The work presented here was funded by Sandia National Laboratories, Albuquerque (SNLA), under contract 53-9663, to define the potential for weight and cost reduction in point-focus, stretched-membrane concentrators. The first phase of analysis was directed toward optimization of the optical element, demonstration of critical fabrication techniques, and conceptual design of the mirror module support system.

The optical surface of a stretched-membrane dish is a thin diaphragm, or membrane, which is attached to a circular ring at the perimeter only. The membrane has no flexural rigidity. The parabola is defined by the initial membrane shape and a biaxial tension in reaction to a uniform pressure load imposed by a fan.

The optical element developed in this optimization effort comprised three separate membranes, the circular ring frame, and spokes that radiated from a central hub or mast to the ring. A flat polymer membrane was attached to the ring and hub to provide a reflective surface. A metallic membrane, yielded to form a parabola, provided the initial or fundamental concentrator shape. The third, or rear membrane, was fabricated from a commercially available composite cloth. These membranes created a plenum, which was partially evacuated to provide a differential pressure source. A schematic representation of the dish is provided in Figure 1.1. A conceptual support system is also shown in the figure.

The metal membrane was formed to a parabolic shape with a free-form yield process. Plastic deformation was implemented without mandrels or molds. An accurate shape was produced through structural response to a controlled load distribution. A hydrostatic load, combined with uniform pressure, was required to produce a parabolic shape.

The support system provided for load transmission from the concentrator to ground and allowed tracking in two axes. Elevation tracking was provided through a four-bar link; rotation of the ground link provided azimuthal freedom. The conceptual support system allowed two paths to ground for efficient transfer of stow loads.

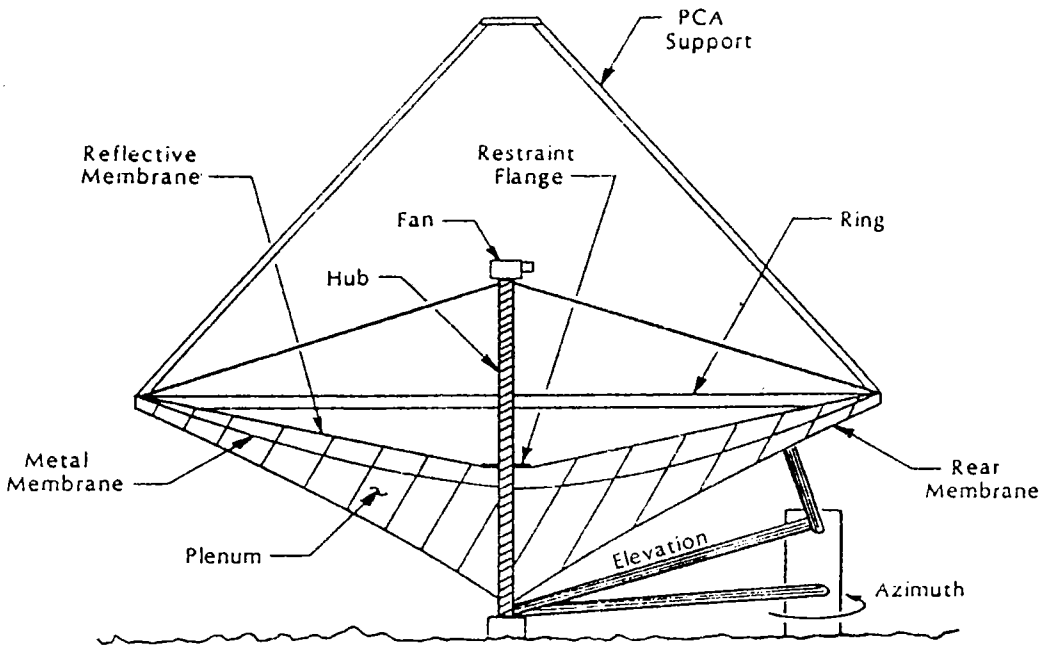

Figure 1.1 Schematic View of the Stretched-Membrane Dish.

The Phase I results are presented in five major sections:

Optical Geometry. A single, monolithic facet with a focal length to diameter (f/D) ratio of 0.6 provided optimum performance.

Material Selection. The fundamental optical surface selected was metal. Aluminum was chosen, but stainless foil was an option at a slight cost penalty.

Development of Membrane Forming Techniques. An empirical analysis of free-form yielding indicated that precise membranes could be formed. The free-form process relies upon structural response, rather than flexural rigidity in the dish or tooling.

Structural Analysis of the Optical Element. The hub, spoke, and ring frame combined to form a lightweight tensegrity capable of providing membrane support.

Conceptual Support System. The rotating link drive selected as a conceptual design was compatible with the optical element frame and provided a second load path to ground during stow.

A summary is provided in each section and for the entire effort.

A substantial fraction of the information on forming was gained through an empirical analysis. All data collected from testing at two scales is provided in tabulated and graphical formats in Appendices A and B.

The first phase of this investigation indicated that stretched-membrane technology could be effectively applied to a parabolic dish. The combined weight of the mirror module and support system discussed here was approximately 6.6 lb/ft^2 (32 kg/m^2) at the commercial (14-m diameter) scale. The predicted peak flux, based upon measurements of formed membranes, was bounded by a parabola with 2 mrad of error at the 1.4-m scale, and 4 mrad at the 3.7-m scale.

2.0 Optical Geometry

Definition of the optical geometry was the first step explored in the development of the stretched-membrane dish design. The major variables in this definition were the ratio of focal length to diameter (f/D), and the size or number of facets. Design goals for the optical characteristics of the collector were defined by contract [Ref. 1] and are listed in Table 2.1. These goals formed the basic parameters in the optimization of geometry.

Table 2.1
Optical Design Goals Established by Contract

Total Aperture Area	150 m2
f/D	0.6
Slope Error[1]	2.0 mrad
Peak Optical Efficiency	0.91
Peak Thermal or Collector Efficiency	0.82
Receiver Operating Temperature	800°C

The contract also imposed a restraint in the scope of the analysis: the total aperture had to be defined with a maximum of five facets. A single, monolithic reflector element was a stated goal of the project.

Two additional constraints limited the scope of the analysis. First, the optimization effort considered axisymmetric facet shapes only. This constraint had a substantial impact upon the performance of multiple-facet geometries. The astigmatic error inherent in off-axis axisymmetric shapes represented the major source of performance reduction in the multiple facet concentrator. This astigmatism can largely be countered through an elliptical facet geometry as described by Riedl [Ref. 2]. This limitation was imposed, in spite of the impact upon the optimization efforts, to reflect a qualitative decision that fabrication difficulties would be a function of the order and complexity of the membrane shape function. No effort was expended upon refinement of this

[1] Slope error is consistently reported as one standard deviation in an assumed circular normal distribution unless specifically defined as a measured value.

initial assumption because no evidence was found, during empirical investigations, that a multiple-faceted membrane would be easier to manufacture. In fact, the reduced facet focal length to facet diameter ratio (f_f/D_f), is likely to increase the forming error in the selected manufacturing technique.

Secondary reflector systems were not considered in this analysis, and their absence represented the second major limitation in scope. The secondary reflector was defined as an added complexity in the fabrication of a concentrator to improve the performance of shapes that substantially deviated from a parabola, in a random or systematic fashion. This deviation was not identified as an inherent problem in stretched-membrane dish design at this stage in development. The effect of secondary concentrators on single- and multiple-faceted geometries has been explored by Wendelin and Lewandowski of SERI using the same basic tools and methods outlined in this development; the reader is directed to Reference 3 for secondary analysis.

The results of this analysis strongly directed all further contract efforts toward the development of a single, monolithic-facet geometry. This geometry provided the only path, given the limits of the analysis, of approaching or achieving the stated performance goals. The establishment of a single-facet baseline for development did not impose severe restraints on the selection of material, define the manufacturing method, or harness the concentrator with cost penalties based upon qualitative consideration of these issues.

2.1 Development of the Optimization

CIRCE, a code designed to model the optics of a collector system, was the primary tool used for definition of the optical geometry. This software was developed by Ratzel and Boughton of Sandia [Ref. 4] to specifically emulate the optics of a dish, and has the capability to address single-and multiple-facet geometries and define the membrane shape with random or systematic deviations from paraboloids. The limitations of scope on the optimization analysis, which are defined in the previous section, were conducive to use of this software as an analytical tool. CIRCE did not impose significant limitations on the analysis, in and of itself.

The selection of sun shapes, target divisions, concentrator divisions, and other variables that are required as inputs to the CIRCE code did have a limited effect upon the actual optical efficiencies predicted by the model.

The development of the optical geometry was based upon collector efficiency. Collector efficiency was defined as the product of optical and receiver efficiencies, which required definition of the receiver aperture. The following analyses were based upon 150 m^2 total aperture to simplify the presentation of variables such as the f/D ratio and sensitivity to slope error. The receiver efficiency was defined at 800°C operation

(the reference temperature provided by contract). A reduction of receiver temperature decreased the sensitivity of the optimization to most variables; the referenced receiver temperature reflected a typical value capable of achieving DOE program goals in the Stirling cycle engine-dish systems [Ref. 5]. Consequently, the majority of the data presented in this analysis is for an 800°C receiver. The efficiency curve used to parametrically define the receiver operation is shown in Figure 2.1.

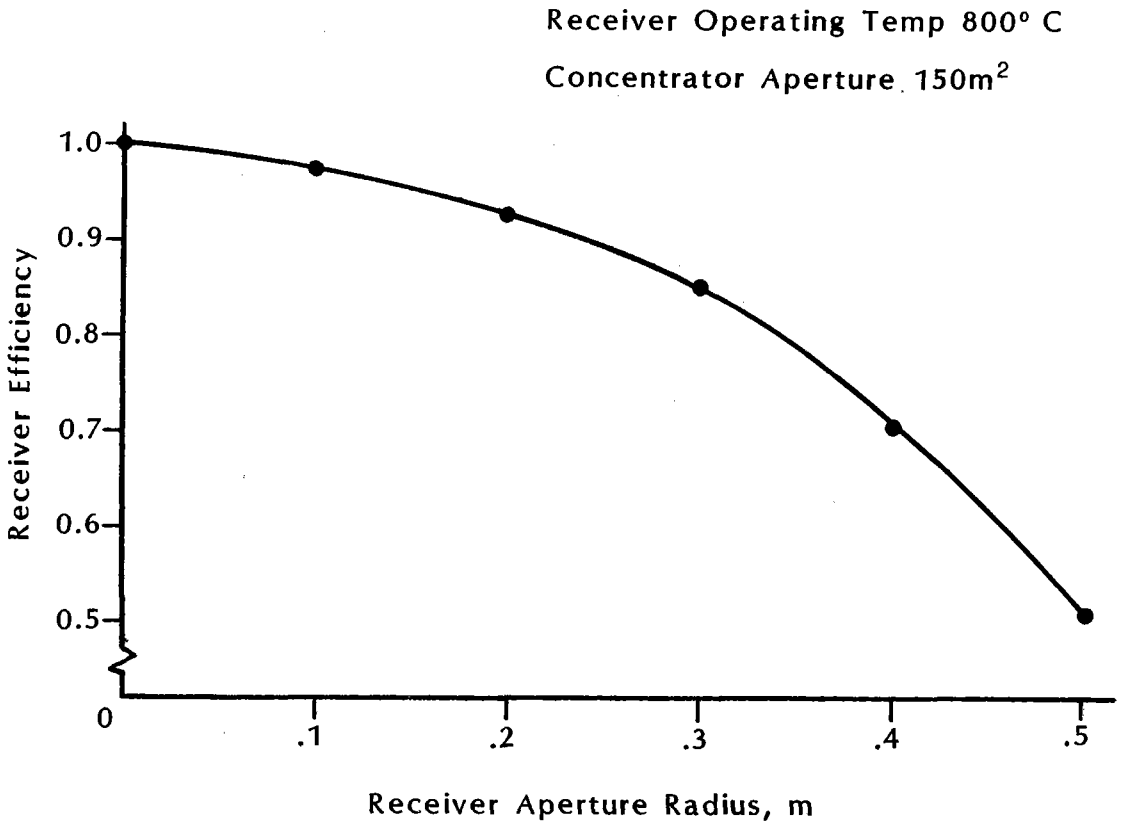

Figure 2.1 Receiver Efficiency Model Used for the Development of Collector Efficiency.

2.2 Results of the Optimization

A comparison of fundamental trends in collector efficiency as a function of the number of facets was performed without any attempt to optimize the optical variables. Multiple facets were initially assumed to be in a close-packed geometry, with facet vertices on the surface defined by the single-facet parabola with an f/D of 0.6. A typical arrangement is shown in Figure 2.2. The individual facets required an f_f/D_f ratio larger than the 0.6 f_o/D_e for the modeled geometry. This comparison indicated a substantial difference in collector thermal efficiency, ranging from 0.89 for the paraboloid, to 0.62 for

the three-facet geometry (an analysis with similar trends was performed by Ratzel, et al. [Ref. 4] and later by Wendelin, et al. [Ref. 3]). The difference in performance was largely attributed to the astigmatic effect of axisymmetric shapes packed in an off-axis configuration.

The first step executed in the optimization of geometry was a review of the basic f_o/D_e selection. Figure 2.3 illustrates this optimization based upon collector efficiency for different numbers of facets. In each case, the receiver apertures were adjusted to maximize the collector efficiency based upon the receiver performance curve presented in Figure 2.1. The optimum f_o/D_e for a single-facet was consistent with the 0.6 value stated as a contract goal. The range of optimum ratios was fairly broad, and the trends were consistent with previous findings of other researchers using different performance approximations [Ref. 6].

The range of optimum f_o/D_e ratios for multiple-facet dishes remained relatively large, given the particular condition analyzed. The optimum ratios were clearly not 0.6; the optimum collector efficiency and f_o/D_e at which it occurred were noted in Figure 2.3. The increase in performance was attributed to the reduction in astigmatic error with an increase in focal length. In other words, as the focal length of the parabola approximated by multiple geometry increased, the accuracy of the approximation increased as well. In the limit, a perfectly flat surface could be exactly approximated by a series of flat surfaces of equal gross aperture. In practice, the increase in slant range (the distance between a point on the reflector surface and the receiver aperture) and corresponding beam spread of a reflected ray limit the focal extension.

The contract goal of 0.6 ratios was maintained for the monolithic designs, but abandoned for three-and five-facet designs. All subsequent optical analysis was based upon the optimized f_o/D_e for multiple-facet geometries.

The fundamental surface geometry of single and multiple facets was also considered in the optical geometry definition. In particular, a comparison of spherical and paraboloidal shapes was made as a function of the number of facets (see Figure 2.4). This comparison was made to reflect the shape that an "idealized membrane" (e.g., a soap bubble) assumes under a uniform tension load: spherical rather than paraboloid. The individual facet's focal-length-to-diameter ratio, f_f/D_f which corresponds to the different numbers of facets, is also provided in Figure 2.4. The curve indicates that a significant performance penalty would apply to single-facet geometries, while the multiple-facet geometries enjoy some independence from the particular uniform shape selected for the facet. This independence is a result of two factors. A sphere is a better approximation of a parabola as f_f/D_e increases, for reasons similar to the flat shape analogy used in the optimum f/D development presented previously. Collector efficiency for multiple-facet geometries is also optimized at a larger receiver radius. Consequently, the multiple-facet geometries are less sensitive to a systematic error, or deviation from the ideal parabolic shape.

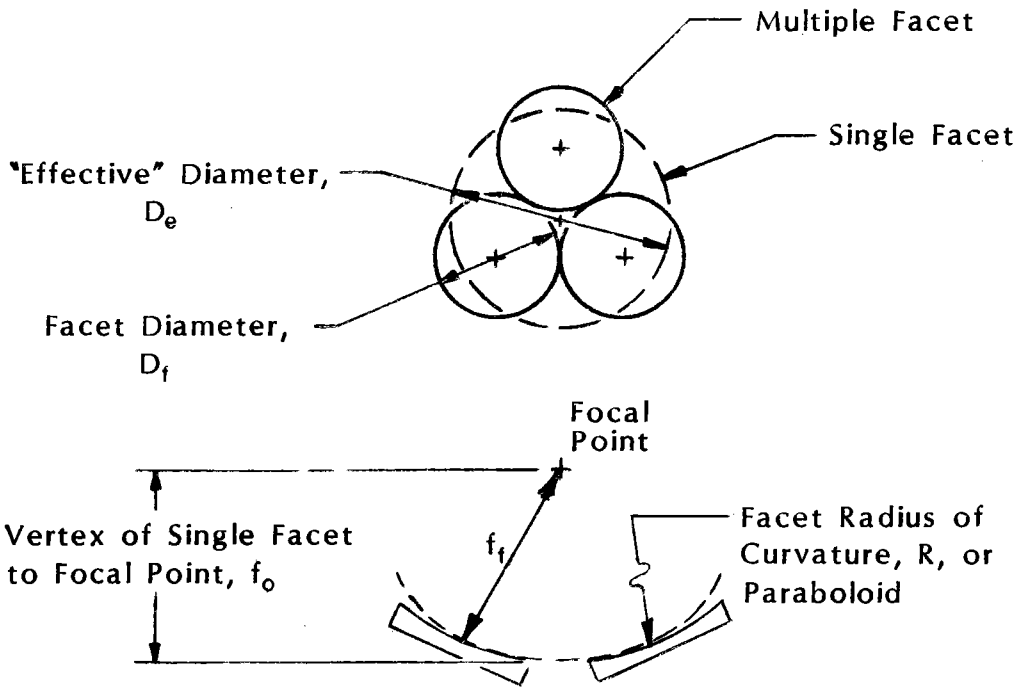

Figure 2.2 Close-Packed Multiple-Facet Geometry Used for Analysis with CIRCE.

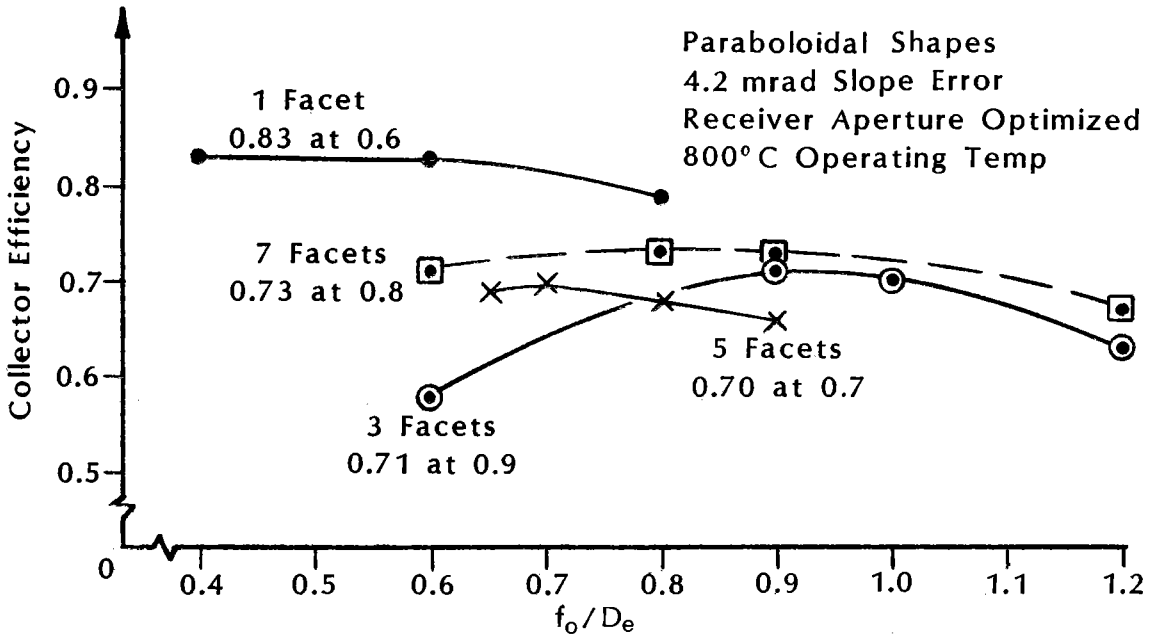

Figure 2.3 Optimization of the Focal-Length-to-Diameter Ratio Based Upon Collector Efficiency.

The actual collector efficiencies are also plotted in Figure 2.4. For spherical shapes, the monolithic facet remained the best geometry within the five-facet limitation imposed by the contract.

The decrease in performance sensitivity for multiple facets, by comparison to a single-facet geometry as a result of the larger receiver aperture, was directly explored through a similar comparison of slope error presented in Figure 2.5. The magnitude of performance penalties for single facets was larger than the penalty for multiple facets with equivalent concentrator apertures. The actual performance figures, also illustrated in Figure 2.5, continued to favor monolithic geometries.

The interpretation of this analysis, with respect to the development of a stretched-membrane concentrator, was that a single- facet geometry would be the best selection based upon optical considerations alone. Multiple-facet geometries would be acceptable only if substantial random or systematic deviation from parabolic shapes occurred in the fabrication of a membrane, or if a severe cost penalty would be imposed upon single-facet geometries. The parabolic deviation in stretched-membrane dishes was explored in empirical fashion, and is presented in a following section of this report. In essence, this empirical investigation indicated that parabolas with focal-length-to-diameter ratios of 0.6 could be approximated.

2.3 Additional Considerations in Multiple-Facet Geometries

Cost penalties, with respect to the number of facets, were explored in a qualitative fashion at this point in the analysis. Efforts were directed toward dish support structures and membrane forming. Shipping constraints were immediately discounted, as the five-facet limitation combined with the 150-m^2 aperture goal would result in final assembly at the site for any geometry considered.

The first step in the assessment of membrane formation issues, with respect to the number of facets, was to consider the possibility of purely elastic shapes. In other words, the single-facet shapes require a minimum average strain in excess of 3% from flat to form a membrane with an f/D ratio of 0.6. The five-facet geometry (f/D of 1.7) requires an average strain of only 0.4% from flat. The lower strain value for the multiple-facet geometry made operation in the elastic region a possibility for low-tensile modulus materials such as polymers. The use of flat membranes, which required no forming, were considered to be a major cost advantage.

The shape assumed by circular membranes operating in the elastic region was explored by Murphy and Tuan. Their conclusions indicate that a flat membrane, under uniform pressure loading, would not assume either a spherical or parabolic shape. They also estimated that optical membranes with f/D ratios of less than two would demonstrate unacceptable errors in the elastic region [Ref. 7]. Consideration of elastically formed

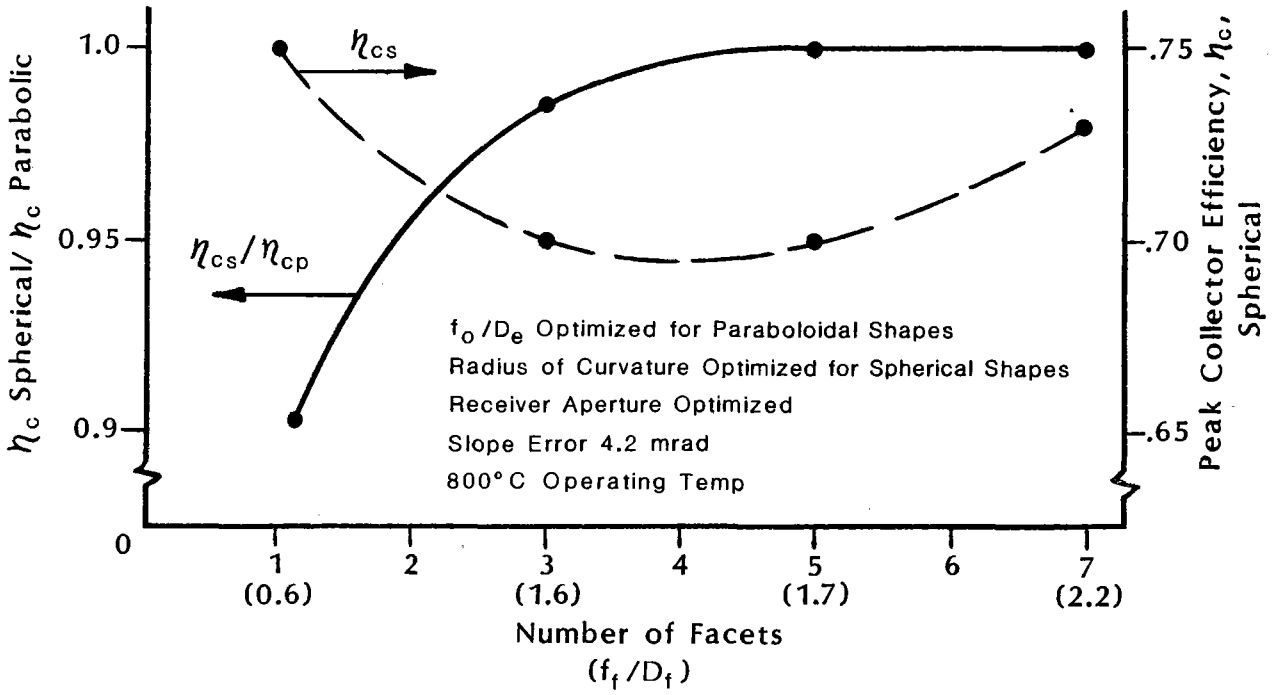

Figure 2.4 Sensitivity to Surface Shape for Single-and Multiple-Facet Geometries

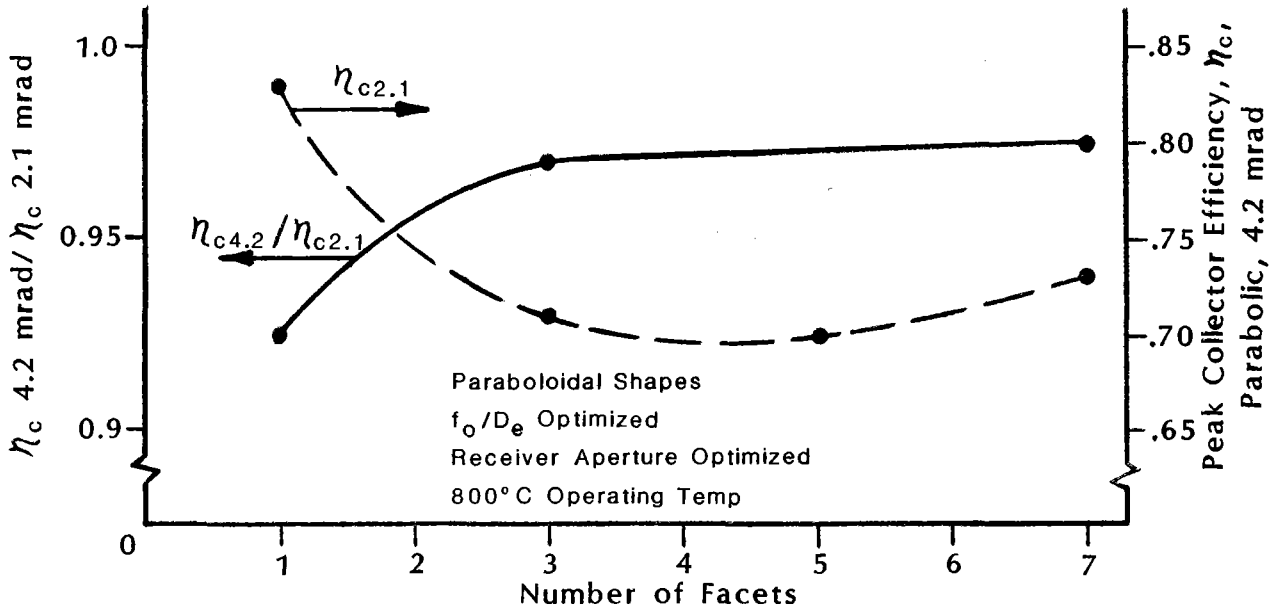

Figure 2.5 Sensitivity to Random Surface Error for Single-and Multiple-Facet Geometries

membranes from an initially flat shape was subsequently abandoned as an avenue for cost reduction to offset performance loss in multiple-facet geometries.

Preliminary investigations on an empirical basis were also performed in this contract to consider membranes formed in the plastic region at the reduced f/D ratios that correspond to multiple-facet concentrators. These experimental attempts were conducted by yielding membrane materials with a controlled load, and in the absence of any mandrel or mold. (This free-form yielding process was, ultimately, adopted for the final design. The technique is discussed fully in later sections of this report.) The results of this investigation indicated that no measurable gain in surface accuracy was obtained for f/D ratios in the range of 0.6 to 1.8. The error inherent in elastic shapes suggested, in theory, that increased plastic forming was desirable. As the amount of permanent strain increases, the residual impact of elastic stress should decrease.

The combination of experimental results and theoretical indications that error would decrease for lower f/D ratios, and the inability of five-facet geometries to perform in the elastic range, provided the basis for a qualitative conclusion: multiple-facet geometries would not enjoy a cost advantage to offset performance loss as a result of membrane formation.

The final assessment of potential for multiple-facet cost advantage was made with respect to supports. The advantage that multiple-facet geometry provided was the ability to support the concentrator at or near a weight centroid without substantial shading of the active aperture. This potential would reduce the static or dead load moment on the concentrator through counterbalance of the dish and receiver weights. A secondary potential advantage was the ability to transfer the receiver dead loads to ground with little probability of inducing a surface error through concentrated loads imposed upon the optical element. A major disadvantage of multiple support was the increased distance between area or pressure centers and a central drive system. Secondary disadvantages included the potential for systematic error from facet pointing (or an increase in complexity or stiffness to reduce pointing error through adjustment).

No fundamental laws or principles provided an estimate of the relative merits of single- and multiple-facet support systems. A strictly qualitative assessment or judgement was made that multiple-facet supports would not provide an advantage that could offset the performance loss. The near-centroid support point reduces static overturning moments. The magnitude of the weight- induced moment in single-facet designs was assessed as a significant fraction of the total: 15% at the worst wind geometry; 50 mph velocity, for the proposed support system. A reduction in this moment would reduce the moment on those components that transfer loads to ground from the central drive point (e.g., a pedestal in conventional support designs). The wind moment, on the other hand, would actually increase in multiple-facet geometries on the structure responsible for transfer of loads from the facets to the central support point (c.g., radial cantilever or space frames in conventional designs). This increase was anticipated as a result of the increase in distance between the central support and facet area or pressure centers.

Both support systems suffer from a potential secondary error. The single-facet systems will likely feed receiver loads to ground through elements at least weakly coupled to the optical surface. The multiple facet suffers from the potential of initial misalignment of facets or misalignment as a result of the oscillatory load environment faced by a concentrator.

The scope of this contract was limited to conceptual support design only. The optical element design, and demonstration of stretched-membrane feasibility for dish collectors, represented the thrust of contract efforts. The additional moments seen by the facet-to-drive structure were arbitrarily assumed to offset the moment reduction from drive to ground; the reduced error from receiver support were assumed to offset the increase in pointing error. This judgement can be refined only through comparison of actual structures, which was outside the scope of this effort. The lack of a quantifiable solution to the relative merits of support systems, within contract limitations, provides a potential avenue of investigation in stretched-membrane dish optimization. A recommendation for further research in this area is not suggested, however, due to a clear and consistent engineering judgement that multiple-facet supports will not offset the performance advantage of single-facet geometries.

2.4 Summary of Optical Geometry Selection

This analysis of optical geometry clearly indicated that single-facet concentrators provide the best collector performance. No quantitative or qualitative reason was identified to select a multiple-facet geometry.

The scope of this analysis was limited by contract to consideration of a large-aperture concentrator defined by a maximum of five facets. The optimization effort considered axisymmetric facet shapes only. No attempt was made to refine this assumption, as multiple-facet geometry can only approach single-facet performance, rather than exceed it. No evidence was found during this development to indicate that multiple facets would provide a better geometry. Secondary concentrators were also not considered in this optical analysis. The secondary concentrator was seen as an appropriate element to consider in design analysis if substantial systematic or random deviations from parabolic shapes occurred. The stretched-membrane dish analysis and empirical work to date indicate that these deviations can be controlled through adjustment of fabrication efforts.

The results of our analysis indicated that single-and multiple-facet geometries optimize at different fundamental f/D ratios. The larger individual facet f/D ratios of the multiple geometries increase the accuracy of spherical approximations for parabolic shapes. The larger receiver aperture sizes of the multiple-facet dishes also decrease the sensitivity to surface error. The magnitude of these insensitivities to shape and random error remained small with respect to the overall performance reduction. The

single-facet demonstrated better performance even under error conditions of twice the contractual goals, with f/D ratios optimized for each geometry.

The sensitivity of membrane fabrication to f/D ratios was addressed from a theoretical and empirical approach. Both paths led to the conclusion that no gain in surface accuracy could be achieved through an increase in facet focal-length-to-diameter ratios. Supports were qualitatively assessed; no quantifiable justification for multiple- or single-facet supports was defined within the limitations of the contract. An engineering judgement was made that multiple-facet support systems would not provide an advantage in the design development of a stretched-membrane dish.

Single-facet geometry was established as the baseline for additional development of the stretched-membrane dish. The only avenue for retreat from this design position was the potential inability to fabricate an accurate concentrator surface in large sizes. All efforts in the first phase of this analysis have demonstrated the potential for cost-effective success in the single-facet approach.

3.0 Material Selection

The selection of materials for the design development presented here focused upon the optical membrane. This membrane demonstrated the largest number of design constraints, and, in some respects, the most ambiguous restraints for all elements of a stretched-membrane dish. Materials for the support frame were selected to provide an accurate membrane platform under load.

The optical membrane selection required investigation of different material groups defined by contract: polymers, composites, and metals. The selection from this group of materials was directed by consideration of performance during operation, rather than fabrication limits. Fabrication problems were addressed in a limited fashion after basic requirements of a material in operation were assessed.

Fundamental distinctions in material properties were identified, and the analysis addressed the optical and/or structural impacts of these differences. The distinctions highlighted were viscoelastic behavior, tensile modulus, and surface characteristics. The impact of these properties was developed through several simplifying assumptions to make the analysis tenable. The assumptions in the analysis were subsequently examined to define the type of error introduced.

Metals were selected as the best material group for the optical membrane. Aluminum provided the best combination of material properties and cost, and was selected. A caveat was added at the end of this phase of investigation. There were potential fabrication limits in forming tempered aluminum, which were not investigated. Stainless steels, particularly when combined with lower cost ring materials, offered attractive alternatives to aluminum at slight cost penalties.

3.1 Material Group Selections

The contract under which this work was performed required consideration of polymers, composites, and metals for the the optical membrane. The approach to selection of a single material group was based upon several constraints. The principal requirements established at the beginning of analysis were

*the membrane must carry load with uniform and predictable deflection which can be forced into a parabolic shape, and

*the material must present a smooth and highly specular reflective surface.

The fundamental distinction among the identified material groups, with respect to the principal requirements, were viscoelastic behavior, tensile modulus, and surface characteristics.

Polymers, and the matrix of composites, exhibit viscosity behavior. This material property was loosely described as the non-linear dependency of strain on load, time, and environmental conditions. There was no clearly defined proportional limit that described the onset of significant flow in viscoelastic materials. The properties were generally expressed in terms of creep or stress relaxation. Creep was defined as the strain that occurs with time under a constant load too small to produce immediate measurable plastic deformation [Ref. 8]. Stress relaxation was the reduction in load required to maintain a constant strain as a function of time. Both creep and stress relaxation describe the same viscoelastic behavior under different test conditions [Ref. 9]. This type of behavior was assumed not to occur in metals at ambient conditions [Ref. 8]. Viscoelastic behavior, or creep, was identified as a significant property because the shape of the membrane would change as a function of time. Optical performance was dependent upon the membrane shape.

The tensile modulus described the stiffness or immediate response of a material to load, and was defined as the ratio of stress to strain in the elastic range. Polymers and composites do not have a well-defined range of elastic or linear behavior, and the tensile modulus was an approximation of response. The tensile modulus of metals was found to be an order of magnitude greater than polymer or composite moduli. Tensile modulus was a critical property because it also defined the basic shape of a membrane, though the effect was independent of time.

The surface characteristics of metal and polymers have demonstrated excellent specularity. Composites, on the other hand, have not demonstrated good surface characteristics for optical reflectors. The investigation accomplished here was directed at selection of appropriate materials in the development of a dish design. Material development was not considered unless a specific material group demonstrated a quantifiable gain in the dish performance or value.

3.1.1 Viscoelastic model

Viscoelastic behavior is a complex material response that depends upon load, load rate, load history, time, and environmental variables such as temperature and humidity. This analysis applied a very simple model to define viscoelastic behavior: creep was assumed to be uniform. In other words, the impact of directional response, position in the membrane, and environment was neglected. This assumption limited the accuracy of the investigation to consideration of order of magnitude effects.

The uniform assumption was modeled as a difference in thermal coefficients in the membrane or ring. A linear finite element model was constructed so that each element defined approximately the same amount of aperture. A membrane with a relapsed parabolic shape defined by an f/D ratio of 0.6 was attached to a simple support boundary, and the reference temperature was changed to impose a uniform expansion in the plane of the membrane. A uniform pressure was applied to the membrane to simulate the stabilization load used in the dish. The membrane produced shapes with constant uniform pressures, but different planar expansions were approximated with high-order polynomials. CIRCE [Ref. 4] was subsequently used to define the performance of the curve fit shapes.

A membrane with a relapsed parabolic shape defined by an f/D ratio of 0.6 was loaded with a uniform stabilization pressure, but no uniform expansion or creep was applied. The performance of the loaded shape was compared to an idealized parabola. The optical efficiency comparison presented in Figure 3.1 required optimization of the focal length of the loaded parabola for each receiver radius. This uniformly loaded membrane, with a parabolic relapsed shape, defined the basis for comparison in the investigation of creep.

The magnitude of viscoelastic or creep-induced error with no compensatory control was established with this model. The optimum receiver aperture of the loaded parabola (with no creep) was established and held constant. A uniform strain was imposed on the model membrane; the resultant shape was curve fit; and the curve fit was used as an input to CIRCE [Ref. 4]. The reduction in performance as a result of uniform creep is shown in Figure 3.2. This analysis indicated a performance loss in excess of 20%. The conclusion was that creep either required a compensatory control, or would result in unacceptable degradation of performance.

The primary mechanism for compensatory control investigated in this contract was adjustment of stabilization pressure. The conceptual approach was defined as a classic stress relaxation problem: strain in the membrane would be held constant through a reduction in the pressure load. The results of this analysis indicated that performance would remain constant while the uniform pressure load was positive. No degradation from creep would occur while stabilization pressure was applied to the concave side of the membrane, given the linear response and uniform creep assumptions.

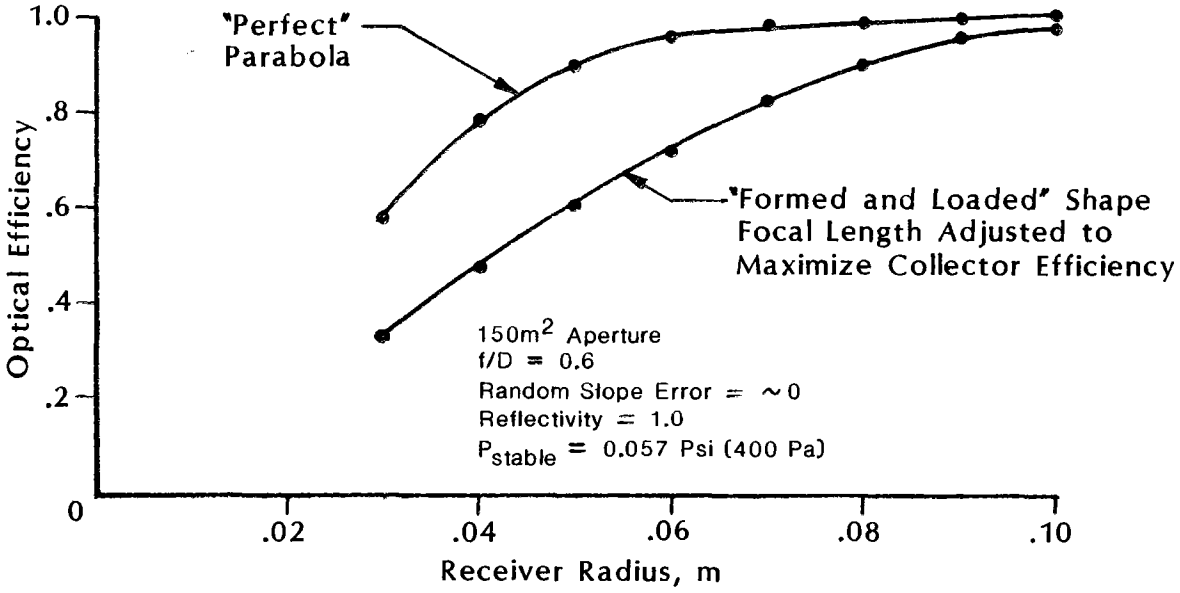

Figure 3.1 Comparison of the Optical Performance of an Idealized Parabola and a Uniformly Loaded Membrane, With a Relapsed Parabolic Shape.

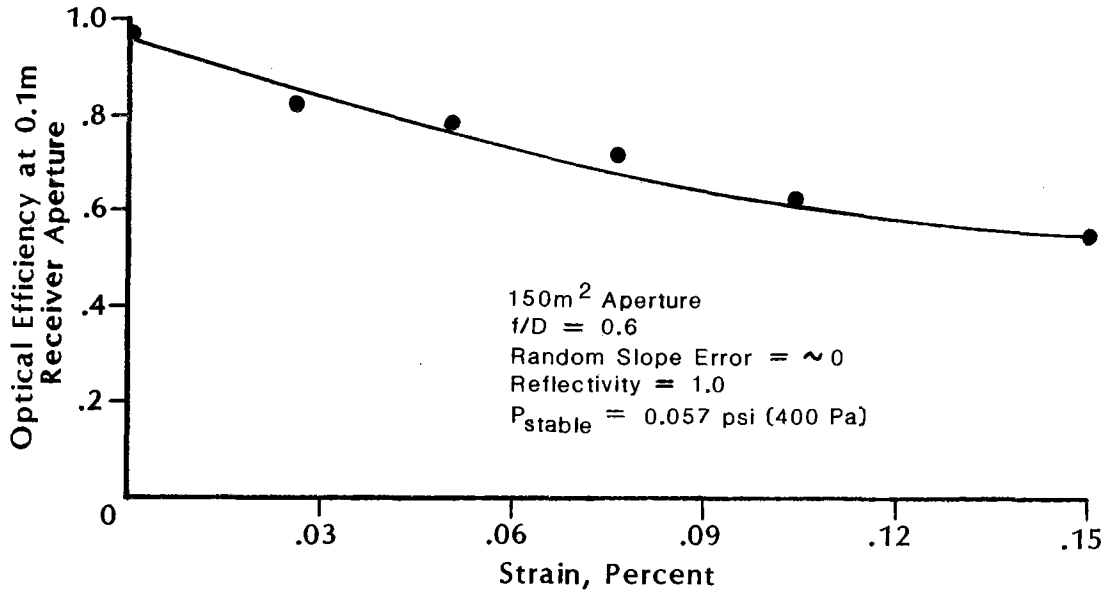

Figure 3.2 Performance Degradation From Uniform Creep. Receiver Optimization Based on Figure 3.1.

Stabilization load was assumed to be applied by creating a slight negative pressure in the plenum formed by the front and rear membranes. The operating wind environment was arbitrarily defined as 27 mph (12 m/s), with a corresponding dynamic pressure of 0.013 psi (88 Pa). The wind creates a vacuum on the leeward side of a bluff body with a relatively constant magnitude of 60% of the dynamic pressure [Ref. 10]. Consequently, the stabilization pressure must exceed 0.008 psi (53 Pa) to maintain concentrator performance.

The minimum stabilization pressure will occur at the end of the defined creep cycle. Two stabilization pressures were defined. The final pressure (p_f) was the stabilization pressure after creep. The initial pressure (p_i), required before any creep occurred, was defined with the uniform creep assumption and application of the membrane shapes produced by the methods of Steele and Balch [Ref. 11]. The final shape, after creep, was assumed to be a relapsed parabola with an f/D ratio of 0.6. The length of this parabolic arc was determined. The shape of the membrane, prior to creep, was also assumed to be parabolic, and the initial f/D ratio was calculated. This approach provided an initial and final relapsed membrane shape with different f/D ratios.

The minimum final pressure was established at the leeward vacuum imposed by the wind, and pressures at and above this minimum were arbitrarily selected. This final pressure was applied to the final membrane shape, and the focal length was determined based upon collector efficiency. The initial pressure was defined by iteration, so that the focal lengths for the initial and final concentrator shapes were identical. The process is illustrated schematically in Figure 3.3.

Figure 3.4 illustrates the initial pressure requirements, given the final pressure and a constant focal length, as a function of creep strain. The difference in pressure was actually used to simplify the presentation of data. The relationship was linear, and independent of the actual final pressure selected over the range investigated. It was also of interest that the difference in pressure was essentially proportional to the membrane thickness. In other words, as the membrane thickness increased, the difference in final and initial pressure requirements increased in proportion.

The final step in the analysis was to estimate the magnitude of uniform strain anticipated in the membrane. The first contributor to variable strain that had to be compensated for in the pressure adjustment was the difference between thermal and hygroscopic coefficients of expansion (TCE, HCE) in an aluminum ring frame and polyester membrane [Ref. 12, 13]. The total strain to be accommodated was based upon a maximum change, from assembly to operating environment, of 50% relative humidity and 72°F (40°C). The total value of uniform strain, as a result of these environmental changes, was 0.058%. The minimum initial stabilization pressure was redefined as the the sum of the initial wind requirement (0.008 psi), and the pressure required to compensate for environmental changes (0.018 psi for 0.010" membranes, 0.036 psi for 0.020"

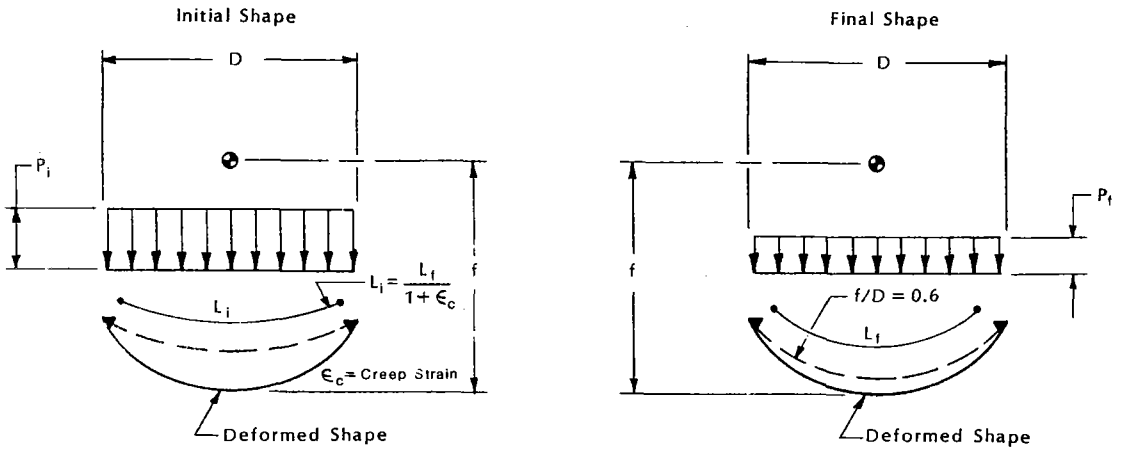

Figure 3.3 Schematic Representation of Initial and Final Membrane Response for theViscoelastic Model.

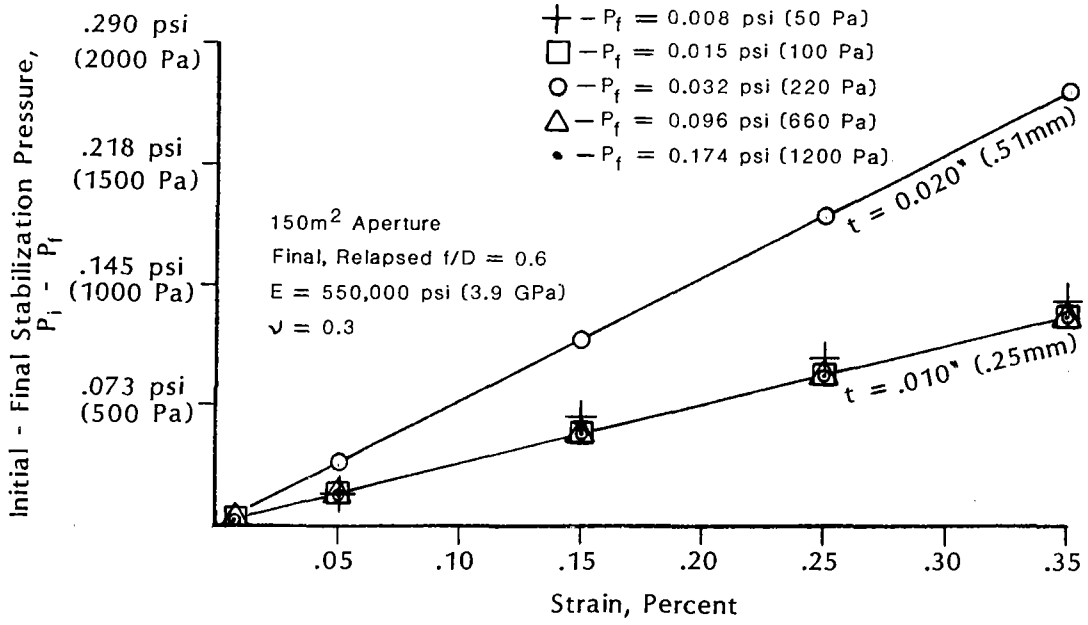

Figure 3.4 Initial Pressure Requirements to Compensate for Uniform Strain in a Membrane.

membranes). The minimum initial pressures were 0.026 psi (175 Pa), and 0.044 psi (300 Pa), respectively.

The second, and major contributor to strain, was viscoelastic behavior in the polymer. The load in the membrane was assumed to be a result of the stabilization pressure alone, and membrane tension was defined with the Steele and Balch solution [Ref. 11]. Ideally, the polymer creep strain rate would be defined as a function of membrane tension or stress. The creep strain rate, combined with a dish life, would subsequently define the initial pressure requirements. Unfortunately, this material property could not be found in the literature.

Estimates were made by looking at expected ranges. For example, at the minimum pressure required for wind, TCE mismatch, HCE mismatch, and no creep strain, the stress in the membranes was predicted to be 860 psi (5.9 MPa) for the 0.010" membrane, and 730 psi (5.0 MPa) for the 0.020" membrane.[1] Consequently, the creep strain curves of interest would be for loads larger than 730 to 860 psi (5.0 to 5.9 MPa). Creep data at 2000 psi (13.8 MPa) were available. Biaxial creep of PET and creep of a composite, PET/ECP-300^R (ECP-300^R is a silvered acrylic reflective material made by the 3M Company), was presented by Dr. Cakmak, of the University of Akron in September of 1987 [Ref. 14, 15]. Creep for the same PET/ECP-300^R composite was presented by B. Benson of 3M at the same meeting [Ref. 16]. This information is summarized in Figure 3.5.

The relative similarity between the University of Akron and 3M data indicated that the creep tests were repeatable by different researchers. The data also indicated that creep strain would be substantial, even for a single hour decade (an hour decade occurs between 10-100 hours, 100-1000 hours, 1000-10000 hours, etc.). The creep between 100 and 1000 hours, for example, was 0.17%. Creep rate can generally be extrapolated by one decade in hours [Ref. 9]. Consequently, for 4-416 days, a creep of 0.34% would be anticipated if the load were constant.

---

[1] It is interesting to note that doubling the thickness does not reduce the stress by half. This apparent inconsistency was a result of the higher initial pressure requirements as a function of membrane thickness (see Figure 3.4).

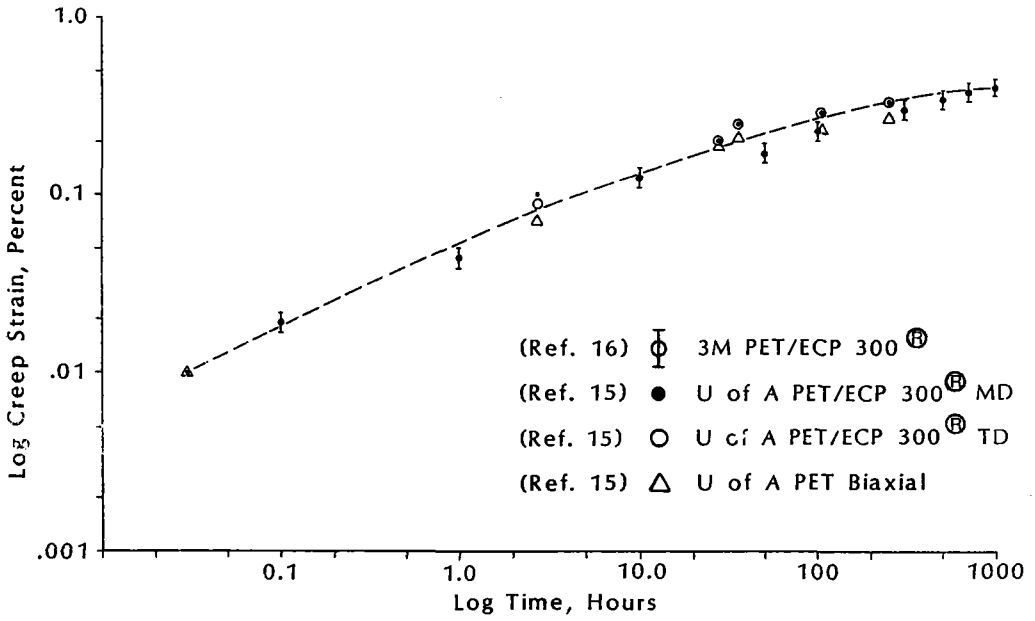

Figure 3.5 Creep Strain for PET and PET/ECP300^{R} Polymers at 2000 psi (13.8 MPa). [Ref. 15, 16].

The creep strain was used to predict the initial pressure requirement (see Figure 3.4), based upon a final pressure just adequate for wind, and the TCE/HCE mismatch. The results are shown in Table 3.1. The mean stress was assumed to be a reasonable indicator of the mean creep. Consequently, the creep values of 2000 psi (13.8 Mpa) were considered reasonable for the minimum conceivable final control pressure.

Table 3.1

Stress in a PET Membrane with Compensatory Pressure Control

Membrane Thickness in. (mm)	Initial Stress psi (MPa)	Final Stress psi (MPa)	Mean Stress psi (MPa)
.010 (.25)	4600 (31.7)	860 (5.9)	2730 (18.8)
.020 (.51)	4800 (33.1)	730 (5.0)	2760 (18.8)

The results indicated two key points. First, an increase in thickness did not reduce the impact of viscoelastic behavior. The initial and final stress states were nearly the same for a variation in thickness by two, as a result of the proportionality between thickness and load difference. Consequently, the creep strain would also be similar for each membrane. Second, the creep over 2-hour decades alone resulted in substantial initial stabilization pressures and membrane stresses. This result indicated that control of creep through pressure adjustment was marginal, at best. If any safety factor were applied to the final stabilization pressure, if any creep continued at the final pressure, or if the operational lifetime of a concentrator exceeded 2-hour decades, visocelastic response in a polymer membrane would overcome compensatory pressure control.

3.1.2 Limitations of the viscoelastic model.

The major limitations or assumptions in the model were the inherent linear response assumed with the use of a linear finite element code (ANSYS-PC, Ref. 17), the ability of a polynomial to represent the membrane shape, and the uniform creep assumption. Some qualitative measures were used to explore these assumptions.

The linear assumption was tested by defining an initial or relapsed parabolic geometry corresponding to an f/D ratio of 0.6. A pressure was applied, and the deflection near the center was determined with the finite element code. The deformed geometry was used to define a second shape, to which the same uniform pressure was applied. This approach was similar to load application in two equal steps, except the stiffness matrix was calculated between each load application. This calculation insured that any increase in geometric stiffness was accounted for in the model. The ratio of deflection near the center for the first and second load application was assumed to define linearity. The results and schematic approach are shown in Figure 3.6.

This test did not account for other non-linearities such as material stiffening or edge effects. The material stiffening aspects were tested by applying the same procedure in the more general, non-linear ANSYS finite element code. The results were nearly identical [Ref. 18].

The edge effects were considered through the application of the solution developed by Steele and Balch [Ref. 11]. This edge solution supported the linear assumption near the center of the membrane, but indicated a non-linear solution at the edge. This indication was ameliorated by the use of the linear produced shape as the basis for comparison. In other words, throughout the previous development the "best" performance was based upon the geometry defined with ANSYS. Creep was considered only by defining the reduction in "best" performance.

The ability of a polynomial to represent a membrane shape was explored with a test case. The CIRCE optical code allows a power series to define membrane position. Membrane slope is defined as the derivative of that series. Both position and slope

contribute to performance error. A single polynomial power series cannot generally be defined that precisely represents a general function and function derivative, without regard to order.

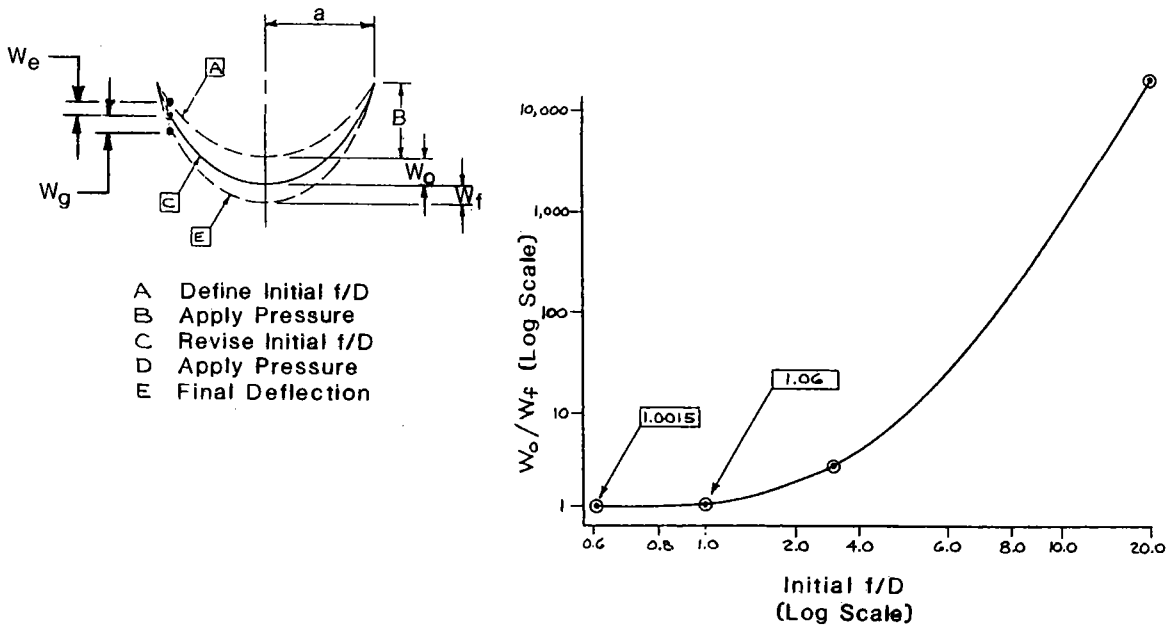

(Ref. 11) Supported Linearity Near Center

f/D	W_o / W_f
0.6	1.00
1.0	0.99

(Ref. 11) Indicated Nonlinear Near Edge

f/D	W_e / W_g
0.6	0.84
1.0	0.74

Figure 3.6 Linearity Test Applied to Viscoelastic Model.

The relationship between position and slope error in a sphere (the test case) was defined as a function of radial position. The spherical slope was subsequently curve fit with different orders of polynomials, the slope function was integrated to define the position power series, and the position error was related to slope error. The sum of position and actual slope error ("equivalent slope error") was plotted as a function of polynomial order in Figure 3.7. This analysis indicated that a sphere, at least, could be represented with a third-order polynomial based upon slope, or a fourth-order polynomial based upon position. A fourth-order shape was used for the viscoelastic model. The error from this curve fit was therefore assumed small. No attempt was made to verify the accuracy of CIRCE to predict optical performance.

Polymer response is generally dependent upon the temperature, load rate, load history, and load magnitude [Ref. 9]. Any variation in creep response, as a result of these vari

ables, was neglected with the uniform model. The creep strain testing referred to in the previous section was conducted at 122°F (50°C). The impact of temperature on creep strain for the referenced polyester was investigated by Dr. Cakmak (identified as 3x3 PET samples in Ref. 15). The variation in strain rate was less than 10% over the 85-122°F (30-50°C) temperature range. The ambient conditions across the aperture at any time were assumed to be constant. Consequently, localized strain from temperature variation was neglected. The cumulative impact of a difference in mean concentrator ambient and test conditions could affect the estimates of cumulative strain in the dish, but would not affect the procedure used. The estimates of average strain probably have greater uncertainties than those imposed by temperature, however.

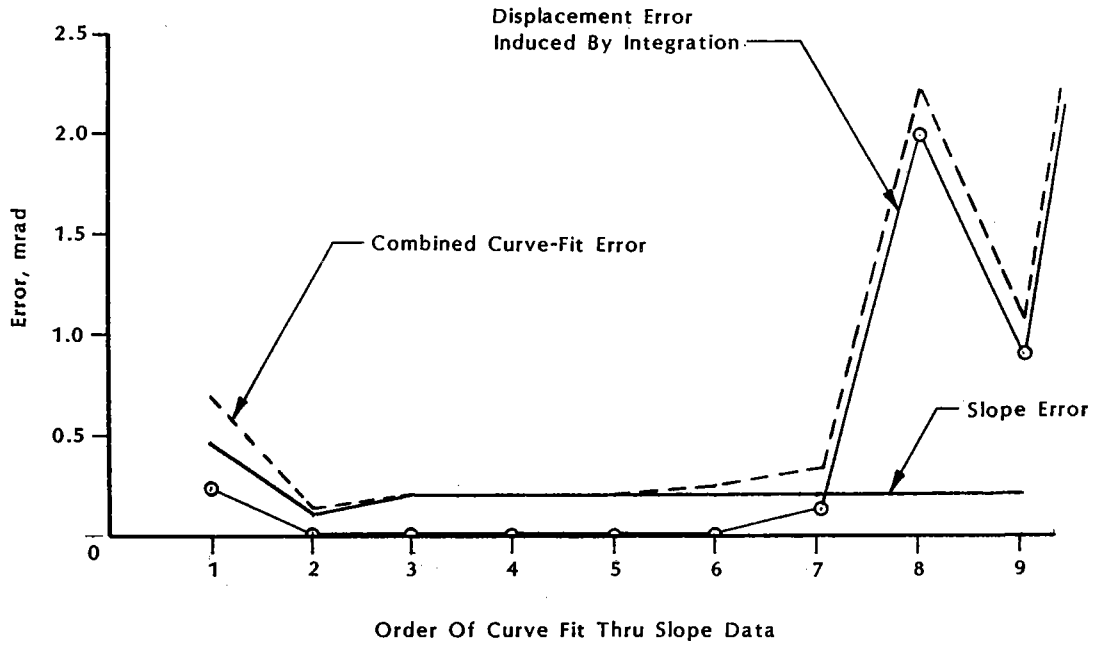

Figure 3.7 "Equivalent Slope Error" Associated with a Polynomial Representation of a Sphere.

Load rate was not assumed to have a major impact on the stretched-membrane response, as the load was controlled. Consequently, rate impacts on viscoelastic behavior were neglected.

Load history was used here to identify the processing that occurred during fabrication. The variation in creep, as a function of the machine and transverse directions, was less than 10% and reduced as strain increased [Ref. 16]. This error was neglected in the viscoelastic model, but will likely have a significant optical impact in an actual concentrator. The anisotropic creep response may be important because the relationship

between meridional and circumferential tensions define the membrane shape, the material processing directions will not be aligned with the membrane axes, and an axial asymmetry will be introduced. The magnitude of anisotropic response was not defined, but was assumed to reduce optical performance as a result of the asymmetry. Consequently, the viscoelastic model used here was probably not adequate to establish good optical performance. The conclusions with respect to the inability of pressure to compensate for creep remain unaffected.

The final issue explored in th uniform creep assumption was the uniformity of load. The solution for membran and bending stress developed by Steele and Balch [Ref. 11] was used to define the radial and circumferential tension. A set of typical polymer properties was defined in conjunction with a relapsed parabolic shape with an f/D ratio of 0.6. The stabilization pressure was varied over a range of 0.015 to 0.17 psi (100-1200 Pa).

The tensions induced in a membrane under uniform pressure are shown in Figures 3.8 and 3.9. The tensions were plotted as a function of the normalized radial position (the ratio of the radial position to the outside radius). The radial tension, shown in Figure 3.8, was relatively constant over the range of pressures. The variation in load was less than 5% up to a pressure of 0.096 psi (660 Pa), and approximately 10% at the substantial pressure of 0.17 psi (1200 Pa), used essentially to bracket the pressure range.

The circumferential load, shown in Figure 3.9, was not constant as a function of radial position. The stress diminished in the circumferential direction at the membrane edge because of the circumferential fix. The non-linearity increased with increasing pressure. The effect of variation in the circumferential load was not assessed, with respect to viscoelastic behavior (the edge effect solution was not available during the majority of the reported contract effort).

This variation was probably the major limitation or inaccuracy imposed upon the viscoelastic model presented in the earlier section. The only qualitative assumption made with regard to this model limitation was that creep was unlikely to create a parabolic membrane. The membrane was assumed to progress toward the minimum strain energy shape: a sphere. This assumption indicates that the viscoelastic model presented here would predict better performance than might be achieved with a polymer membrane. This limitation again indicated a potential failure in the ability of this model to establish good performance of a membrane subject to creep. The results, which indicated an inability of pressure to compensate for the viscoelastic response, were probably not affected.

The viscoelastic model used here was an approximation of membrane response. The analysis indicated that creep cannot be accommodated without a compensatory control. The model was also adequate to demonstrate that pressure control was marginal

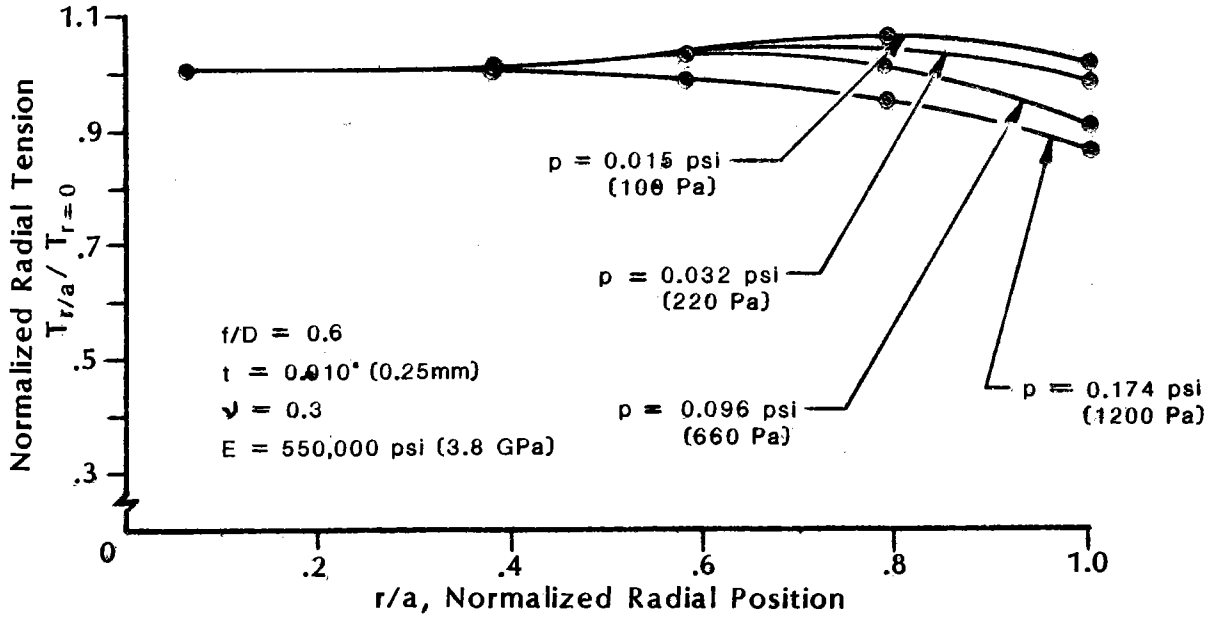

Figure 3.8 The Uniformity of Radial Load in a Pressure-Stabilized Membrane.

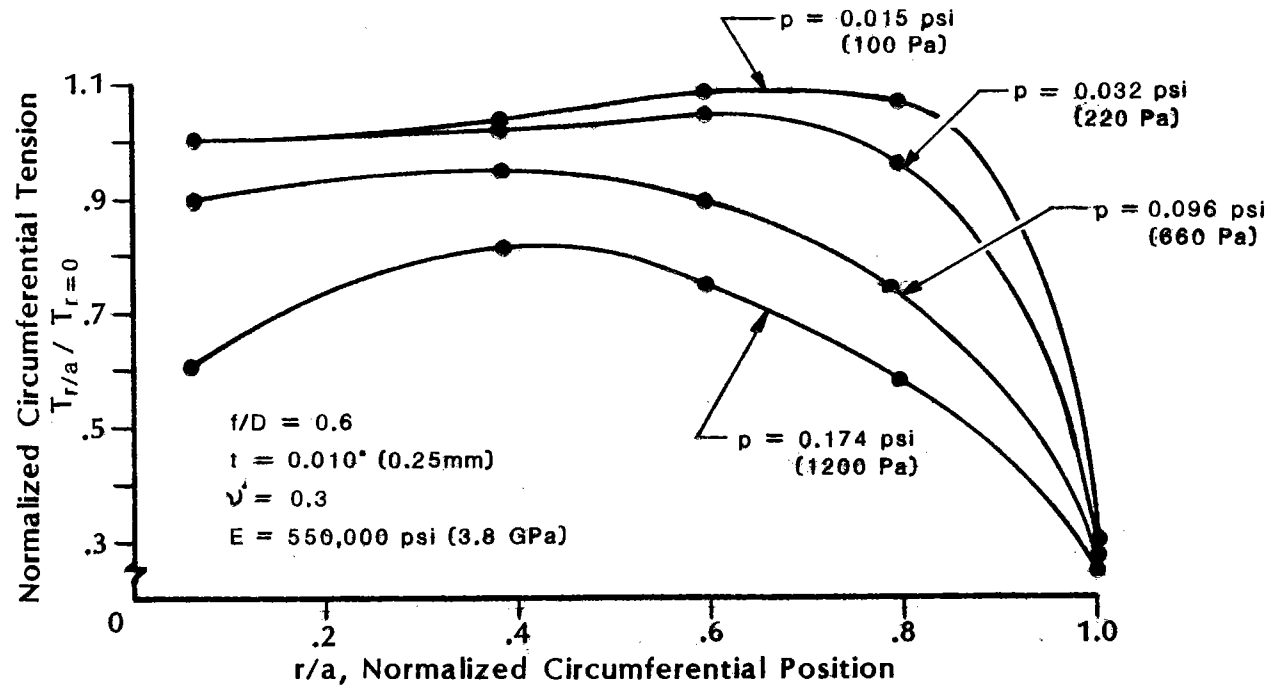

Figure 3.9 The Uniformity of Circumferential Load in a Pressure-Stabilized Membrane.

or unsuitable as a reaction to creep in a membrane. The model's accuracy was limited, particularly by the non-uniform load in the circumferential direction imposed by the boundary. The magnitude of optical errors from non-uniform response, whether induced by material anisotropy of this load dependence on radial position, was not defined. In general these responses should reduce optical performance. The immediate, as opposed to time-dependent, impacts of the boundary are investigated in the following section.

3.1.3 Tensile modulus

The second fundamental property distinction among the groups of materials considered for membranes was the tensile modulus. This material property was defined as the ratio of stress to strain within the elastic region. Polymers and composites do not exhibit a clearly defined elastic region, but the modulus can still be defined with relative certainty. The tensile modulus was independent of time. This property was considered important because of its effect upon shape, particularly at the edge or boundary of the membrane.

Typically, thin shells were assumed to carry all loads in the plane of the membrane, and bending moments were assumed to be zero. In fact, the boundary conditions induced some bending stress, which resulted in a deflection and caused optical error. This error was limited to an area "near" the edge, where "near" was a function of the tensile modulus. The area that was affected by bending stresses was defined by Steele and Balch [Ref. 11] in terms of a decay distance. The radial decay distance, d, where bending stresses were reduced to approximately 4% of maximum was defined as:

$d = (pi)(rc)^{1/2}/ß$ where
$r = 2f/\cos H$
$c = t/[12(1-v^2)]^{1/2}$
$ß = [g-(g^2-1)^{1/2}]^{1/2}$
$g = pr^2/(4Etc)$

[Ref.11]

f = focal length
H = angle, optical axis to surface normal at edge
t = membrane thickness
v = Poisson's ratio
E = tensile modulus
p = stabilization pressure

The decay distance was plotted as a function of tensile modulus for representative membranes in Figure 3.10.

The decay distance essentially determines the region where the bending moment imposed by the boundary restraint affects membrane performance. The relationship to tensile modulus was strong for all pressures and thicknesses considered for the membrane dish. The decay distance, and by inference the aperture affected by edge effects, was substantial for low modulus materials.

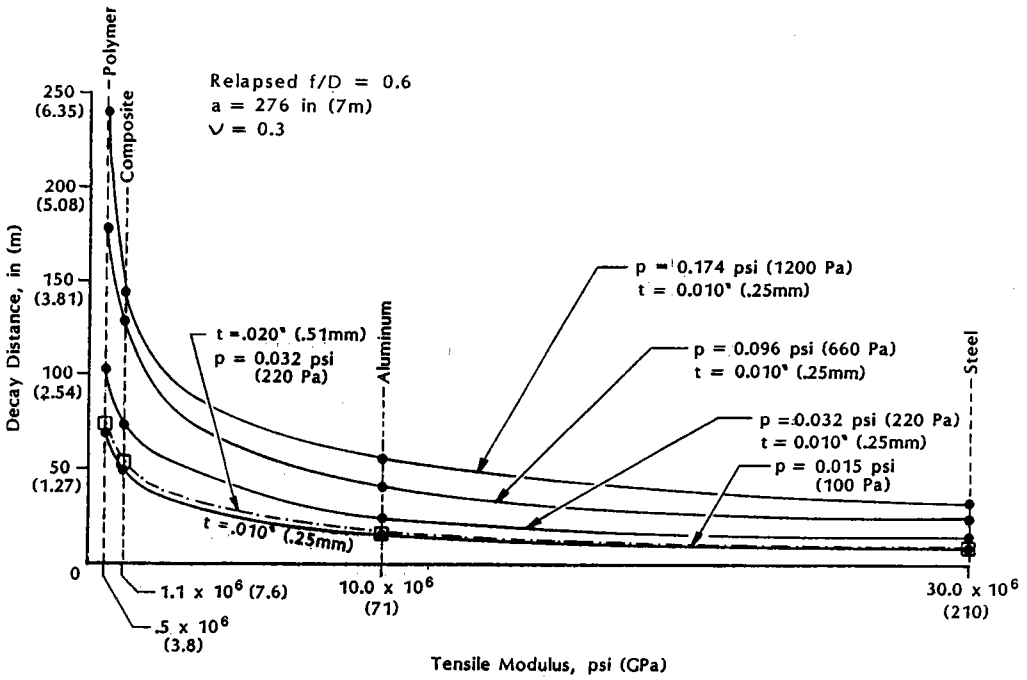

Figure 3.10 Relationship of Bending Stress Radial Decay Distance and Tensile Modulus.

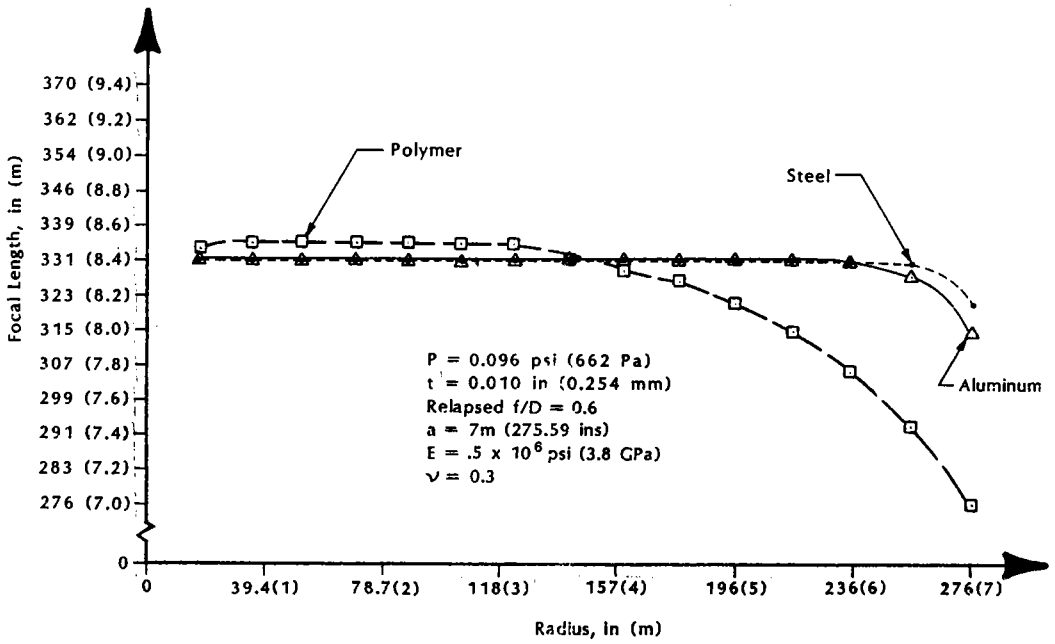

Figure 3.11 Bending Decay for Three Membrane Materials Presented in Optical Terms.

The impact of bending stress is defined in optical terms in Figure 3.11. Three materials were selected to encompass the tensile modulus range, and the focal length was plotted as a function of radial position for a representative membrane case. An ideal parabola would exhibit a constant focal length from center to edge. The concentrator shapes predicted by the edge effect solution were subsequently represented by a high-order polynomial, used with CIRCE to predict optical efficiency, and convolved with the receiver efficiency of Figure 2.1 to define collector efficiency. Random errors were set at near zero, and reflectivity at 0.93. The focal length was optimized in CIRCE to maximize collector efficiency. The high modulus membranes (aluminum and steel) exhibited a predicted performance in excess of 90%. The predicted collector efficiency of the polymer membrane was 55%. This analysis was repeated with a random, circular, normally distributed error of 3 mrad on all membrane shapes. The collector performance for metallic membranes was predicted at 0.85; for polymer membranes the predicted performance was 0.52. It was interesting to note that the area weighted average of focal length was an excellent prediction of the optimum focal length developed with iterations in CIRCE.

The performance penalties associated with edge effect were determined to be strongly related to the tensile modulus of the material and boundary conditions. The high-modulus membranes, such as aluminum or steel, have minimal performance loss associated with edge effects. The polymers and composites, when combined with a circumferential fix at the boundary, suffer a severe performance penalty.

Alternate boundary conditions have been explored by other researchers [Ref. 19], and relationships between materials and performance were substantially affected by the circumferential attachment. Specifically, the attachment diameter may be increased to offset the loss experienced by low modulus membranes with relapsed parabolic shapes. The adjustment of attachment diameter has also been suggested as a compensatory control for creep, which does not suffer from the increases in load associated with pressure compensation.

The requirement for attachment diameter control was explored briefly in the proposal, and early in the analytical and empirical phases for this contracted effort. The approach was abandoned. No control was required for high-modulus membranes; low-modulus membranes did not provide a quantifiable advantage in material cost or performance based upon operation of a stretched-membrane dish. Consequently, the complexity associated with an additional, controlled degree of freedom in dish operation was not imposed upon the design by material selection.

3.1.4 Surface characteristics

The material group selected for the membrane was required to provide a smooth substrate to achieve a specular reflector. The actual reflective surface, in all material groups considered, was assumed to be a silvered polymer. Silver was the only material

that provided a reflectivity capable of achieving performance goals. Silvered polymers have consistently been identified as a comparatively inexpensive, specular-reflective surface suitable for solar concentrators [Ref. 20]. The silvered polymer also provided the advantage of low weight and flexibility, by comparison with glass reflectors.

The performance of commercially available silvered polymers, particularly ECP300^R, has been predicted through extensive testing. The specular reflectance of unlaminated, stretched ECP300^R was defined at 0.93, with a one sigma, standard deviation, specularity error of 0.5 mrad [Ref. 21]. Specularity error represented less than ten percent of the error goal for the concentrator.

The reflective film can be laminated to the substrate membrane; this lamination will generally increase the specularity error. The same research that defined stretched ECP300^R performance was used to define the performance of films laminated to aluminum, yielding a specularity error of 1.25 mrad.[1] Lamination of ECP300^R to float glass has been described by Schissel and Neidllinger, with a specularity error of 0.7 mrad [Ref. 20]. The float glass substrate was exceptionally smooth. Polyester laminate values using the same measurement procedures were not available from these researchers, but Schissel and Neidllinger have indicated good optical performance [Ref. 20] with the polymer laminates (0.93 reflectivity into a full cone angle of 4 mrad). Comparisons between the laminates considered and glass demonstrated the relative importance of the adhesive layer, and the surface roughness of the substrate. The specularity of the metal substrates, with or without the error induced by the adhesive layer, represented a significant fraction of the error goal (18-31%).

Similar measurements on composite substrates with silvered polymer reflective films were not widely available. Reflectivity measurements of ECP300^R laminated to a glass and polyester composite provided one sigma values of 3.3 mrad specularity error [Ref. 19]. These measurements indicated that the use of a composite, or at least some composites that have been developed for stretched-membrane use to date, would represent approximately 80% of the error goal defined by contract. It should be noted that these measurements were made on a substrate that had not been loaded at tension levels anticipated in the stretched-membrane dish for any significant length of time. Creep of the composite matrix, after time at load, was anticipated to increase the level of glass cloth "print-through" and reduce the specularity of the composite substrate further [Ref. 22].

---

[1] Schissel and Neidllinger reported substantially higher values of specularity error for ECP300^R laminated to bare aluminum: 4.7 mrad. [Ref. 20]. These values were partially attributed to curvature of the aluminum plate. The variation in measurement was substantial (one sigma: 2.4 mrad). Consequently, the values provided by Petit [Ref. 21] were used for aluminum laminates.

Limited measurements of reflectivity and specularity have also been made on glass and vinyl ester composites. These measurements were made with a different type of reflectometer, were difficult to reduce to the comparative terms used to describe reflector quality, and were limited by the gross shape or slope of the substrates. High values of specular reflectivity (0.94 at 8.4 mrad full cone angle, 0.97 at 15 mrad full cone angle, 660 nm) were obtained with a 15-20 mil (0.38-.51 mm) gel coat and calcium carbonate filler. No apparent improvement with surface veils was observed [Ref. 16]. These measurements were also conducted on samples that were not loaded.

The availability of specular reflectance measurements was severely limited during the course of this investigation. In general, the performance of all composite substrates for reflective films measured during this effort was poor by comparison with polymers and metals. The measurements for the referenced composites were considered optimistic, as they did not include any time-dependent material effects.

3.1.5 Secondary considerations in material group selection

Several secondary properties were associated with the materials considered for the optical membrane. These properties included structural coupling, elastic response, anisotropic response, cost, and fabrication limits imposed by the material selections. These effects were not fully quantified or not considered a major determinant in the selection of a stretched-membrane material.

Structural coupling was defined as an enhancement of the ring frame stiffness to radial and normal deflections as a result of the interaction between the membrane and frame. This issue is discussed fully in the structural section of this final report. Essentially, the membrane did not stiffen the frame, particularly for the hub and spoke support system, without regard to the membrane material properties. Coupling was defined as non-determinant in material selection.

At the onset of this contract effort, consideration was given to the elastic response of different membrane materials. The research conducted for moderate deformation of flat optical membranes under uniform pressures by Murphy [Ref. 23] indicated that a low-modulus material would experience less variation in radial and circumferential tension, as a function of position. Additional analysis and review of later works by the same researchers [Ref. 7] indicated that performance with flat membranes operating in the elastic region would provide unacceptable performance levels for reasonably short f/D ratios. After the need for initial forming was clearly determined, it actually became desirable to reduce the elastic deformation associated with stabilization pressure loads. In other words, the high-modulus materials were desirable candidate materials from the elastic perspective. This effect was not quantified, because the examination presented in earlier sections led to the selection of a high-modulus material.

The anisotropic or directional response of substrate materials within the operating range of the dish, corresponding with the elastic region of the material, was not quantified in terms of concentrator performance. Polymers exhibit anisotropy in TCE, HCE, tensile modulus, and creep strain. The quasi-isotropic (structurally isotropic within the membrane plane) composites referenced in this investigation will also exhibit directional response as a result of the compound curves in the glass fiber and matrix creep. Optical degradation was not quantified because the previous investigation identified a material group, metals, that is generally isotropic in the elastic or operating region [Ref. 8].

Material cost was not exclusively used to select a membrane material, but does present some interesting relationships amongst the groups considered here. Composites were the most expensive, with estimates ranging from \$0.64 to \$1.34/ft^2 (\$6.89-\$14.42/m^2) dependent upon quantity [Ref. 19]. Polyester costs for 20 mil (0.25 mm) were estimated at \$0.36 to \$0.40/ft^2 (\$3.87-\$4.30/m^2) [Ref. 24]. Aluminum costs ranged from \$0.14 to \$0.33/ft^2 (\$1.51-\$3.55/m^2),[1] for a thickness of 10 mils (0.25 mm) dependent upon quantity. Ferritic stainless steel costs were estimated at \$0.39/ft^2 (\$4.19/m^2) for 3 mil (0.08 mm) [Ref. 25]. The thicknesses used to present polyester and metal costs were based upon a constant ratio of operating to yield stress. The material costs tended to support the selection of metallic substrates for the membrane.

The final secondary consideration in material selection was the fabrication limits imposed by the relative material groups. Fabrication limits were a secondary consideration in the selection of a material group because of the stage of design development in stretched-membrane dish technology. No estimates of costs associated with fabrication problems imposed by each material group was available from the literature. Production costs were delegated to future work in this technology by contract. Consequently, the fabrication costs, without detailed investigation, were not considered as a fundamental determinant for material group selection.

A qualitative assessment of fabrication feasibility for the various material groups was considered appropriate. The purpose of this assessment was to determine if the selection of a material group, based upon its properties in operation, would ultimately impose a severe cost or performance penalty as a result of fabrication at moderate to large volume (1000-10000 concentrators per year). This assessment was limited to composites and metals, as the viscoelastic behavior of unmodified polymers was assumed to eliminate this candidate.

[1] Aluminum costs in experimental quantities were based upon prices paid during this contract effort. Volume prices were based upon large aluminum purchases made by SKI.

The major limitations imposed by metals were judged to be membrane forming in the plastic range, seams, and the potential requirement for in situ forming, or field fabrication of a membrane. Forming through the plastic range was successfully addressed in this effort at two scales, and is discussed in a later section of this report. The forming process was accomplished with a controlled load and proceeded through yield without the use of a mandrel or mold (free-form). In situ forming was also a conclusion of this Phase I effort. Field forming was dependent upon the development of a repeatable process; repeatability was demonstrated only at smaller scale in this contract activity. The impact of seams on the membrane was not quantifiably determined. Several potential approaches of fabrication to limit the error associated with seams were identified. Metals provided the basic requirements for a membrane (near parabolic contour, specular surface). No severe limits in fabrication were identified. Some questions about cost inevitably remained at the completion of this effort.

The major fabrication limits judged to be associated with the composite material group were enhancement of specularity and long cure cycles. Specularity in glass cloth composites was not demonstrated at the time of this effort. Research into composites was being conducted by SERI, but techniques that provided adequate specularity under load had not been developed [Ref. 19]. The experimental composites currently being investigated have cure times as long as 4-hours, even at temperatures of 150°F (65°C). Longer cycle times were required for ambient cures [Ref. 16]. These cure times will be a significant disadvantage in volume production, but were not judged to be a "show-stopper." Composites, to date, were unable to provide the fundamental material requirements outlined in the proposal and throughout the development of this design: specularity remained a major problem in composite use for optical membranes.

The metallic group was selected based upon three primary properties and some secondary considerations. First, performance loss from creep was not an inherent problem with metal membranes. The polymer group, and composites that have been measured to date, exhibit creep that required controlled compensation. The compensation, at least for the polymer group, could not be implemented through the exploitation of the differential pressure inherent in stretched-membrane design. Alternate compensation systems, such as active changes in the attachment diameter, would have added controlled degrees of freedom to the design.

The second primary property that favored metals was the relatively high-tensile modulus. This material property limited the optical error associated with edge effects (i.e., bending moments imposed by the boundary). The optical error of low-modulus materials could also be offset by changes in the attachment diameter.

The final primary property that favored metals and polymers was the surface smoothness or specularity. The "print-through" of the glass cloth in existing composites sheets would represent the majority of the error defined as a goal for this project.

Secondary considerations in the selection of a material group also stacked in favor of metals. The limitation of elastic response, in other words, the minimization of deflec-

tion as a result of stabilization or dynamic pressure, favored metals for the high modulus. Metals were also assumed to equal or better the response of the other materials with respect to directional properties during operation. Raw material costs clearly favored metals over composites, and were equal or slightly better than polymers. No major fabrication limits that imposed severe cost or performance penalties were identified for the metallic group.

The creep of polymers with no reinforcement was considered to be unacceptable for the optical membrane. Composites are designed to reduce creep problems, but carry a specularity performance loss. Both materials, polymers and composites, required an adjustment in the attachment diameter after fabrication. Metals have no performance loss as a result of creep and required no variable attachment diameter. The primary performance variables, particularly when combined with a cost advantage, defined metals as the best selection.

3.2 Selection of a Material

The selection of a membrane material within the metallic group was primarily based upon operating characteristics and material cost. Some consideration was also given to physical characteristics during forming. The introduction of secondary elements was allowed in selection within the material group, because the operating disparity among metals with respect to tensile modulus was small (see Figures 3.10 and 3.11). Ring materials were selected to match the optical membrane material. The selection of a material for the rear membrane was limited to a material suitable for closing the plenum. An exhaustive selection process was not applied to the rear membrane material during this effort.

The primary operating characteristic, which limited the selection of membrane materials, was corrosion. The metals that provided the best atmospheric corrosion resistance were aluminum, austenitic stainless steel, and martensitic stainless steel. Grades providing representative corrosion resistance, cost, and availability within each alloy group were 5052 aluminum, T304 stainless, and T430 stainless, respectively [Ref. 14]. Carbon steel and ferritic stainless steels were rejected as membrane materials on the basis of corrosion. No other metals were considered for the membrane substrate.

The major operational requirements of the ring material were a high yield strength and tensile modulus; these requirements basically limited the material selections to metal. Compatibility between the membrane and ring, with regard to the TCE differential and attachment, was also considered. Table 3.2 summarizes the equivalent strain for a temperature difference between assembly and operation of $50^{\circ}F$ ($28^{\circ}C$), and the estimated performance loss with no pressure control (see Figure 3.2) for some different material combinations.

Ferritic stainless and carbon steel, in addition to the like materials, were considered to be suitable candidates for the ring from the perspective of corrosion. Carbon steel, in

the thicker gages, can generally be protected if the structure is an open section. The oxidation of ferritic stainless, in thicker gages, actually forms a barrier to limit further oxidation [Ref. 14]. This alloy was consequently assumed to be acceptable for open or closed section rings.

In general, the ring and membrane were required to be like alloys from the perspective of thermal coefficients, with two notable exceptions. The martensitic stainless membrane was combined with a ferritic stainless or carbon steel ring for material cost development. Some consideration was also given to the potential for welded attachment between the membrane and ring. All like alloys selected here can be welded to one another. The ferritic and martensitic stainless alloys may also be welded to each other without extraordinary process control, though the corrossion resistance of the martensitic stainless at the weld suffers to some degree and heat treating may be required [Ref. 26]. Martensitic and carbon steel were assumed to produce a relatively poor weld from corrosion and strength perspectives.

Table 3.2

Performance Loss for Thermal Coefficient Mismatch Between the Ring and Membrane.

Membrane Material	Ring Material	Equivalent Strain	Relative Performance
Aluminum	Carbon steel	0.034%	0.85
Aluminum	Ferritic/Martensitic	0.038%	0.82
Aluminum	Aluminum	0.000	1.00
Aluminum	Austenitic	0.019%	0.92
Martensitic	Carbon steel	0.004%	0.98
Martensitic	Ferritic/Martensitic	0.000	1.00
Martensitic	Aluminum	0.038%	0.82
Martensitic	Austenitic	0.019%	0.92
Austenitic	Carbon steel	0.015%	0.94
Austenitic	Ferritic/Martensitic	0.038%	0.82
Austenitic	Aluminum	0.019%	0.92
Austenitic	Austenitic	0.000	1.00

For the definition of performance, see Figure 3.2.

A difference in thermal expansion coefficients at a circumferential fix will also result in some increase in stress. The only material mismatch considered here was a martensitic membrane and a ferritic stainless or carbon steel ring. The total stress induced by thermal loads in the membrane at the boundary was determined to be insignificant (none for ferritic, 1200 psi/ 8.3 MPa for carbon steel ring).

The specific material costs for suitable ring and membrane combinations are shown in Figure 3.12. The costs were developed using membrane thicknesses defined in Section 3.1.5. Ring area was not held constant, but optimized based on weight with the procedures developed in the following sections on structural analysis. The results of this specific cost comparison indicated that aluminum was the best selection for the membrane and ring. The martensitic stainless/carbon steel combination was a close second with only a slight cost penalty. The difference between the two material selections was near to or within the uncertainty of the material costs and optimization procedures used for ring design. It is important to note that the later material combination was, however, only practical with an open ring section. The martensitic and ferritic stainless steel combination was acceptable for open or closed sections, but the cost penalty was substantial. Austenitic stainless steel was rejected on the basis of cost.

The properties critical in free-form yield were also identified for the membrane materials (see Figure 3.13). The stainless steels and annealed aluminum have a substantial advantage in terms of ductility, and the margin between yield and ultimate strength, by comparison to tempered aluminum. Annealed aluminum, because of its low strength and softness, was not considered to be a membrane material candidate. These properties were included to indicate the alteration in physical properties with temper, and because the majority of the empirical work with membranes was accomplished with zero temper material. The tempered aluminum properties were considered adequate, although less desirable than stainless steel, for the average 4% strain experienced in the free-form yield process.

The only objective defined for the rear membrane material was to provide a closed plenum. The selection of a material for this membrane was not exhaustive, as the membrane required relatively few material properties. The metal selected for the optical membrane was assumed to provide an acceptable choice. Commercial composite films, such as polyolifin with nylon scrims, were also considered an appropriate material. Relatively little importance was attached to the selection of a rear membrane material, because the properties have no impact upon other components or performance of the stretched-membrane dish.

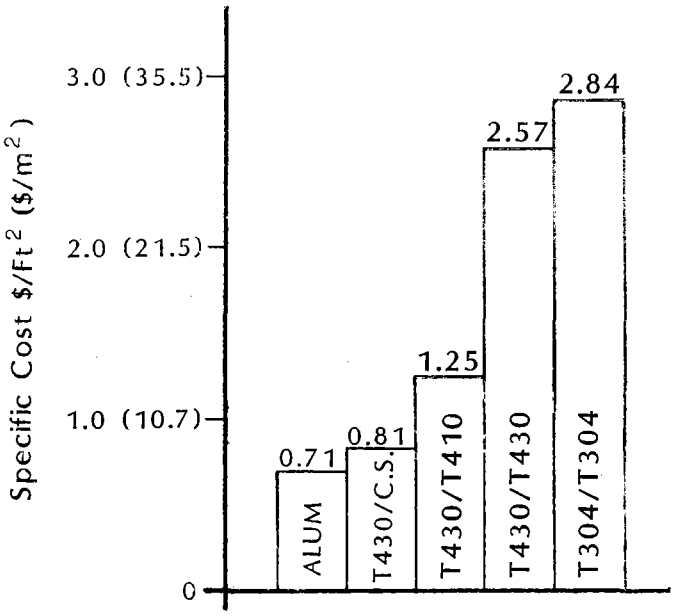

Figure 3.12 Specific Material Cost Comparison for Ring and Membrane Material Combinations.

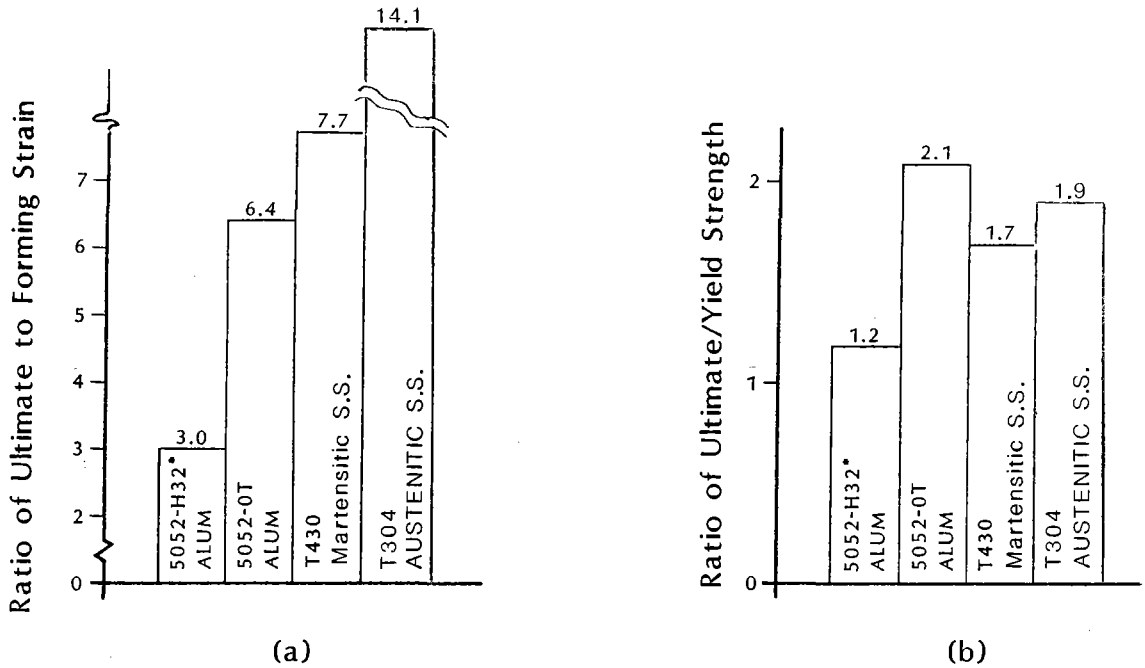

Figure 3.13 Significant Forming Membrane Material Properties

3.3 Summary of Material Selection

Metals were selected as the best material group for the optical membrane. This selection process was designed around the properties of the materials in operation, rather than fabrication. A distinction in the selection logic was made for two basic reasons. First, the cost advantage for different fabrication approaches was assumed to be irrelevant until the performance and operational costs of different materials were described. Second, the feasibility of different fabrication approaches can generally be determined only through conceptual design of the processes. No conceptual process designs were available for these evaluations. Selection of a material based upon transportability, for example, was considered to be substantially less important than viscoelastic behavior, tensile modulus, or surface characteristics, particularly when the accuracy of a separately transported membrane, attached to a frame in the field, has not been resolved.

The scope of this investigation was limited to material selection, rather than development. There were several issues that were considered in the design development of a stretched-membrane dish, of which the membrane material group was one. Material development would have consumed a substantial fraction of the time and materials available for this investigation. The development risk of composites was simply judged to be high by comparison to the benefits. Raw material costs for composites were large compared to metals, and the material development would have been directed at the alteration of a fundamental, rather than secondary, property requirement: specularity. The only significant benefit to be obtained was the elimination of seams. The reduction of error associated with seams in metal membranes was judged to provide a lower risk path to high performance, which would retain a lower material and control cost.

The viscoelastic behavior (creep) of polymer materials was investigated with a linear finite element model and CIRCE. Creep was assumed to be uniform, similar to thermal expansion. The initial or relapsed shape investigated was a parabola, described by an f/D ratio of 0.6. This model predicted that creep, without some compensatory control, was unacceptable from an optical perspective.

A variable stabilization pressure was investigated as a potential compensation for creep. The model used here predicted that pressure compensation would prevent performance loss, while the pressure differential remained positive. The difference in initial and final pressures required to maintain this positive differential was found to be substantial, proportional to the anticipated creep strain, and proportional to the membrane material thickness.

The substantial increase in initial pressure implied a high initial stress, and significant creep. The proportionality of pressure difference and material thickness limited the practicality of an increase in material thickness to reduce creep through a reduction in final stress levels. The final result of this model was that pressure, used as a control

variable to offset creep, was not suitable for materials that exhibited large values of creep strain, such as polymers.

The viscoelastic model was limited by three assumptions: linearity, polynomial representation of a surface, and uniformity of viscoelastic behavior without regard to material direction and membrane position. The linearity and polynomial representations were both approximations, but were not judged to have a substantial impact upon the results of the model. The uniform assumption was not entirely correct. Polymers typically indicate anisotropy in all material properties, and the load was not uniform with respect to membrane position. This assumption was judged to limit the application of the model, particularly to situations in which acceptable performance was predicted.

Alternate compensatory controls for creep have been investigated by other researchers, but were not explored in this contract effort. Those models were also based upon the uniform assumption, and actively altered the boundary of the concentrator to maintain a constant focal length. This control system was not considered here, because it required the addition of a controlled degree of freedom, rather than the exploitation of a system inherent in stretched-membrane dishes of any material. The predictions, with uniform assumptions, have indicated the acceptability of this control for creep. Models with increased accuracy are required to predict actual performance, as all uniform model assumptions are optimistic with respect to performance.

The tensile modulus was also an important material property in material selection. The region of the membrane dominated by edge effects was found to be a strong function of the material modulus. The tools used in this analysis were a combination of the edge solution developed by Steele and Balch and CIRCE. The results of this investigation indicated that materials with a relatively low tensile modulus would have unacceptable optical performance if a circumferential fix were imposed at the membrane to ring frame connection. Both composites and polymers have a tensile modulus at least an order of magnitude smaller than metals. The lower tensile modulus of these materials required a circumferential boundary that provided for an increase in the circumferential tension. Metals did not require this compensation at the boundary.

Composites, developed to date for use as membranes in a dish, have not demonstrated acceptable specularity for use as an optical membrane. The surface roughness has been attributed to "print-through" of the woven cloth used to reinforce the material. This effect was considered to worsen from creep in the matrix under the continuous tensile load imposed on a stretched-membrane. Specularity measurements available during this effort were considered optimistic because the time-dependent properties of the material at load have not been measured.

Secondary issues were also considered in the selection of a membrane material group. The significant issues in this category were anisotropy, material cost, and fabrication

limits. Anisotropy was considered to be a major factor if polymers or composites were chosen as the candidate group. These groups were not selected as a result of the primary investigation. Consequently, the directional dependency of these materials in the operating range was not considered. Material costs favor the selection of metals. Finally, the limits imposed by metals and composites with respect to fabrication were not judged to provide a clear design path selection.

Metals were selected as the best material group for the optical membrane. This selection was based upon the absence of significant creep at operating conditions, the high-tensile modulus, which limited the edge effect area, and good surface characteristics for a specular substrate. Secondary considerations tended to favor the selection of this material group as well.

Aluminum was selected for the optical membrane. This choice was made both on operating characteristics and cost. Material cost was added to the selection process, because the difference in optical performance, within the metal-group, was considered trivial. The metals considered were drawn from conventional engineering alloys that exhibited good atmospheric corrosion resistance. Carbon steel and ferritic stainless alloys were not considered because of corrosion; aluminum, martensitic stainless, and austenitic stainless steels were acceptable.

The allowable mismatch in thermal expansion coefficients between the ring and membrane was also explored. The results of this analysis indicated that the martensitic membrane could potentially be coupled with a carbon steel or ferritic stainless steel ring to reduce the specific cost combination. Carbon steel rings were considered acceptable only for open sections, while ferritic rings were acceptable for open and closed rings.

The aluminum membrane and ring provided the lowest specific cost for any material combination. The only reservation in the selection of aluminum was made with respect to temper. The annealed aluminums were not considered to be suitable for commercial membranes because they were soft and highly susceptible to damage. Empirical investigations in membrane response were conducted with annealed aluminum to keep forming pressures at small diameters tenable. Tempered aluminums have smaller ductility and yield/rupture margins. Consequently, some fabrication problems may encroach on future work at commercial scales as a result of the aluminum temper.

All efforts conducted during this contract indicated that metals represented the best material group for the optical membrane. The baseline material selection for the ring and optical membrane, within that group, was aluminum. The only potential change anticipated in this baseline, during future work, would be the result of fabrication problems in large-scale concentrators.

4.0 Development of Membrane Forming Techniques

Free-form yield was selected for a detailed empirical development of membrane-forming techniques. An initially flat membrane was plastically formed to a parabolic shape in the absence of a mold or mandrel, hence, free-form. The membrane shape was defined through control of the load distribution applied to the thin diaphragm attached at its perimeter only.

Alternate forming methods were briefly considered, but not intensively developed, as was the free-form yield process. The alternate techniques included consideration of elastic deformation, stretch forming, and contoured seam attachment. Elastic deformation was abandoned because of the substantial deformations that were required to form the parabola from flat sheet. Stretch forming is similar to the free-form yield process, except the shape of the membrane is determined by the shape of a forming tool, or mandrel. A large and extremely precise tool would be required to implement this approach. Contoured seam attachment requires that the precise shape of each gore or petal be determined and seamed to create a parabola under a pressure stabilization load. Some faceting error would be inevitable with this technique. Free-form yield was the first approach selected for development. This process was selected for detailed development primarily because the empirical efforts demonstrated immediate promise.

The objective of the development was to define the critical process variables that controlled the yielding process. The experiments were directed by the results of optical and material analyses presented in previous sections. Aluminum was the only substrate material considered intensively in this development. The forming experiments were generally carried out with the intent of forming a parabola with an f/D ratio of 0.6.

This empirical analysis is presented in four sections: equipment, bench-scale results, test-scale results, and a summary of the key process variables. The actual test data, along with the preliminary data reduction, are provided in Appendices A and B.

This empirical development identified several important process variables. Control of these variables ultimately led to membranes that had predicted performances similar to a parabola with less than 2 mrad of slope error in bench-scale testing, and 4 mrad in test-scale experimentation.

4.1 Membrane Test Equipment, Measurement Equipment, and Data Reduction

Empirical testing of membrane-forming techniques was conducted to define the process variables and control requirements at two scales. The smaller, or bench-scale, was 54" (1.4 m) in diameter; the larger, or test-scale, was 144" (3.7 m) in diameter. Direct contact measurement was employed on the bench-scale membrane testing to define displacement. The slope was calculated from displacement data. The test-scale membrane shape was defined with a laser ray trace. These ray trace results provided a direct slope measurement. Data reduction was based upon an area weighted slope error, and performance estimates with a code designed to predict optical efficiency of a parabolic dish concentrator. This section describes the equipment used to form and measure membranes at both scales.

4.1.1 Bench-scale testing

The bench-scale testing approach was developed to provide economical testing of several process variables. The 54" (1.4 m) diameter was selected to allow the membrane and forming fixture to fit within the active region of coordinate data measurement (CDM) equipment. The CDM was developed for direct contact measurement of concentrator surfaces. This equipment was described in a previous report [Ref. 27].

The majority of the membranes tested at bench-scale were 0.002" (0.05-mm) thick, 1145-0T aluminum. Aluminum was selected to correspond to the anticipated material selection results presented in a previous section. The thickness and soft temper were used in this set of experiments to permit forming with unit loads similar to those that would be experienced in the commercial-scale dish (551", 14 m diameter). This thickness also represented the thinnest material from which we could fabricate flat membranes.

The equipment that acted as the test bed for bench-scale forming experiments is shown schematically in Figure 4.1, and with a polyester membrane in place in Figure 4.2. Membranes were stretched over a cylinder, approximately 54" (1.4 m) diameter, 14" (0.36 m) tall, and 0.75" (19 mm) thick. The cylinder and fitted flanges (see Figure 4.1) were massive by comparison to the final ring design. The substantial area properties provided rigidity in the ring, and allowed the forming properties of the membrane to be wholly isolated from any secondary ring deformations.

Several intentional flexibilities were built into the bench-scale forming bed and are outlined in the schematic representation of Figure 4.1. The major provisions for process control adjustments included the stiffness of the attachment, adjustment of the attachment diameter before forming (initial or pretension), and after forming (post tension), forming pressure, and stabilization pressure. The attachment stiffness was toggled, hard or soft, with the use of clamping band #1 (see Figure 4.1). The attachment stiffness was soft when the bladder was inflated and band #1 was not used. The membrane

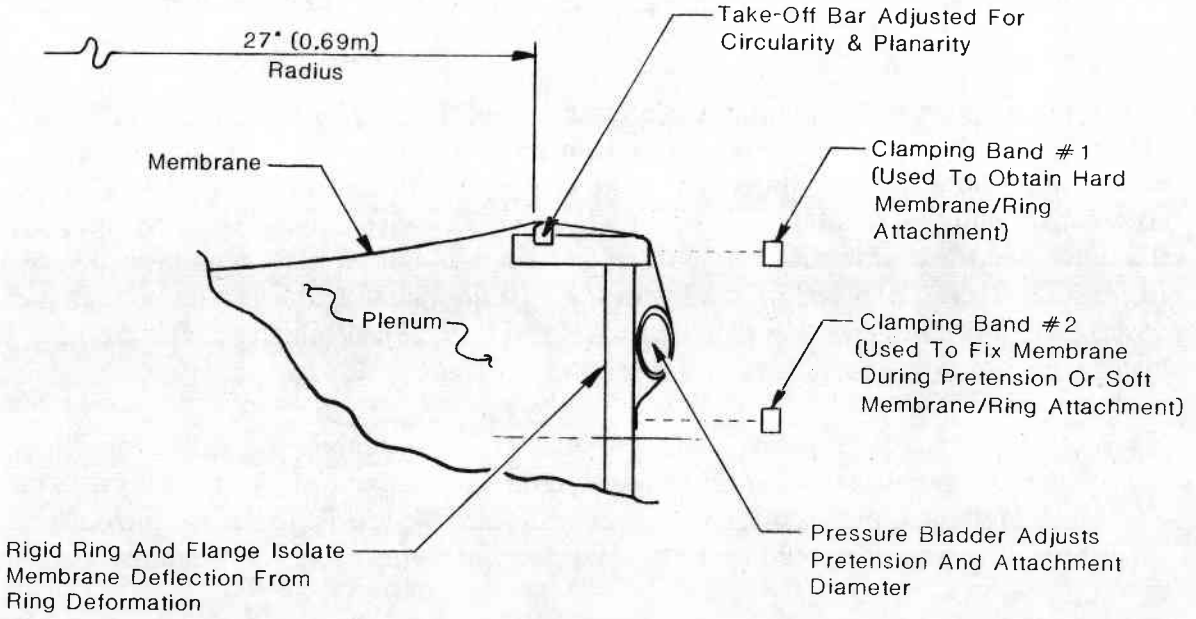

Figure 4.1. Schematic Representation of Bench-Scale Membrane Yield Equipment

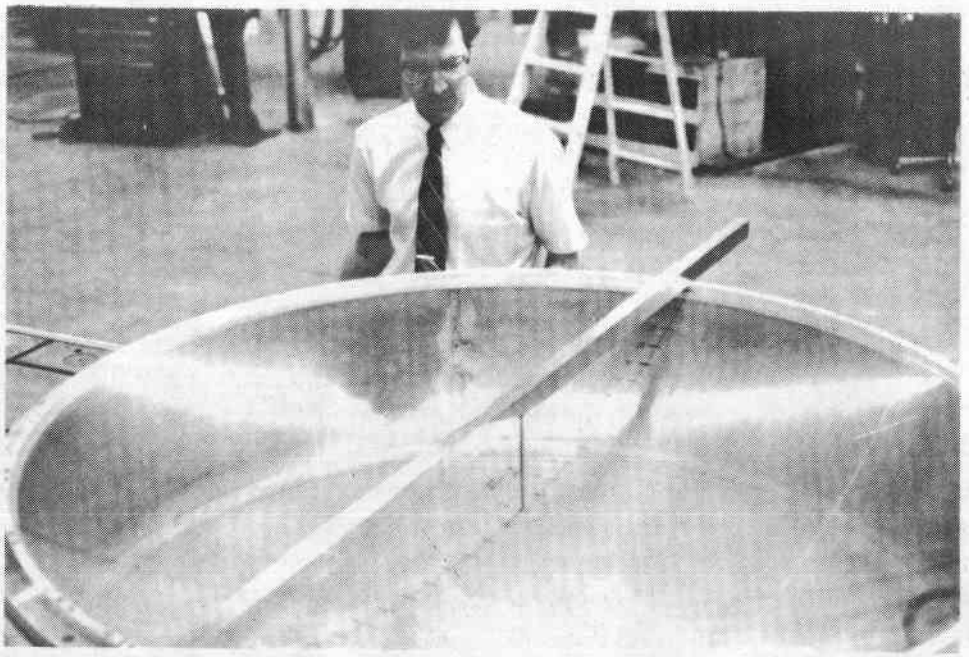

Figure 4.2 Bench-Scale Membrane Yield Equipment; Formed Polyester Membrane in Place

was held in place with the second clamping band. Consequently, a hard or soft attachment could be achieved during forming or measurement, with or without pre/post tension.

The adjustment of the attachment diameter was achieved after forming, and before measurement, by removing band #1 and inflating the bladder. This caused any arbitrary point on the membrane (except the center) to move toward the ring. This increase in attachment diameter was originally described as a change in the circumferential tension at the membrane boundary and was defined in terms of bladder pressure. Reference in terms of attachment diameter adjustment was incorporated to match the description promoted by other researchers [Ref. 11, 19, 28], although the effect is identical.

Pretension was achieved just as post tension or attachment diameter adjustment was implemented: pressurization of the bladder in the absence of clamping band #1. The difference in pre and post tension was simply whether the tensile force was introduced before forming when the membrane was flat, or after, when the membrane was concave.

The forming pressure was defined as the differential pressure across the membrane during yield. A differential pressure load in the elastic region, which added stability to the membrane, was defined as the stabilization pressure. The stabilization pressure was representative of the operating load imparted by a fan, for example. Each pressure was independently adjustable.

Polyester membranes were not intensively investigated during membrane experimentation, although these membranes were transparent and, subsequently, useful for the photographic presentation of yield equipment in Figure 4.2. The bar, which sits on top of the 54" cylinder, defined the ring plane or departure point for the membrane. A machinist scale (6" long) illustrates the center deflection of this particular membrane: approximately 5.625" (143 mm).

The deflection of the membrane at different radial positions was actually measured with a micrometer head affixed to the CDM. Measurements were made by lowering a micrometer probe until a visible deflection in the membrane surface occurred. This process, shown in Figure 4.3, was repeatable within the resolution of the micrometer ($\pm$0.0001", 0.0025 mm). The uncertainty in measurements was dominated by global uncertainties in radial and normal position of the probe holder. The total uncertainty in radial position was 0.005" (0.12 mm), and 0.001" (0.25 mm) uncertainty existed in the normal direction [Ref. 27]. These errors were independent, and assumed to be normally distributed, resulting in an uncertainty of 1.7 mrad (one sigma value) for bench-

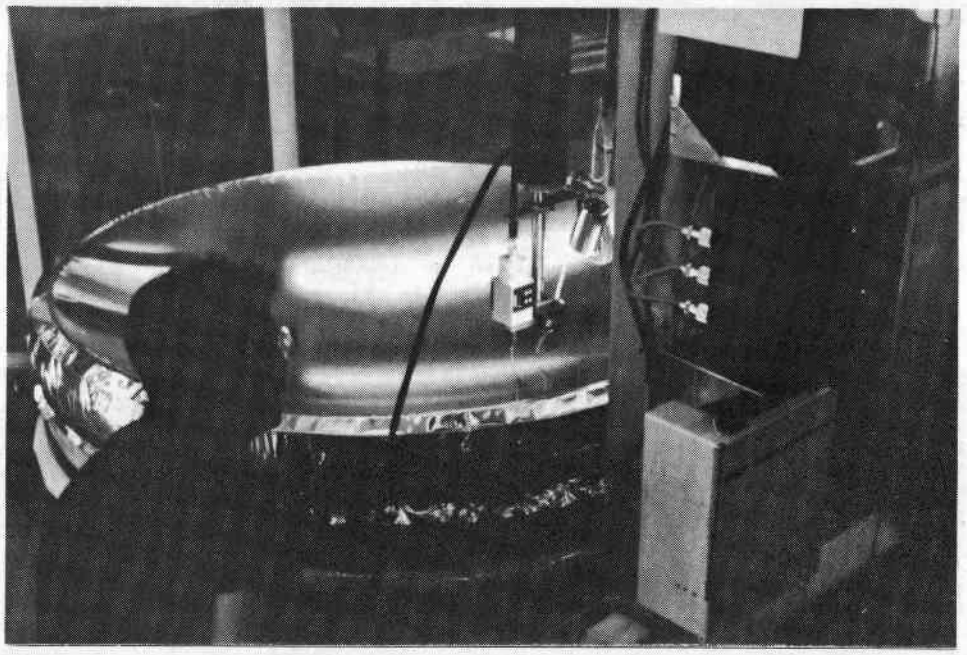

Figure 4.3 Direct-Contact Measurement of a Formed, Bench-Scale Membrane with a Micrometer Probe

scale measurements. This uncertainty was judged to be acceptable in anticipation of substantial errors in the forming process until variables were identified. Slope uncertainty at the larger test-scale was reduced by changing to a direct-ray-trace-system.

4.1.2 Test-scale experiments

The test-scale membrane experimentation demonstrated the impact of size on forming techniques. The thinnest zero temper aluminum that could be consistently welded with "in-house" equipment was 0.006" (0.15 mm). The smallest diameter that allowed welded membranes to be formed with water as the nonuniform load source was 144" (3.7 m). The scaling relationship provided by Murphy and Tuan was used to define this diameter:

$p(f/D) = S_y t/D$ where [Ref.7]

and

p = forming pressure,
f = focal length,
D = membrane diameter,
t = membrane thickness,
S_y = yield stress.

The nonuniform loads most successful at the bench-scale ranged from 460 to 650 lb (101 to 146 N). The ratio of nonuniform load to area was assumed to remain constant. The minimum test-scale was consequently defined at 65 to 77" (1.65 to 1.96 m) based upon the minimum thickness for welded membranes.

The concept of a massive ring and flange assembly to isolate ring deflection from membrane displacement was also implemented at test-scale. The variation in process controls (e.g., attachment diameter and attachment stiffness) was not incorporated. Bench- scale testing indicated that this control was not required to fabricate free-form yield membranes. The test-scale yield fixture is shown in Figure 4.4.

The slope of membranes formed at test-scale was directly measured with a laser ray trace system. This measurement equipment is schematically illustrated in Figure 4.5, and shown in Figure 4.6, as well. A target was located at the focal point of the test-scale membrane. The normal beam incident on the membrane was radially placed by reflecting a horizontal laser beam through a moving penta-prism. This approach allowed the laser to remain stationary, while the lighter penta-prism transited the rails. The penta-prism eliminated or substantially reduced sensitivity to displacement or rotation of the bearing from any sag in the rails. Some radial offset error was introduced by the beam

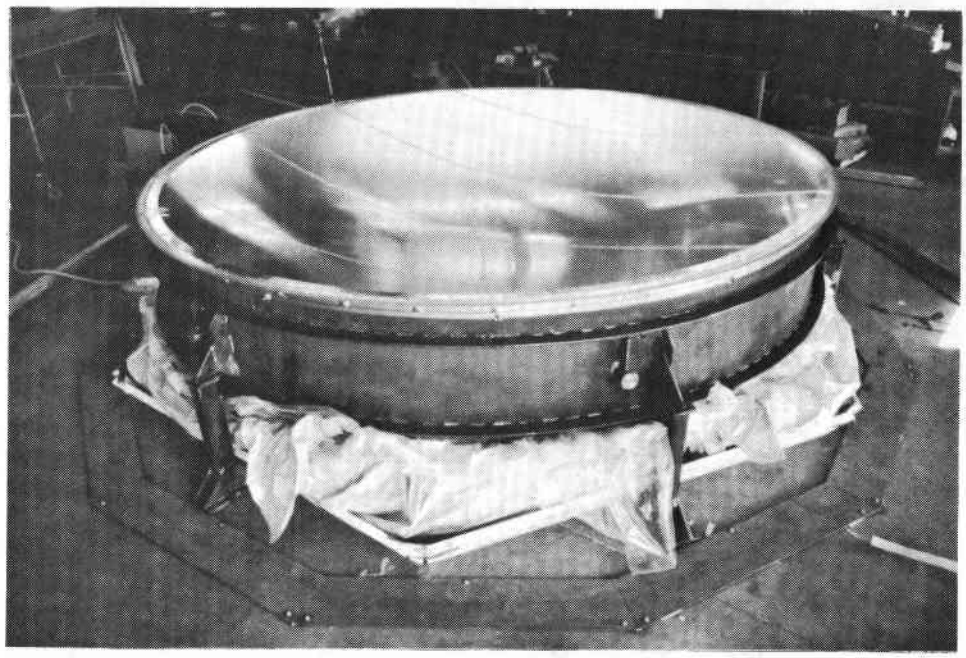

Figure 4.4 Test-Scale Membrane Yield Equipment; A Formed Aluminum Membrane (without reflective film) is Shown in Place.

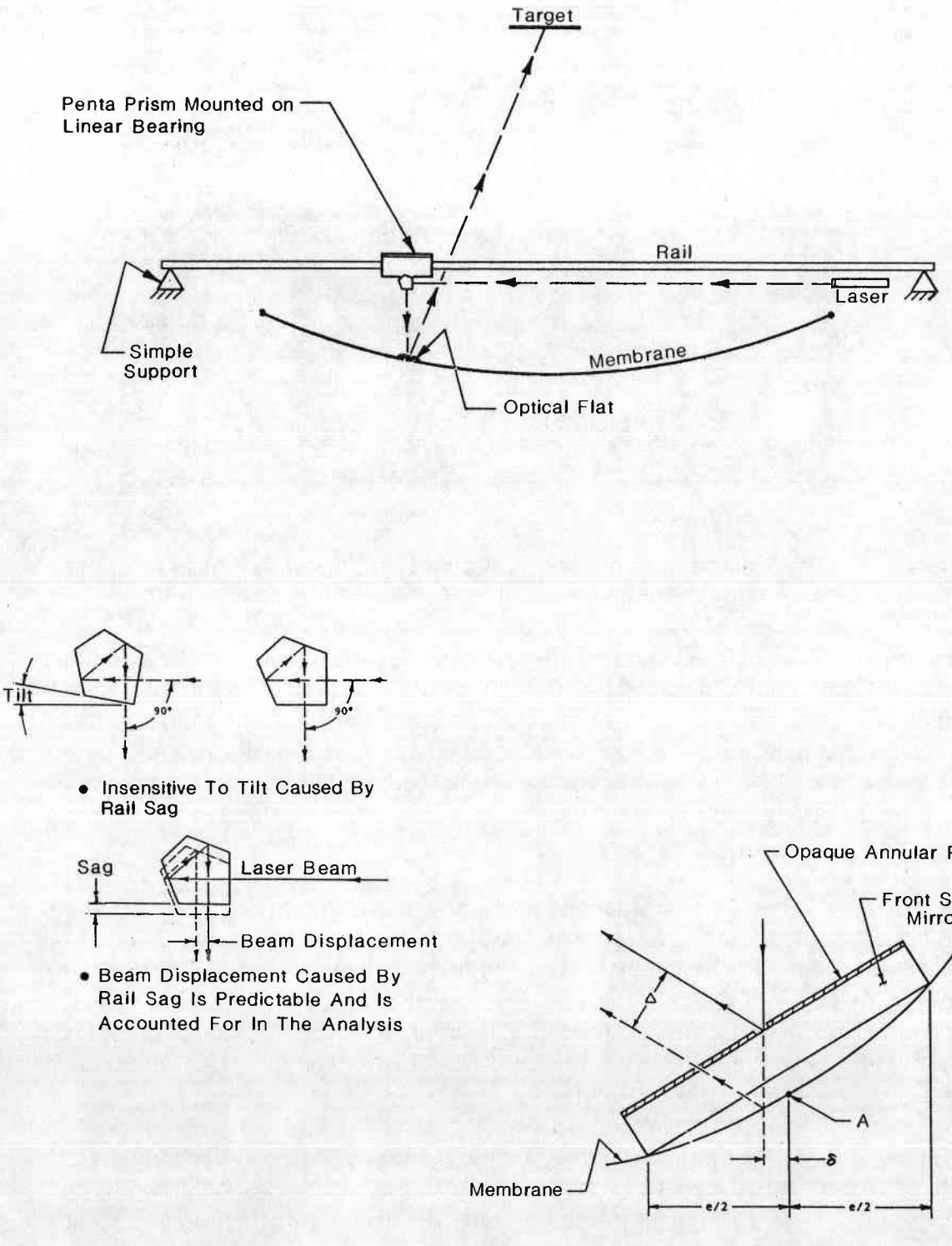

Figure 4.5 Schematic Representation of Test-Scale Membrane Measurement Equipment.

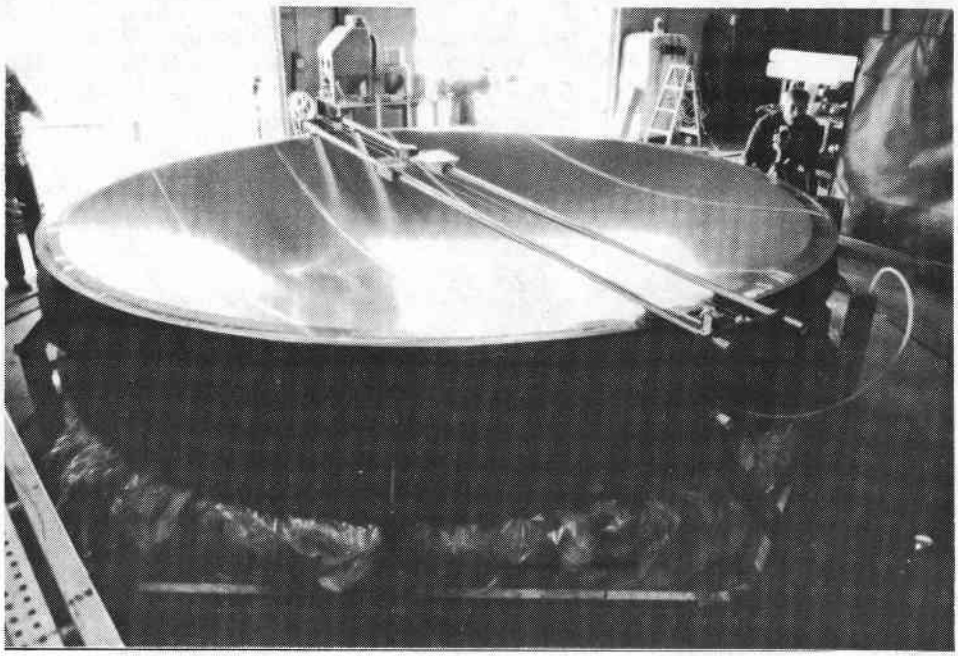

Figure 4.6 Test-Scale Membrane Measurement Equipment; A Formed Aluminum Membrane (without reflective film) is Shown in Place.

displacement. This error was corrected, with relatively little uncertainty, by estimating sag and roll as a function of radial position for a simply supported beam. In instances in which reflective film was not installed prior to measurement of membrane shape (such as the example shown in Figure 4.6), an optical flat was positioned at different radial positions and used for redirecting the normal beam to the focus. The finite thickness of the flat also introduced some measurement uncertainty, which can be removed analytically.

These errors were not entirely independent, although this simplifying assumption was made to determine the uncertainty associated with this ray-trace approach for direct slope measurement. The magnitude of uncertainty associated with each source of error is shown in Table 4.1. The major sources of error were a result of inaccuracy in measuring the radial position, the level of the stationary laser, and the beam spread of the laser when measurements on reflective film were being made. The one sigma uncertainty of the slope measurements was 0.6 mrad.

Membrane-forming experiments during Phase I were conducted at two diameters: bench (54", 1.4 m) and test (144", 3.7 m) scales. Testing at both scales was accomplished with substantial rings to isolate the impact of frame distortion from membrane displacement. The membrane shape was defined with direct-contact measurement at bench-scale, and slope was calculated (one sigma uncertainty = 1.7 mrad). Membrane slope was directly measured at the test-scale (one sigma uncertainty = 0.6 mrad).

Table 4.1
Measurement Uncertainty and Source
in Test-Scale Equipment

Radial Position	
Radial position measurement, $\pm$0.060"	< 0.3 mrad
Analytical correction, penta-prism	< 0.2 mrad
Analytical correction, target horiz pos	< 0.01 mrad
Normal Position	
Target to vertex measurement, $\pm$0.060"	< 0.2 mrad
Analytical correction, optical flat	< 0.01 mrad
Slope	
Laser level, $\pm$0.06"/140"	< 0.3 mrad
Prism uncertainty	< 0.05 mrad
Specularity	
Beam spread, $\pm$0.060"/100"	< 0.3 mrad
One sigma uncertainty	< 0.6 mrad

The yield and measurement equipment was developed to achieve the test objective: demonstrate the ability of the free-form yield process to create a near-parabolic shape with an f/D ratio of 0.6. Ultimately, the equipment achieved this purpose. A simple figure of merit to compare membranes was developed to match the available data.

4.1.3 Data reduction

The measurement data at bench-scale were provided as displacement from the ring plane in the CDM Cartesian coordinate system. These data were subsequently resolved into an "r-z" coordinate system; the r-axis represented radial position, the z-axis represented the optical axis, and the coordinate origin was at the center of the membrane. Following coordinate transformation, the slope was defined with the assumption that the membrane was a series of axisymmetric, conical shell elements, with displacements known at the measured points. This "faceted" approximation was compared to the slopes generated with the same conic assumption applied to an ideal parabola.

Slope was directly measured at the test-scale. The reduction technique was similar to the bench-scale approach. Coordinate transformation and analytical reduction of displacement to slope data were not required.

The focal length of the measured membrane was not known. An arbitrary focal length was selected, the deviation between measured and ideal slope data was calculated, and the focal length was iterated upon until the weighted mean error was forced to zero. The weighting factor was the area of each annular conic facet. This area weight was required to accommodate the increase in projected aperture area with uniform radial increments. The result of this data reduction process was referred to as the "parabolic deviation", or Pdev, and the solution process is shown as a flow chart in Figure 4.7.

Table 4.2
CIRCE [Ref. 4] Inputs Used for Performance Predictions

Solar Intensity	1000 W/m^2
Sun Shape Filename (Tabulated)	SUN.DAT
Reflectivity	0.93
Specularity Error	1.0 mrad
Tracking Error	none
Shading	none
Target Divisions	20,1
Dish Radius	test diameter
Dish Subdivisions	15

Slope measurements taken at the radial position used by CIRCE when 15 dish subdivisions identified.

The ultimate figure of merit for forming is to estimate the performance of the membrane. This approach was not applied to each membrane due to its complexity, and the difficulty in illustrating the errors (displacement and slope) as a function of radial position. Performance was used as an indicator of membrane quality at the end of the analysis. Specifically, the CIRCE [Ref. 4] code was used for performance prediction. Membrane shape was input as a high order polynomial. The remaining factors that characterized predicted dish performance are summarized in Table 4.2.

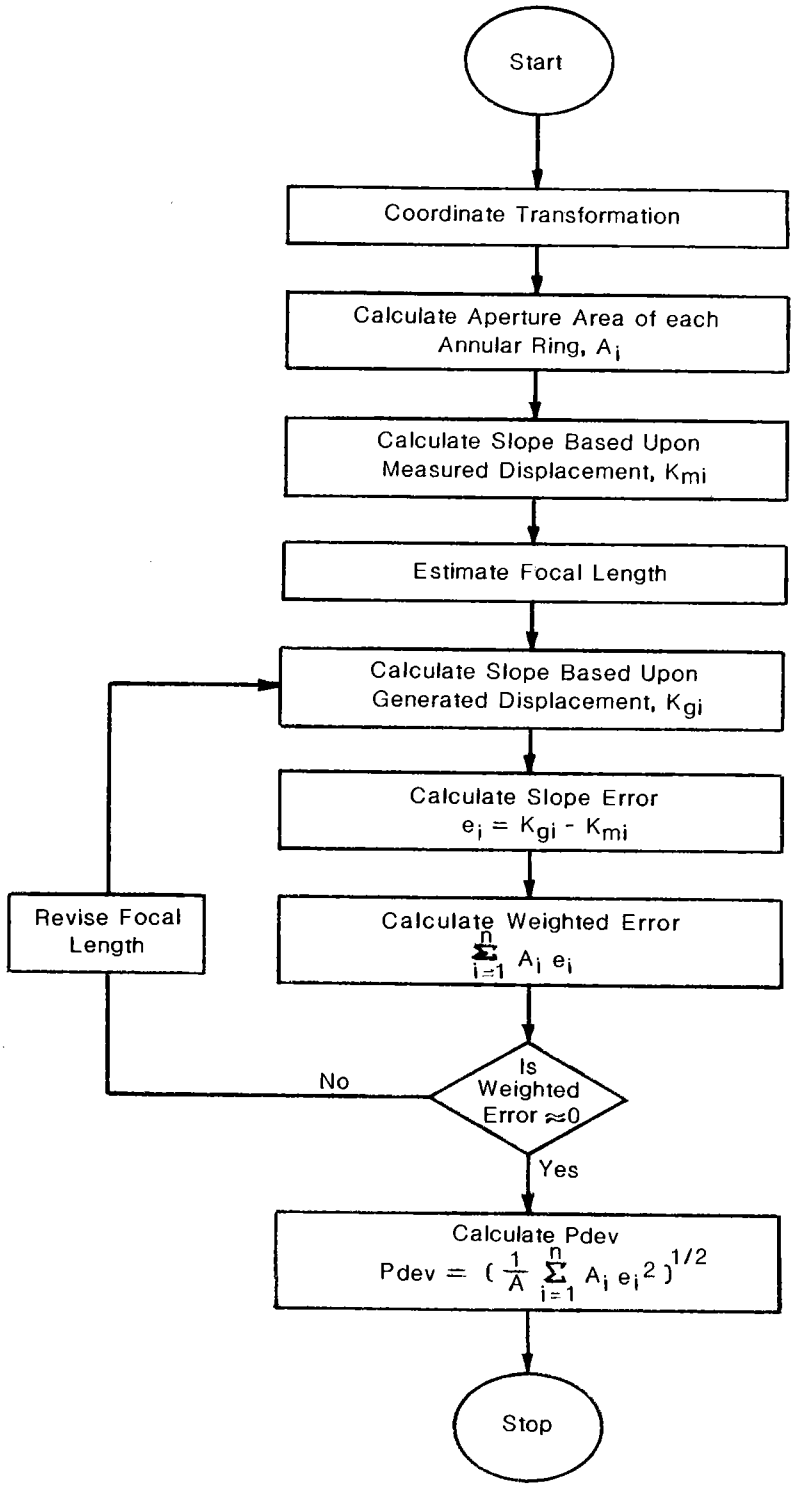

Figure 4.7 Flow Chart Representation of the Pdev Data-Reduction Process Applied to Bench-Scale Membranes.

Other figures of merit have been proposed, which include the impact of the increase in slant range and the reduction of apparent target size from a cosine effect. The Pdev technique was compared to an approach that included area weight, distance, and cosine effects. The test case was a sphere, with a center f/D of 0.6. The difference in the Pdev and the combined figure of merit was less than 3% [Ref. 29] for this representative test case. The figure of merit was applied to a bench- and test-scale membrane. The results are provided in Appendix B. The standard figures of merit used were the Pdev reduction and the CIRCE performance predictions presented in the following sections.

4.2 Bench-Scale Test Results

The free-form-yield test objective at bench-scale was to identify the impact of process control variables on membrane shape. Specifically, the objective during this empirical analysis was to develop a fabrication technique that resulted in a membrane with a parabolic shape for a solar concentrator. The analysis was not expanded to include the effects of variables on general shapes, shapes with f/D ratios other than 0.6, or materials other than aluminum. These limitations on the investigation were a result of the optimized f/D ratio and material selections presented in the previous sections. The empirical analysis was also developed with expectations of the impact of process variables, but in the absence of firm mathematical relationships. No specific attempt was made to repeat the experiments to quantify the relationships developed by other researchers after this empirical investigation was under way or complete.

The results of experiments at bench-scale are provided in Appendix A. These experiments were conducted to define the impacts of attachment stiffness, attachment diameter, stabilization pressure, repeated measurement sets on the same membrane over time and along different radial lines, film laminated to the aluminum membrane, forming pressure, and the distribution of the forming pressure. The distribution of pressure proved to be one of the most important process variables.

4.2.1 Nonuniform load profiles

The major problem encountered in the empirical development of a fabrication technique for parabolic membrane forming through free-form yield was the tendency to form a shape similar to a sphere. This tendency is illustrated in Figures 4.8 and 4.9. Figure 4.8 shows an ideal parabola, with the focal length determined by the Pdev reduction of data for membrane 8M3 (formed with a uniform pressure distribution). The actual shape of the measured membrane was exaggerated by magnifying the displacement error by a factor of 10, and superimposing the magnified error on the ideal shape. The free-formed membrane was too flat in the center, and too steep near the edge. The slope error of membrane 8M3 is shown in Figure 4.9, with the slope error of a sphere with the same f/D ratio at the center. This figure, with the displacement plot, indicated the spherical nature of a membrane formed with uniform pressure only. In fact, a membrane formed under uniform pressure was typically worse (from an optical performance or Pdev perspective) than a perfect sphere.

The empirical approach taken to obviate the spherical tendency of a free-formed membrane was to alter the pressure distribution with the intent of producing a membrane with a reversed slope error curve. In other words, the load profile was adjusted to create an "M" on the slope error curve. A uniform profile would subsequently be applied, and the superimposition of the "W" slope error shape would result in a parabolic membrane. The nonuniform load was defined as a hydrostatic case, where the pressure was approximately proportional to the depth and density of the material

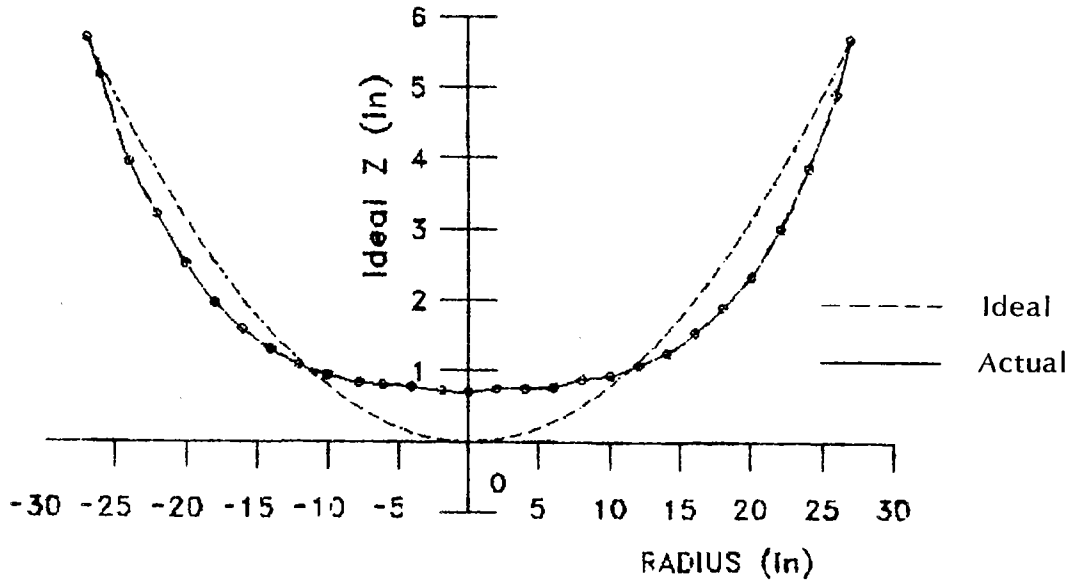

Figure 4.8 Standard Displacement Plot of Membrane 8M3, Formed With a Uniform Pressure Load. The Ideal Shape is Parabolic. The Errors of the Measured Membrane are Exaggerated by 10x.

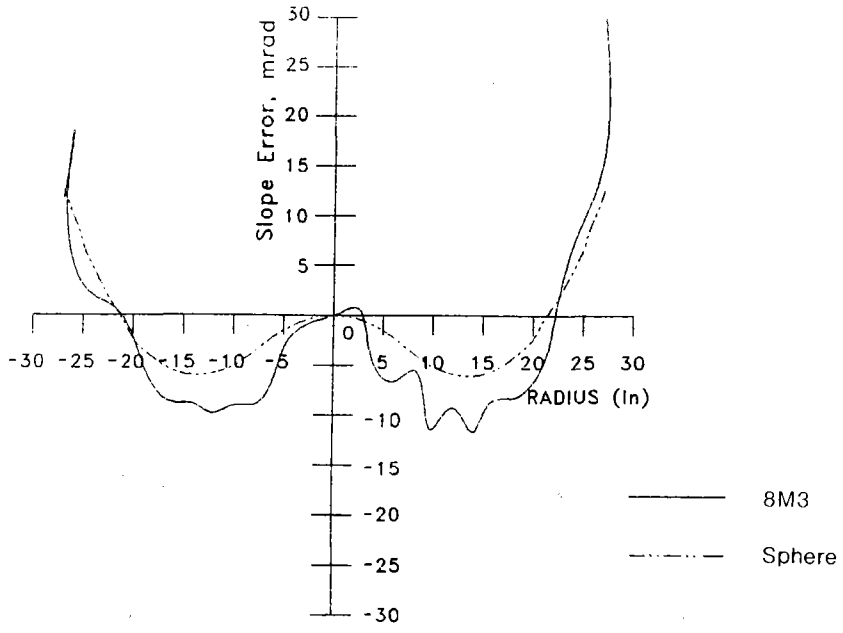

Figure 4.9 Slope Error as a Function of Radial Position for a Membrane Formed with Uniform Pressure, and a Perfect Sphere.

loaded on top of the membrane. This concept is illustrated in Figures 4.10 and 4.11, with sand as the load medium. The profile was controlled by loading the sand in a conic fashion. The height of the sand, and hence the pressure, was determined by the height of the cone and the depth of the membrane at any radial position. This hydrostatic profile was used to improve the accuracy of the membranes during the free-form process. This nonuniform load process allowed the formation of membranes that ranged from a shallow center and steep edge to a steep center and shallow edge.

This range of control allowed rational consideration of errors as a function of radial position. The objective of the data manipulation of membrane 13M6 and 8M3, non-uniform and uniform load profiles respectively, was to illustrate (see Figure 4.12) the amount of area associated with the edge effect.

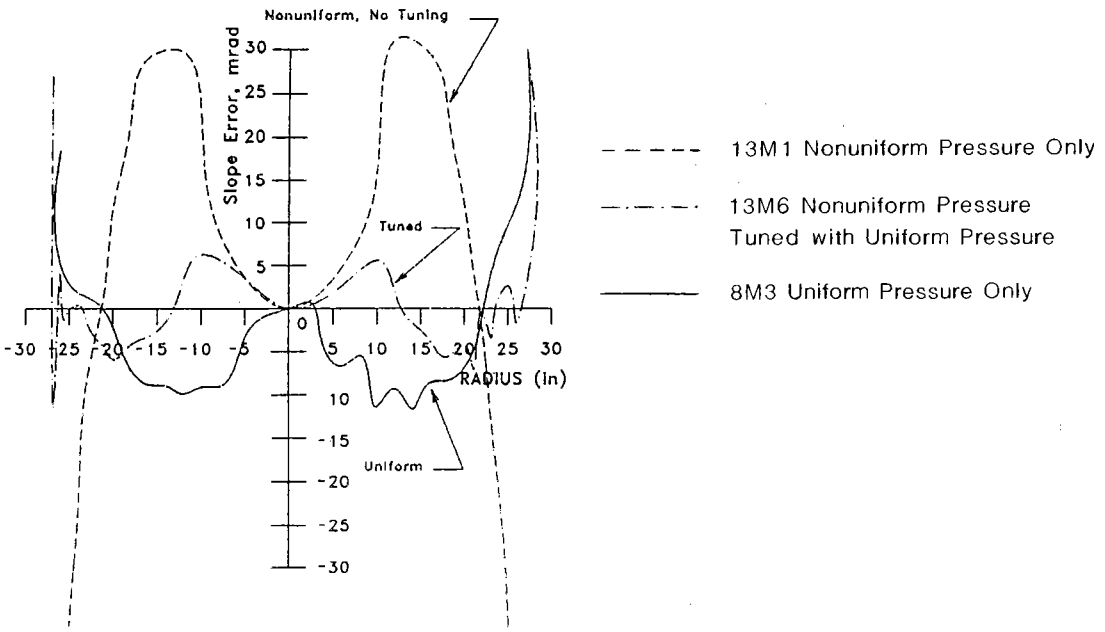

Figure 4.10 Slope Error vs. Radial Position. 13M1 Formed with Sand. 13M6 is the Same Membrane, Reformed with a Uniform Pressure.

4.2.2 Edge effects

Edge effects were defined as the region where the boundary formed by membrane attachment had a significant impact upon the characteristic shape. This region was described mathematically as a decay distance (see Figures 3.10 and 3.11 of the previous section), or the distance from the perimeter through which the boundary-induced error

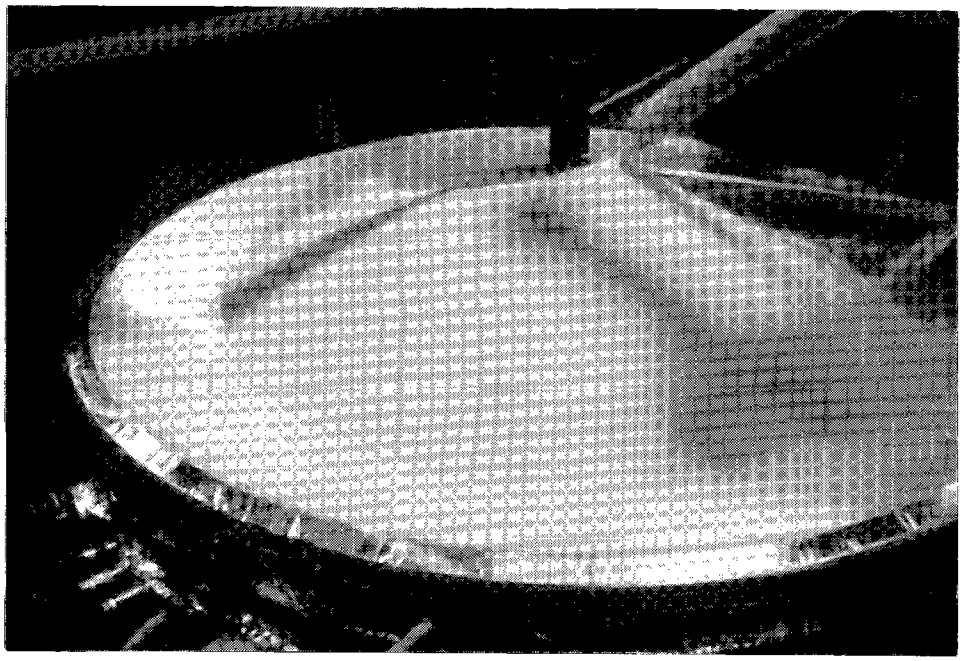

Figure 4.11 Sand Loading on a Bench-Scale Membrane

decayed to 4% of its peak value. At bench-scale the decay distance was 1.24" or 91% of the original aperture. This entire region need not be abandoned, however, as the focal length can be adjusted to compensate for a part of the affected region without performance loss. The impact of neglecting the edge for a uniformly and nonuniformly loaded membrane is shown in Figure 4.12.

As the active aperture area was decreased, the accuracy of a parabolic representation increased. This reduction in weighted slope error was anticipated for membranes that demonstrated a systematic shape error. The membrane yielded with a nonuniform profile, on the other hand, demonstrated a decrease in error only for a narrow region at the attachment. The relatively constant slope error, even with reduction in the active aperture, indicated a random error in a parabolic shape rather than a systematic shape error.

4.2.3 Membranes laminated with reflective films

Laminated membranes imposed additional error on the membrane shape. The reflective film was laminated to the aluminum substrate with a contact adhesive. When this laminated membrane was taken into the plastic region of the metallic substrate, the modulus of the reflective film (approximately 350000 psi, or 2.4 GPa) actually exceeded the aluminum plastic modulus (approximately 200,000 psi, or 1.4 GPa). Consequently, the forming process was actually dominated by the properties of the film, rather than the metallic substrate. This reversal of dominant material, from metal to film, when the metallic stress crossed the boundary between elastic and plastic regions, had two

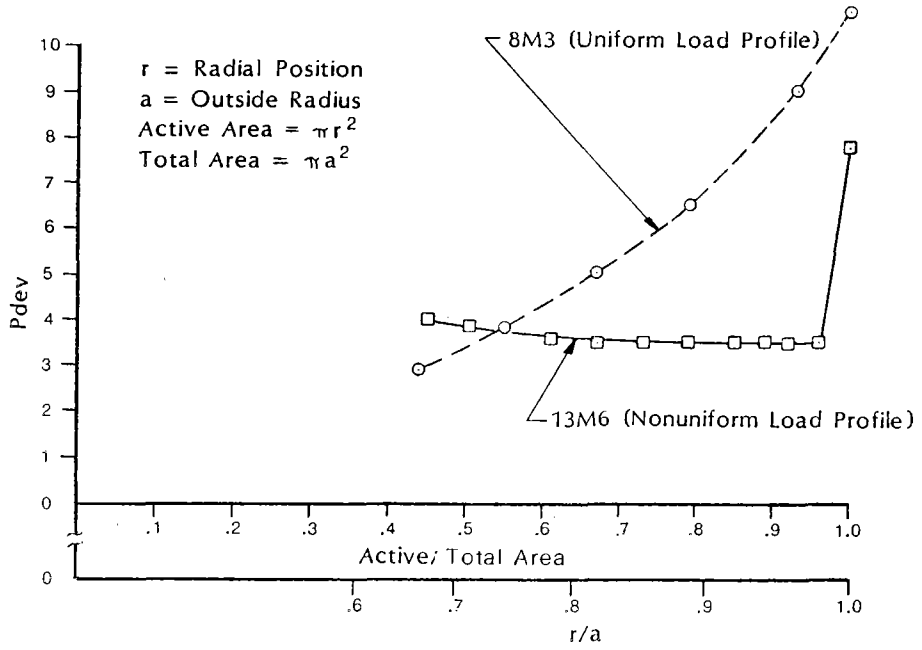

Figure 4.12 Pdev as a Function of Active Aperture for a Uniform (8M3) and Nonuniform (13M6) Membrane

major deleterious impacts. First, all strain tended to occur at any seam in the reflective film. This strain concentration resulted in rupture of the substrate. The second problem was the anisotropic characteristics of the film and/or the lamination process, which resulted in a poorly shaped membrane even when rupture did not occur.

The initial approach adopted to counter these negative impacts of forming a laminated membrane was to allow the reflective film or contact adhesive to creep during forming. This set of experiments was conducted at the coupon test level, as shown in Figure 4.13. The approaches considered for forming a laminated substrate included controlling the rate of strain and the temperature of the membrane. The impact of these variables was determined by placing a seam in the reflective film laminated to the coupon. The seams were left untaped, taped on one side, or taped on both sides. Laminated coupons with no seams, and bare aluminum coupons were used as controls. The results of this coupon testing essentially indicated that rupture would occur before 3% strain occurred in all samples, except the bare aluminum controls. Consequently, forming a laminated membrane was abandoned.

The reflective film was subsequently added as a wholly separate membrane. Contact between the structural membrane and the reflective film was guaranteed by the stabilization pressure. The stress induced in the metal membrane by the stabilization load was elastic. Consequently, the metal properties dominated the shape. This concept was demonstrated by forming an unlaminated aluminum membrane, removing the

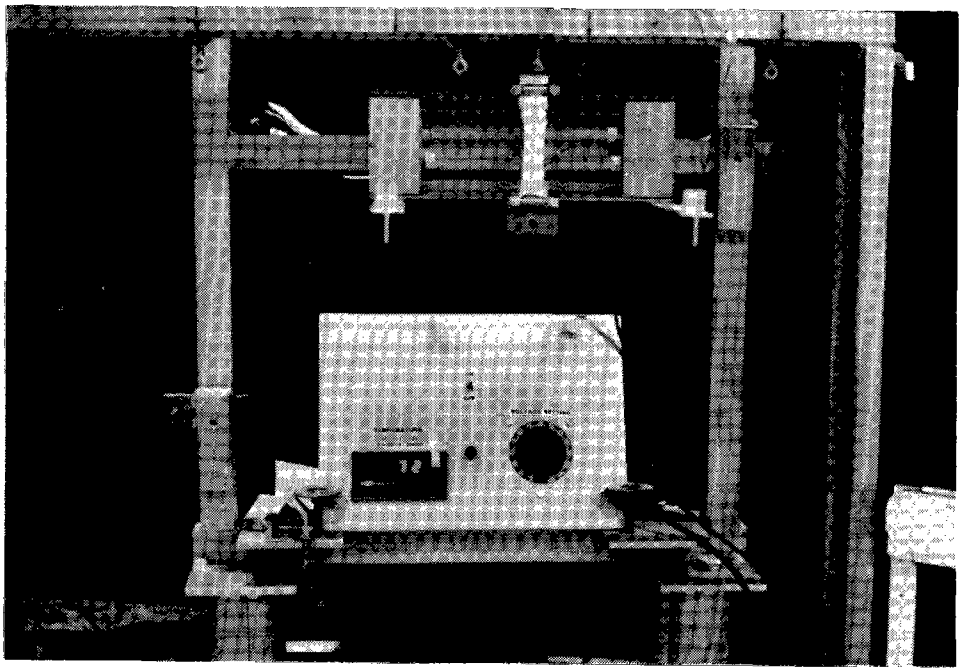

Figure 4.13 Laminated Aluminum Coupon Test

forming load, adding a reflective film membrane, and applying a stabilization pressure. The key element was the difference in slope or displacement between the aluminum only, and aluminum with separate film membrane (23M1 and 23M2, respectively). The experimental results are summarized in Figures 4.14 through 4.17. The addition of a separate reflective membrane, held in contact with the metallic membrane under stabilization load only, had no impact upon the fundamental shape of the formed substrate.

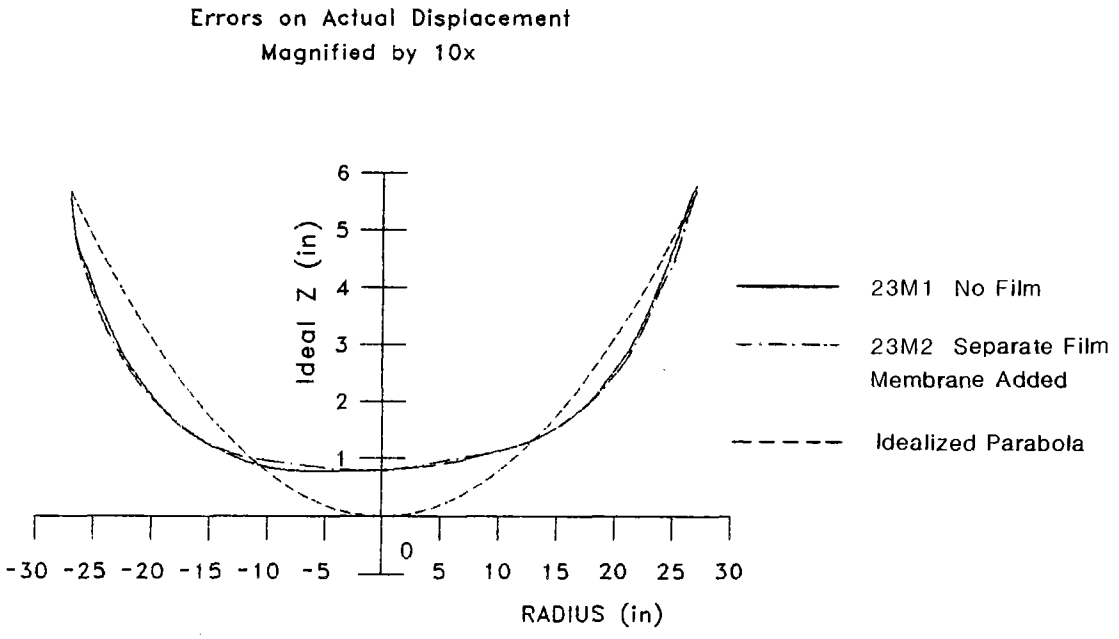

Figure 4.14 Standard Displacement Plot of a Uniformly Pressurized Membrane. 23M1 is an Aluminum Membrane Only. 23M2 is the Same Membrane with a Separate Film Membrane Added After Forming.

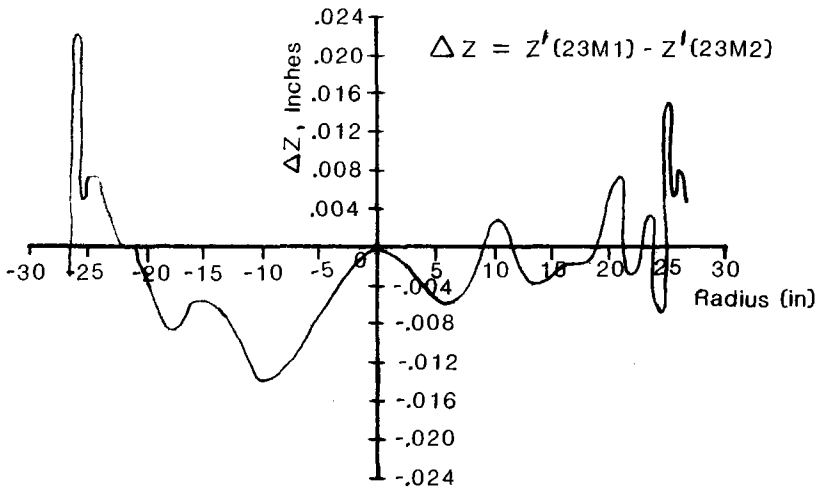

Figure 4.15 The Difference in Displacement Before and After a Separate Film Membrane is Added to a Formed Aluminum Membrane.

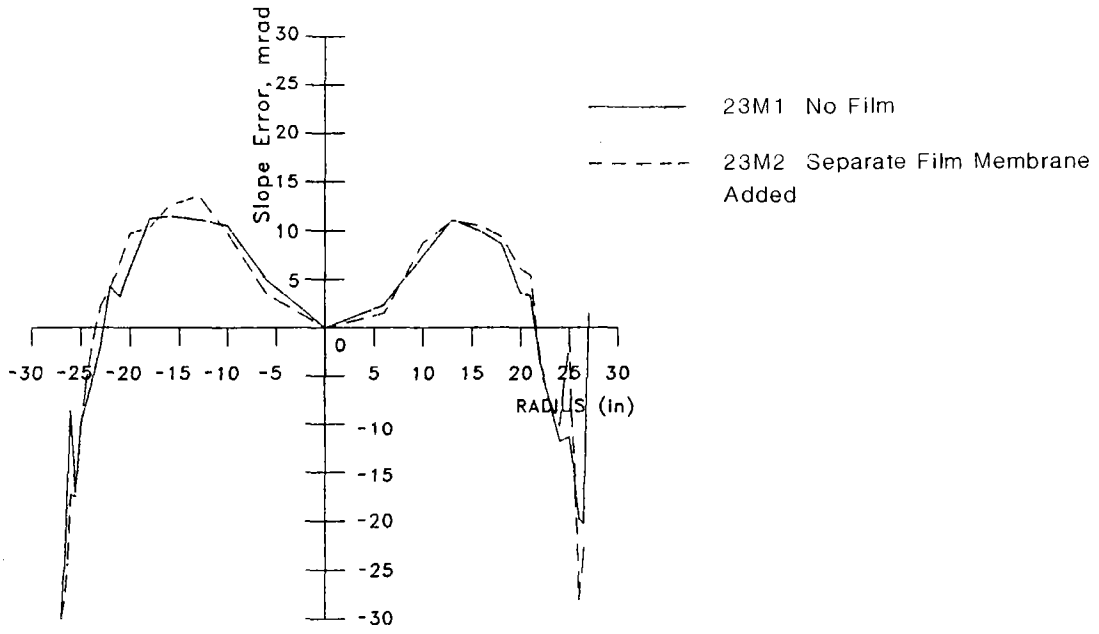

Figure 4.16 Standard Slope Error Plot of a Uniformly Pressurized Membrane. 23M1 is an Aluminum Membrane Only. 23M2 is the Same Membrane with a Separate Film Membrane Added After Forming.

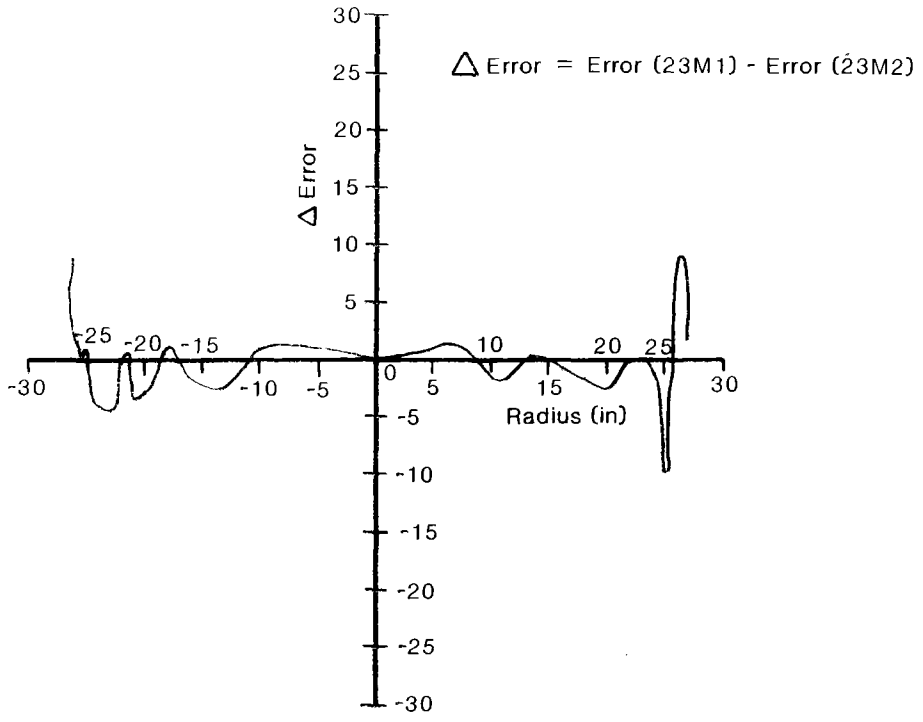

Figure 4.17 The Difference in Slope Error Before and After a Separate Film Membrane is Added to a Formed Aluminum Membrane.

4.2.4 Stabilization pressure

The membrane's stiffness in response to stabilization pressure was investigated by subjecting a formed membrane to a range of operating loads. Comparisons of the slope errors and displacements of membranes 8M1, 2, 3, 4, and 5 (see Appendix A), measured under pressures that ranged from 0.023 psi to 0.0023 psi (150 to 15 Pa), indicated that virtually no change in surface shape occurred. These tests were conducted on membranes that were formed with a uniform load. The test was not repeated with a hydrostatically formed membrane, because gross stiffness was assumed to be independent of structurally minor variations in shape imposed by the forming load distribution.

4.2.5 Stiffness and diameter of an attachment

The adjustment of bladder pressure during forming, essentially a variation in initial tension, was accomplished on membranes 1M, 2M, 3M, and 4M. These test results are shown in Appendix A, as well. The results indicated that initial tension had little impact upon the forming process. A hard attachment, exhibited on membrane 5M, indicated that the attachment's stiffness was also a minor or insignificant process variable during the forming process.

The effect of different bladder pressures after forming did have an impact upon membrane shape, albeit negative. The test results of 6M1, 2, 3, and 4, shown in Appendix A, illustrated a relatively constant Pdev, with a substantial increase in error at large bladder pressures. Variation in bladder pressure after the membrane was formed effectively represented an increase in the attachment's diameter, a concept discussed by several researchers [Ref. 11, 19, 28]. An illustration of adjusting the attachment's diameter after forming is provided in Figures 4.18 and 4.19. A machinist rule was set at the edge of a bench-scale membrane. Figure 4.18 shows a moderate bladder pressure applied to membrane 6M2; Figure 4.19 is the same membrane at a high bladder pressure (6M4). The slope at the attachment was actually reversed. The negative effect of variation in bladder pressure during measurement indicated that the membrane's shape could be altered with this process variable. Consequently, this test was repeated with a hydrostatically formed membrane.

Membranes 10M1, 2, and 3 essentially repeated the previous experiment with a membrane that was formed with water and a uniform pressure. The increase in attachment diameter clearly improved the membrane's shape. The Pdev at low bladder pressures was 10.6 mrad; at high bladder pressures this figure of merit dropped to 5.2 mrad. Adjustment of the attachment's diameter provided a path to improve membranes that were essentially parabolic. Ultimately, membranes with a hard fix during measure equaled the performance gains obtained through control of the attachment's diameter. Consequently, the attachment's diameter adjustment was not provided in the final recommended design. This experimental evidence does support the theories advanced by other researchers that alteration of the attachment's boundary conditions improves the accuracy of the membrane's shape.

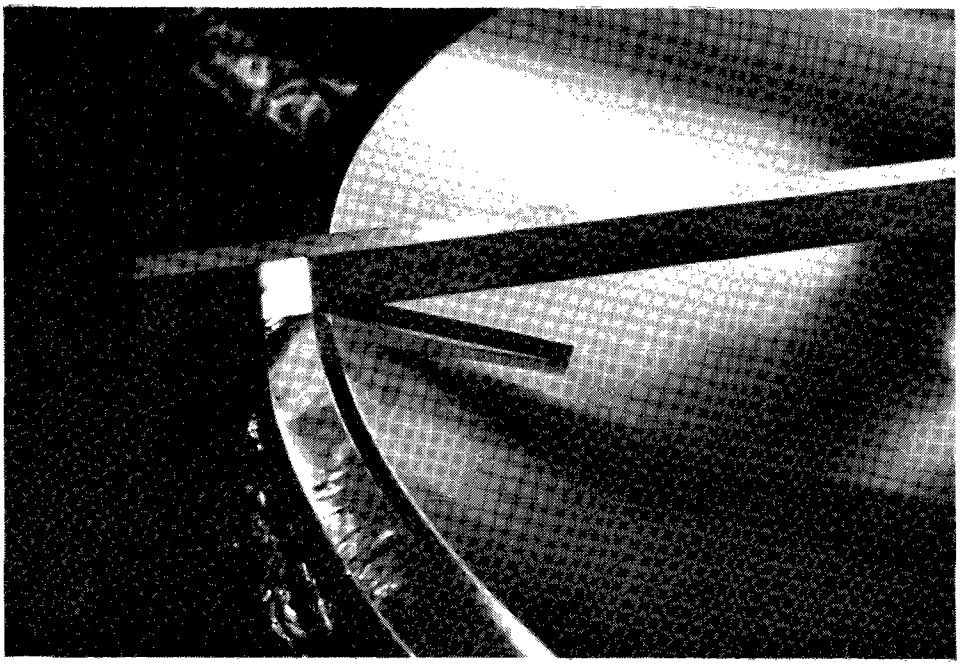

Figure 4.18 A 6" Machinist Scale at the Edge of Membrane 6M2 Illustrates the Membrane's Shape Before a Substantial Increase in Attachment Diameter.

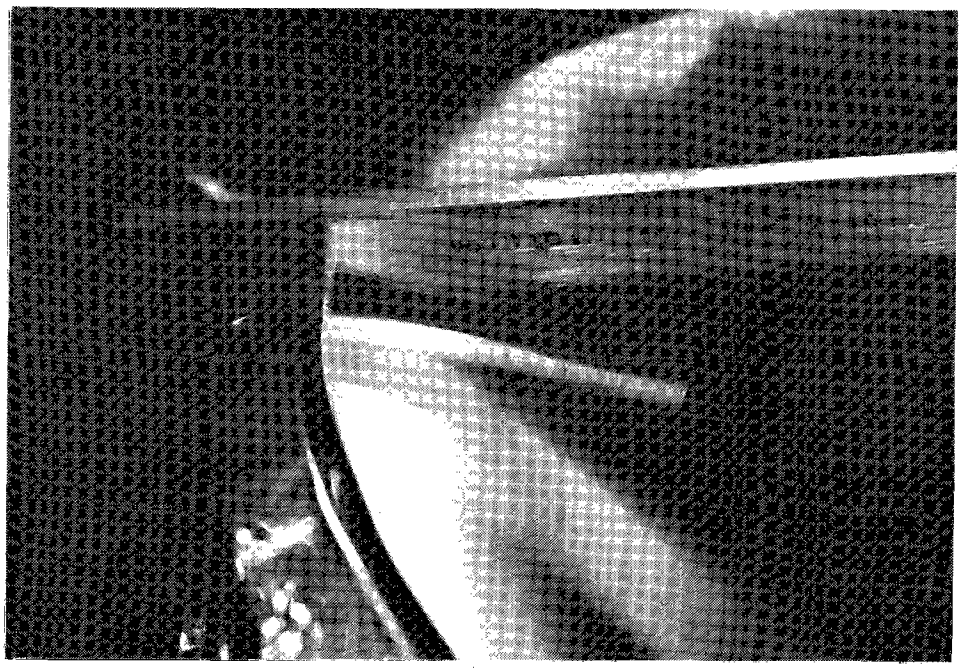

Figure 4.19 A 6" Machinist Scale at the Edge of Membrane 6M4 Illustrates the Membrane's Shape After a Substantial Increase in Attachment Diameter.

The change in the attachment's diameter was not implemented in further experiments at bench or test-scale. Control of the nonuniform load profile appeared to be adequate for forming experiments at this scale. Consequently, this additional degree of freedom in dish design and/or operation was not incorporated in the final design. The final step in bench-scale testing was demonstration of repeatability in the forming technique selected: a hard attachment with a nonuniform load profile followed by a uniform forming pressure and evaluation at 97% of the aperture area.

4.2.6 Repeatability

Membranes 18M1, 19M1, 20M1, and 21M1 were the experiments devoted to replication of 13M6. The first attempt, membrane 18M1, was formed with the same sand and uniform pressure load. The resultant Pdev, 8.67 mrad at 96% of the area, did not com-

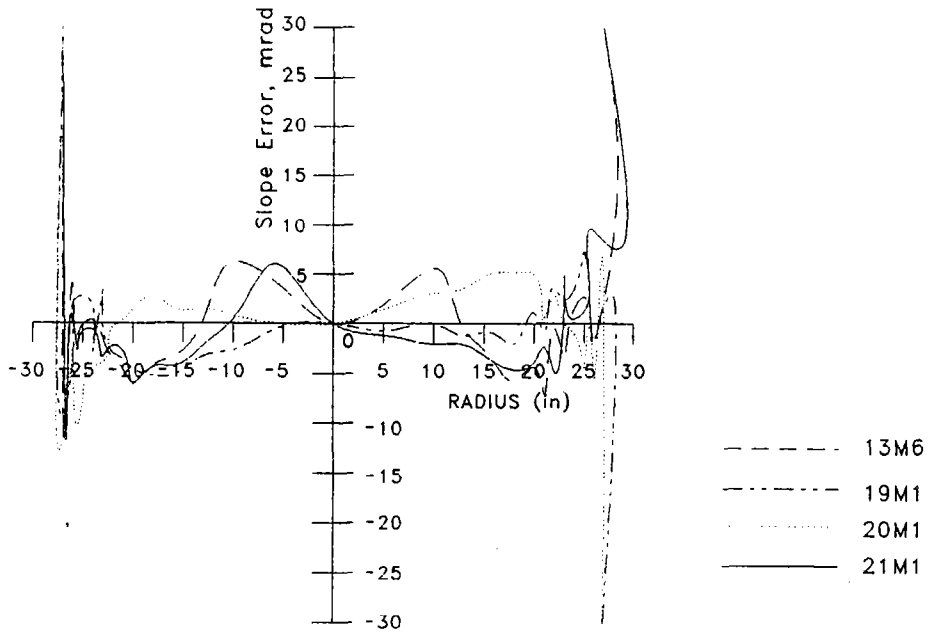

Figure 4.20 Slope Error as a Function of Radial Position for Repeatability Testing at Bench-Scale.

pare well with the Pdev for membrane 13M6 (3.52 mrad at 96%). The forming process was revised slightly. The total weight of the sand remained constant, but the uniform pressure load was increased until the center deflection of the membrane was approximately the same as for 13M6. This approach was substantially more successful at repeating the results: 2.89, 4.34, and 3.62 mrad for membranes 19, 20, and 21M1, respectively, evaluated at 96% of the aperture area. These fluctuations were within the one sigma uncertainty of the measurement equipment and data reduction process. In accordance with the original objectives, these membranes were considered to indicate repeatability. In other words, relatively accurate shapes could be consistently formed through control of the identified process variables. Figure 4.20 presents the slope error as a function of radial position for the four membranes in standard format. This set of experiments essentially completed the bench-scale testing program. The results were subsequently applied to the test-scale development.

4.3 Test-Scale Results and Predicted Performance

The empirical development of free-form yield techniques continued at 144" (3.7 m) in diameter, or test-scale. The primary objective of this testing was to demonstrate the results of bench-scale at a larger diameter. Aluminum membranes were formed with a nonuniform load profile; this profile was supplied with water rather than sand. The reflective film was added as a separate membrane. The membrane boundary was fixed, and no adjustment of the attachment's diameter was made after forming. The membrane itself was welded from 0.006" (0.15-mm), 1145 0T aluminum sheet. Slope was directly measured on the two membranes formed at this scale with a laser ray trace system. Figure 4.21 shows the yield fixture, with a membrane in place during hydroform. Figure 4.22 shows the same membrane after forming, with a separate reflective film membrane held in place with stabilization pressure.

4.3.1 Test-scale results

The Pdev data reduction technique, discussed in the previous section, was initially used as an indication of the membrane shape's accuracy. The slope data for the test-scale membranes was also fitted to a high-order polynomial, and the anticipated optical performance of the membrane was estimated with CIRCE [Ref. 4]. Performance estimates of bench-scale results were also implemented to provide a basis of comparison.

The scaling relationship used to determine the test-scale diameter was developed by Murphy and Tuan [Ref. 7] and is discussed in a previous section on yield and measurement equipment. This approximation predicted a linear relationship between the centerline deflection of the membrane during forming and the pressure. A brief examination of results at bench-scale, in particular, measurements made during a uniform pressure experiment, also demonstrated a linear relationship in the same two variables. No other attempts were made to verify the scaling formulae.

The most significant process variable defined by empirical testing at bench-scale was the nonuniform load profile. The scaling approximations employed suggested that the pressure was directly proportional to the membrane's thickness, and inversely proportional to its radius. The increase in thickness (3x), and increases in radius (2.67), very nearly offset one another. These ratios were applied to the total pressure exerted by sand at the membrane's centerline in bench-scale results to estimate the required load at centerline for the test-scale. The centerline pressure was determined by assuming a parabolic membrane shape during the forming process. The reduction in specific gravity for the forming material (bench-scale sand to test-scale water) was a result of the increase in distance between the ring plane and vertex, as a parabola of constant f/D ratio increases in radius.

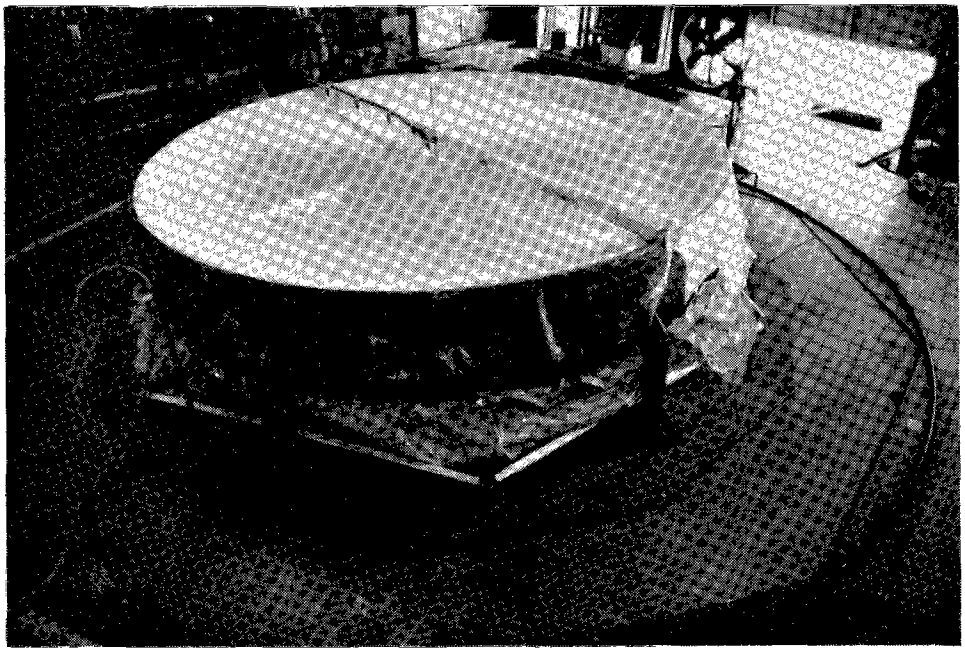

Figure 4.21 Test-Scale Membrane During Hydrostatic Forming.

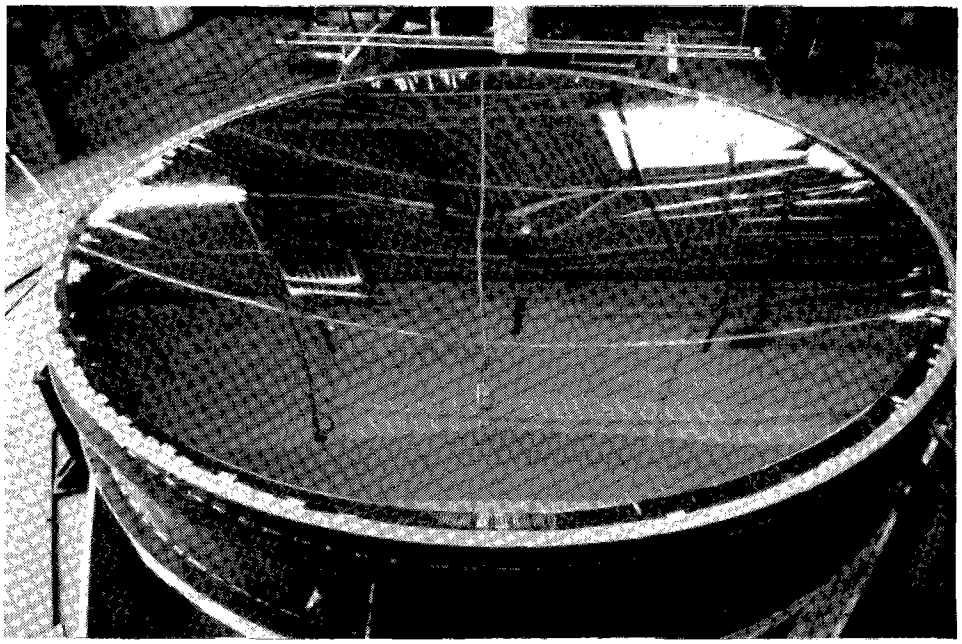

Figure 4.22 Formed Test-Scale Membrane with a Separate Reflective Film Membrane Held in Place with Stabilization Pressure.

The Pdev data reduction approach was applied to measurement data from the first membrane formed at test-scale. The slope error results are shown in Figure 4.23. The figure demonstrates the shape error after the nonuniform hydrostatic load only was applied (1D), and the shape of the membrane after a uniform pressure was applied (1J), and reapplied (1N). The error was substantially reduced by the first application of a uniform load, but the error remained systematic: too steep at the center and too shallow at the edge. In other words, the centerline membrane load was too high. Uniform pressure was reapplied in an attempt to correct the shape. The second application could not offset the original error.

The decay distance for the test-scale membrane was 4.77" (121 mm). One slope measurement on each radius was taken in this region with the 15-unit subdivision used for CIRCE. All results were presented based upon consideration of 100% of the membrane area.

Measurements along two-diametral lines were made on this membrane; the results are summarized in Figure 4.24. Measurements along the 90/270^{o} line ran between seams, while the 0/180^{o} line ran across membrane seams. Both curves indicated the same systematic error in membrane shape.

A second membrane was made at test-scale; the standard slope error presentation for this membrane is shown in Figure 4.25. The nonuniform pressure exerted at the center of the membrane was reduced slightly, but no reduction in error was apparent. The lack of correlation in error and load reduction was considered inconclusive, until a membrane could be formed at test-scale with a substantially reduced nonuniform load component. Plastic forming is a path-dependent process. The ratio of the nonuniform to uniform load, as well as the order in which each is applied, affects the final membrane shape. Forming at the bench-scale developed both load ratios and paths on an empirical basis after several failed attempts. Time limitations prevented the same level of detail being applied to the test-scale. Two membranes only were formed at the larger scale. The final step in the empirical analysis was the prediction of optical performance for both bench- and test-scale membranes.

4.3.2 Predicted performance

The slope error data generated from test-and bench-scale membranes were fitted with a high-order polynomial, to be used as an input for CIRCE [Ref. 4]. A polynomial order of six was selected based upon reducing the variance between the data and fit, while avoiding introduction of spurious deflection errors associated with the analysis summarized in Figure 3.7. The predicted performance was also based upon dish characteristics such as reflectivity (0.93), specularity error (1.0 mrad), and other inputs specific to the optical analysis program as summarized in Table 4.2.

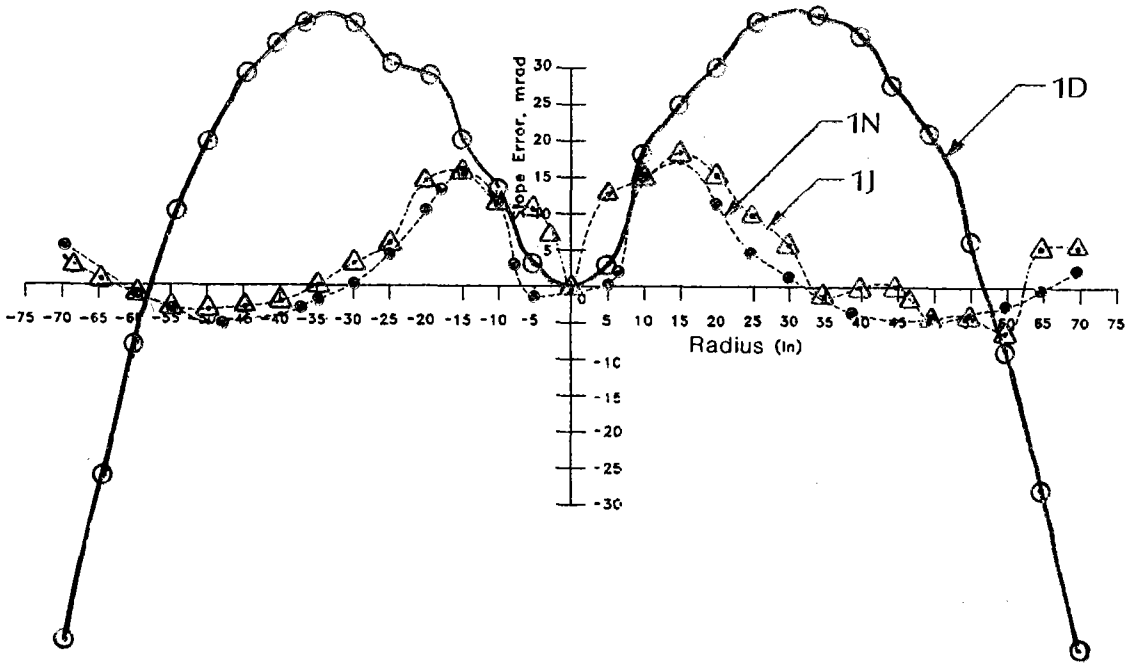

Figure 4.23 Slope Error as a Function of Radial Position for Test-Scale Membrane #1 After Nonuniform Loading Followed by a Uniform Load.

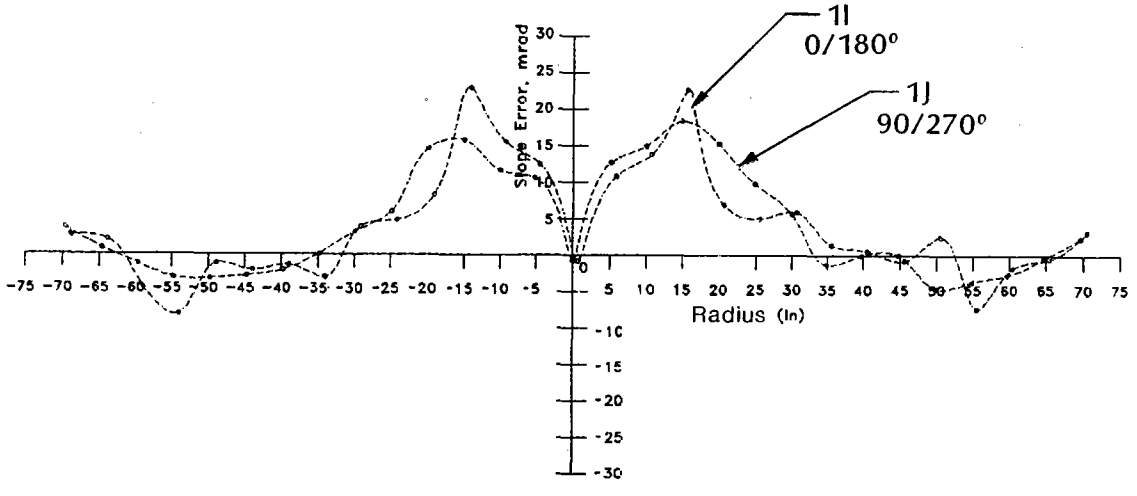

Figure 4.24 Slope Error Along Different Diametral Lines. 0/180° Parallel, 90/270° Perpendicular to Seams.

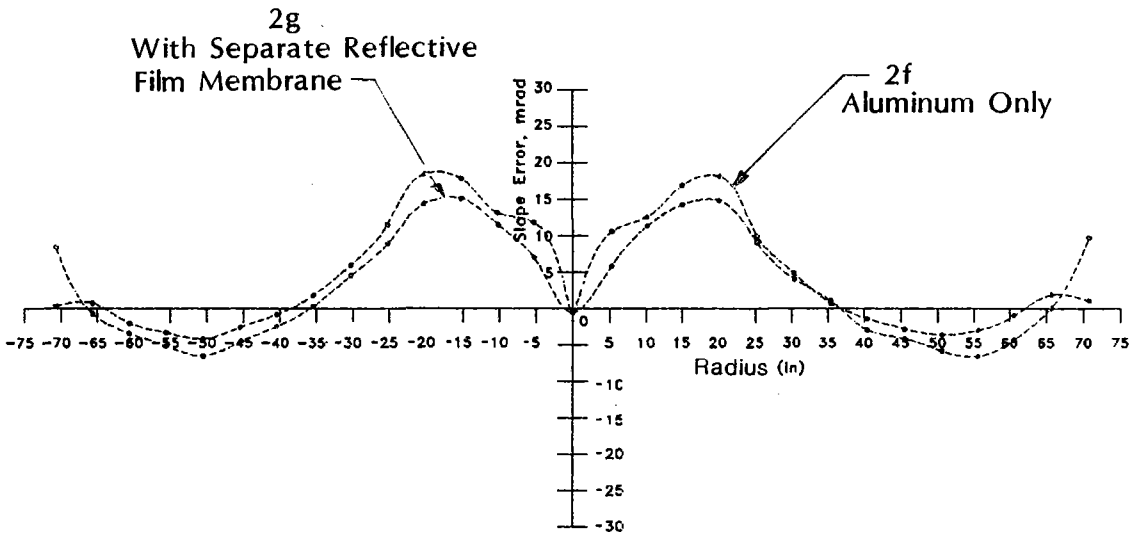

Figure 4.25 Slope Error as a Function of Radial Position for Test-Scale Membrane #2 After Nonuniform Loading Followed by a Uniform Load.

The "best" focal length for the polynomial curve fit was determined within the CIRCE optical code, based upon collector performance (the convolution of receiver and optical efficiency, see Figure 2.1). The flux density at the focal plane was subsequently plotted as a function of receiver radius, or radial distance from the ideal focal point.

CIRCE was subsequently used to define the performance of a parabolic membrane with a circular normal, random slope error distribution. The standard deviation of the error distribution was selected to bound the peak flux generated by the polynomial data. In other words, the polynomial representation of measured data was compared to a parabolic membrane with random error. The random slope error, a common figure of merit used to describe the accuracy of a parabolic dish concentrator, was estimated by bounding the peak flux.

The results of this performance prediction are shown in Figures 4.26 and 4.27 for the test- and bench-scale membranes, respectively. The test-scale polynomial representative peak flux was bounded by a one sigma circular normal slope error of 3 to 4 mrad; the bench-scale was bounded by a 1 to 2 mrad error. Additional plots of optical performance predictions, based upon the polynomial representation for different dispersions on circular normal sun shapes, were required by contract and are included in Appendix B.

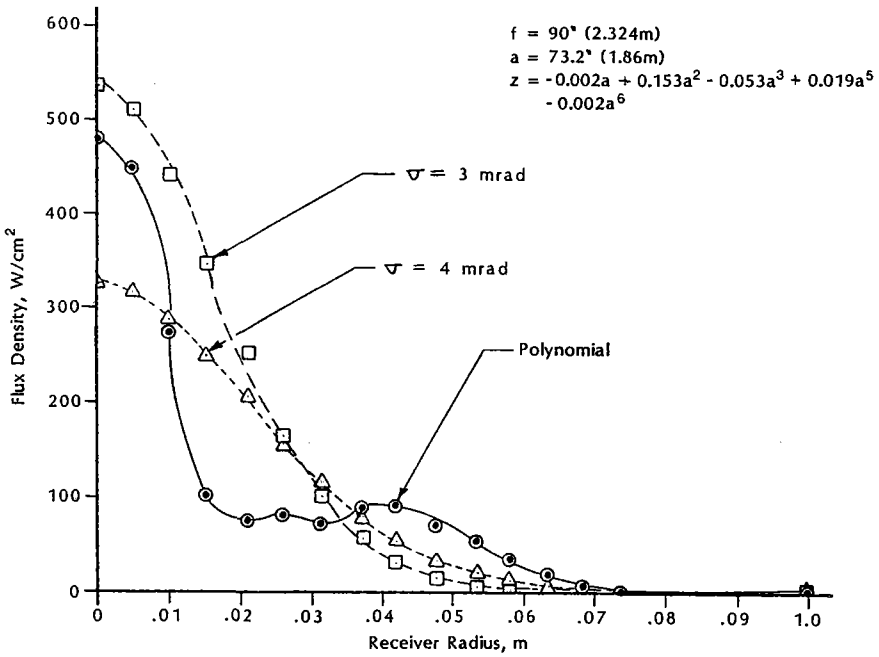

Figure 4.26 Optical Efficiency as a Function of Receiver Size, 144" (3.7 m) Diameter, Polynomial Fit and Ideal Parabolas with Random Errors.

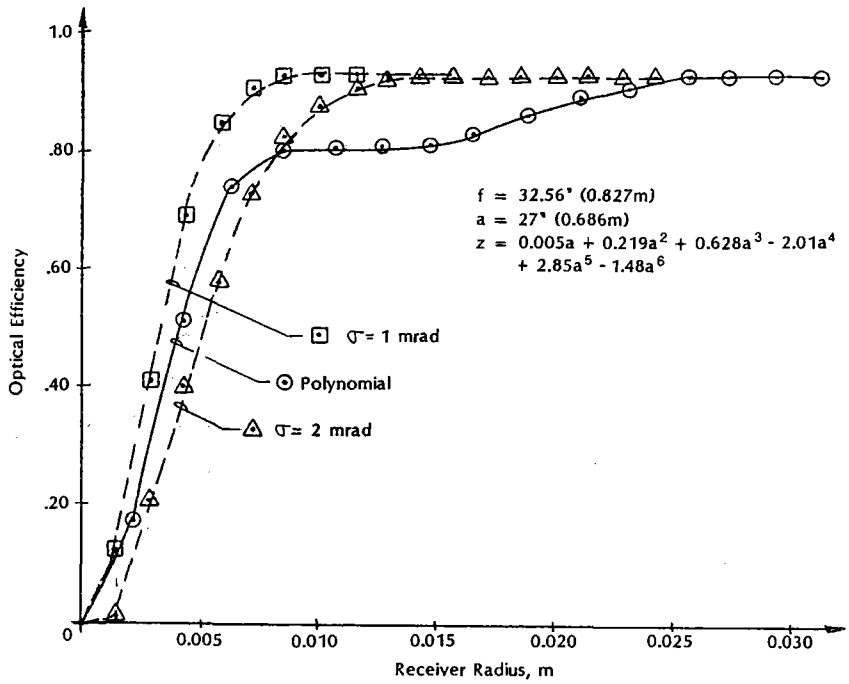

Figure 4.27 Optical Efficiency as a Function of Receiver Size, 54" (1.4 m) Diameter, Polynomial Fit and Ideal Parabolas with Random Errors.

4.4 Summary of Membrane Forming Analyses

Membrane forming techniques were developed empirically at two scales: bench-scale experiments were conducted with 54" (1.4 m) diameter membranes and test-scale with 144" (3.7m) membranes. A wide range of anticipated process variables were examined at bench-scale. Test-scale experiments were limited to a scale increase of final bench test results. The membrane shapes were characterized with direct-contact displacement measurements and laser ray trace measurements of slope. A figure of merit data reduction technique was applied to these membranes to permit comparison and judge the impact of subtle changes in process variables. This data reduction technique compared an area-weighted slope error. Performance estimates for the last membranes of each scale were also made with CIRCE [Ref. 4]. The test data are provided in Appendices A and B.

Several conclusions were drawn from bench-scale testing:

1. The load distribution used during forming is critical to the membrane's shape. Substantial improvements in accuracy can be achieved with proper control of the distribution.

2. Laminated aluminum membranes cannot be formed to small f/D ratios. The tensile modulus of the film exceeds the plastic modulus of the metal during forming. Rupture occurs in the metallic substrate at seams in the film.

3. Stabilization pressures, which load the membrane elastically, have relatively little impact upon the optical shape for small f/D ratios.

4. Stiffness of the attachment and initial tension do not substantially alter the formed shape of a membrane.

5. The attachment diameter of the membrane can be increased (effectively an increase in circumferential tension at the boundary) to improve performance.

6. The weighted error can be substantially reduced on membranes formed with a non-uniform load if a small fraction of the area (approximately 3 to 4%) at the perimeter is considered inactive aperture.

Repeatability in membrane accuracy, with the process variable controls identified at bench-scale, was also demonstrated.

Two test-scale membranes were formed using water as a nonuniform load source. These membranes demonstrated a reasonably accurate surface, but were not as precise as the membranes formed at bench-scale. The limited number of experiments prevented accurate definition of the most crucial process variable: the nonuniform load profile.

Performance estimates for membranes at test- and bench-scale were determined by representing the measured membrane slopes with a high-order polynomial. This polynomial was subsequently used in CIRCE to define the flux as a function of radial position on a centered target. The peak flux was bounded by perfect parabolas with a circular normal slope error distribution. The value of these bounding one sigma slope errors was:

3 to 4 mrad at test-scale (144", 3.7 m diameter), and
1 to 2 mrad at bench-scale (54", 1.4 m diameter).

5.0 Structural Analysis of the Optical Element

The optical element of the stretched-membrane dish was defined by a parabolic front membrane, a conic rear membrane, a circular ring, a central mast or hub located at the optical axis of the dish, and spokes that radiated from the mast to the ring. The double membrane design, combined with the circular ring, formed a plenum. A differential pressure was imposed across the membranes through partial evacuation of the plenum with a fan. This pressure load tensioned or stretched the membranes; hence, the name: stretched-membrane dish.

The membrane support frame included a hub and spoke structure to transfer loads. The hub and spoke support system was similar to a bicycle wheel. A structural tensegrity was formed with two elements loaded in axial compression (the ring and mast), and a set of elements loaded in tension (the spokes), with no connecting members loaded in bending. This type of support frame was selected for structural efficiency, or low weight, in response to three major criteria: ring height, structural coupling, and number of supports.

The circular ring frame should be compact. The distance between the vertex and ring plane of a commercial-scale dish, with an f/D ratio of 0.6 was 57.5 in (1.46 m). The second membrane, required to close the plenum, was located behind the optical membrane. The support frame provided stiffness to the rear membrane so that the ring height was substantially smaller than the vertex displacement. This was achieved in the selected design by draping the rear membrane over the rear spokes. If the geometry of the front membrane had been allowed to dictate ring height, a tall, heavy ring would have been required.

Structural coupling enhances the stiffness of a frame by forcing the elements to carry load by virtue of their attachment as well as their independent stiffness. The spokes provided resistance to out-of-plane deformations directly, but also provided radial stiffness symmetrically offset from the ring centroid. This attachment increased the torsional stiffness of the ring frame and reduced roll in response to loads. Roll and vertical deflection are intimately coupled deformations in any circular ring. Consequently, the spokes provided a secondary resistance to out-of-plane deformations.

Sag between supports creates error in the optical element. This deflection was proportional to the cube of the distance between supports. The hub and spoke system provided a large number of supports, with virtually no increase in support weight intrinsically associated with quantity. Consequently, the ring deformation was checked without adding weight to the structure.

The optimization and analysis presented in this section were limited to a review of the hub and spoke system only. No alternate support system was investigated. The analysis was also limited by optimization and design of the optical element independent of the PCA and dish support structure, as required by contract. These structures, and the concentrated loads they imposed upon the optical element, were not given major weight in optimization efforts.

The structural analysis was broken down into two major sections: loads and geometry. The loading used for the stretched-membrane dish was unusual in that it incorporated initial and environmental loads. The initial loads were invariant and were established by the stabilization pressure and spoke pre-loads. The environmental loads were primarily imposed by the wind. A baseline geometry was established, and the analysis was used to optimize that geometry. The structural response was modeled with finite element techniques. Following the discussion of loads and geometry, the limitations of the analysis and a summary of results are provided.

The structure selected for analysis optimized at a specific weight of 2.3 lb/ft^2 (11.0 kg/m^2) for the optical element.

5.1 Stabilization Pressure and Loads

Stabilization pressure was defined as the differential load per unit of area across the optical membrane. The optical membrane, rear membrane, and circular ring frame defined a closed plenum. The differential pressure across the optical membrane was imposed through partial evacuation of this plenum. The optical membrane was a very thin diaphragm with a large span. This membrane cannot sustain compressive load without buckling. The pressure differential maintained a tensile load in the membrane. Four criteria were used to establish the stabilization pressure: response to a uniform operating load, stability in all anticipated operating loads, sensitivity to nonuniform operating loads, and contact between the front structural membrane and reflective membrane being maintained.

The membrane's response to loading was investigated with linear finite element analysis [ANSYS, Ref. 17] and the edge solution of Steele and Balch [Ref. 11]. The finite element approach was similar to that described in Section 3.1.2. The numerical model was defined by a membrane with a relapsed parabolic shape, a stabilization pressure applied in the first load step, and an operating pressure added in the second step. The operating pressure was defined by contract as 0.0057 psi (40 Pa). The difference in the slope of each element, over the inner 97% of the aperture, between the first load step (stabilization) and second step (stabilization plus operating load) was defined as the error.

The analysis was intended to establish a minimum stabilization pressure. As the stabilization load increased, the operating load became a smaller fraction of the total load. Consequently, the relative difference in shape decreased. The model also indicated that parabolic membranes with small f/D ratios were stiff to uniform pressure loads. The slope error was approximately 1 mrad for stabilization pressures as low as the operating pressure.

The edge solution [Ref. 11] was also applied to a relapsed parabola. An area-weighted focal length was determined for the stabilized membrane and compared to a membrane loaded with stabilization and operating pressure. For the lowest stabilization pressure considered, 0.0057 psi (40 Pa), the change in focal length under combined loading was 0.08% (7 mm variation at commercial scale, 150 m^2 dish with a nominal f/D of 0.6). In other words, the fundamental membrane shape was virtually unaffected by uniform operating loads. No minimum stabilization pressure was defined by this stage of the analysis.

A positive pressure differential is required to maintain stability in the optical membrane. Stability is a requirement under all operating conditions. Consequently, the stabilization load must be greater than the leeward vacuum imposed by the wind. This vacuum is generally defined as 60% of the dynamic pressure [Ref. 10]. An arbitrary wind speed of 50 mph (33 m/s) was assumed to represent the worst operating condition;[1] the resultant leeward vacuum was 0.027 psi (190 Pa). This pressure was adopted as a minimum stabilization load for a sensitivity analysis of nonuniform operating pressure distributions.

A "pill-box" operating load distribution, with 0.0043 psi loads on one half of the membrane, and 0.0071 psi on the remaining half (30/50 Pa), was applied to a finite element model of quad shells to consider sensitivity of error to nonuniform pressure distributions. The load was applied in five steps. The first step was the stabilization pressure (0.027 psi, 190 Pa). The following steps added one-fourth of the operating load with each increment. The stiffness matrix of the deflected shape was calculated after each application of load. The analysis, therefore, included geometric stiffening effects and asymmetry in the membrane. The finite element model predicted a slope error of less than 1 mrad.

This analysis indicated that a membrane with an f/D of 0.6 was stiff in comparison to the loads applied by wind and weight. The error remained small in a uniform and non-

[1] The highest wind loadings occur in stow. These pressures were not considered in the establishment of a stabilization pressure because the separate reflective membrane was assumed to provide protection for the metal membrane. In other words, stabilization pressure was not coincident with stow wind loadings.

uniform profile. The analytical effort was supported by the empirical investigation discussed in Section 4.2.4, which also indicated that changes in membrane shape as a result of operating loads were insignificant. This result had an important ramification in the dish design: active control of the plenum pressure in response to changes in wind pressure was not necessary.

The final step taken in Phase I to establish a minimum stabilization pressure was analysis of the separate reflective film membrane. The reflective film membrane was assumed to be initially flat. The formulas developed by Murphy [Ref. 23] were used to predict the pressure requirements to ensure contact between the polymer and metal membranes. The pressure range was 0.055 to 0.11 psi (380 to 760 Pa) at commercial scale. The same formulas were applied to the empirical results at bench and test scales.

The pressure required for contact was at the low end of the predicted values. The lower pressure was added to the anticipated vacuum at high wind speeds to yield a stabilization pressure of 0.09 psi (620 Pa). The application of these formulas was not precisely correct, as the reflective membrane is near yield, the tensile modulus is not constant, and creep will occur over a period of time. The correlation at the two empirical scales made the assumption appear reasonable, however. The minimum stabilization pressure was defined by the requirement to maintain contact between a flat reflective membrane and a structural membrane yielded to an f/D ratio of 0.6.

The stabilization pressure required by the separate reflective film was used for the remainder of the structural analysis. This minimum was not absolute, and could have been reduced with a preformed reflective membrane. This option was not explored during Phase I. No attempt was made to refine the stabilization pressure assumption.

The uniform survival pressures imposed at stow were defined by contract as 0.149 psi (1030 Pa). The dish support system defined a stow position with the dish facing the zenith (see Section 6.0). The worst operating load on a membrane at any position was assumed to be the sum of stabilization pressure and 60% of the dynamic pressure at 50 mph: 0.135 psi (930 Pa).

5.2 Structural Geometry

A baseline geometry for the dish was defined, and the structural analysis was used to refine the initial assumptions. The initial dish geometry is schematically illustrated in Figure 5.1. The perimeter of the front and rear membranes was attached to a circular tube with a rectangular cross-section. Three sets of spokes radiated from that circular frame and were subsequently attached to a central mast, which defined the optical axis of the dish. The rear membrane was actually draped over the rear spokes.

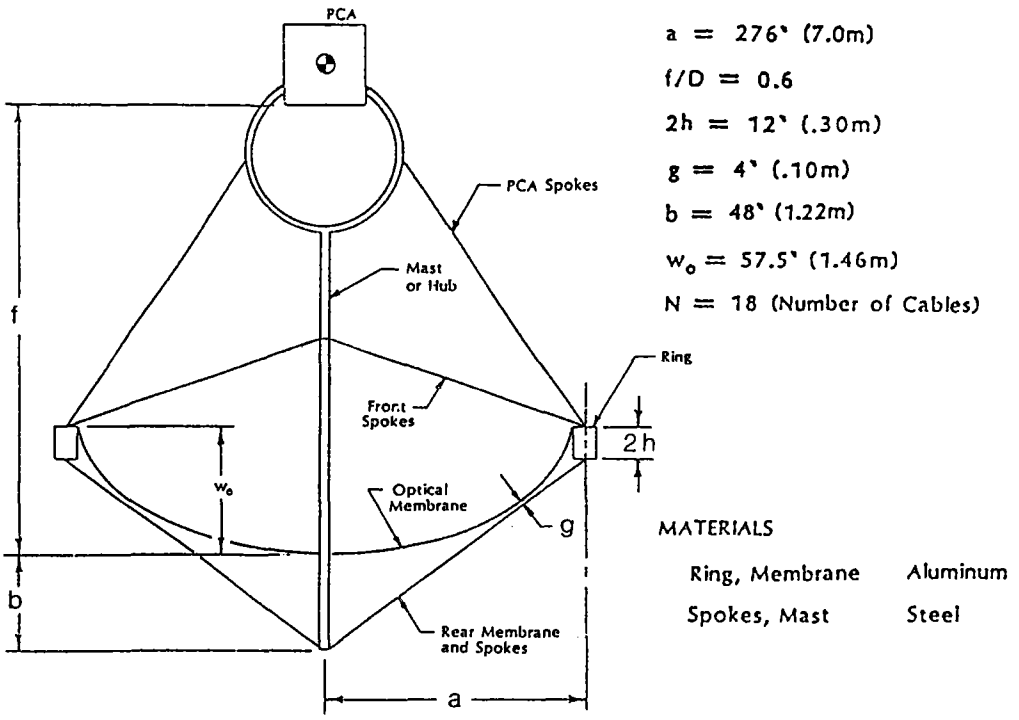

Figure 5.1 Initial Dish Geometry Selected for Analysis.

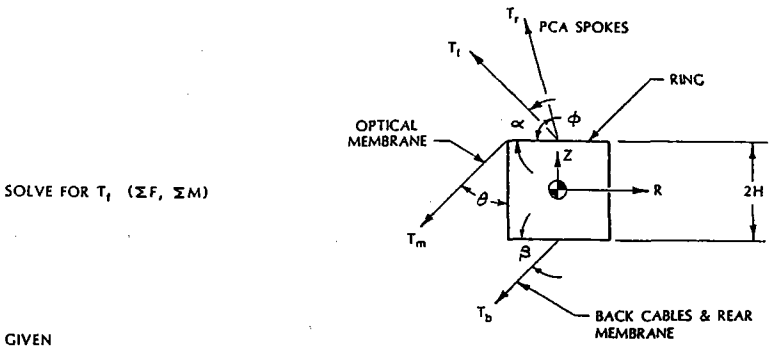

SOLVE FOR T_f (ΣF, ΣM)

GIVEN

T_r = RECEIVER CABLES. DEFINED BY DETERMINING MINIMUM T_o TO PREVENT STRESS REVERSAL AT HORIZON. Rcvr = 1000 kg (2200 lbs). $F_s = 2$

ϕ = fn (f/D)

T_m = MEMBRANE z COMPONENT fn (a,p)
MEMBRANE T_o fn (T_{mz}, θ)

θ = fn (f/D)

T_b = BACK MEMBRANE REPLACED WITH 'CABLES'. FINAL SHAPE BASED UPON DERIVATION OF RESPONSE FOR A RAMPED LOAD. GIVEN MINIMUM GAP, 2H FIND T_o

β = fn (p,2H,T_o,gap)

Figure 5.2 Force Diagram of the Ring Frame for the Baseline Geometry.

The radius of the commercial-scale dish was defined by the aperture goal stated in Table 2.1, while the optical analysis confirmed the goal for the f/D ratio of the front membrane. A baseline ring height of 12 in. (0.3 m) was arbitrarily selected, and subsequently modified as a result of the analysis. The mast was extended behind the vertex of the front membrane to provide a center attachment for the rear spokes and membrane. The distance for this extension, the ring height, and the number of radial spokes were arbitrarily selected for the baseline. Materials were chosen based upon the analysis presented in Section 3.0.

Figure 5.2 illustrates the forces applied to the baseline ring frame at each support point. The cable pre-load and angle of departure from the ring were based upon some simplifying assumptions. First, the PCA was assumed to be supported by the central mast. Moment loads were eliminated in the mast by transferring lateral loads, primarily the weight of the PCA when facing the horizon, to ground through the PCA spokes. The pre-load for this set of spokes was defined at twice the tension required to prevent compressive stress at any dish orientation. Spoke statelier elements can carry load in tension only; tension was maintained at all positions to avoid shock loading in the spokes or spoke attachments. The departure angle for the PCA spokes was defined by the radius and focal length of the dish.

The magnitude of the forces applied by the front membrane was a result of the pressure load only and was easily determined. The forces were distributed, rather than concentrated, at each support point. The departure angle of the membrane was determined by the f/D ratio of the dish.

The forces applied at the bottom, or rear face of the ring frame, were imposed by both the back cables and rear membrane. The differential pressure across the rear membrane was assumed to be transmitted through the rear spokes and subsequent to the ring. The pressure load applied to the membrane resulted in a ramped linear load on the spoke, as the membrane area supported by each back spoke increased from center to the perimeter. The shape of a cable under a ramped linear load was analytically derived, and the front membrane and rear cable shapes were defined in a single coordinate system. The back cable tension was increased until there was no interference between the two membranes at any operating load condition. Consequently, the gap between membranes enforced on the baseline determined the magnitude of back cable pre-load. The load applied at the ring by this cable set was a combination of the pre-load, and the additional tension imposed by deformation in response to the pressure differential across the rear membrane. The angle of departure from the ring plane was defined by the analytical derivation of cable shape in response to a ramped load.

The forces imposed on the ring frame by the PCA spokes, rear spokes, and front membrane were known. The vertical, or Z-axis, forces required balance as a condition of statics. The moment about the circumferential axis was minimized to avoid roll in

the ring and the subsequent error that this deformation would impart to the membrane. These balance conditions were achieved by selecting the departure angle and pre-load in the front spokes. The baseline geometry and forces were consequently described.

The geometry and forces associated with the PCA spokes and front membrane were determined by the stabilization loads, operating loads, PCA weight, and fundamental optical geometry of the dish. These loads and geometries were not optimized based upon structural parameters. The front cable pre-load and geometry were a result of the loads and geometry of the rear spoke set. Consequently, variation in the baseline geometry began with consideration of the rear spoke set.

The rear spoke tension was determined by the separation required between the front and rear membrane to avoid optical distortion and concentrated loads in the optical surface. The fundamental baseline geometry was altered to maintain this separation, while reducing the spoke pre-load, by increasing the distance between the parabolic vertex and the rear end of the mast. The cable pre-load is plotted as a function of the rear extension in Figure 5.3 for the baseline ring height and the ring height that was ultimately selected in the structural analysis.

The forces in the radial direction, imposed by spokes and membranes on the ring frame, are balanced by deformation and loading in the ring itself. Consequently, the spoke load should be minimized. The majority of the pre-load reduction can be obtained with a mast extension of 60 in (1.52 m). The baseline geometry was subsequently modified to incorporate this rear extension.

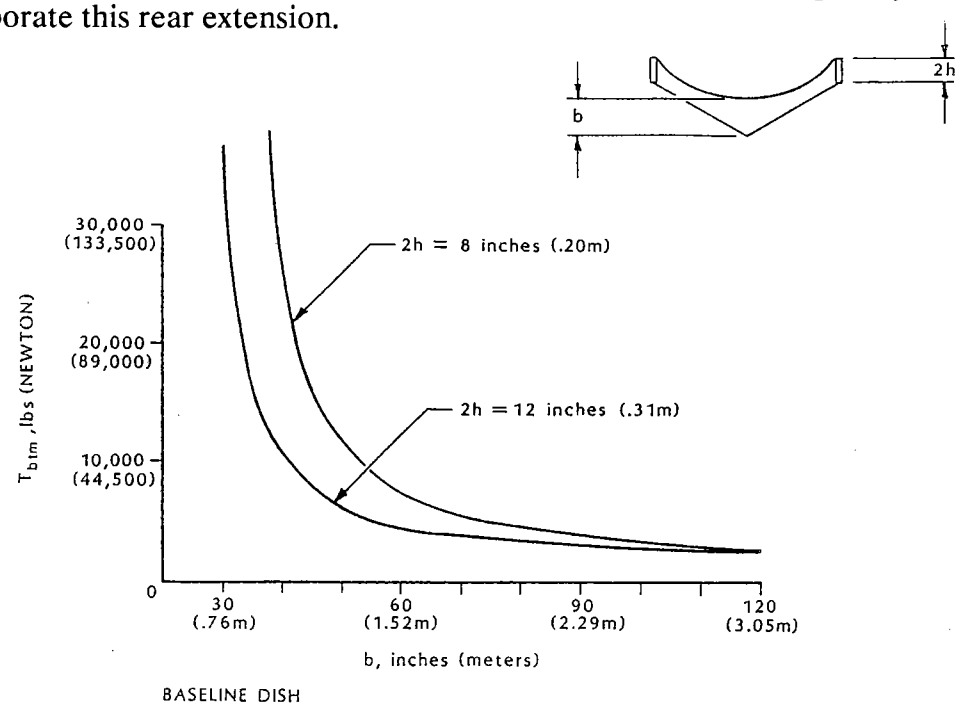

Figure 5.3 The Variation in Rear Spoke Pre-Load as a Function of the Mast Extension.

The next step in revision of the model baseline was to consider the impact of membrane modulus. The coupling between the front membrane and ring frame was analyzed by changing the tensile modulus or stiffness of the membrane, while leaving the stiffness of the ring frame unaltered. The membrane tensile modulus was varied from 500,000 to 30,000,000 psi (3.4 to 207 GPa), corresponding to a typical polymer and steel, respectively. The stress in the ring frame under survival loads and the deflection at operating load were virtually independent of the membrane material. The membrane material selection had no structural impact upon the ring frame. The coupling in the ring frame was dominated by the spokes, rather than the membrane.

The next step in the analysis of the baseline geometry was the investigation of the number of spoke supports. The number of concentrated load points determined the magnitude of the moment loads about the radial (out-of-plane) and circumferential (in-plane) axes imposed upon the ring frame. A concentric compressive load or hoop stress only (no moment) would be imposed by an infinite number of spokes, for example. Conversely, if two spokes were used, the moment would be maximum at the half-point, and equal to the product of pre-load and radius, while the hoop stress at the coincident point would be zero. In the first case, the compressive load would drive the ring frame design. The frame design would be determined in reaction to the moment load in the second case. The ring property required to resist the compressive load was simply the cross-sectional area (A); the out-of-plane moment of inertia (Iyy) and in-plane moment of inertia (Izz) were the key properties to sustain a moment load.

The number of supports in the baseline structural model was varied, and the requirements for the key ring properties were determined in response to the survival load conditions. The results of the analysis are shown in Figures 5.4a, b, and c. The ring shape was determined by running the finite element structural model to establish the moments and direct loads in each axis. These forces and moments were subsequently applied to an arbitrary tube cross-section to determine the bending and axial stress state in the ring at the support (maximum direct load), the point halfway between supports (maximum moment load), and the point one-quarter of the distance between supports (maximum torsional load).

The arbitrary cross-section was then modified to produce a shape with the least weight that could sustain the loads at any of the points examined without exceeding the allowable stress (the allowable stress in the ring was defined as 75% of the yield strength). A secondary stability constraint was also imposed: the shape was examined for localized buckling failure with the formulas developed by Timoshenko [Ref. 30]. The optimized shape was subsequently used in the finite element model, and forces and moments were developed again. The purpose of this iteration was to allow for changes in the loads as a result of changes in the frame's stiffness. This iterative procedure was repeated (generally, one iteration was adequate) until the finite element model predicted an acceptable stress level.[1]

[1] This procedure was implemented for different ring materials as well as shapes. The impact of material selections is discussed in a previous section.

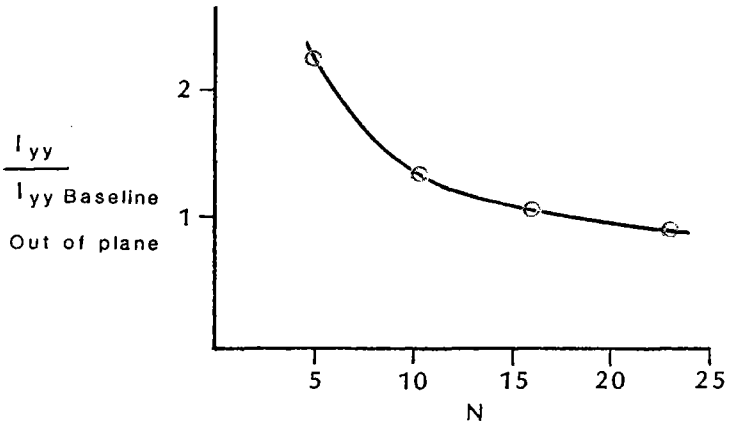

(a) Out-of-Plane Area Moment as a Function of the Number of Supports

See Figure 5.1 for Baseline Geometry Design Based on Stress and Stability.

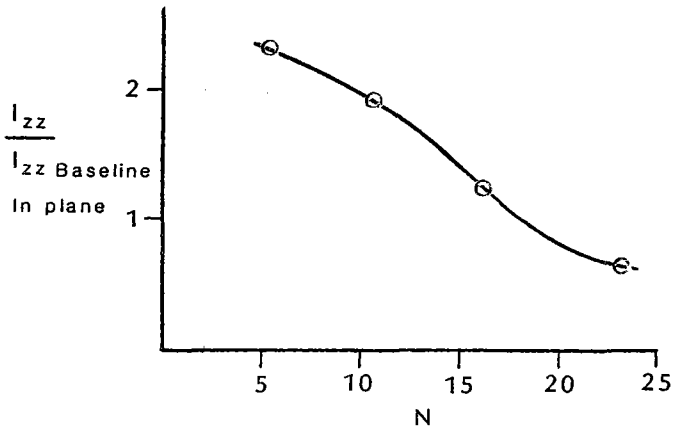

(b) In-Plane Area Moment as a Function of the Number of Supports

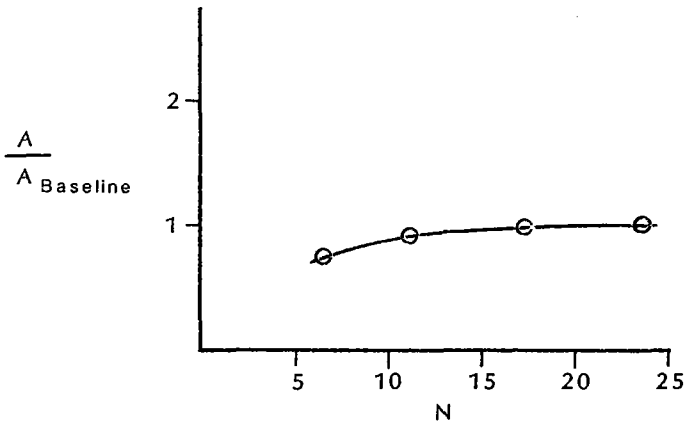

(c) Cross-Sectional Area as a Function of the Number of Supports

Figure 5.4 Variation in Required Ring Properties as a Function of the Number of Supports.

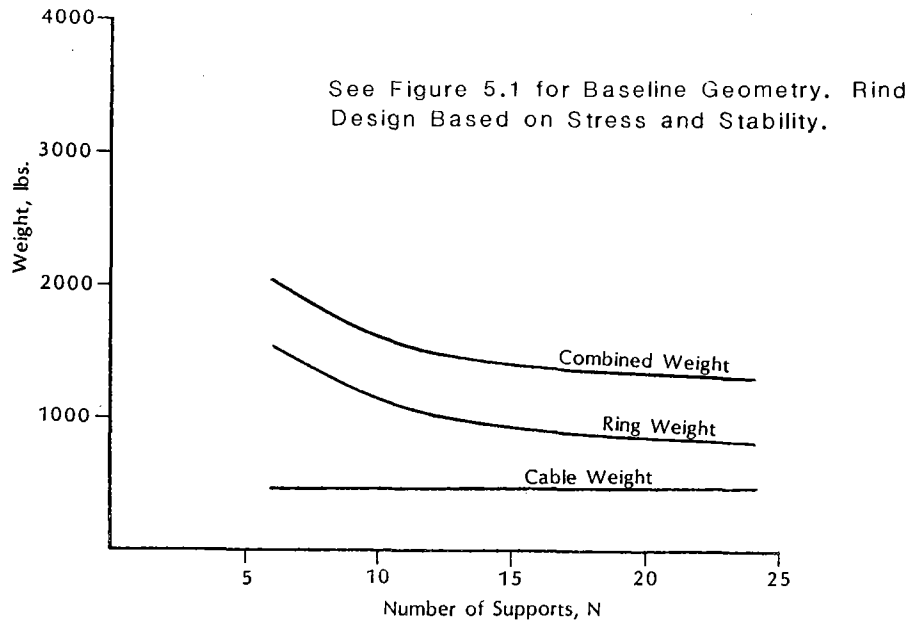

Figure 5.5 Frame Weight Optimization as a Function of the Number of Supports.

The results of ring optimization as a function of the number of spokes are shown in Figure 5.5. The cable weight was essentially independent of the number of supports. The ring weight decreased as the number of supports increased. The weight asymptotically approached the minimum weight defined by the hoop stress requirement at an infinite number of supports. The optical error, which occurred with ring roll or deflection, was also reduced as the number of supports increased.

Analysis of the optical element was required by this contract, but optimization of the PCA and dish-support structures were relegated to a later contract. A cursory examination of the mast PCA support system was conducted, however, during this structural analysis. The ring, shown at the top of the mast in Figure 5.1, was designed based upon stress and stability. The tube cross-section required intercepted a substantial fraction of the concentrated light: 4-6% based upon the ring's diameter. The ring was subsequently rejected, in favor of a tripod, at an estimated weight penalty of 200 lb (91 kg, 890 N). This analysis was not exhaustive and may require investigation in a subsequent phase of analysis. This alteration in the design required that spoke pre-loads be redeveloped, as the PCA spokes were no longer required.

The rear membrane and back spokes were also redefined as distinct elements in the final analysis, rather than the lumped element used for the definition of the fundamental geometry. This distinction required that the separation between the optical and rear membrane be made at the midpoint between spokes, rather than at the spoke itself. An increase in spoke pre-load was required to accommodate this change in the final analysis.

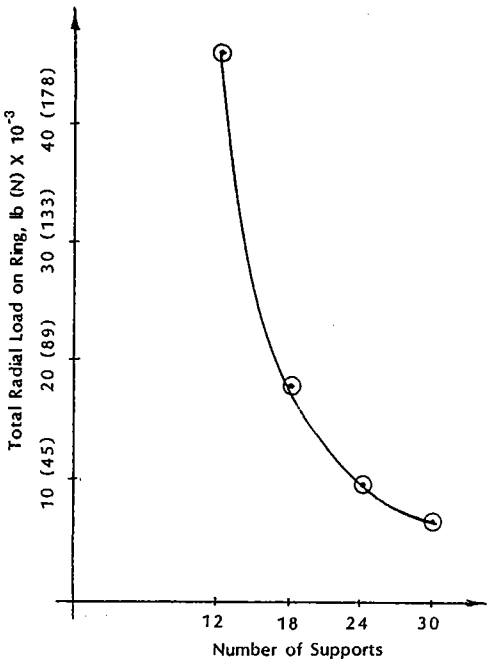

Figure 5.6 Radial Load Imposed on the Ring Frame as a Function of the Number of Supports.

The sag at the cable and between the spokes was a strong function of the span, or number of supports. The sag was reduced by adding tension to the spokes. The pre-load in the cables, and tension in the membranes, imposed a radial load or hoop stress on the ring. Consequently, the radial load imposed upon the ring decreased as the number of supports increased. The hoop stress was directly proportional to the radial load and determined the asymptotic minima illustrated in Figure 5.5. The radial load is shown as a function of the number of supports in Figure 5.6. The number of supports selected for the final design was 24, based upon radial load.

The ring cross-section, based upon this final geometry, was a rectangular tube: 7 x 8 x 0.22 in (180 x 200 x 5.6 mm). The cable diameter was 0.50 in (13 mm).

The mast or central column was designed based upon the AISC allowable compressive concentric loads on columns [Ref. 31]. The concentric load was defined as 82 kips (365 kN) by the spoke pre-load. All support connections were assumed to be ball jointed, so that localized moments would not be applied to the column. The column length was determined by the 60-in (1.52-m) rear extension, and the departure angle required for the front cables to balance loads. The result of this code design was a 10-in nominal, standard weight (270 x 9-mm) pipe, and a column length of 240 in (6.1 m).

Table 5.1
Optical Element Weight, Final Geometry

Ring Frame, Aluminum	1012 lb (460 kg)
Front Membrane, Aluminum	235 lb (107 kg)
Central Column, Steel	810 lb (368 kg)
Spokes, Steel	812 lb (369 kg)
Misc. Brackets and Flanges, Steel	650 lb (295 kg)
Reflective Membrane, Plastic	38 lb (17 kg)
Rear Membrane, Plastic	85 lb (39 kg)
Total Optical Element Weight	3642 lb (1655 kg)
Specific Optical Element Weight	2.3 lb/ft^2 (11.0 kg/m2)

The membrane's thickness was not optimized based upon a structural analysis. The thickness of the front structural membrane was established at 0.010 in (0.25 mm) based upon the ability to handle large-diameter metal diaphragms demonstrated in previous work with stretched-membrane concentrators [Ref. 32]. The general stress level in the optical membrane was slightly less than 8000 psi (55 MPa), providing a safety factor, on yield, of approximately three. Further optimization of the structural membrane will not provide any substantial reduction in weight, because the membrane represents a small fraction of the total optical element weight.

The miscellaneous component weights, which were a part of the optical element, were estimated based upon past experience. No rigorous design or optimization procedure was applied to these items.

The breakdown of optical element weight is provided in Table 5.1.

5.3 Limitations of the Structural Analysis

Limitations in the structural analysis were imposed by the scope of the investigation, the selection of the structure that was modeled, and the numerical techniques used to define the response to loads. Phase I investigation of the stretched-membrane dish was directed toward refinement of the optical element design. This design analysis was essentially conducted in isolation from the PCA and dish support systems. As these concentrated loads are incorporated into the ring frame design, some modifications may be required. In particular, the spoke stiffness at the support system attachment points may increase. Local ring reinforcement at attachment points will also be required.

Receiver and dish support loads were determined in this preliminary analysis, based upon the conceptual support system presented in Section 6.0. The magnitude of the support loads was not large by comparison to the pre-load of the spokes. Consequently, a substantial increase in the weight of the optical element is not anticipated in response to these concentrated loads.

A single optical-element support system was selected for analysis and optimization in this investigation. The system was structurally efficient, as evidenced by the relatively low specific weight of the structure. A potential for weight reduction in the optical-element support system was identified late in the analysis, however. The first objective in selection of a structure to be optimized was a provision to avoid substantial ring height. A corollary of this objective was to allow the loads, or response to the loads, to define the structure rather than the geometry of the optical membrane. The objective was achieved, albeit not the corollary, by draping the rear membrane over the rear spokes to prevent contact between the two membranes.

The gap between membranes was maintained by increasing the spoke tension. The spoke pre-load impacted the ring frame design. Consequently, the geometry of the optical membrane ultimately affected the frame weight. The frame may benefit from a separate structure to maintain the gap between the optical and rear membranes. This option was not investigated during Phase I and remained a limitation in the analysis.

Finally, the structural models used for analysis were linear. The linearity was adequate for the developed optimization, except gross ring stability failure was not considered (local buckling or "web crippling" was incorporated analytically). This nonlinear analysis should be accomplished prior to implementing the presented design.

5.4 Summary of Structural Analysis

The optical element of the stretched-membrane dish was optimized in Phase I. The structure selected for analysis included the optical membrane, rear membrane, circular beam, hub, and spokes. The hub-and-spoke optical-element support system was selected to complement the fundamental stretched-membrane dish requirements and achieve three major objectives. First, the circular beam was compact as a result of the element support system. Second, structural stiffness was achieved through the coupling of spoke and ring, as well as the individual stiffness of each element. Finally, a large number of supports were provided to reduce the optical error and stress associated with ring deformation.

A differential pressure was required across the optical surface to prevent buckling in the membrane; this pressure was referred to as the stabilization load. The stabilization pressure was an initial load, which was invariant during operation of the dish. The environmental loads, predominantly wind, represented a decreasing fraction of the total

membrane load as the stabilization pressure increased. The error induced in the membrane from uniform and nonuniform operating loads was examined at different stabilization pressures. This analysis indicated that the optical surface, at an f/D ratio of 0.6, was stiff with respect to normal loads by virtue of its shape. Substantial stabilization pressures were not required to avoid optical error in the dish. The analysis also had an important design ramification: active regulation of the plenum pressure was not required to maintain an optically accurate shape in the variable load environment.

The stabilization pressure provided the only source of tension in the membrane. Tension was required to avoid stability failure. Consequently, a positive differential pressure must be maintained across the front membrane during all potential operating conditions. A vacuum is created on the leeward side of a bluff body in flow. The stabilization pressure, under no-wind conditions, should exceed the leeward vacuum to maintain a tensile state in the membrane. This requirement defined a lower bound for the stabilization pressure.

The limitations of forming a membrane, discussed in the previous section, required that the reflective membrane be separate from the membrane that defined the optical shape. Contact between these two membranes was maintained by the stabilization pressure. The pressure required for this contact was determined and added to the lower pressure bound defined by stability requirements. Ultimately, this defined the stabilization pressure at 0.09 psi (620 Pa).

The structural geometry of the optical element was also investigated under survival conditions. Component sizing was based upon stress under survival conditions. In general, the design of the optical element was sensitive to the potential operating loads at any position and the initial loads imposed by the stabilization pressure and spokes. The rear spokes served two purposes: support of the rear membrane, and load transfer between the ring and central column. The front spokes also transferred loads, and the pre-load was established to balance forces in the optical, or Z-axis, and minimize moments on the ring. The fundamental geometry, in particular, the mast extension behind the optical vertex, was optimized to reduce the pre-load required in the spokes.

The optical membrane demonstrated the ability to easily change shapes in response to ring deformation and, consequently, did not provide substantial radial or normal stiffness to the ring. The response of the optical element frame was virtually independent of the front membrane. Consequently, structural coupling did not have an impact upon material selection.

Spokes are long, slender structural elements that can transfer load through tension only. The tensile state in a spoke was maintained, without regard to the direction of loading, by providing an initial tension that exceeded the maximum compressive load. This initial tension was required to avoid shock loading in the structure. Shock loading would

occur if spokes alternated between a compressive stiffness of zero, to a substantial tensile stiffness, in response to an oscillatory wind load environment.

In the particular structure optimized here, the rear spokes transferred load between the ring and mast and supported the rear membrane. The rear membrane support determined the pre-load required in the spokes. The front spokes offset the vertical loads imposed by the membranes and rear spokes, while minimizing the moments applied to the ring.

The spoke tension imposed a radial load on the ring, which was resisted by axial, compressive stress in the ring. This compressive stress determined the lower bound of ring weight. Radial load decreased with an increase in the number of spokes, because of the span relationship in rear membrane support. The moment load on the ring, and optical error induced by ring deflection, also decreased with an increase in the number of supports. The majority of the benefit was obtained with 24 spokes, above and below the ring plane, at commercial scale.

The estimated weight of the optical element, including the membranes, ring, hub, and spokes, was 3650 lb (1660 kg) at commercial scale. The specific weight of the structure was 2.3 lb/ft^2 (11 kg/m^2).

THIS SHEET INTENTIONALLY LEFT BLANK.

6.0 Conceptual Support Systems

Three support systems were required to define a complete stretched-membrane collector: the optical element support, the dish support, and the PCA support. Optimization of the optical element system is presented in Section 5.0. This section describes the dish and PCA support system analysis.

Phase I of the stretched-membrane dish development was directed toward optical analysis, material selection, fabrication techniques, and optical element structural design. The dish and PCA supports were designed on a conceptual basis only. The purpose of this conceptual design was to identify systems that were compatible with the stretched-membrane dish collector. The design was not optimized, but was analyzed in sufficient detail to make weight estimates for the structures.

A dish support system was selected for analysis based upon several requirements and goals. The requirements were provision of a stable tracking platform with the freedom to move in two axes and track the sun, to fix the mast against translation, and transfer loads from the dish to ground. The goals of the support system were to reduce the impact of extreme loads in the stow position, avoid transfer of these loads through the drive, minimize concentrated moments on the optical element frame, and achieve the requirements and goals with a lightweight structure.

The PCA support system is discussed in Section 5.2. The requirement for this system was to maintain accurate relative position between the optical membrane and receiver. The goal for the structure was to minimize concentrated moments on the optical element frame. The same lightweight requirement was also imposed.

The result of the conceptual analysis was a dish and PCA support structure with a specific weight of 4.3 lb/ft^2 (21 kg/m^2).

6.1 Description of the Support System

A four-bar link with a rotating "ground" was selected as the dish support structure. The support system is schematically illustrated in Figure 6.1. The four bars of the linkage set were the A-frame, the optical element frame, the sway brace, and "ground." In this case, the "ground" link was actually a king post, rather than a stationary platform. The king post acted as "ground" because it could not rotate about the elevation axis. The jack link was not a part of the four-bar mechanism; this link was actually the elevation drive. Rotational freedom about the azimuthal axis was provided by rotation of the king post.

Figures 6.2 and 6.3 show the dish at two elevations, facing the horizon and zenith, respectively. The zenith position could also be modified to point slightly to the north if required by the latitude at the dish installation or for receiver safety. The second figure also defined the position assumed by the dish during stow.

The jack link consisted of a rigid bar and a linear actuator, or jack. In the stow position, the jack was fully extended. As the jack extension was reduced, the dish rotated about a locus of points defined by the linkage set. The maximum compressive load was imposed on the jack in the horizon position; when the shaft was fully retracted. At full extension, the jack shaft was loaded in tension without regard to wind direction. This combination of load direction and jack position will reduce the stability requirements in the linear drive shaft.

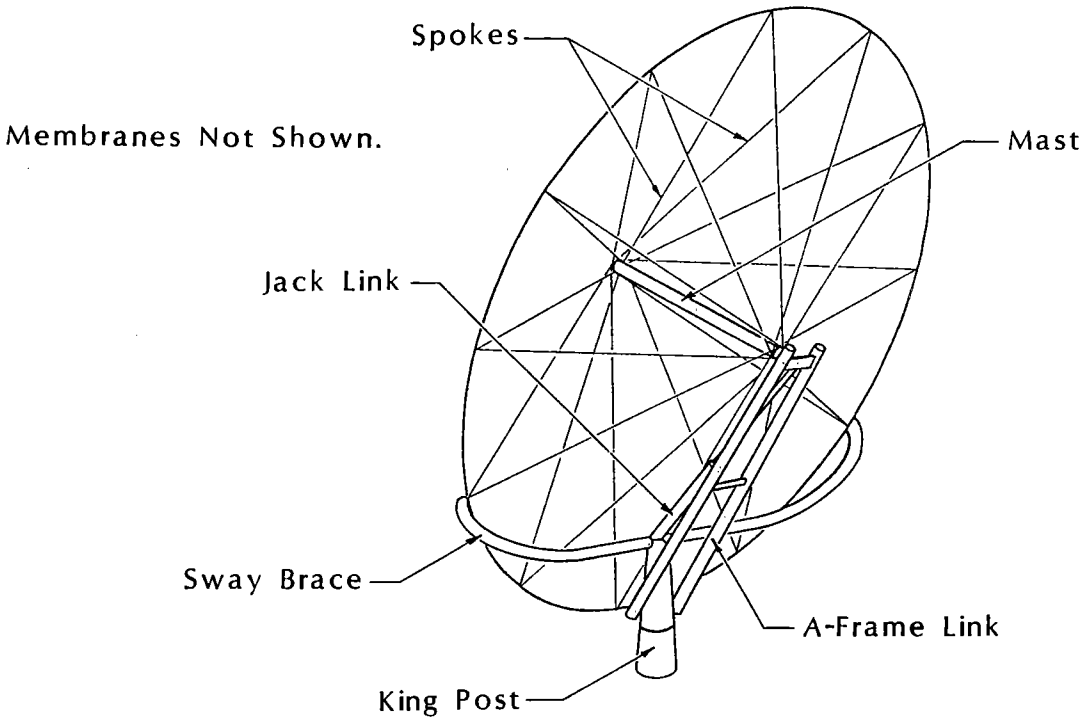

Figure 6.1 Schematic Representation of the Conceptual Dish-Support Structure System.

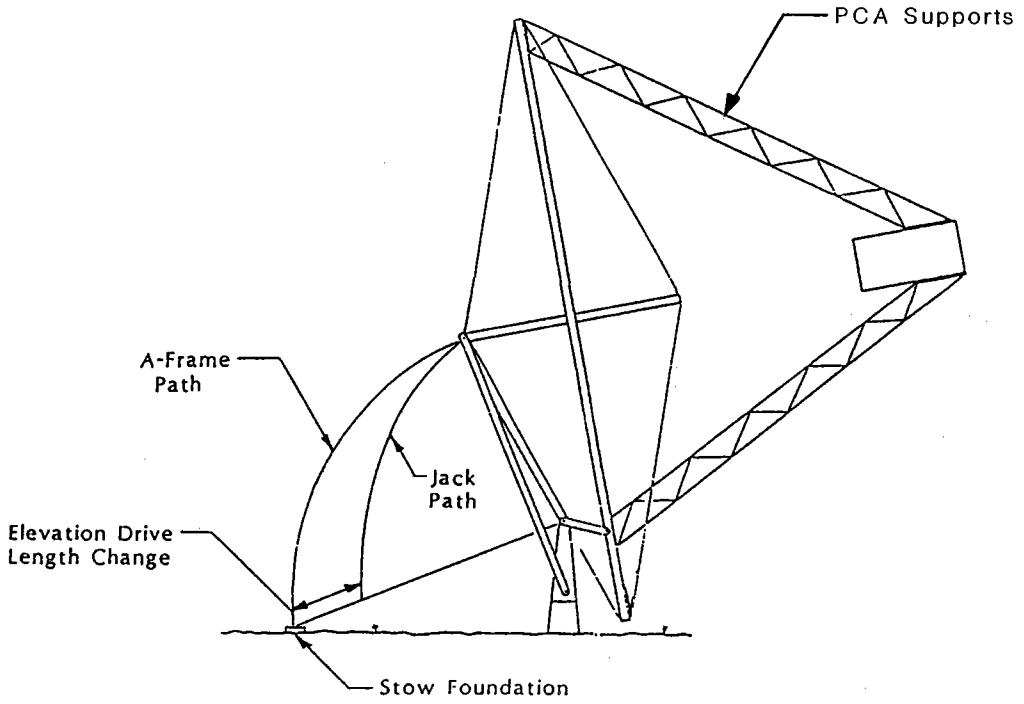

Figure 6.2 Dish Support System in the Horizontal Position.

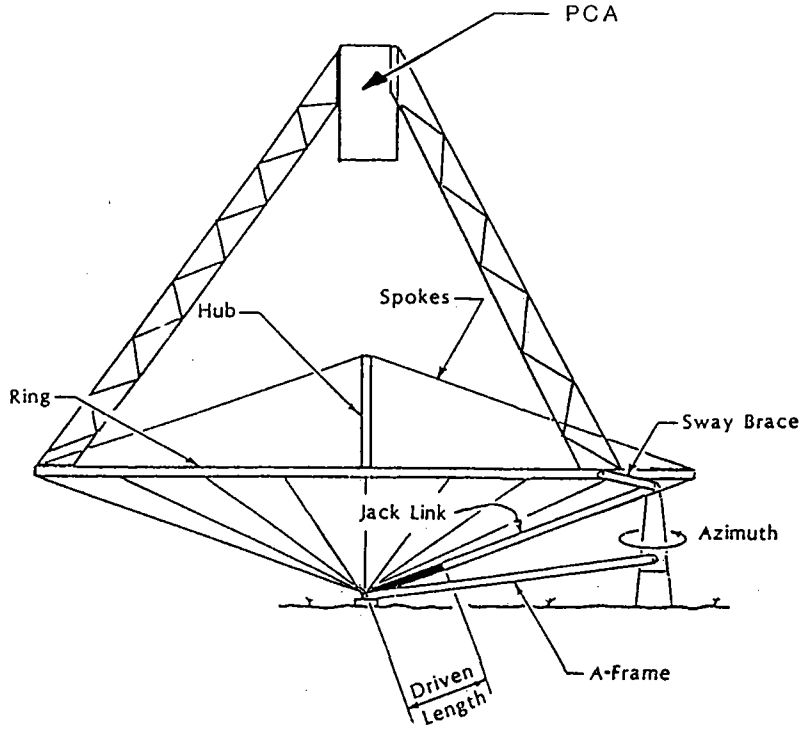

Figure 6.3 Dish Support System in the Vertical or Stow Position.

The king post consisted of a pair of concentric tubes. The inner tube was stationary, the outer tube rotated to provide azimuthal tracking freedom. Thrust and radial load bearings were provided at the top and bottom of the king post in the conceptual design; the azimuth drive was located between these bearing sets. This bearing arrangement allows the primary moment load induced by wind and weight in the operating positions to be transferred to the foundation without passing through the azimuth drive set. The specific type of azimuth drive was not identified in Phase I.

A secondary foundation was provided for the mast in the stow position. The conceptual support design was based upon a tapered mast resting in a conical bushing in the stow foundation. This conical bushing was potentially capable of removing thrust and lateral loads from the mast directly. Consequently, forces were removed at the second foundation and king post without passing through the drive mechanisms.

A conventional tripod structure was selected for PCA support. A spoke stabilized ring frame, located at the front of the mast, was originally considered for receiver support. This approach was abandoned because of the shading, as discussed in Section 5.2. The tripod design was based upon a trussed, open-web, fabricated beam. Cables are attached between the ring and truss midpoints to increase lateral stability. The truss was ball-jointed at the ring, and hinged at the receiver. This type of ring attachment prevented concentrated moments from being induced in the optical-element ring frame. The tripod was oriented so that two of the legs were coincident with the sway brace of the dish support.

6.2 Loads and Structural Analysis.

The dish and PCA support systems were basically determinant structures. In other words, the forces and moments at each attachment were independent of the component's stiffness. Consequently, the loads could be determined through application of the aerodynamic coefficients [Ref. 33] and the constraints of static equilibrium.

The forces and moments applied at each joint were dependent upon the relative orientation of the wind and the dish. The basic load matrix used for analysis is shown in Figure 6.4. Five operating positions were selected, which corresponded to the positions of maximum direct forces or moments. The stow position was also considered. Loads in the operating positions were developed for deflection analysis at 18 mph (8 m/s) and for stress at 50 mph (22 m/s). Stress analysis was conducted for the stow position at 90 mph (40 m/s). The dish and PCA weight was superimposed on wind loads in all analyses.

The distance between the dish centerline and ground determines the position of the collector in the atmospheric boundary layer. The support system selected for analysis was unusual in that this distance varied as a function of elevation angle. For the stow

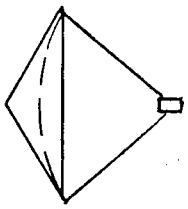

A

Elev 8-22 Deg

Az 0 Deg

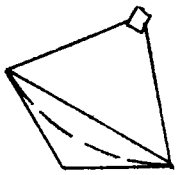

B

Elev 8-22 Deg

Az 60 Deg

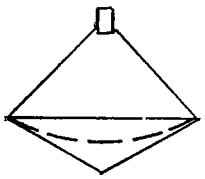

C

Elev 8-22 Deg

Az 90 Deg

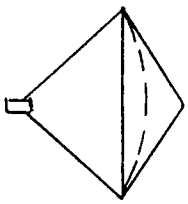

D

Elev 8-22 Deg

Az 180 Deg

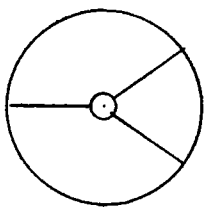

E

Top View of Dish

Elev 83-97 Deg

Az 0, 90 Deg

Wind Direction

Forces and Moments Resolved for Positions A Thru E at 50 mph (22m/s) and 18 mph (8m/s)

Position E 90 mph (40m/s) Also

Uniform Pressure and Coefficients from JPL-1060-66 [Ref. 33]

Figure 6.4 Load Matrix for Structural Analysis of the Dish and PCA support Structure

position, the dish was deep within the boundary layer. The potential load reduction associated with this change was not incorporated into this analysis. The dish centerline was assumed above grade at a distance equal to the ring radius. This conservative approach was adopted because the design was conceptual only.

The allowable limits for stress and stability defined by the American Institute for Steel Construction [Ref. 31] were adopted for support system design. The deflections were expressed in terms of the position of the dish's optical axis. The allowable tracking error was somewhat arbitrarily established at 2 mrad in an 18 mph (8 m/s) wind. Based upon these allowable limits, the survival loadings consistently controlled the design of the support structures.

The dish and PCA support system design was conceptual only. Consequently, no attempt was made to optimize the shape of each component. To simplify the conceptual design process, all support elements were assumed to be fabricated from structural tubing. The only exception to this design approach was the PCA support, which was assumed to be a truss, fabricated from structural tubing. Attachments in the structural support systems were not specifically designed.

Table 6.1
Dish and PCA Support Weight

Sway Braces	1880 lb (860 kg)
A-Frame Link	1130 lb (510 kg)
Jack Link	580 lb (260 kg)
King Post	1350 lb (610 kg)
Misc. Brackets, Bearings, Gussets	800 lb (360 kg)
PCA Tripod	1140 lb (520 kg)
Total Support System Weight	6880 lb (3130 kg)
Specific Support System Weight	4.3 lb/ft^2
	21.0 kg/m^2

A summary of weight by component is provided in Table 6.1. The weight associated with miscellaneous brackets, drive pins, bearings, and gussets was estimated.

7.0 Results, Recommendations, and Conclusions

This section of the report summarizes the results of the Phase I development effort, forwards recommendations for development for future work on the stretched-membrane dish collector, and draws conclusions with respect to the reported effort. The results were summarized according to the five major sections of the report: optical geometry, material selection, membrane forming development, structural analysis of the optical element, and conceptual support systems. Recommendations were based upon limitations of the Phase I effort because of scale, scope, or peculiarities intrinsic to the technology. The conclusion addressed the project goals established at the beginning of this project.

7.1 Summary of Results

The optical geometry of the concentrator was optimized based upon performance. The results of the analysis indicated that a single- facet, or monolithic concentrator provided the best performance. The f/D ratio selected was 0.6, also based upon performance. No impediment peculiar to stretched-membrane dish technology was identified that prevented this optical geometry from being implemented.

A metallic membrane defined the optical shape. The materials considered for this membrane included polymers, composites, and metals. Errors associated with edge effects were particularly pronounced in the low-modulus materials (polymers and composites). A substantial reduction in performance due to creep was associated with the polymers; composites with specular surfaces have not been demonstrated. These technical material limitations, combined with the equal or lower cost of metal, provided the basis for the selection.

Aluminum was the material selected for the optical membrane and circular support ring. The number of candidate membrane materials was limited primarily by the need for excellent atmospheric corrosion protection. Additional properties included the ability to be welded and formed. A close thermal coefficient match was required between the ring and membrane material. Aluminum was selected on the basis of cost. A martensitic stainless membrane combined with a carbon steel ring was a close second in performance and cost.

The membrane forming development led to the selection of free-form yield as a fabrication technique. The final shape of the membrane was determined by controlling the load distribution during plastic deformation. Metal membranes laminated with reflective material could not be formed. The material properties of the reflective material

dominated the forming process after the metal exceeded the yield strength. The transfer of the controlling properties from metal to plastic caused rupture at any discontinuity in the reflector/metal composite during the forming process.

The results of the empirical analysis had a substantial impact upon the dish design. The reflective material was defined as an entirely separate component in the final configuration. The reflective membrane was attached at the perimeter. The optical metallic membrane was perforated at the center. The plenum was subsequently bounded by the reflective membrane, the rear membrane and the circular ring. The stabilization pressure maintained contact between the reflective membrane and the optical membrane. The metal membrane became a platform to define shape.

Free-form yield provided accurate parabolic shapes with proper process control. Membranes were formed at two diameters: bench and test scale, 1.4 m and 3.7 m, respectively. Measurements of the formed membranes were used to define shapes in an optical analysis program. The peak flux of the measured membranes was bounded by parabolic shapes with a random error of 1 to 2 mrad for the bench scale, and 3 to 4 mrad for the test scale. Repeatability in the forming process was demonstrated at the bench scale.

A stabilization pressure stretched the membranes to prevent stability failure. This initial pressure load was determined so that the reflective membrane was held in contact with the metal membrane in a leeward vacuum imposed by wind. Variation in pressure was not required to maintain an accurate optical shape even in response to variable loads. The membrane was relatively stiff to uniform and nonuniform pressure loadings by virtue of its shape.

The optical-element support structure selected for optimization was similar to a bicycle wheel. Spokes radiated from the central hub to the circular ring frame. This structure maintained the shape of the rear membrane to allow a compact ring, coupled with the ring frame to limit stress and deflection, and provided a large number of supports without weight penalty. The optical element support design was sensitive to initial and operating loads at high wind speeds.

The optimized support structure incorporated two sets of spokes: one above the ring plane, the other below. The pre-load in the bottom set was determined by the rear membrane support requirement. The top spoke pre-load balanced the forces and minimized moments imposed upon the ring. Both sets of spokes provided stiffness to normal deflection and roll. The estimated specific weight of the optical element, including the membranes, ring, hub, and spokes, was 2.3 lb/ft^2 (11 kg/m^2).

A conceptual dish and PCA support system was also developed for compatibility with the optical element. The dish support was a four-bar link, with a rotating ground to

provide the second degree of freedom in tracking. A unique feature of the support was a second foundation for transfer of stow loads to ground. A tripod was provided for PCA support. These systems were not optimized, but were analyzed in sufficient detail to provide a specific weight estimate of 4.3 lb/ft^2 (21 kg/m^2).

7.2 Recommendations for Future Work

The stretched-membrane dish development resulted in several unique features in design not commonly employed in previous concentrators. These features included a separate, non-laminated reflective film, a metal membrane plastically deformed to a parabolic shape without the use of a mold or mandrel, and a hub-and-spoke support system for optical element support. Substantial Phase I effort was devoted to development and feasibility demonstration of the stretched-membrane concentrator, but several recommendations were made for additional work on this collector.

The separation of the reflective film and the metal membrane, which defined the optical shape, placed several property demands upon the film. Mechanical properties of the reflective material under large strain were not found in the literature, nor developed in the initial phase of this contract. These properties could impact the design and operating strategy of the dish and should be defined in future efforts. In particular, the creep or stress relaxation properties, cracking in the silver layer, and hazing in the transparent layer of the film should be defined. None of these properties proved to be a problem in the short-term testing conducted during Phase I.

Free-form yield processes, used for forming the membrane that defined the optical shape, required the control of several process variables identified in earlier sections of this report. The relative importance of these variables was determined through direct experimentation, as were the appropriate values of each process control variable. This strict empirical approach should be modified to incorporate an analytical model. The analytical model should reduce the number of iterations required to define process variables, an important consideration in larger scale concentrators.

The Phase I work was limited to bench- and test-scale membranes. Several experiments were conducted at bench scale, but only two forming experiments were conducted at the larger test scale. Additional work at test and larger scales should be conducted in future work to more fully demonstrate accuracy and repeatability at larger sizes. Ultimately, a full-scale concentrator should be built.

The seams in the optical membrane were also not well characterized in the Phase I effort. Some optical error will inevitably be associated with the seams required in the metal membrane, and measurements that characterize the magnitude of the error, along with methods to limit the performance impact of this error, should be developed in future work.

The rear membrane of the stretched-membrane dish, which served to close the plenum, was draped over the spoke support system. This approach was successful, but may not have resulted in an optimum structural shape because of the normal spoke loadings that resulted from the stabilization pressure. Limited consideration should be given to alternate methods of closing the plenum.

Phase I efforts were directed at development of the optical element of the stretched-membrane collector. The concentrator support system was designed on a conceptual basis only. The support system will have an impact upon the optical accuracy of the concentrator, and should ultimately be incorporated into future analyses.

Finally, the stretched-membrane dish departs from both optical and structural convention in dish fabrication. This departure should be accompanied by a careful testing program for loads and performance. Because of the innovative design features, an intermediate or prototype scale concentrator should be fabricated before a full-scale collector is built.

7.3 Conclusion

The first phase of the stretched-membrane dish development was a success. Effort was devoted to preliminary design of the optical element and experimental development of the fabrication techniques in accordance with the requirements of the statement of work. Many of the project's design goals were established as achievable, or were achieved at scale, in this first phase.

A monolithic concentrator, with an f/D ratio of 0.6, was the result of the optical geometry optimization. An aperture of 150 m^2 was selected for analysis. No problem intrinsic to the stretched-membrane dish was identified that would prevent implementation of this geometry or increase the cost of the collector as a result of this selection. The geometry was subsequently implemented at two experimental scales.

A free-form yield process was used to fabricate accurate membranes. An initially flat sheet was plastically deformed into a parabolic shape without mandrels or molds. The peak flux anticipated with the membranes formed and measured at test (3.7 m diameter) scale, was bounded by a parabola with a random slope error of less than 4 mrad. The bench-scale membrane's peak flux was bounded by a perfect parabola with an error less than 2 mrad.

Optimization and preliminary design of the optical element resulted in a hub-and-spoke structure similar to a bicycle wheel. The dish and PCA support design was developed on a conceptual basis, but analyzed in sufficient detail to provide an estimate of weight. The collector's specific weight, from the foundation up (excluding the power conversion assembly only), was estimated at 6.6 lb/ft^2 (33 kg/m^2).

The stretched-membrane technology, applied to a parabolic dish, demonstrated the potential for high performance with low weight.

8.0 References

1. Solar Kinetics, Inc., Stretched Membrane Dish Collector Development Project, Sandia Report, Albuquerque, NM: Sandia National Laboratories, 1988.

2. M. J. Riedl, "Astigmatism and the Spherical Mirror," Electro-Optical Systems Design, Vol. 9, Issue 9, September 1977, pp. 27-31.

3. T. J. Wendelin and A. Lewandowski, A Performance Comparison of Multi-Facet and Single-Facet Dishes, SERI/TP-253-3208, (Golden, CO: Solar Energy Research Institute), October 1987.

4. A. C. Ratzel and B. D. Boughton, CIRCE.001: A Computer Code for Analysis of Point-Focus Concentrators with Flat Targets, SAND86-1866, Albuquerque, NM: Sandia National Laboratories, February 1987.

5. L. L. Lukens and J. F. Muir, editor, "Dish Electric Systems Heat Engine Assessment," Proceedings of the Distributed Solar Thermal Technology Conference, SAND84-2454, Albuquerque, NM: Sandia National Laboratories, April 1985, pp. 177-184.

6. L. D. Jaffe, Optimization of Dish Solar Collectors With and Without Secondary Concentrators, JPL 82-103, Pasadena, CA: Jet Propulsion Laboratories, May 1982.

7. L. M. Murphy and C. Tuan, The Formation of Optical Membrane Reflector Surfaces Using Uniform Pressure Loading, SERI/TR-253-3025, Golden, CO: Solar Energy Research Institute, August 1987.

8. R. M. Brick, A. W. Pense, and R. B. Gordon, Structure and Properties of Engineering Materials, 4th ed., New York: McGraw-Hill, 1977.

9. Modern Plastics Encyclopedia, Vol. 63, Number 10A, October 1986.

10. E. Simiu and R. H. Scanlan, Wind Effects on Structures: An Introduction to Wind Engineering, John Wiley and Sons, 1978.

11. C. R. Steele and C. D. Balch, "Edge Effects in a Shell of Revolution Under Pressure Load," Shelltech, Submitted to SERI, August 1987.

12. "Technical Information, DuPont Mylar^{R} Polyester Film," Bulletin M-2D.

13. Metals Handbook: Properties and Selection, 8th ed., American Society for Metals, 1961.

14. M. Cakmak, "Presentation of Material Tests on Polymers and Composites," SERI Composite Membrane Working Meeting, September 18, 1987.

15. M. Cakmak, "The Effects of Biaxial Stretching on PET Films and Composite Materials," an unpublished work sponsored by the Solar Energy Research Institute, and presented at the Composite Membrane Working Meeting, held at SERI, C. F. Kutscher, editor, September 18, 1987.

16. B. Benson, "Material Properties of Stretched Membrane Composites," an unpublished work sponsored by Sandia National Laboratories, and presented at the Composite Workshop Working Meeting held at the Solar Energy Research Institute, C. F. Kutscher, editor, September 18, 1987.

17. ANSYS User's Manual, Revision 4.2A4, Swanson Analysis Systems, Inc., March 23, 1987.

18. C. Tuan, University of Nebraska, personal correspondence to Solar Kinetics, Inc. with respect to ANSYS nonlinear tests of geometric stiffening in membranes with small f/D ratios, June 22, 1987.

19. C. F. Kutscher, "Membrane Dish Research," an unpublished work presented to the Department of Energy, sponsored by the Solar Energy Research Institute, November 3, 1987.

20. P. Schissel and H. H. Neidllinger, Polymer Reflectors Research During FY 1986, SERI/PR-255-3057, Golden, CO: Solar Energy Research Institute, September 1987.

21. R. Petit, personal correspondence with respect to the specular properties of reflective films, work performed at Sandia National Laboratories, Albuquerque, July 25, 1985.

22. C. F. Kutscher, "Conclusions of the Composite Workshop Working Meeting," an unpublished work sponsored by Solar Energy Research Institute, September 18, 1987.

23. L. M. Murphy, Moderate Axisymmetric Deformations of Optical Membrane Surfaces, SERI/TP-253-3020 and accepted for publication by the Journal of Solar Energy Engineering.

24. "Mylar^{R} Polyester Price List, Type A," DuPont, May 14, 1984.

25. Development of the Stressed Membrane Heliostat Mirror Module, Science Applications International Corp., SAND87-8179, Albuquerque, NM: Sandia National Laboratories, April 1987.

26. Metals Handbook: Welding and Brazing, 8th ed., American Society for Metals, 1961.

27. Point-Focus Concentrator Reflector Assembly, Phase I, SAND87-7014, (Solar Kinetics, Inc., Dallas, Texas,), Albuquerque, NM: Sandia National Laboratories, November 1987.

28. Shiv Joshi, "Analysis and Design of a Large Parabolic Membrane Dish," presented at SERI structural meeting.

29. C. Kutscher, Solar Energy Research Institute, personal correspondence to Solar Kinetics, Inc., September 9, 1987.

30. S. P. Timoshenko and J. M. Gere, Theory of Elastic Stability, 2nd ed., New York: McGraw-Hill, 1961.

31. Manual of Steel Construction, American Institute of Steel Construction, 8th ed., 1980.

32. Development of the Stressed Membrane Heliostat, SAND87-8180, (Solar Kinetics, Inc., Dallas, Texas), Albuquerque, NM: Sandia National Laboratories, April 1987).

33. E. J. Roshke, Wind Loading on Solar Concentrators: Some General Considerations, JPL 1060-66, Pasadena, CA: Jet Propulsion Laboratories, May 1984.

THIS SHEET INTENTIONALLY LEFT BLANK.

Appendix A
Data on the Bench-Scale Membrane

This section provides the original data and preliminary reductions for bench-scale membranes. The test equipment, measurement equipment, and reduction process were defined in the main body of the text (Section 4.1).

The data are presented in the following format:

1. Header. The header describes membrane identifiers, filenames, forming processes, measurement processes, and comments made by the experimenter.

2. Coordinate system. Data are expressed in an r-z coordinate system. The r-axis origin is at the center of the ring plane. The z-axis is coincident with the optical axis; the origin is at the membrane vertex.

   a. Radius. Radial position (inches), from vertex. The positive and negative signs are for notation purposes only. The positive radius is along the 90^{0}theta line, while the negative was along the 270^{0} line.

   b. Z, Z-prime. Vertical position (inches), from vertex. The raw data is Z, Z-prime resolves the raw data into a consistent coordinate system.

3. Z-Ideal. The z dimension (inches), which corresponds to the vertical position of an ideal parabola at the referenced radial position.

4. K-actual, K-ideal. The slope, abbreviated as K (radians), was determined by assuming a straight line between the two points defined by the r-z coordinates.

5. Deflect, Slope Err. The errors were generated by subtracting the ideal from the measured value. The sense (i.e., the sign) was maintained. Positive deflection error (inches), indicated the shape was above the ideal parabola. Positive slope error (mrad), indicated the curve was too steep.

6. Area-eff, Wt.-error. Intermediate variables used in the Pdev approach for defining the ideal parabola.

7. Z-plot, K-plot. Intermediate values used as inputs for the standardized plotting routine.

8. f/D. The focal length to diameter ratio.

9. Pdev., Area Pdev., or the parabolic deviation, was the standard deviation of slope error between the ideal and measured parabolas. The ideal parabola was defined such that the mean slope error was zero. In some instances, Pdev was calculated over less than the full area. In other words, the outer data points may have been neglected. The area percentage indicates what fraction of the aperture was used for the data reduction.

The tabulated data have also been presented in a graphical format. Figure A-1(a), for example, illustrates the ideal and measured displacement data. The ideal data are plotted to scale. The measured data were plotted by magnifying the deflection error by 10 and adding the result to the ideal. In other words, the errors in the actual shape have been substantially exaggerated.

The slope error is shown in the second part of each figure. The ideal shape would have no error. In other words the abscissa represents the ideal parabola. Positive slope error indicates a shape that is too steep; negative is too shallow.

The data were generally splined before plotting to create a smooth curve between points. If specific slopes or displacements are required, the tabulated values should be used. The curves, on the other hand, provide a descriptive data presentation.

Membrane: 1m1
Pdev: 21.127
Area: 100.000

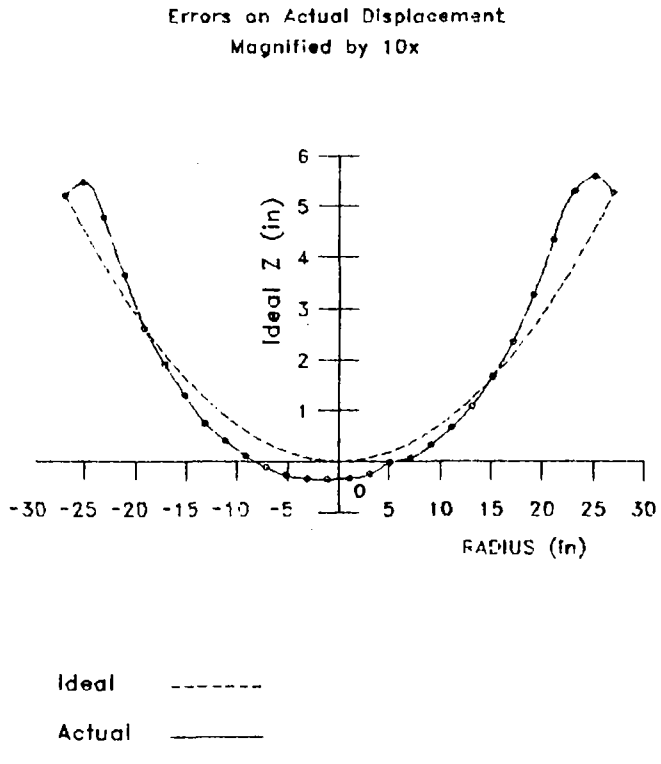

Figure A-1 (a) Ideal and Actual Displacement vs. Radial Position

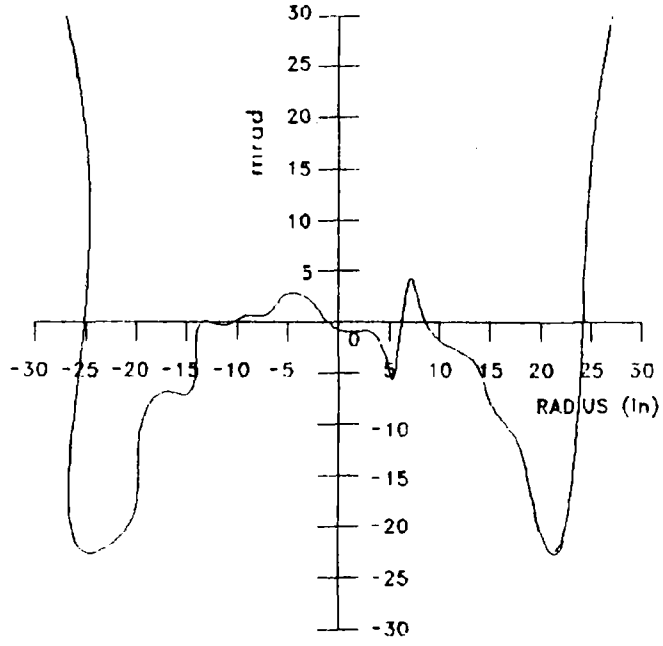

Figure A-1 (b) Slope Error vs. Radial Position

Membrane: 2m1
Pdev: 21.111
Area: 100.000

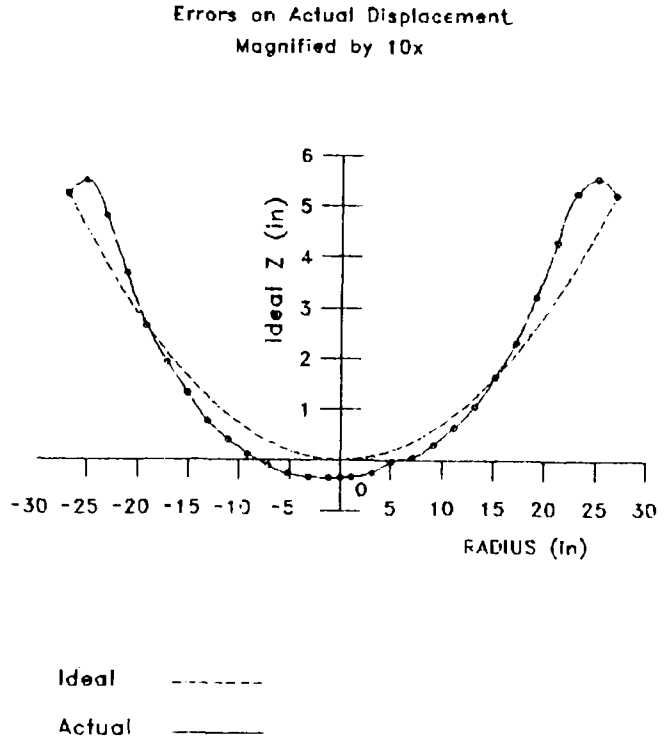

Figure A-2 (a) Ideal and Actual Displacement vs. Radial Position

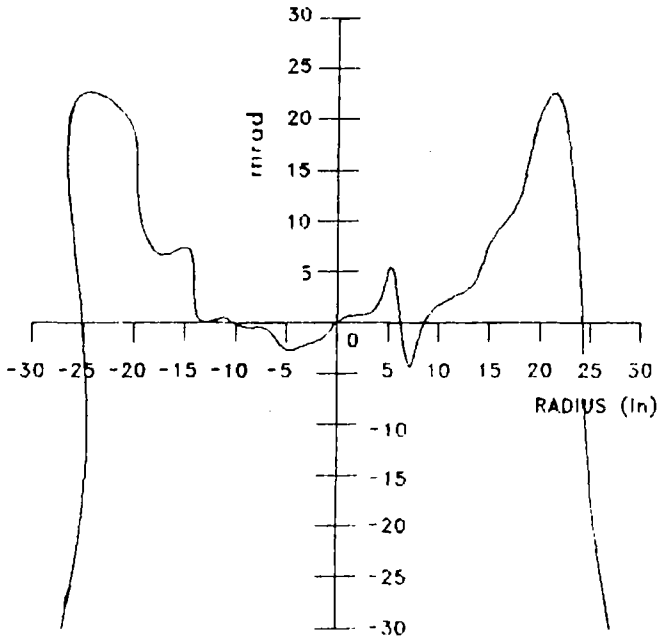

Figure A-2 (b) Slope Error vs. Radial Position

Membrane: 3m1
Pdev: 36.179
Area: 100.000

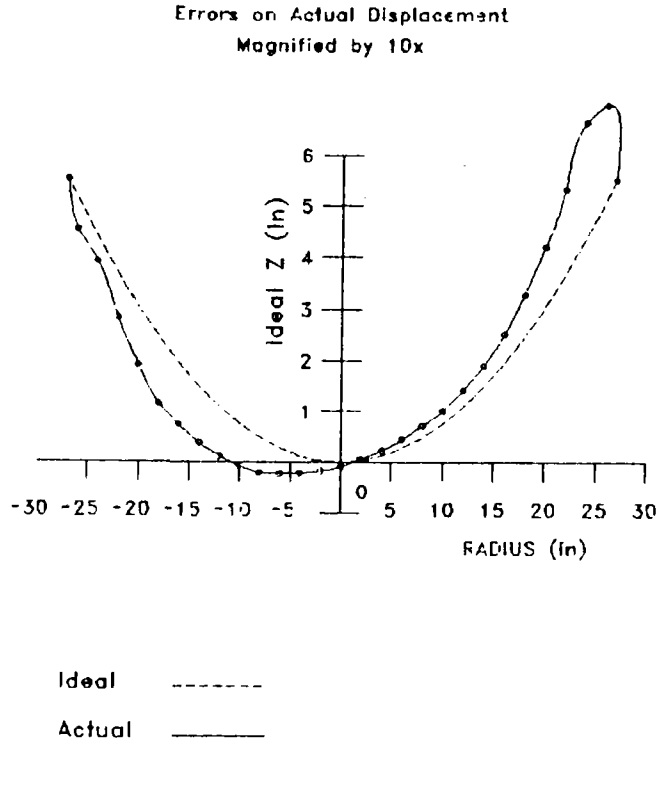

Figure A-3 (a) Ideal and Actual Displacement vs. Radial Position

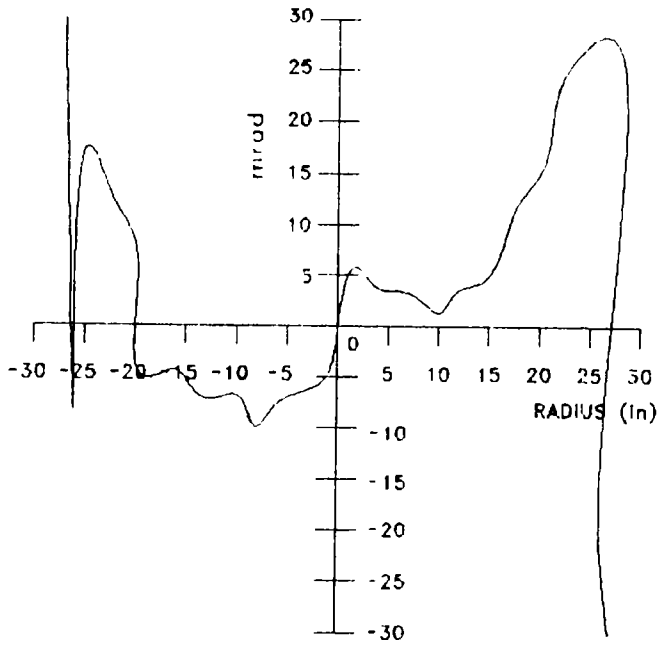

Figure A-3 (b) Slope Error vs. Radial Position

Membrane: 4m1
Pdev: 29.095
Area: 100.000

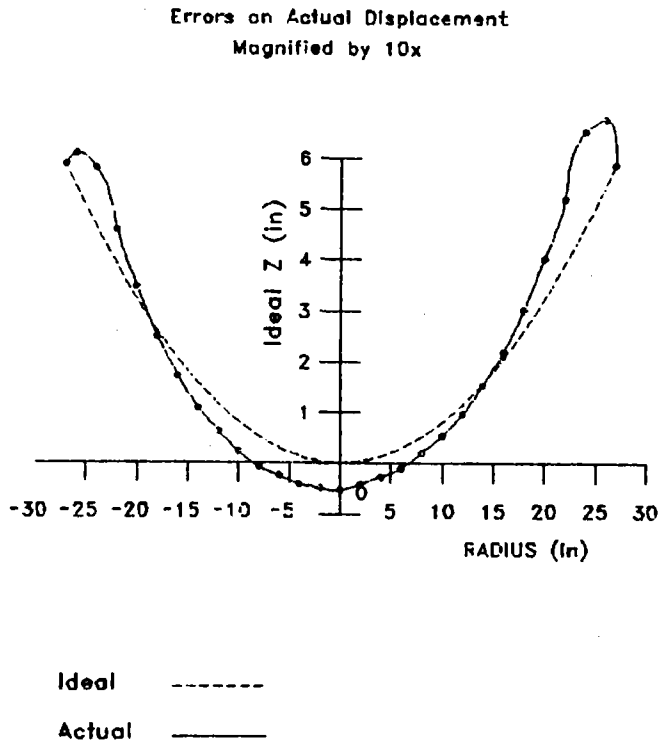

Figure A-4 (a) Ideal and Actual Displacement vs. Radial Position

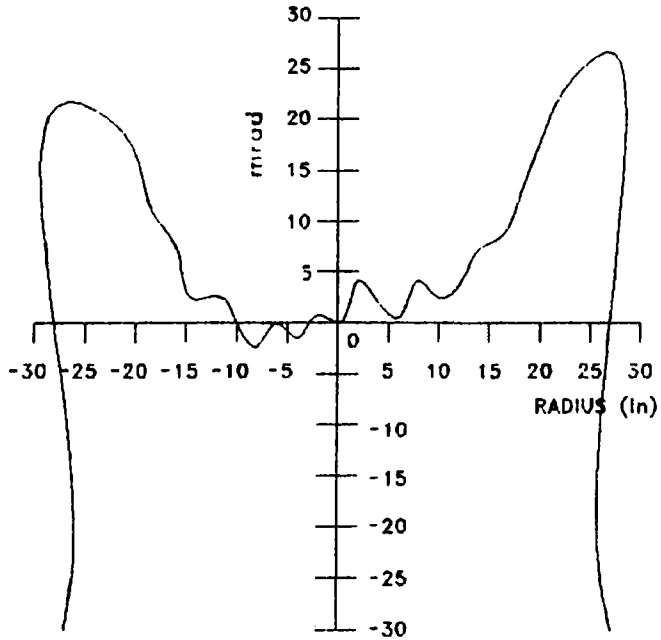

Figure A-4 (b) Slope Error vs. Radial Position

Membrane: 5m1
Pdev: 17.769
Area: 100.000

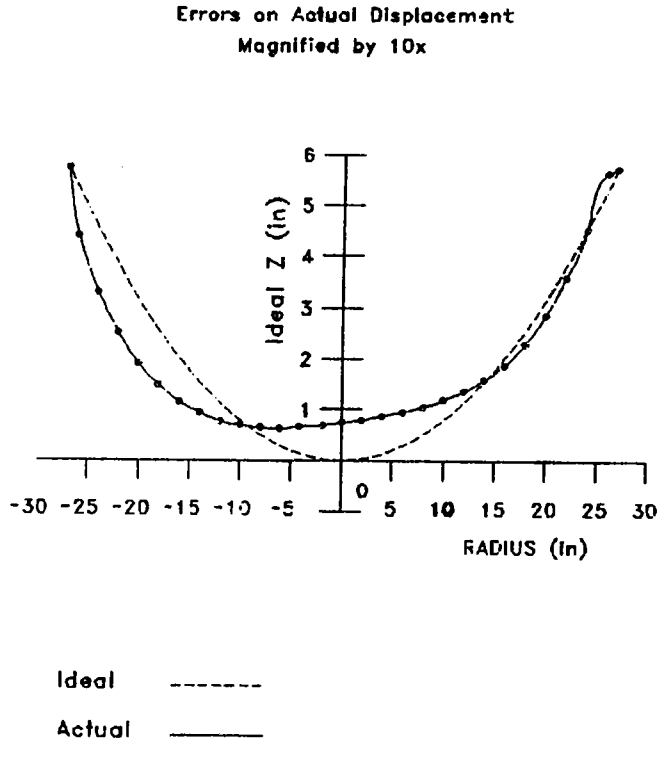

Figure A-5 (a) Ideal and Actual Displacement vs. Radial Position

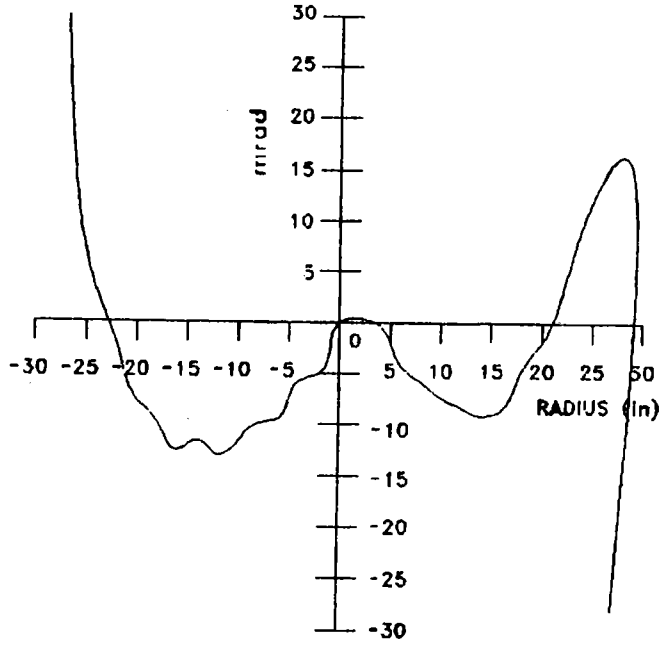

Figure A-5 (b) Slope Error vs. Radial Position

Membrane: 6m1
Pdev: 9.992
Area: 100.000

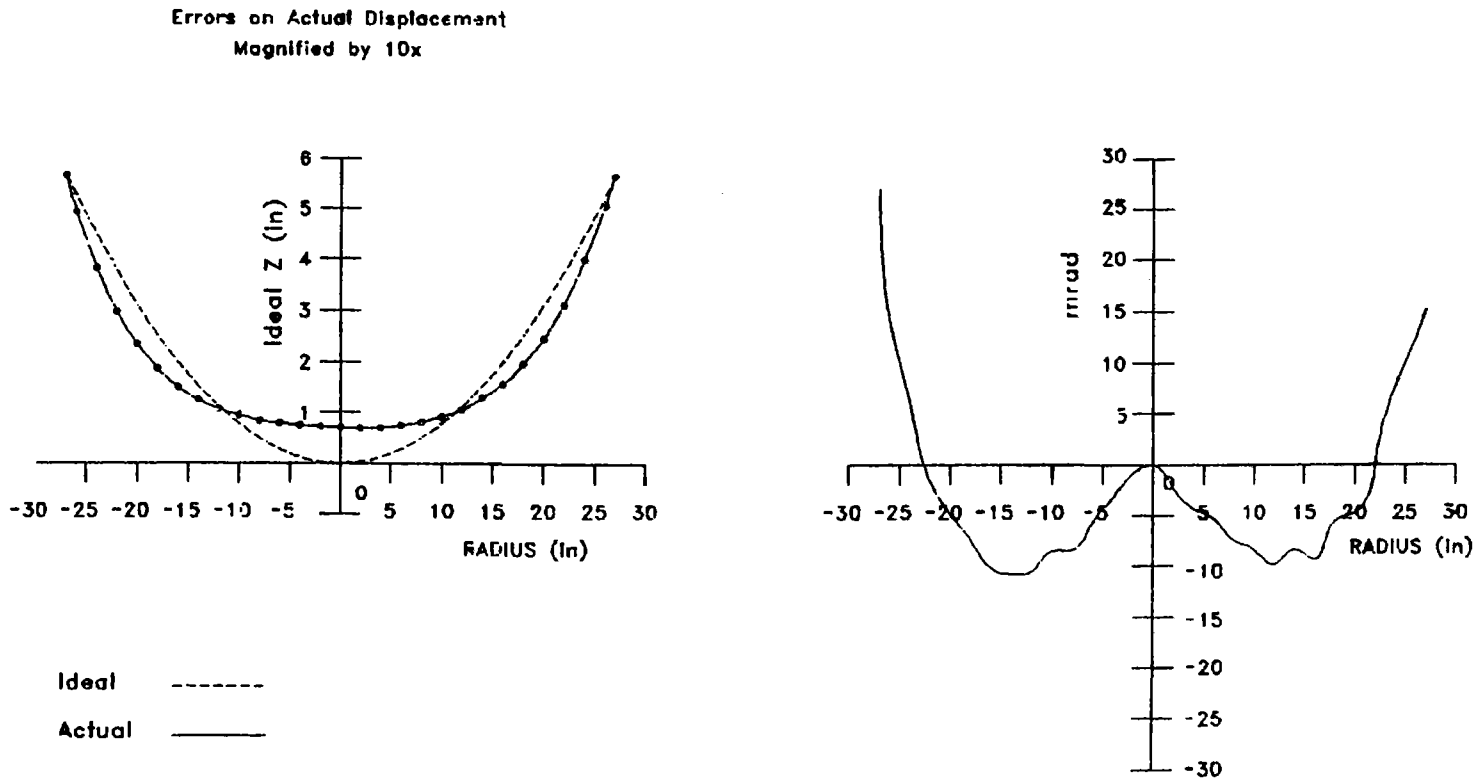

Figure A-6 (a) Ideal and Actual Displacement vs. Radial Position

Figure A-6 (b) Slope Error vs. Radial Position

Membrane: 6m2
Pdev: 9.389
Area: 100.000

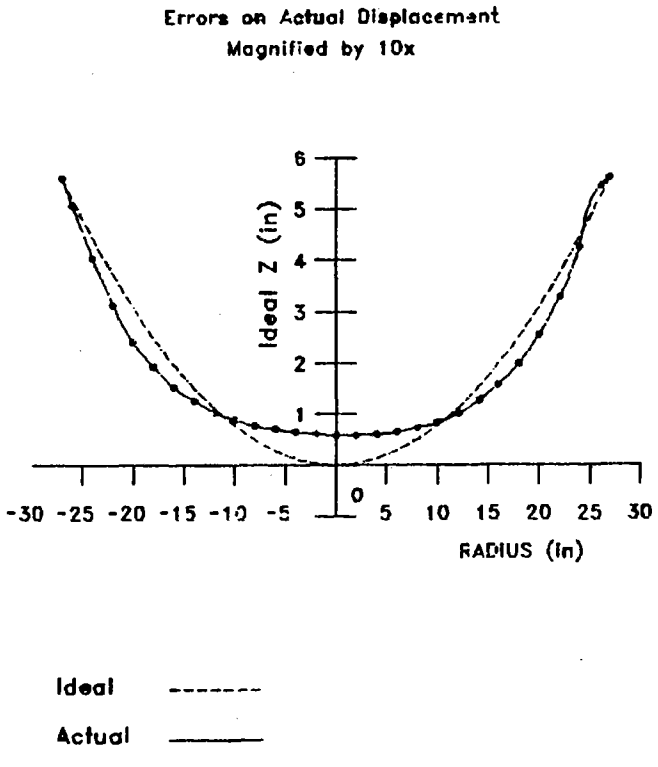

Figure A-7 (a) Ideal and Actual Displacement vs. Radial Position

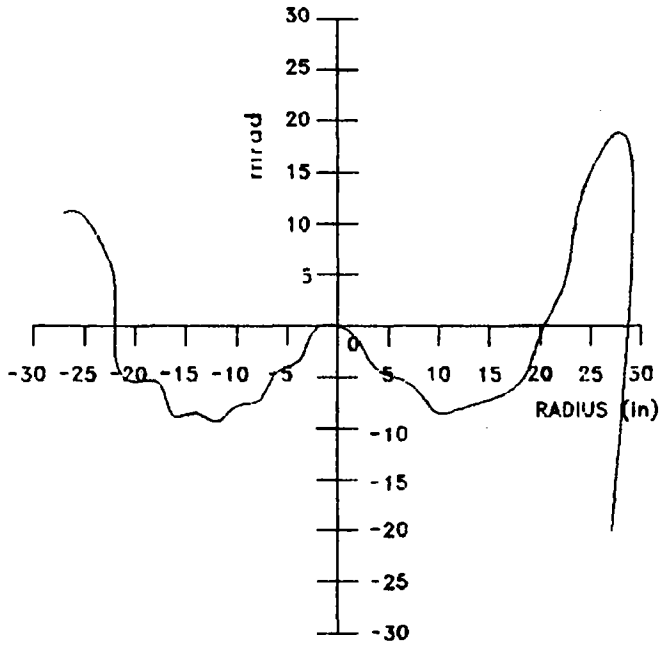

Figure A-7 (b) Slope Error vs. Radial Position

Membrane: 6m3
Pdev: 8.910
Area: 100.000

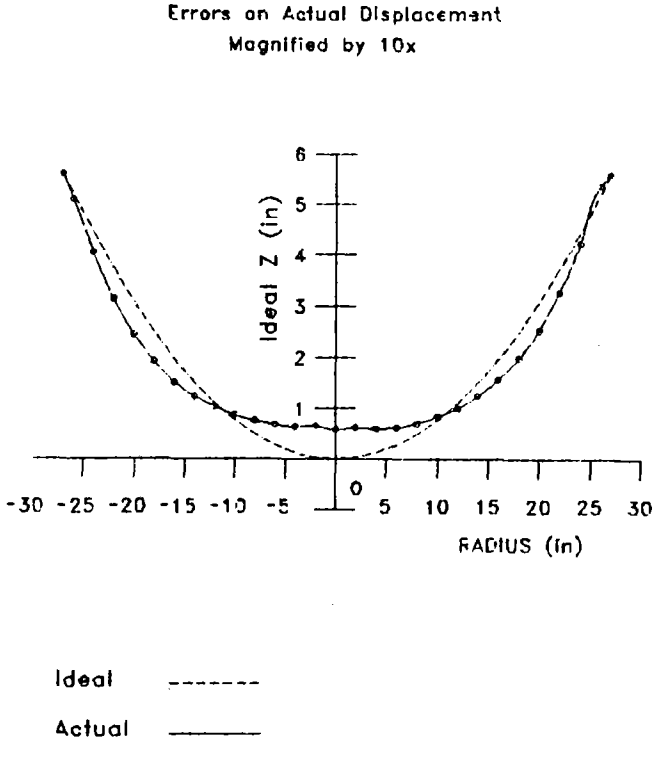

Figure A-8 (a) Ideal and Actual Displacement vs. Radial Position

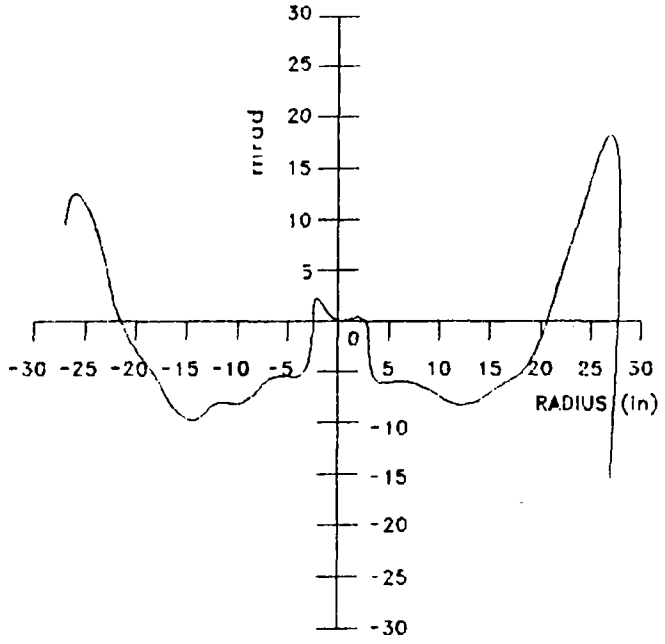

Figure A-8 (b) Slope Error vs. Radial Position

Membrane: 6m4
Pdev: 21.594
Area: 100.000

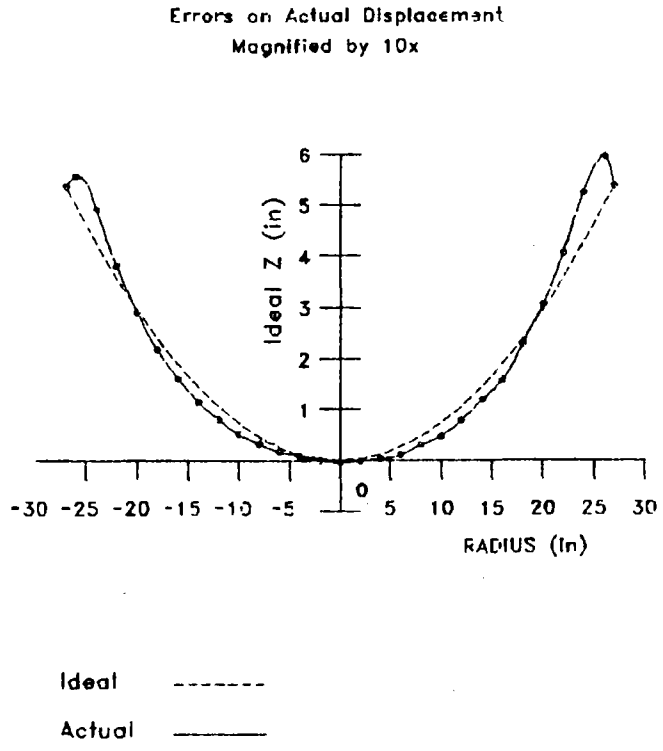

Figure A-9 (a) Ideal and Actual Displacement vs. Radial Position

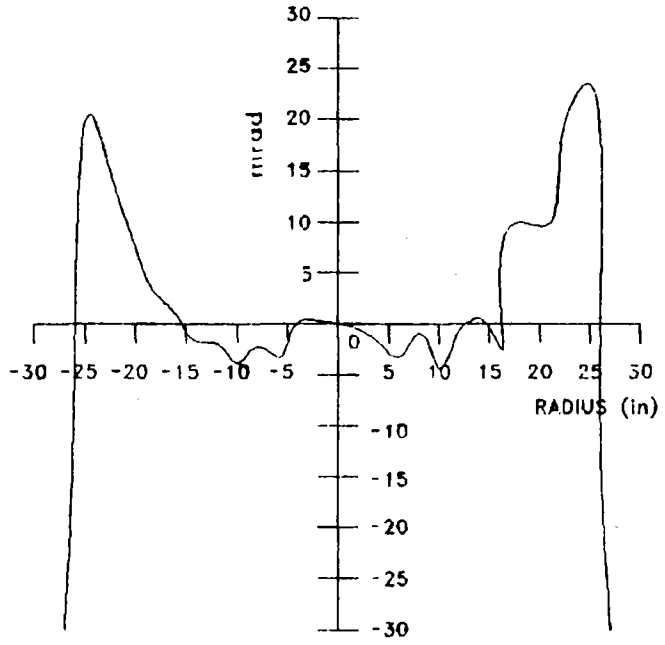

Figure A-9 (b) Slope Error vs. Radial Position

Membrane: 7m1
Pdev: 17.753
Area: 100.000

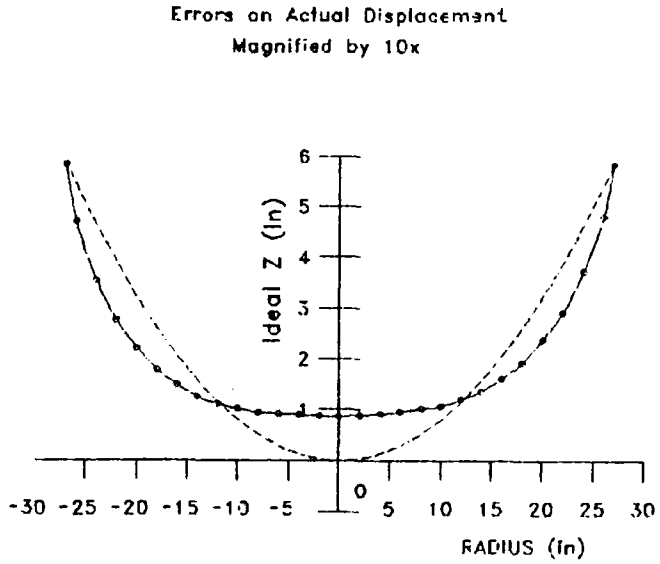

Figure A-10 (a) Ideal and Actual Displacement vs. Radial Position

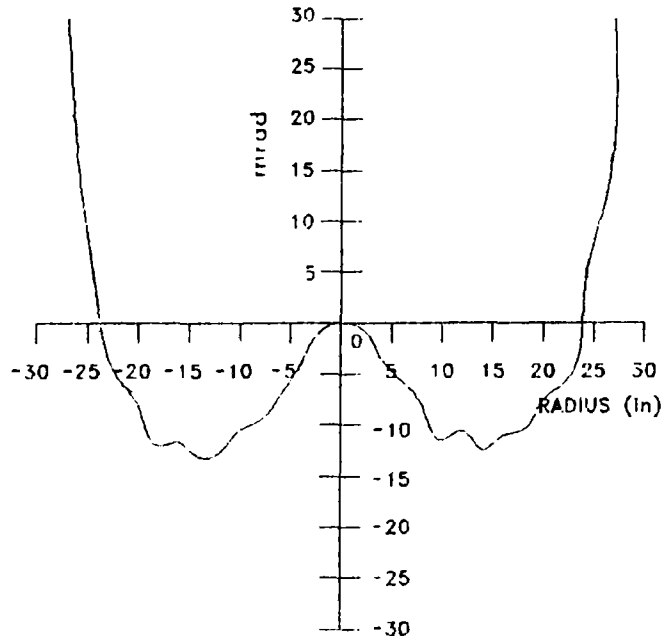

Figure A-10(b) Slope Error vs. Radial Position

Membrane: 7m2
Pdev: 29.238
Area: 100.000

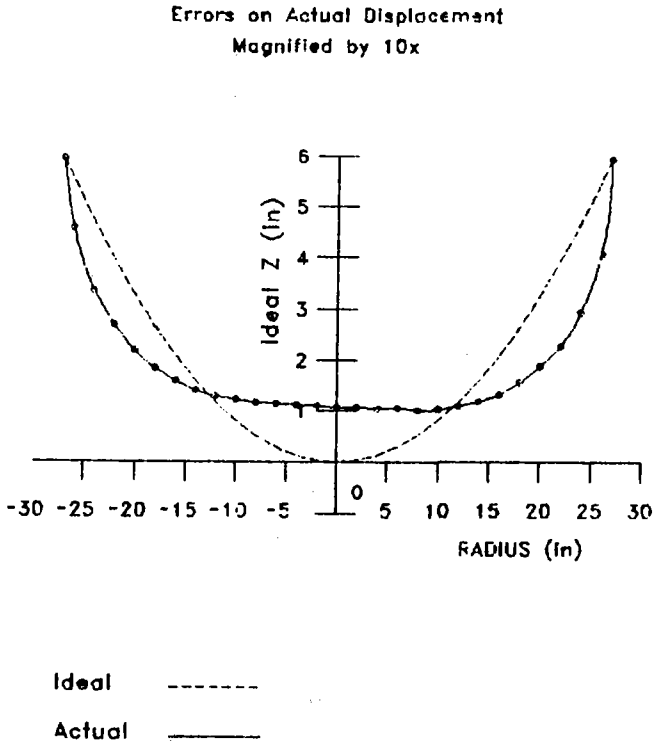

Figure A-11 (a) Ideal and Actual Displacement vs. Radial Position

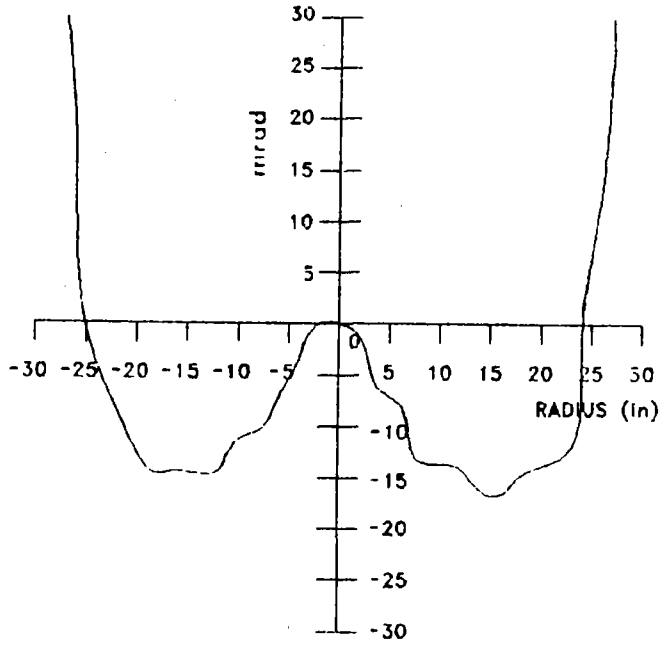

Figure A-11 (b) Slope Error vs. Radial Position

Membrane: 7m3
Pdev: 19.782
Area: 100.000

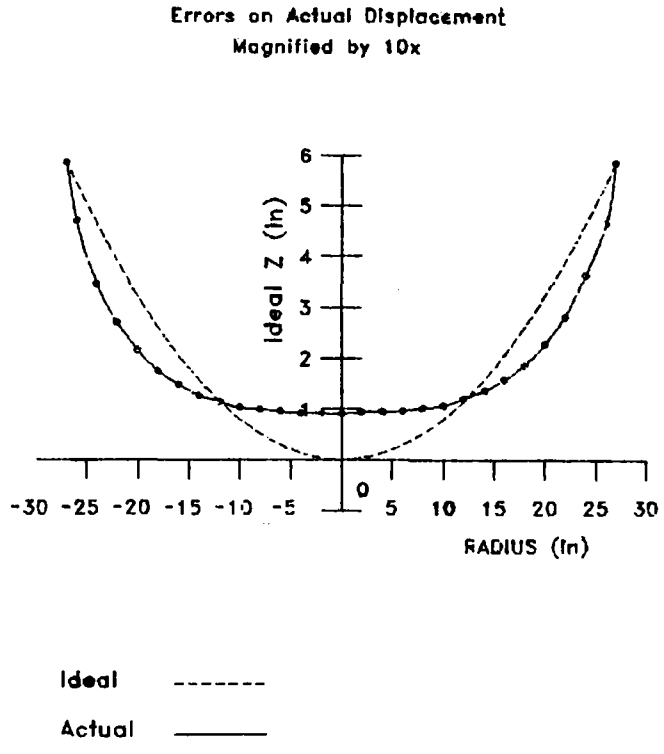

Figure A-12 (a) Ideal and Actual Displacement vs. Radial Position

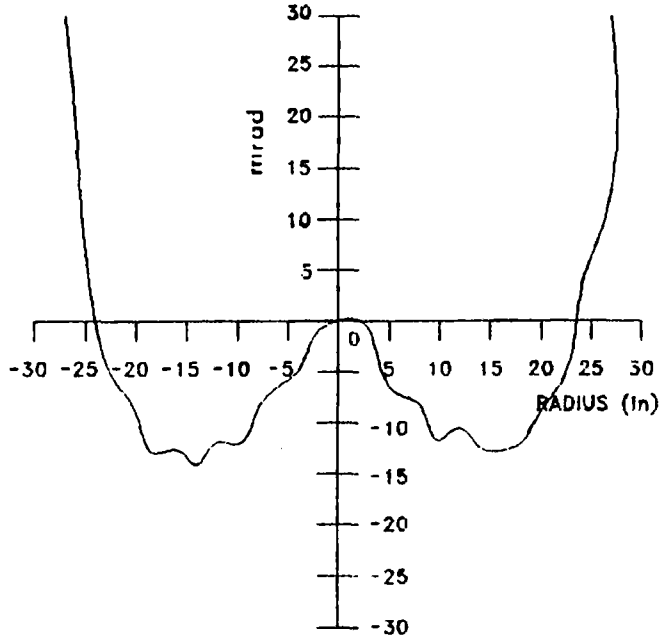

Figure A-12(b) Slope Error vs. Radial Position

Membrane: 8m1
Pdev: 10.677
Area: 100.000

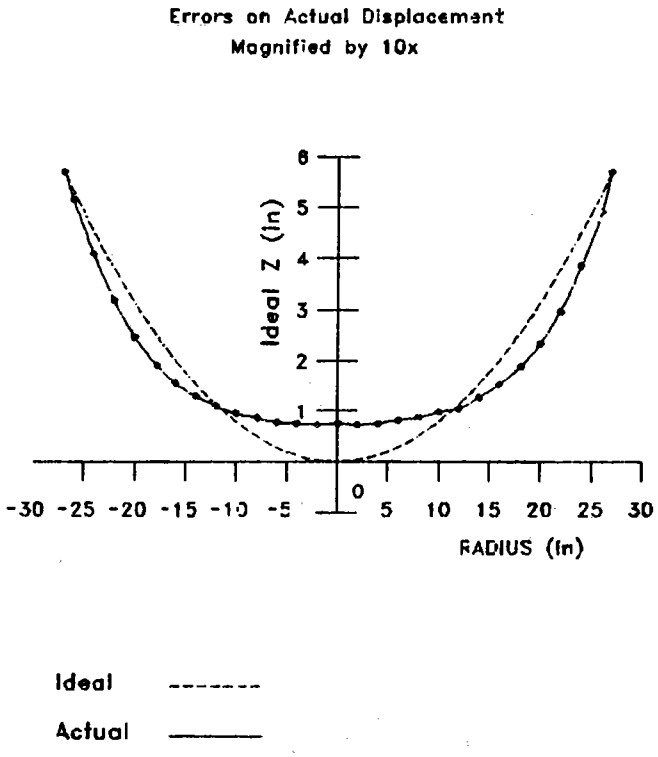

Figure A-13 (a) Ideal and Actual Displacement vs. Radial Position

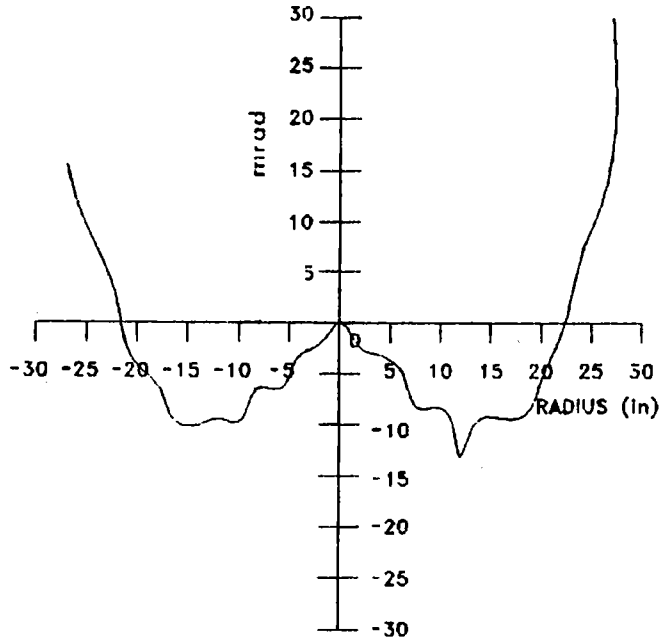

Figure A-13(b) Slope Error vs. Radial Position

Membrane: 8m2
Pdev: 10.345
Area: 100.000

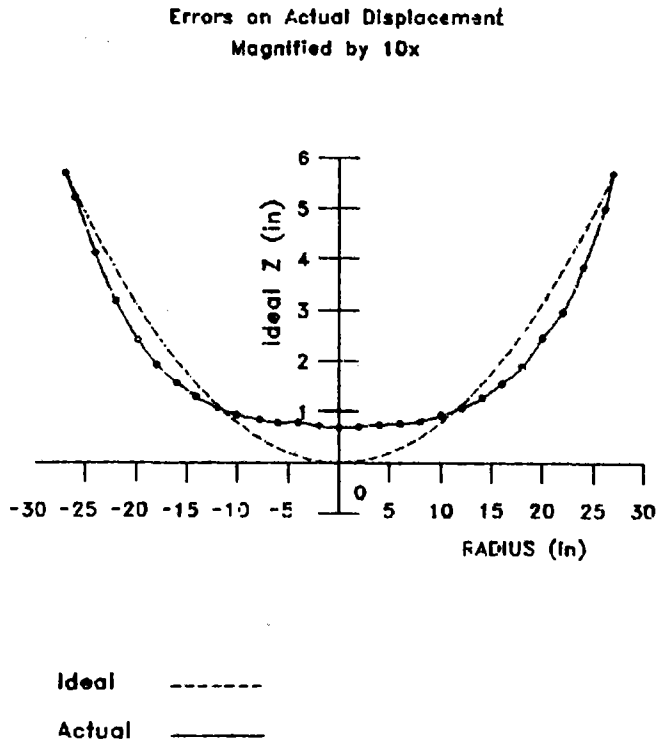

Figure A-14 (a) Ideal and Actual Displacement vs. Radial Position

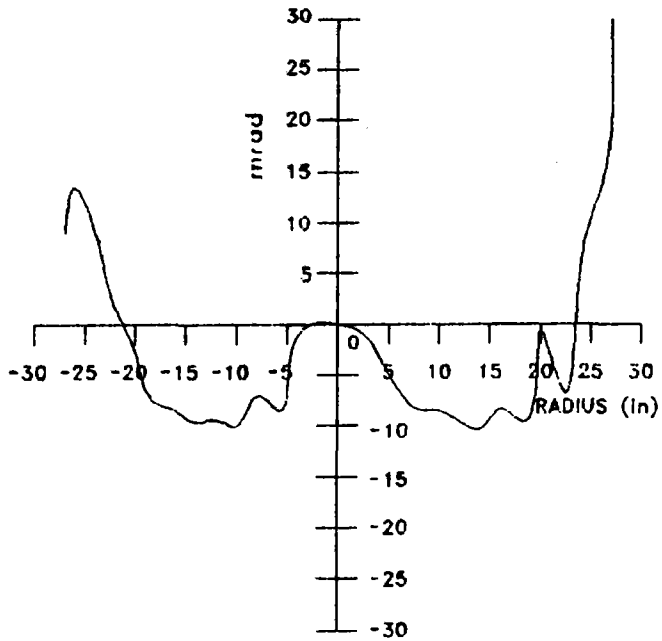

Figure A-14(b) Slope Error vs. Radial Position

Membrane: 8m3
Pdev: 10.716
Area: 100.000

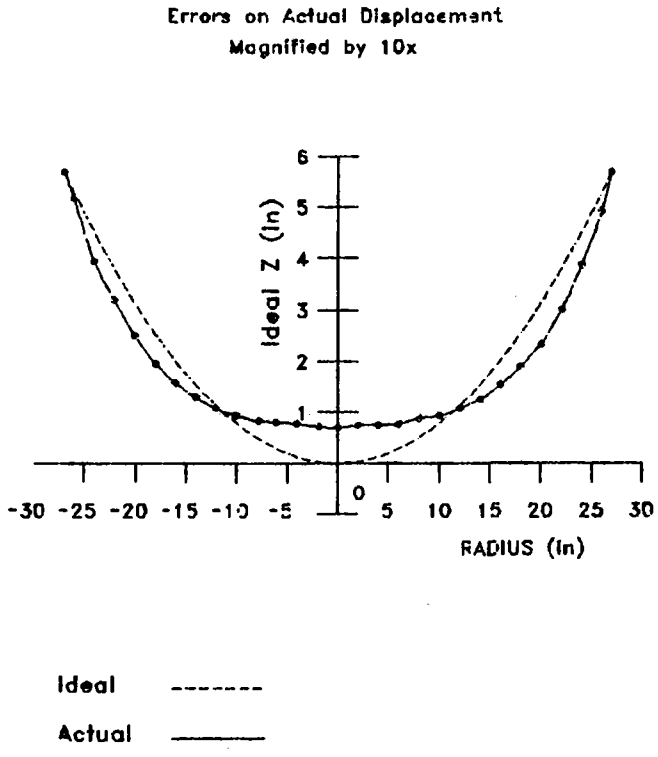

Figure A-15 (a) Ideal and Actual Displacement vs. Radial Position

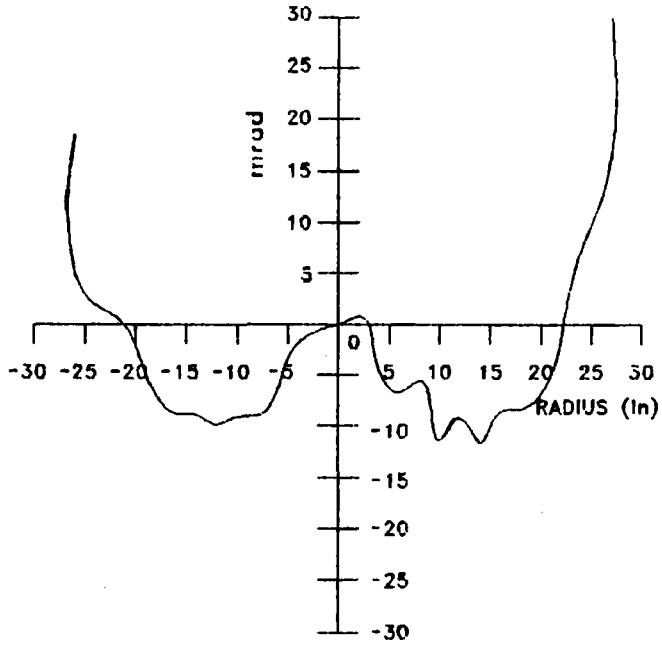

Figure A-15(b) Slope Error vs. Radial Position

Membrane: 8m4
Pdev: 9.481
Area: 100.000

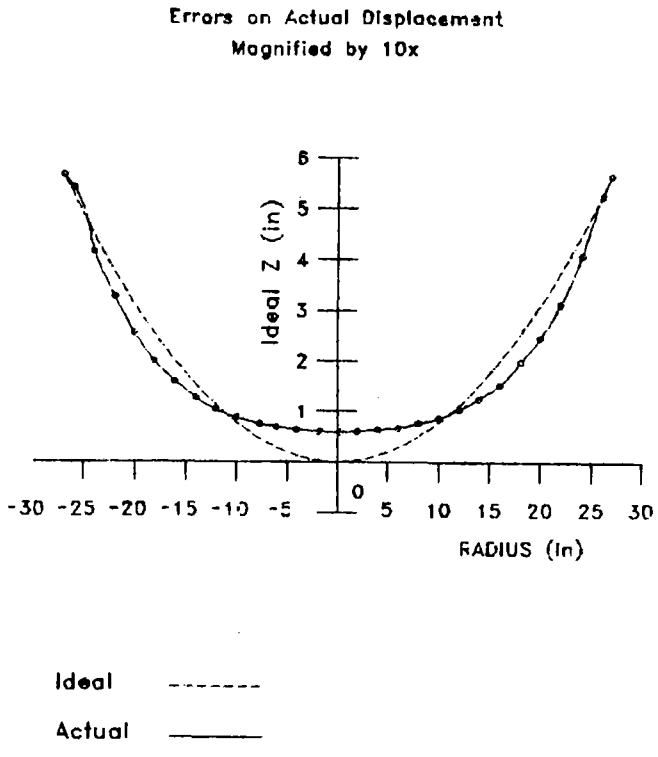

Figure A-16 (a) Ideal and Actual Displacement vs. Radial Position

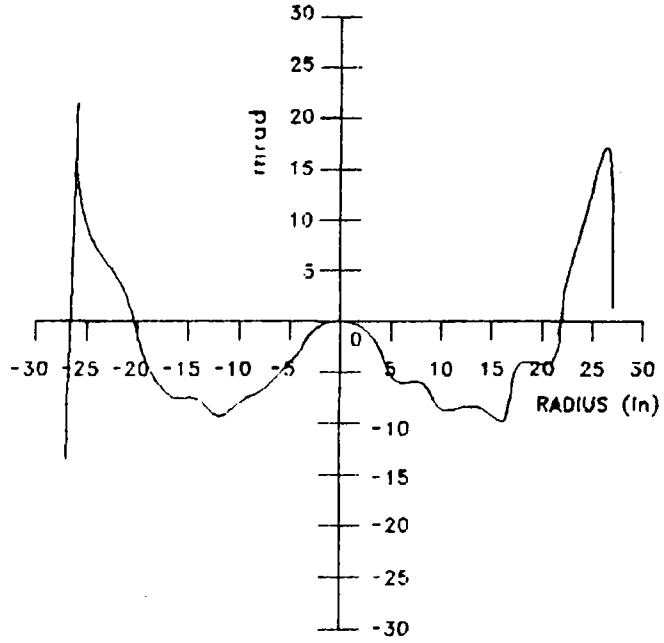

Figure A-16 (b) Slope Error vs. Radial Position

Membrane: 8M5
Pdev: 40.520
Area: 100.000

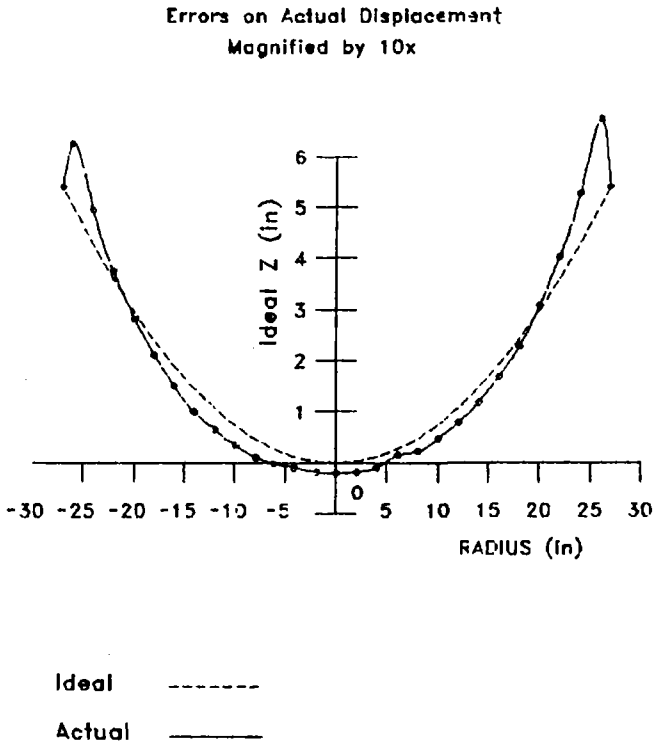

Figure A-17 (a) Ideal and Actual Displacement vs. Radial Position

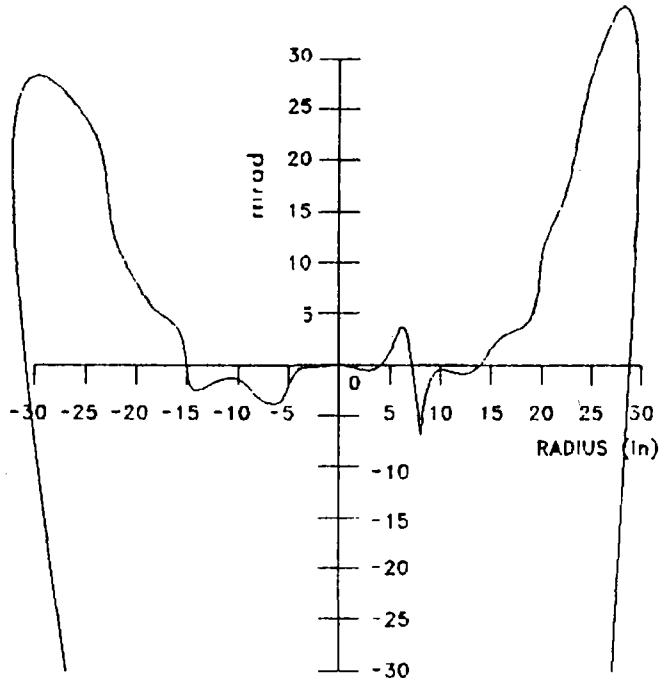

Figure A-17(b) Slope Error vs. Radial Position

Membrane: 9m1
Pdev: 7.665
Area: 100.000

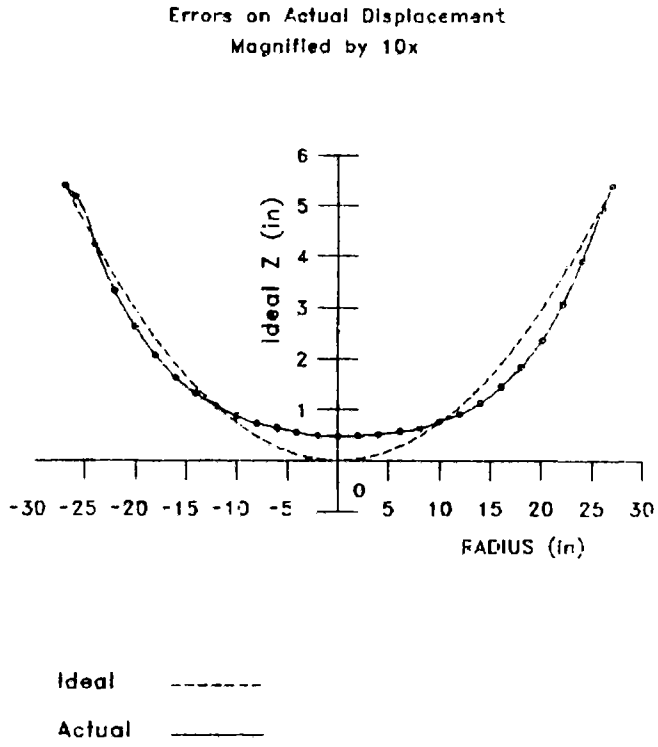

Figure A-18 (a) Ideal and Actual Displacement vs. Radial Position

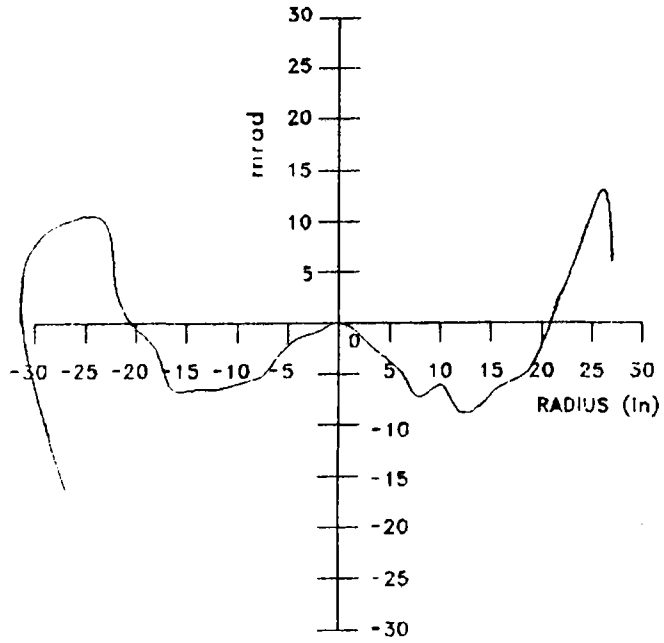

Figure A-18(b) Slope Error vs. Radial Position

Membrane: 10m1
Pdev: 10.633
Area: 100.000

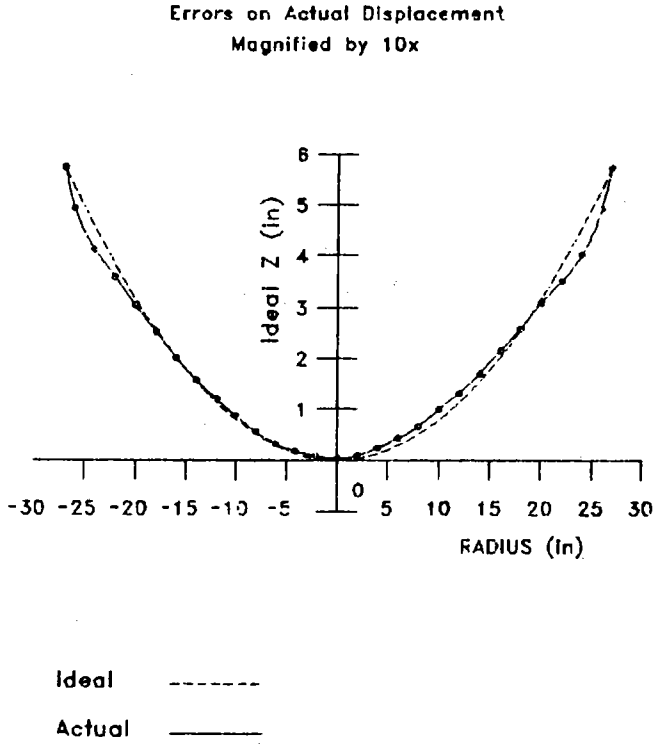

Figure A-19 (a) Ideal and Actual Displacement vs. Radial Position

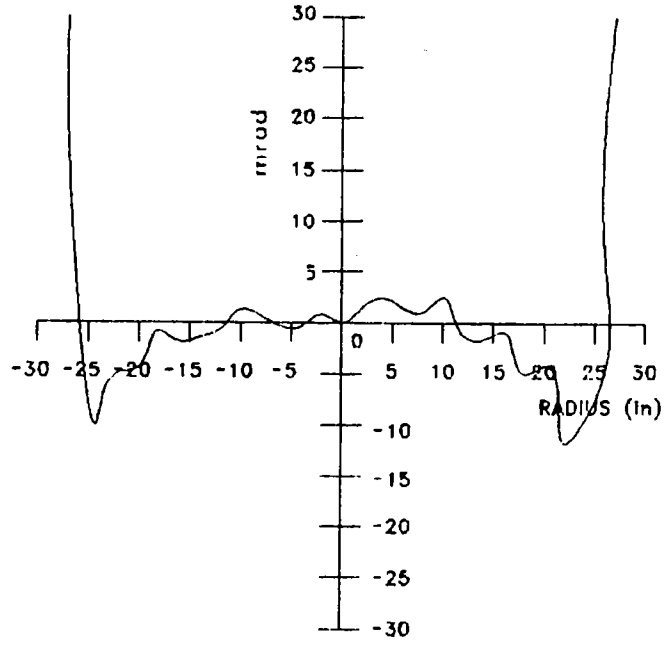

Figure A-19(b) Slope Error vs. Radial Position

Membrane: 10M1
Pdev: 4.555
Area: 92.920

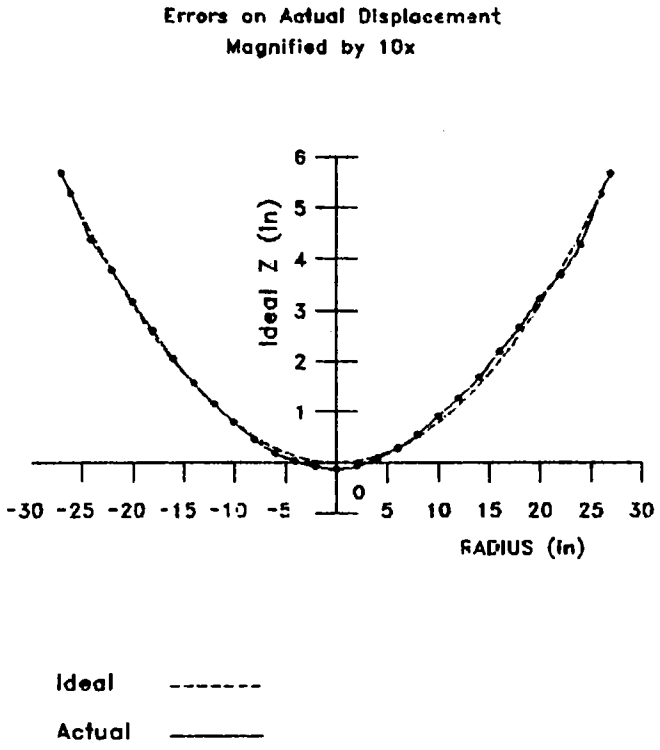

Figure A-20(a) Ideal and Actual Displacement vs. Radial Position

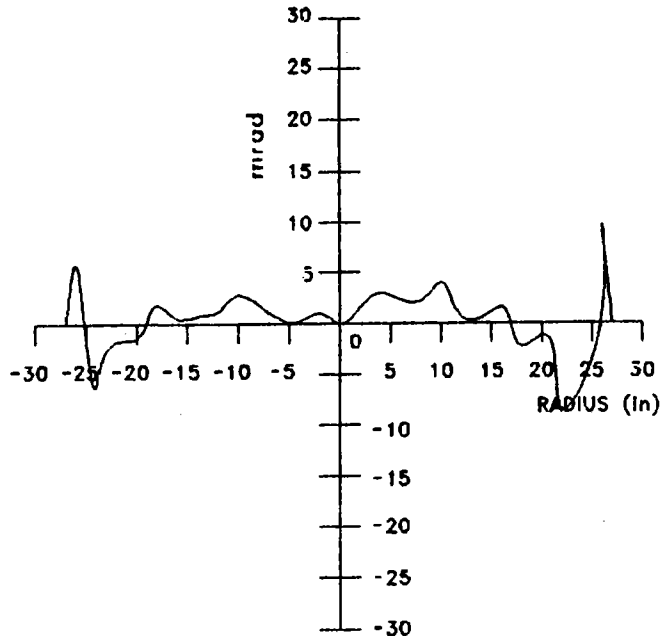

Figure A-20(b) Slope Error vs. Radial Position

Membrane: 10m2
Pdev: 5.116
Area: 100.000

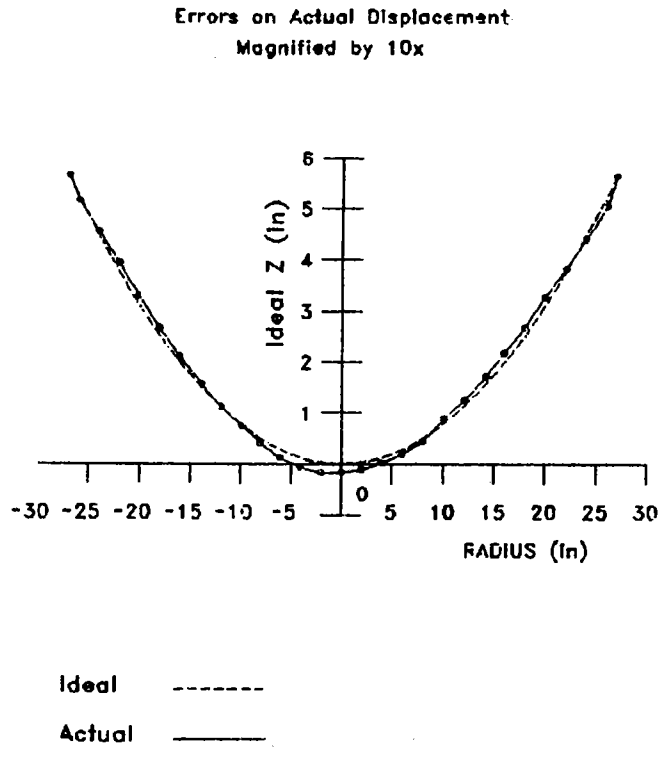

Figure A-21 (a) Ideal and Actual Displacement vs. Radial Position

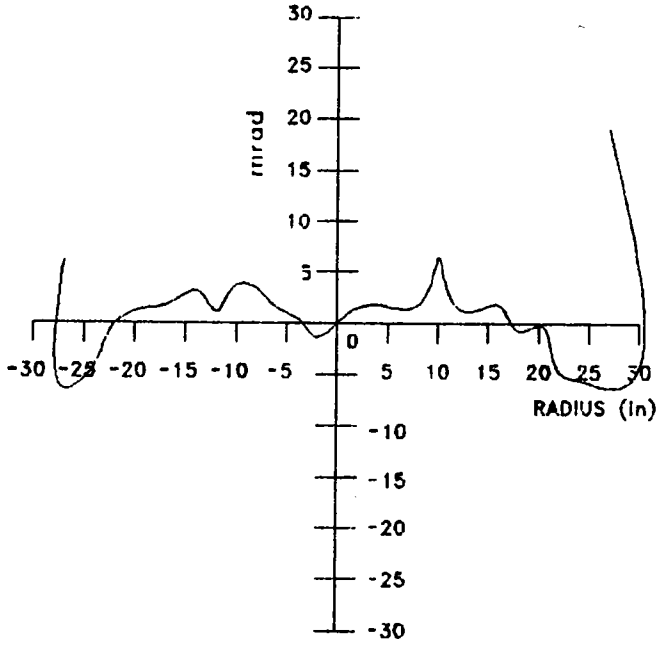

Figure A-21 (b) Slope Error vs. Radial Position

Membrane: 10M2
Pdev: 3.274
Area: 92.890

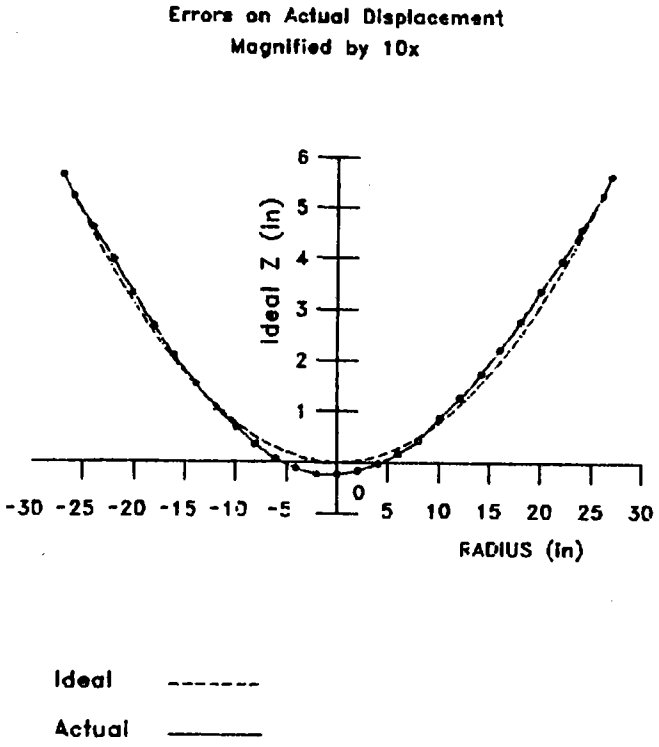

Figure A-22 (a) Ideal and Actual Displacement vs. Radial Position

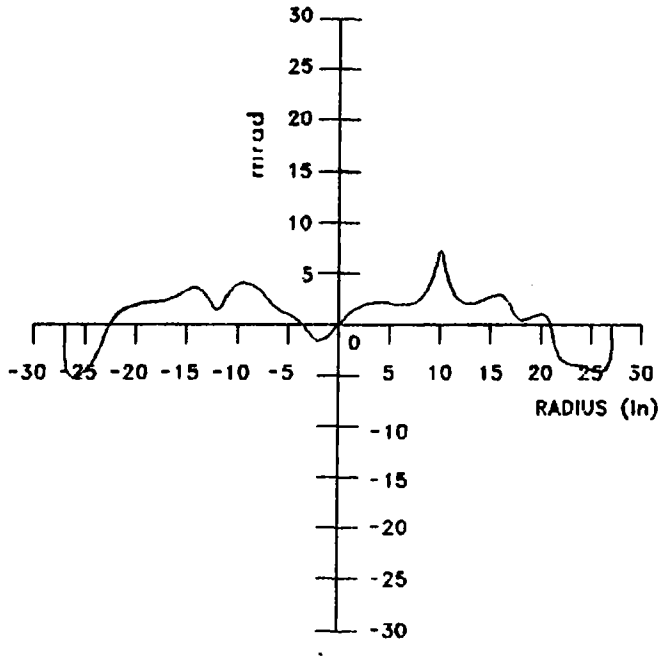

Figure A-22(b) Slope Error vs. Radial Position

Membrane: 10m3
Pdev: 5.191
Area: 100.000

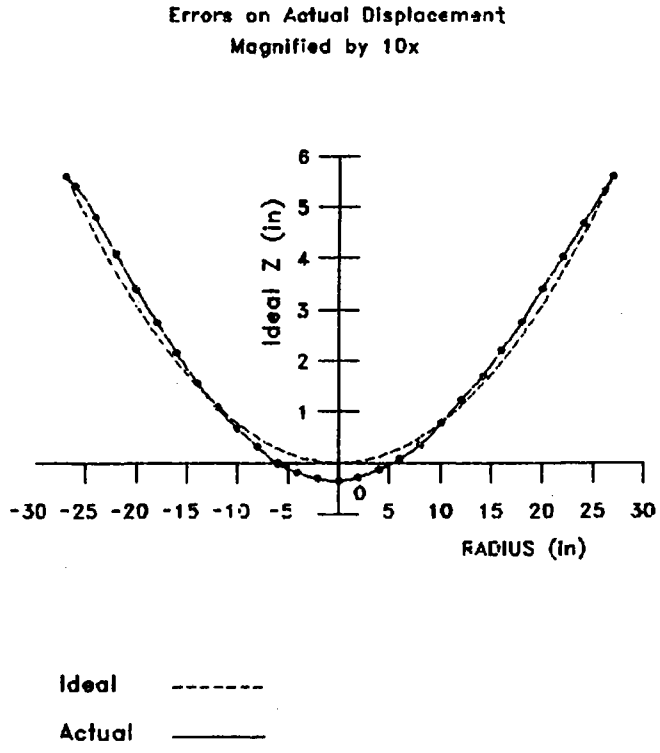

Figure A-23 (a) Ideal and Actual Displacement vs. Radial Position

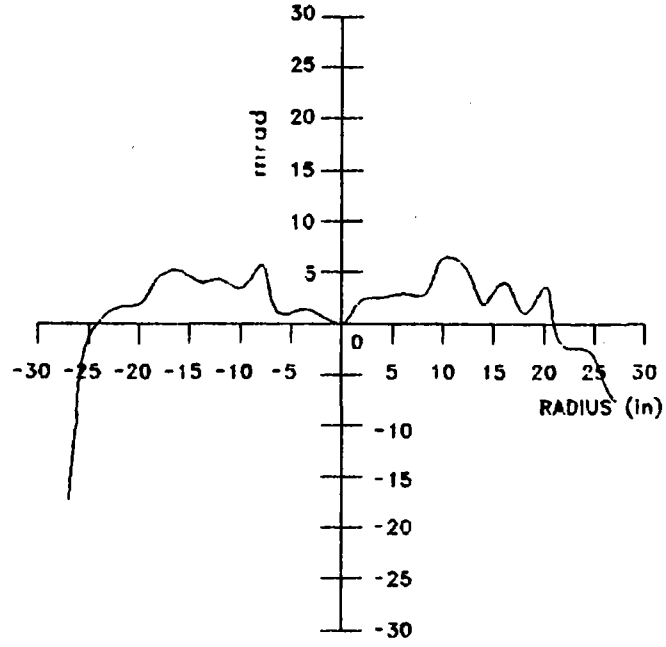

Figure A-23(b) Slope Error vs. Radial Position

Membrane: 10M3
Pdev: 4.076
Area: 93.140

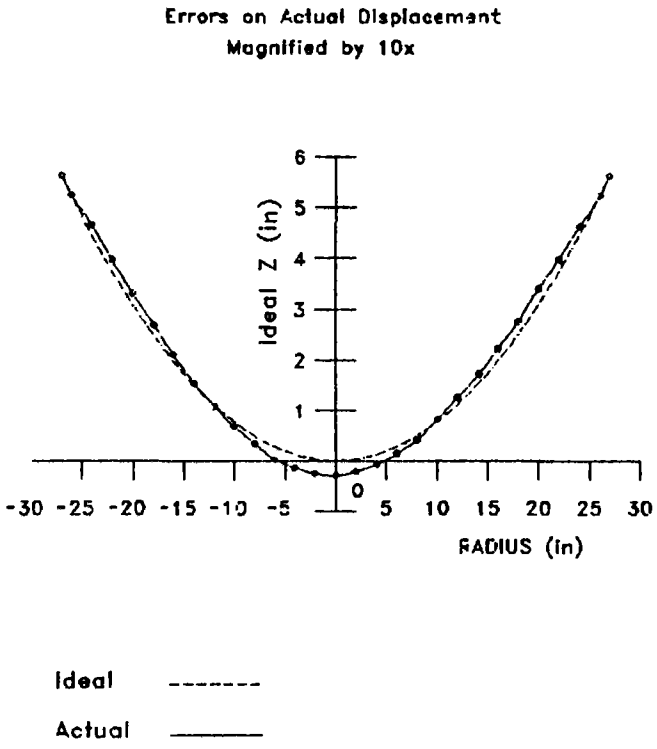

Figure A-24(a) Ideal and Actual Displacement vs. Radial Position

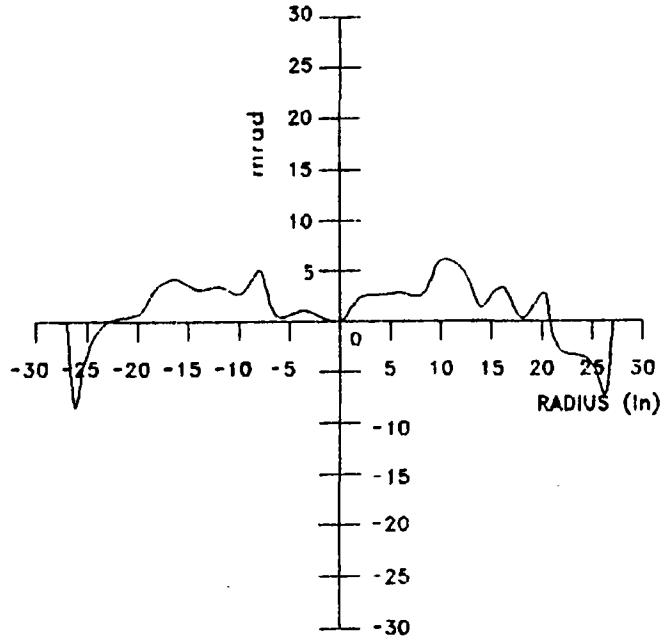

Figure A-24(b) Slope Error vs. Radial Position

Membrane: 10m4
Pdev: 5.142
Area: 100.000

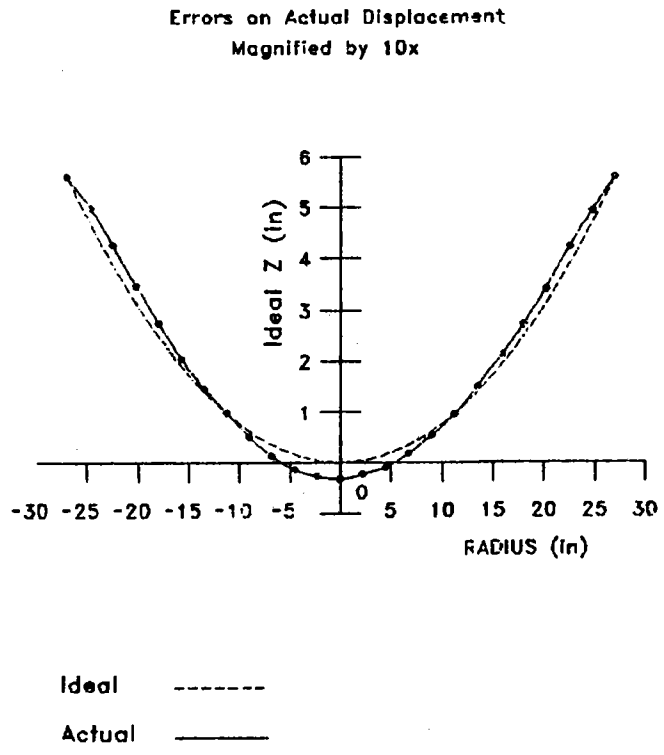

Figure A-25 (a) Ideal and Actual Displacement vs. Radial Position

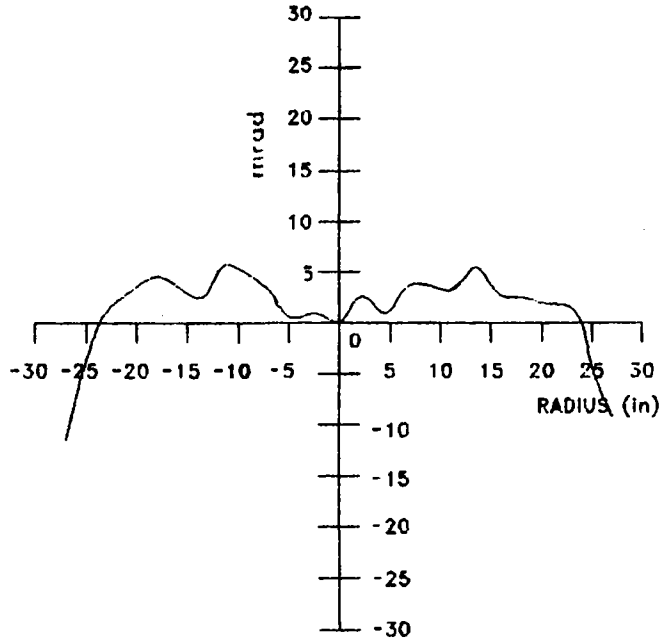

Figure A-25(b) Slope Error vs. Radial Position

Membrane: 10M4
Pdev: 3.041
Area: 83.720

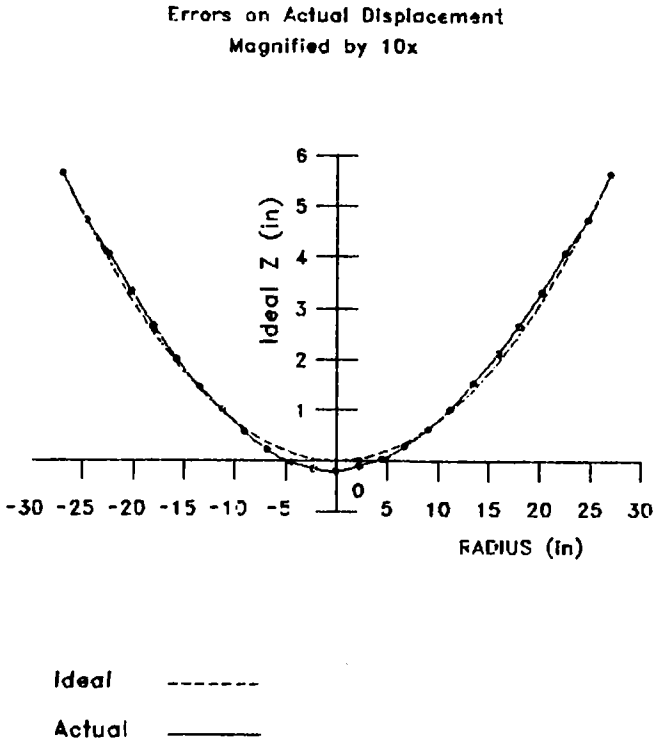

Figure A-26(a) Ideal and Actual Displacement vs. Radial Position

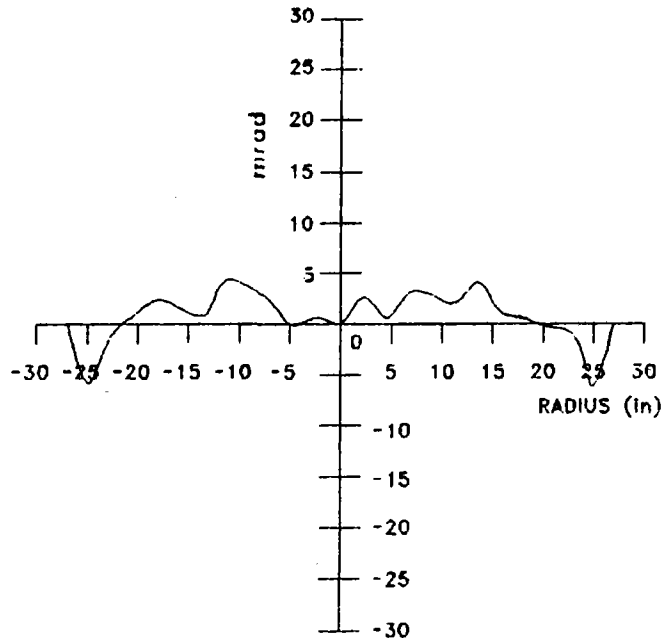

Figure A-26(b) Slope Error vs. Radial Position

Membrane: 12m1
Pdev: 6.018
Area: 100.000

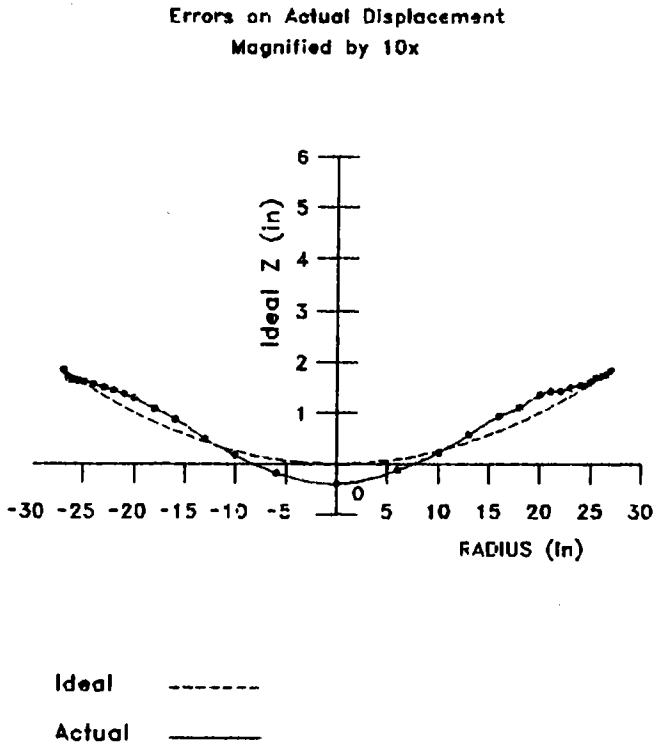

Figure A-27 (a) Ideal and Actual Displacement vs. Radial Position

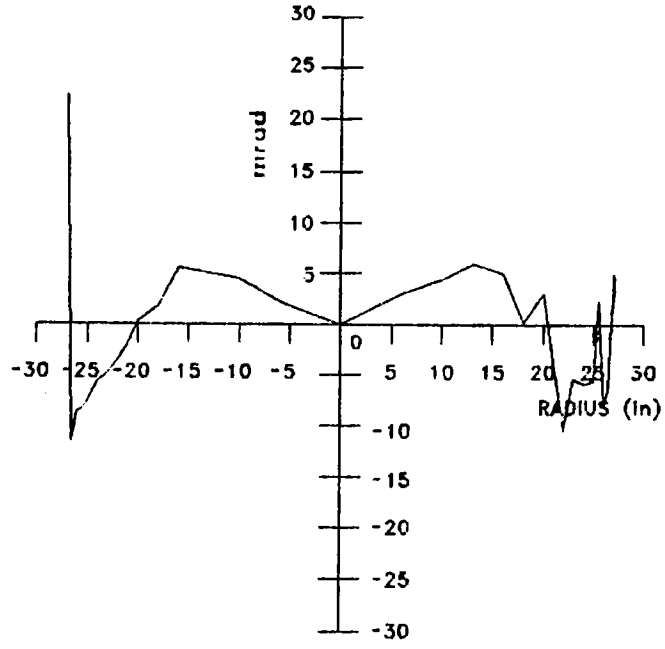

Figure A-27(b) Slope Error vs. Radial Position

Membrane: 12m2
Pdev: 6.325
Area: 100.000

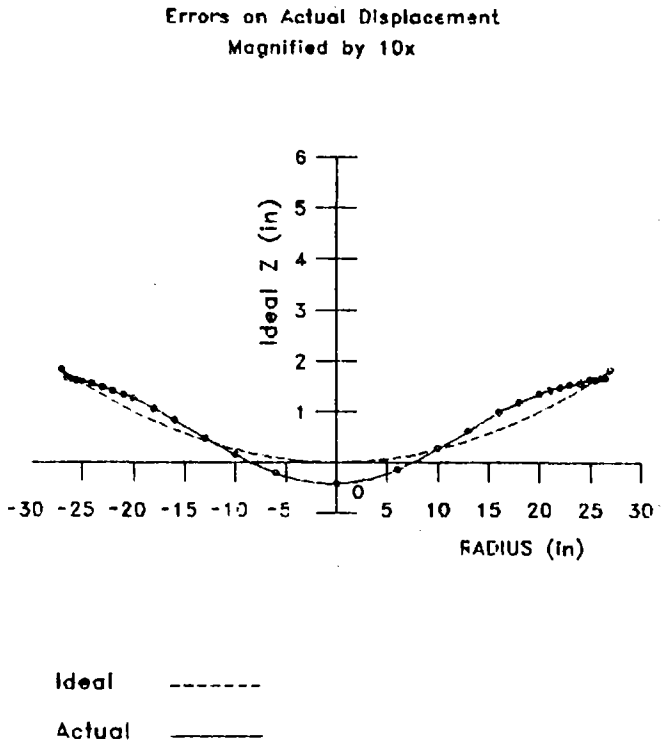

Figure A-28 (a) Ideal and Actual Displacement vs. Radial Position

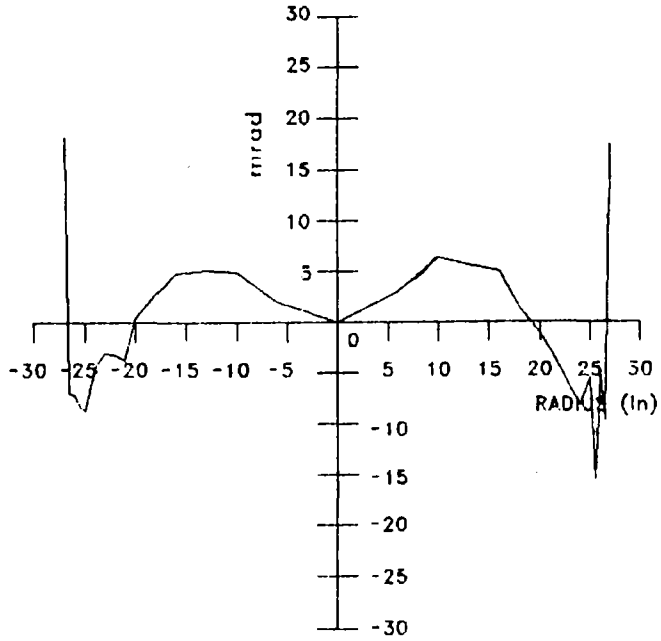

Figure A-28(b) Slope Error vs. Radial Position

Membrane: 12m3
Pdev: 5.702
Area: 100.000

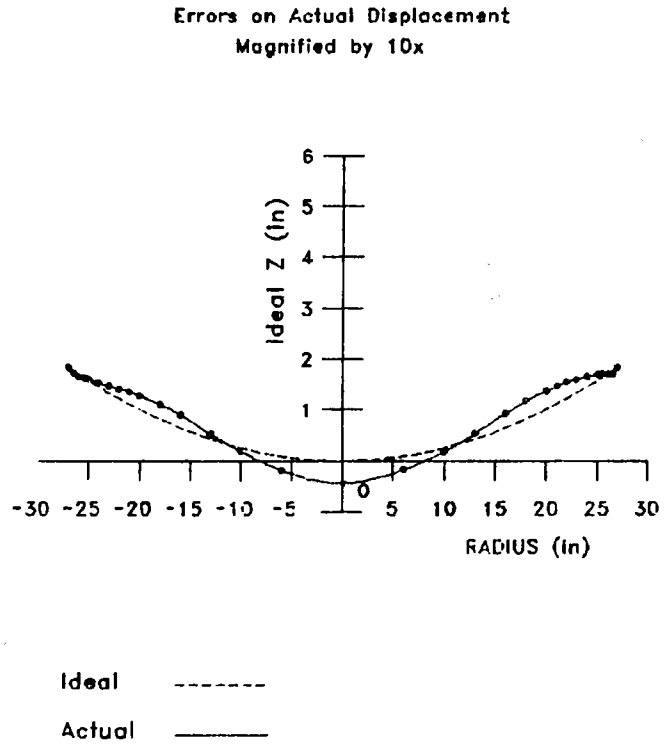

Figure A-29 (a) Ideal and Actual Displacement vs. Radial Position

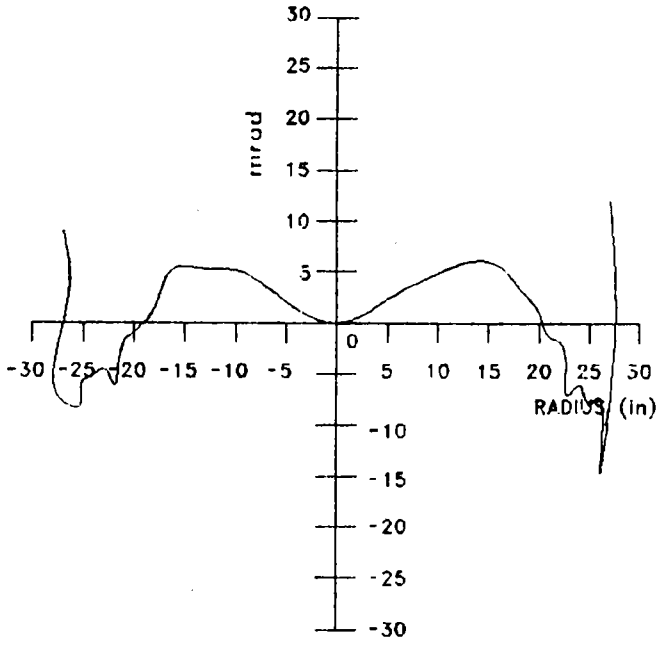

Figure A-29(b) Slope Error vs. Radial Position

Membrane: 12m4
Pdev: 6.466
Area: 100.000

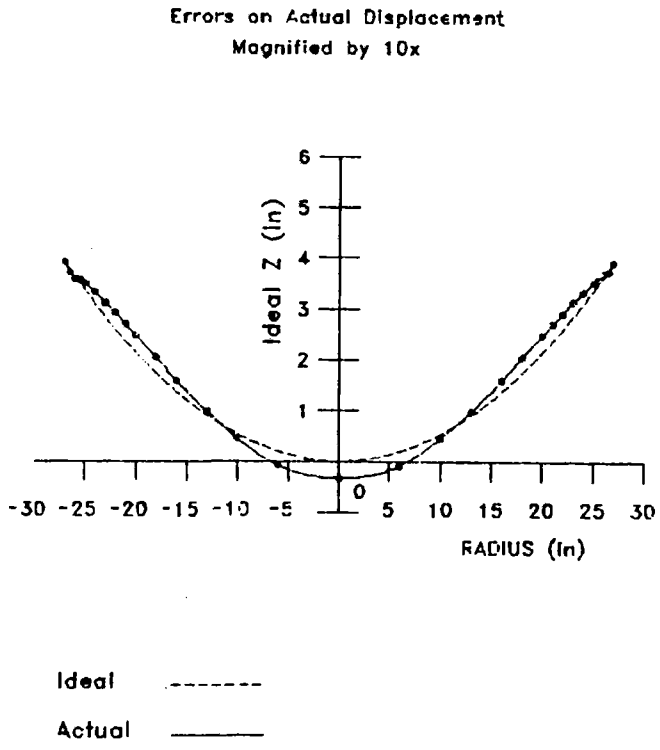

Figure A-30 (a) Ideal and Actual Displacement vs. Radial Position

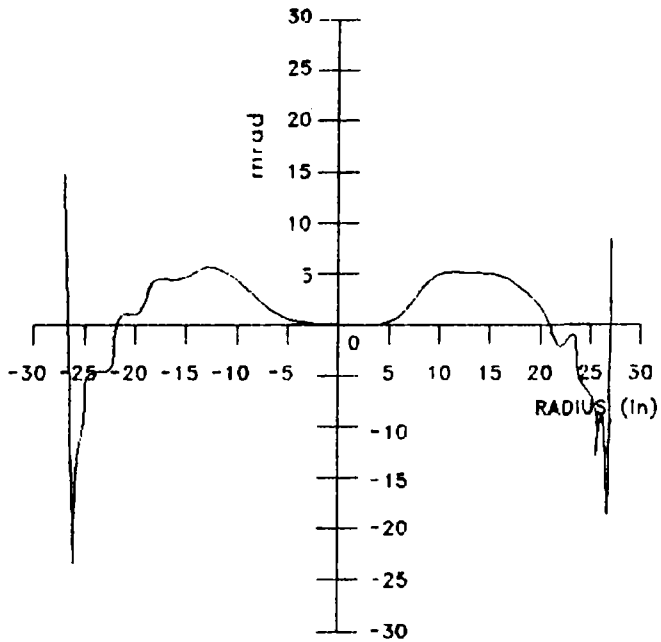

Figure A-30(b) Slope Error vs. Radial Position

Membrane: 12m5
Pdev: 7.674
Area: 100.000

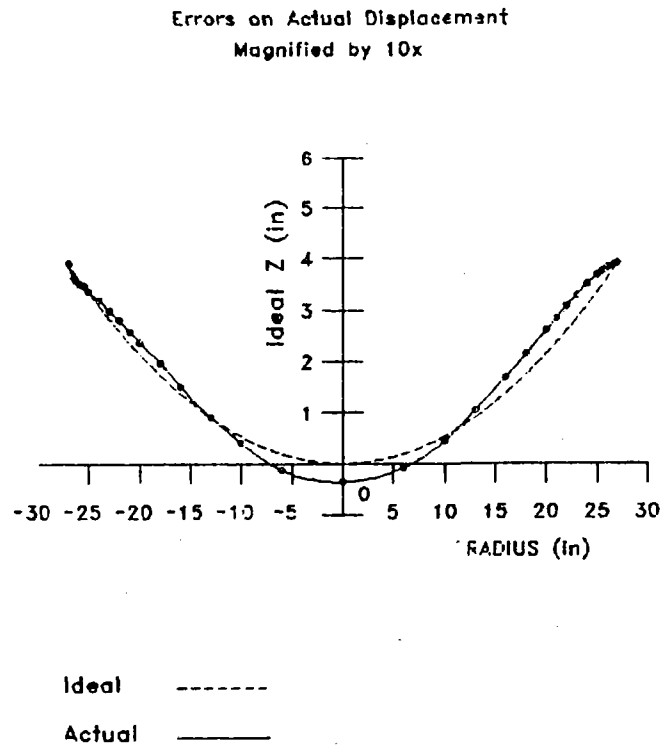

Figure A-31 (a) Ideal and Actual Displacement vs. Radial Position

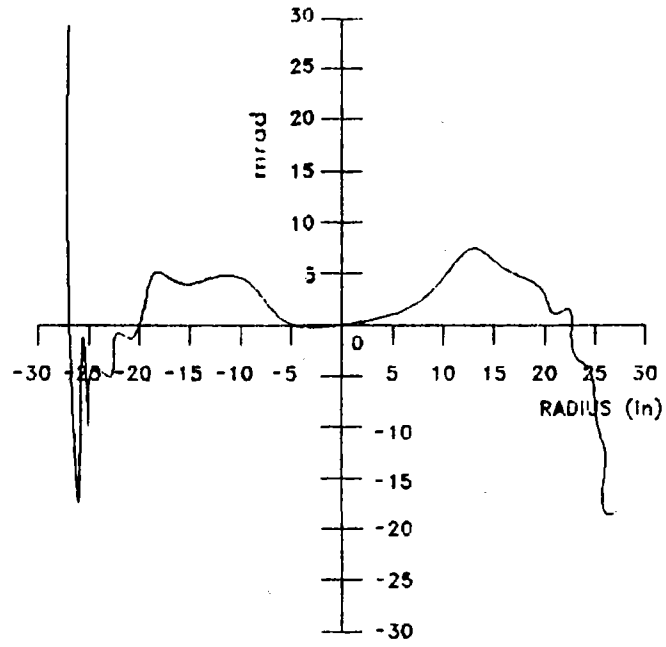

Figure A-31(b) Slope Error vs. Radial Position

Membrane: 13m1
Pdev: 28.521
Area: 100.000

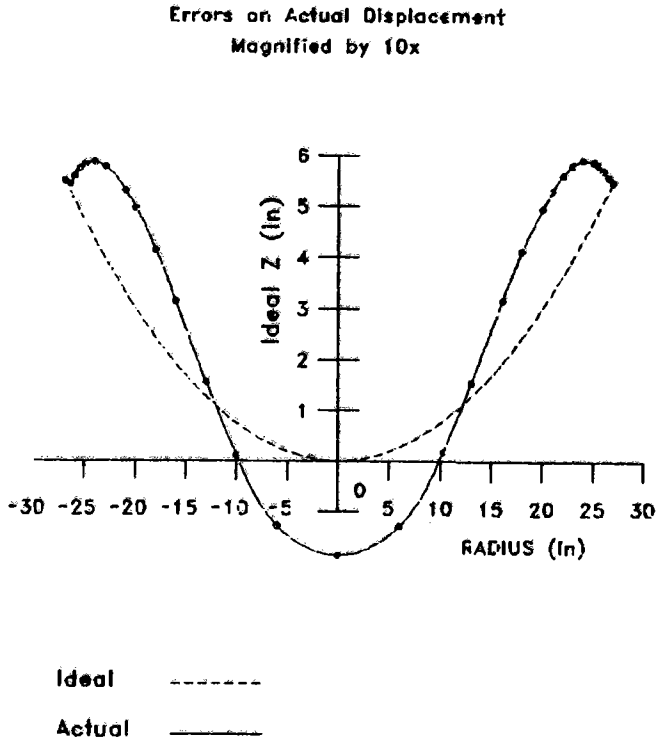

Figure A-32 (a) Ideal and Actual Displacement vs. Radial Position

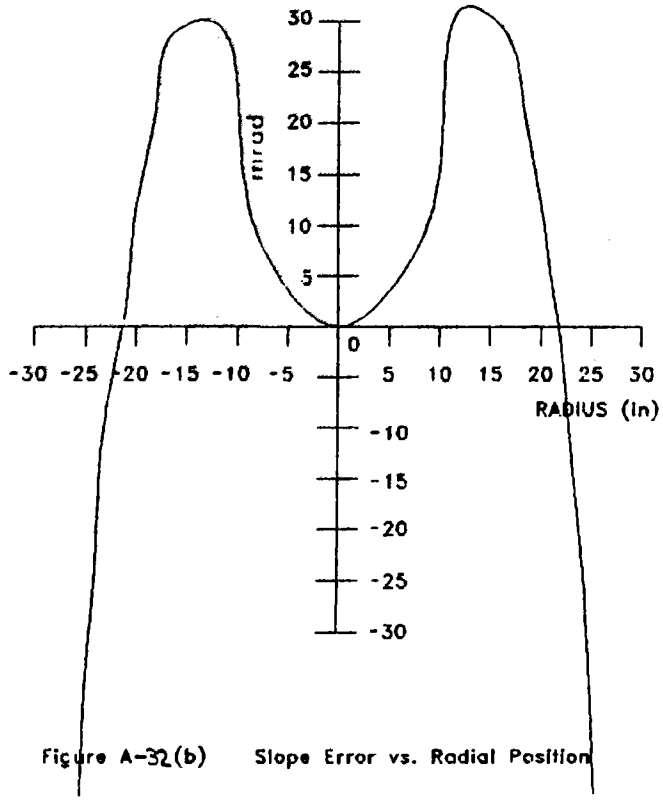

Figure A-32(b) Slope Error vs. Radial Position

Membrane: 13m2
Pdev: 28.556
Area: 100.000

Errors on Actual Displacement
Magnified by 10x

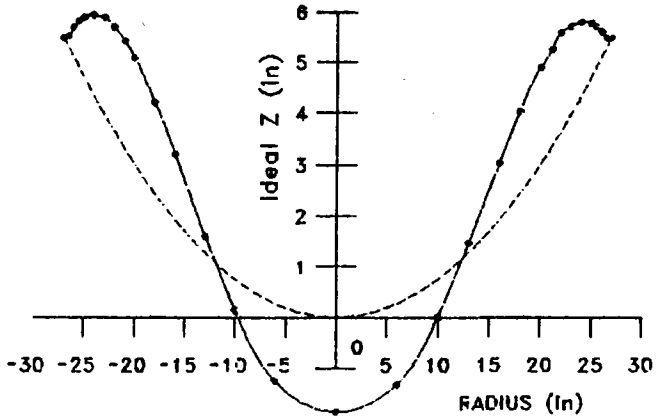

Ideal -------

Actual ———

Figure A-33(a) Ideal and Actual Displacement vs. Radial Position

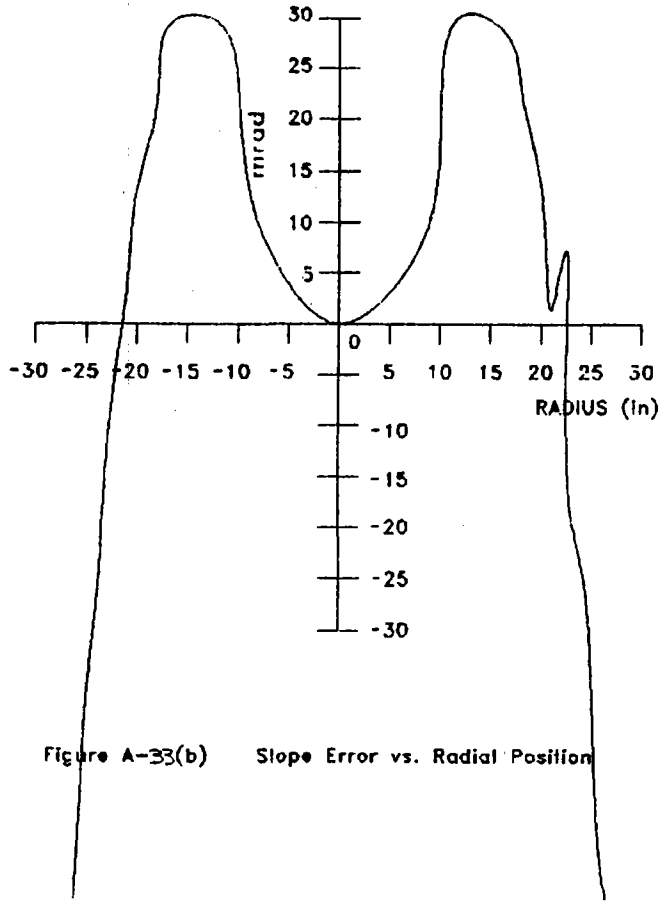

Figure A-33(b) Slope Error vs. Radial Position

Membrane: 13m3
Pdev: 25.848
Area: 100.000

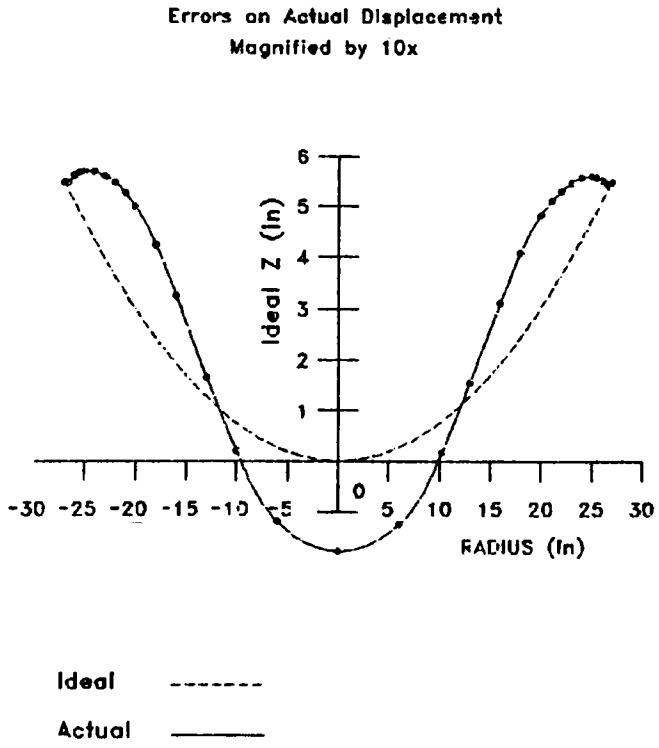

Figure A-34 (a) Ideal and Actual Displacement vs. Radial Position

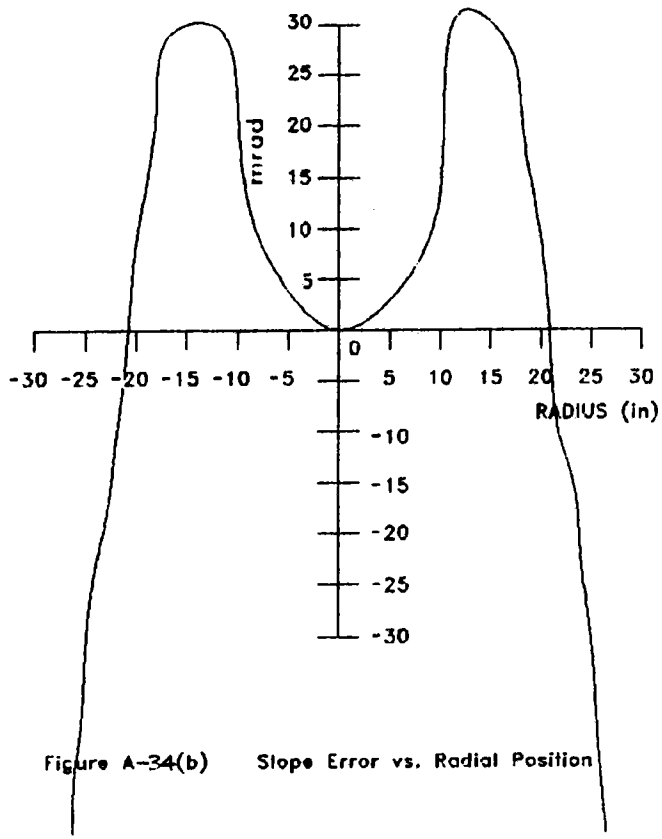

Figure A-34(b) Slope Error vs. Radial Position

Membrane: 13m4
Pdev: 9.816
Area: 100.000

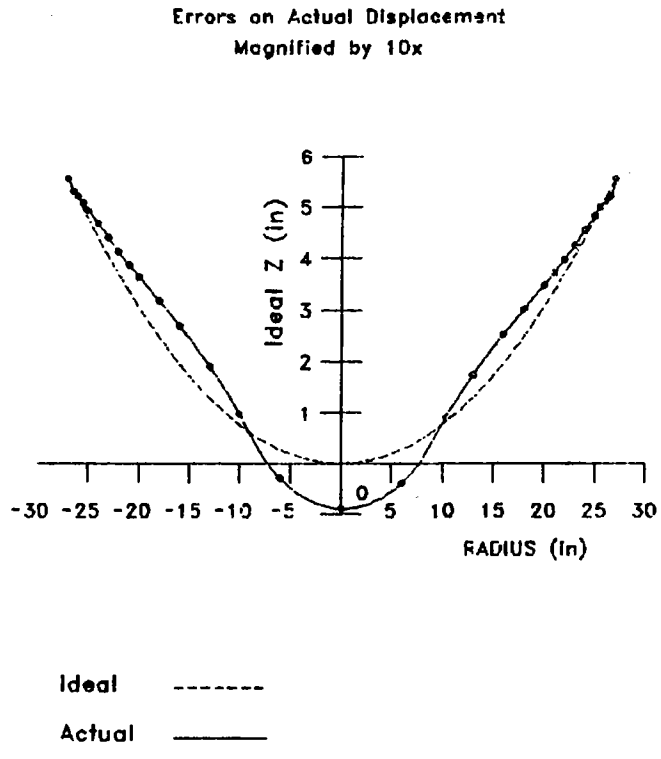

Figure A-35 (a) Ideal and Actual Displacement vs. Radial Position

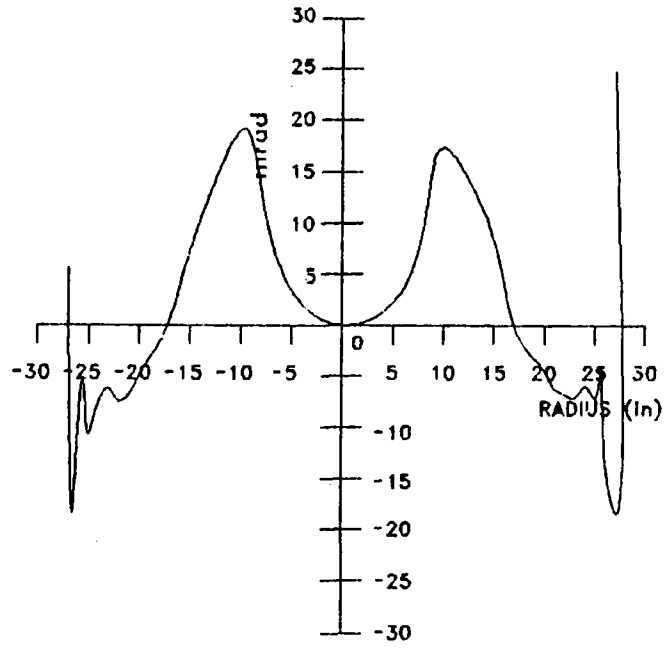

Figure A-35(b) Slope Error vs. Radial Position

Membrane: 13m5
Pdev: 7.361
Area: 100.000

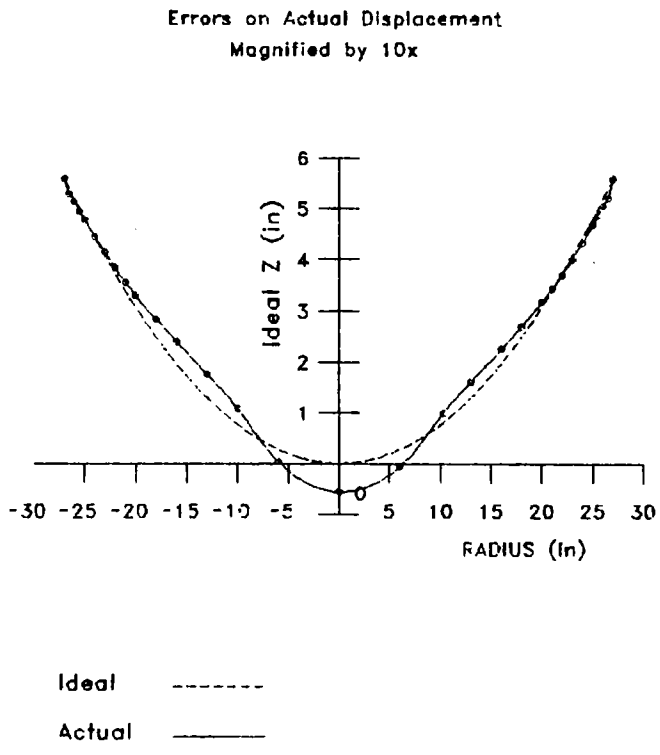

Figure A-36(a) Ideal and Actual Displacement vs. Radial Position

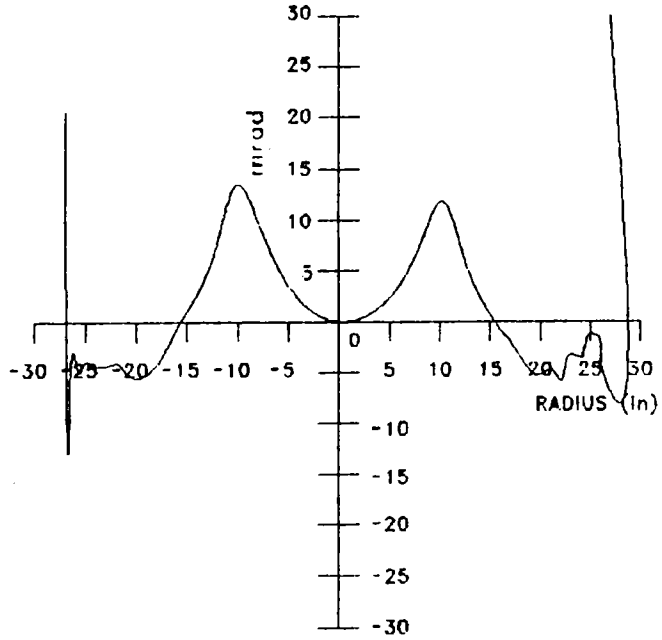

Figure A-36(b) Slope Error vs. Radial Position

Membrane: 13m6
Pdev: 7.711
Area: 100.000

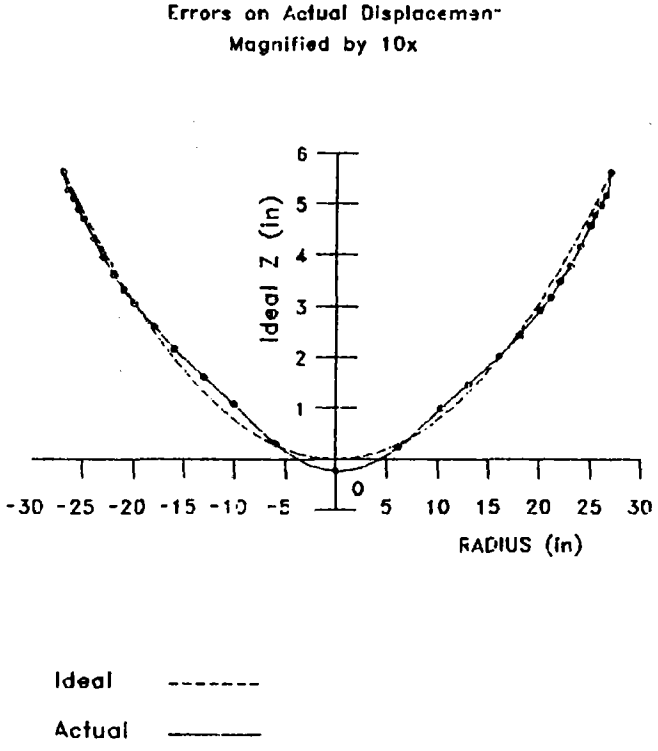

Figure A-37 (a) Ideal and Actual Displacemen- vs. Radial Position

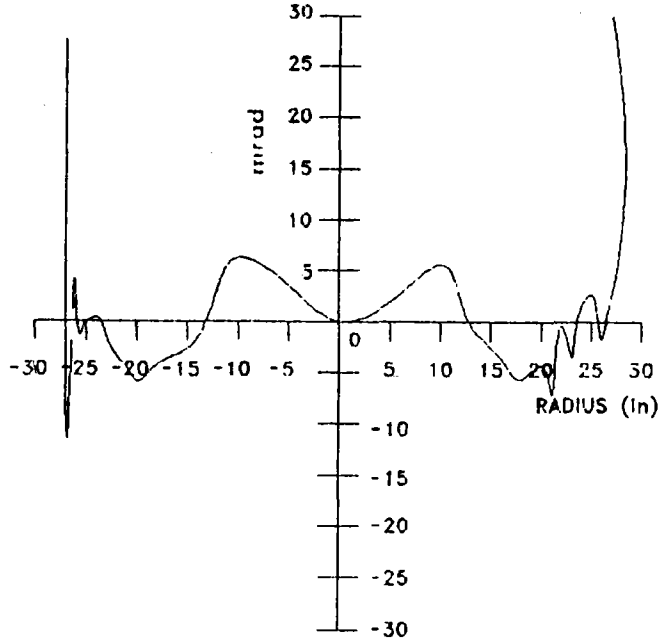

Figure A-37(b) Slope Error vs. Radial Position

Membrane: 13M6
Pdev: 3.523
Area: 96.450

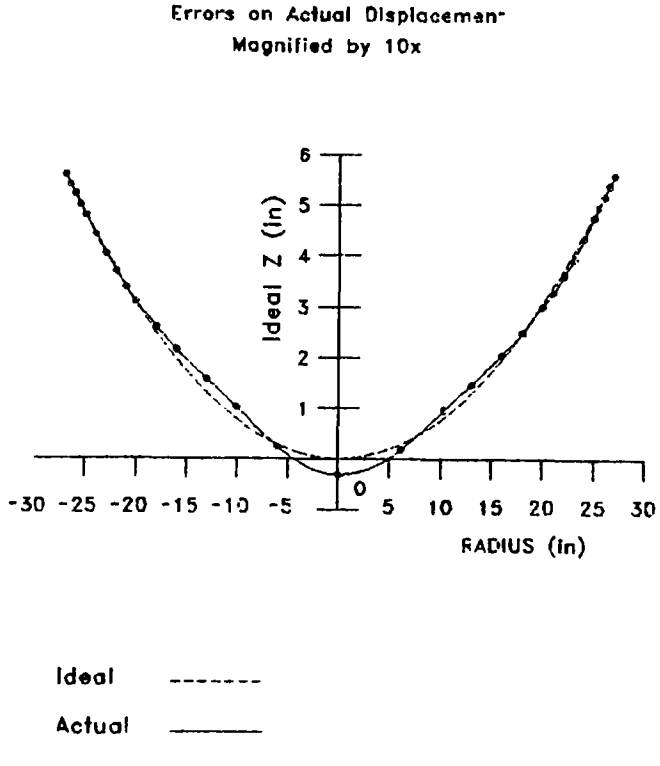

Figure A-38 (a) Ideal and Actual Displacemen- vs. Radial Position

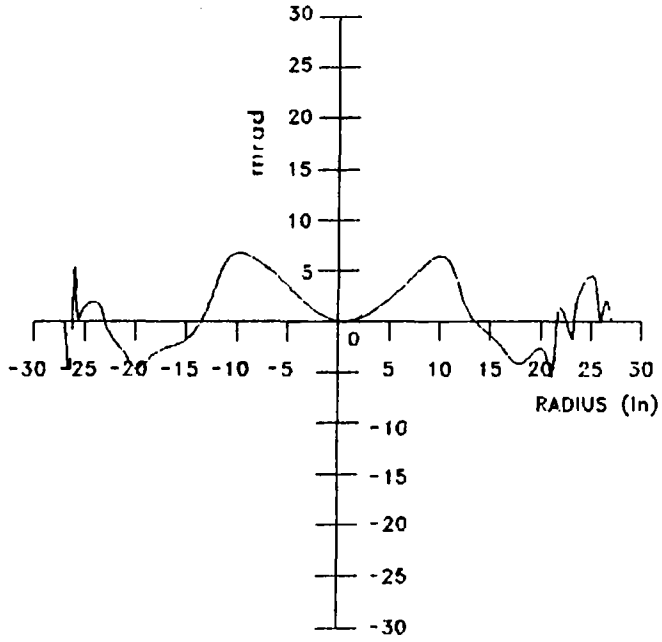

Figure A-38(b) Slope Error vs. Radial Position

Membrane: 15m1
Pdev: 9.073
Area: 100.000

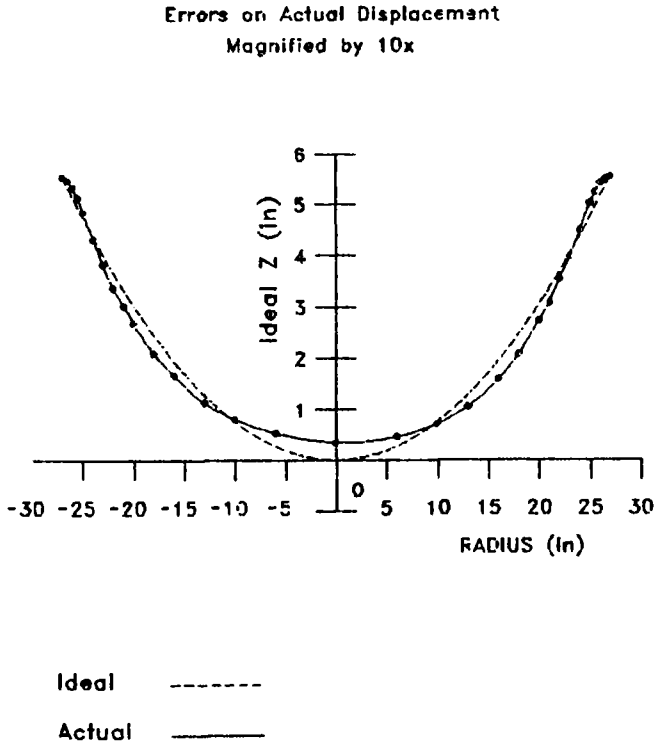

Figure A-39(a) Ideal and Actual Displacement vs. Radial Position

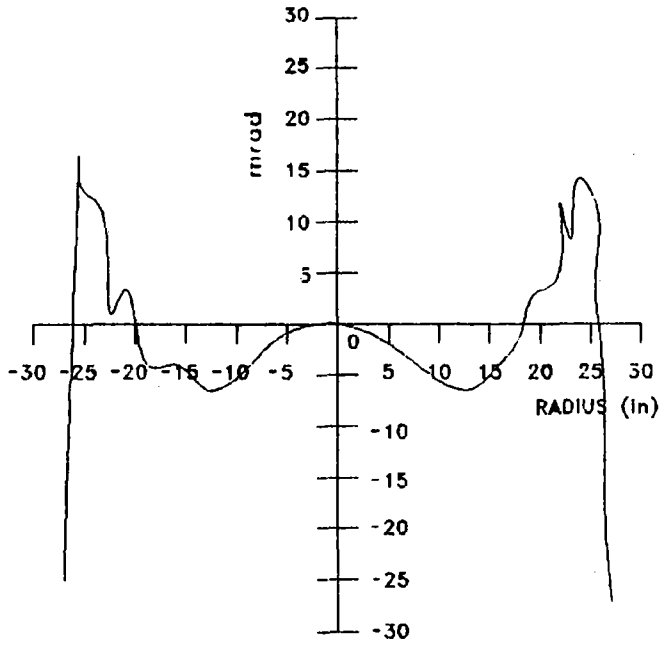

Figure A-39(b) Slope Error vs. Radial Position

Membrane: 16m1
Pdev: 28.960
Area: 100.000

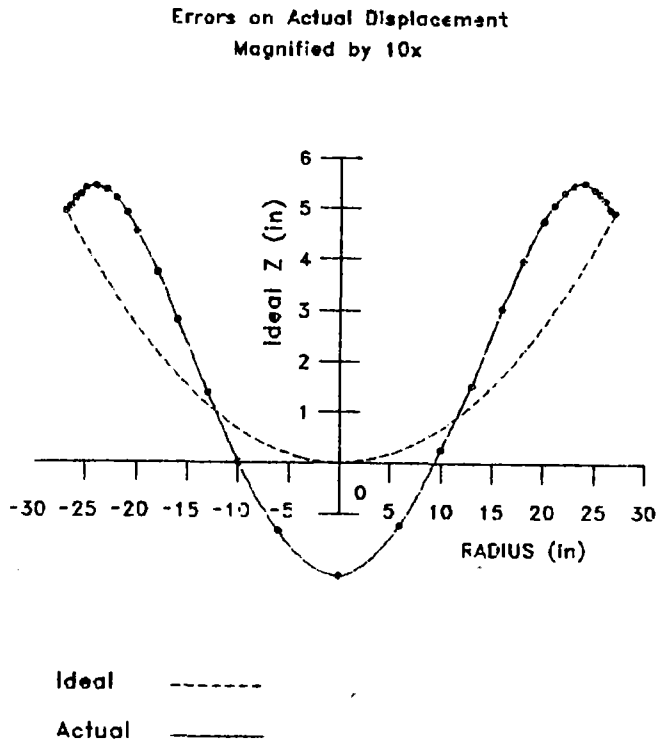

Figure A-40(a) Ideal and Actual Displacement vs. Radial Position

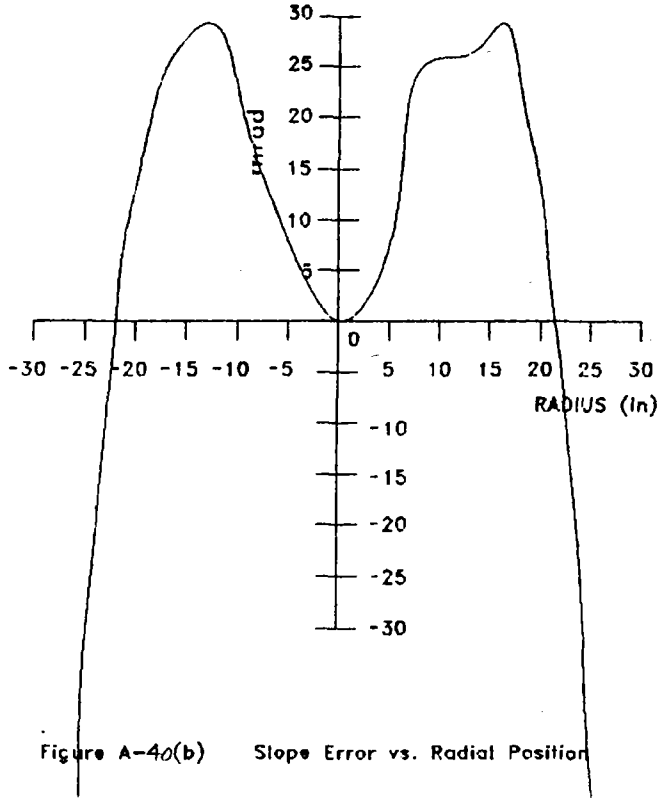

Figure A-40(b) Slope Error vs. Radial Position

Membrane: 18M1
Pdev: 8.971
Area: 100.000

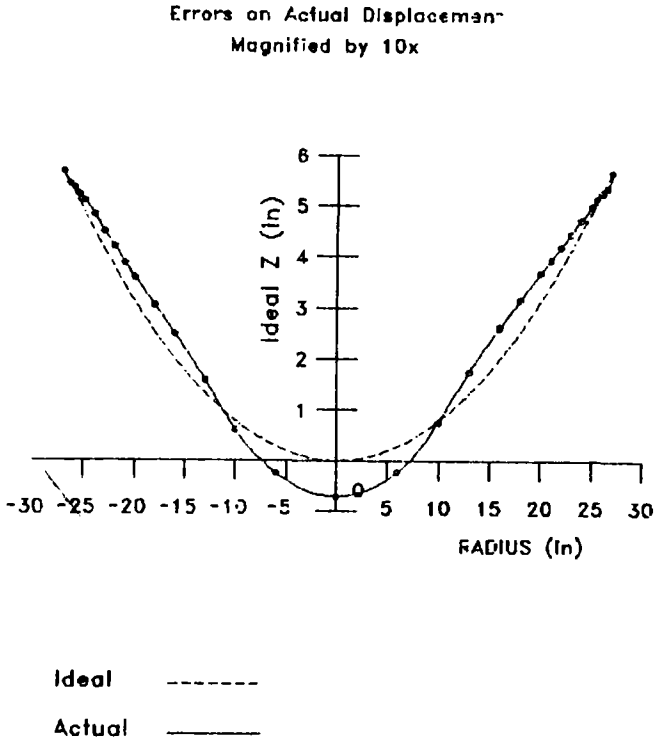

Figure A-41 (a) Ideal and Actual Displacemen- vs. Radial Position

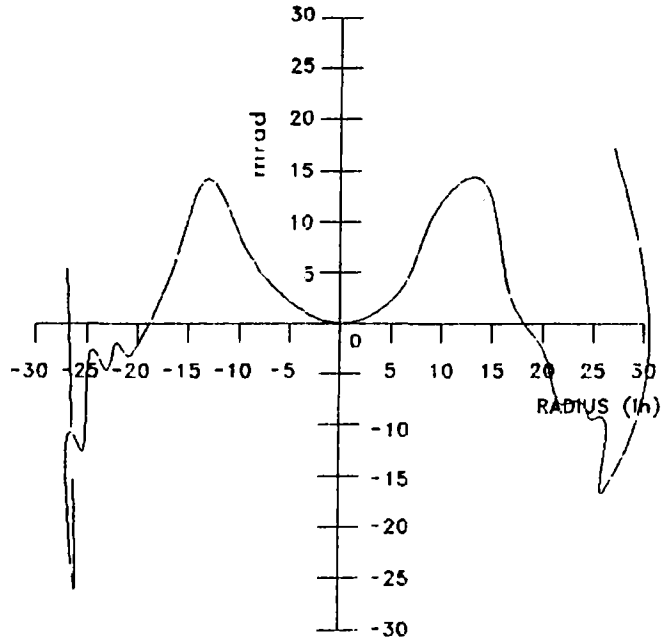

Figure A-41(b) Slope Error vs. Radial Position

Membrane: 18M1
Pdev: 8.669
Area: 96.330

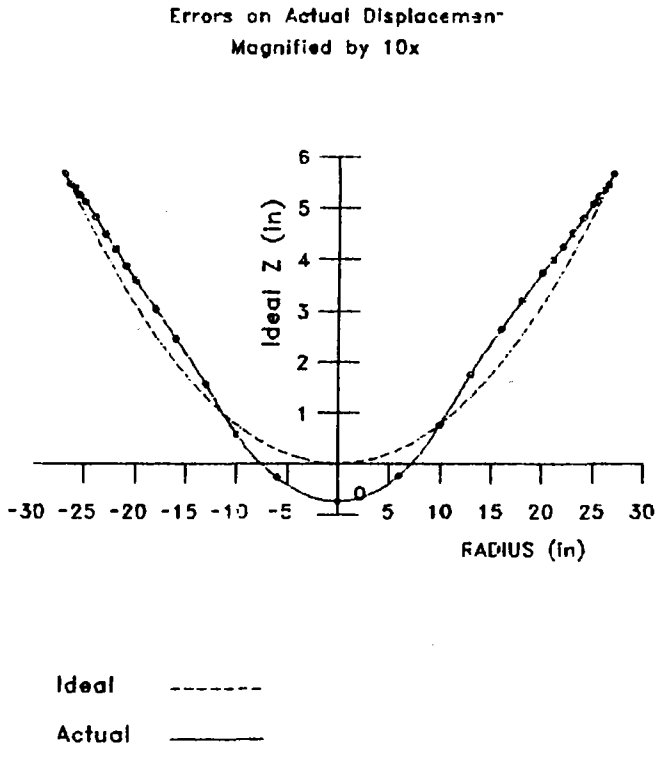

Figure A-42 (a) Ideal and Actual Displacemen- vs. Radial Position

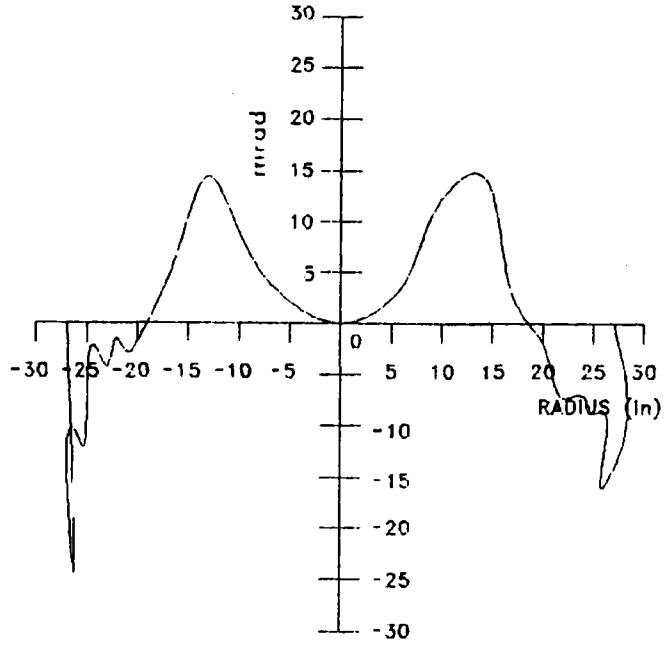

Figure A-42(b) Slope Error vs. Radial Position

Membrane: 19m1
Pdev: 13.222
Area: 100.000

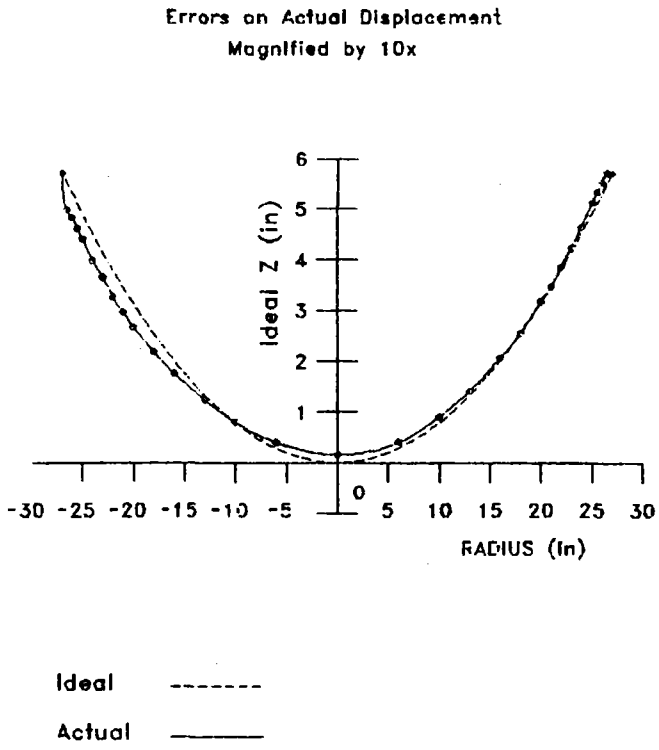

Figure A-43 (a) Ideal and Actual Displacement vs. Radial Position

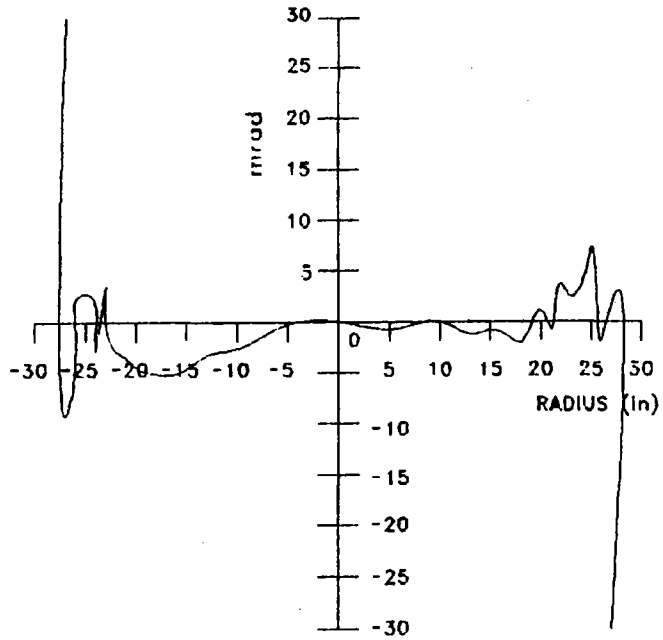

Figure A-43(b) Slope Error vs. Radial Position

Membrane: 19M1
Pdev: 2.890
Area: 96.380

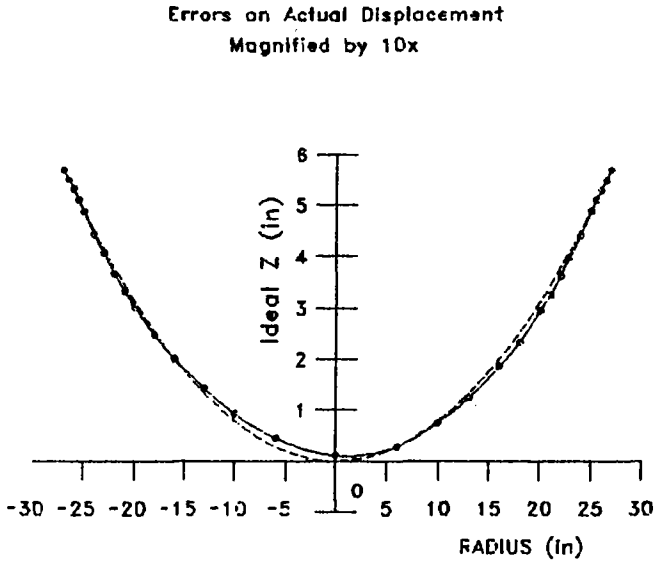

Figure A-44(a) Ideal and Actual Displacement vs. Radial Position

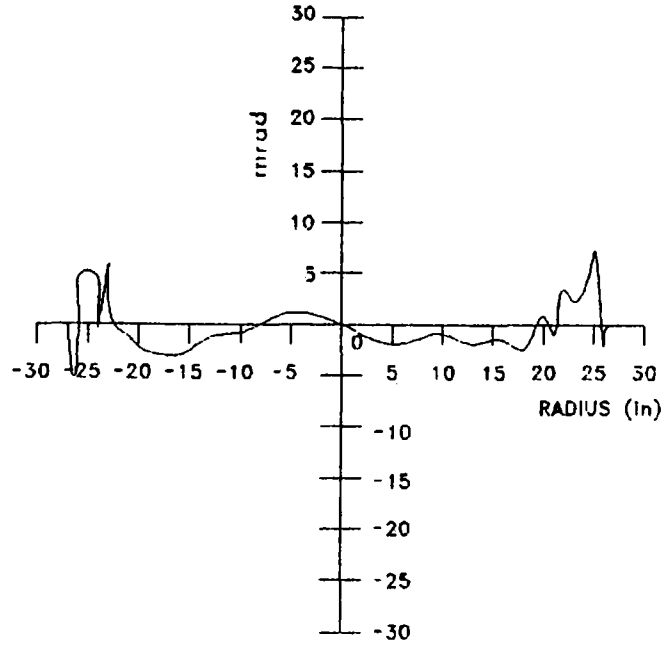

Figure A-44(b) Slope Error vs. Radial Position

Membrane: 20m1
Pdev: 10.220
Area: 100.000

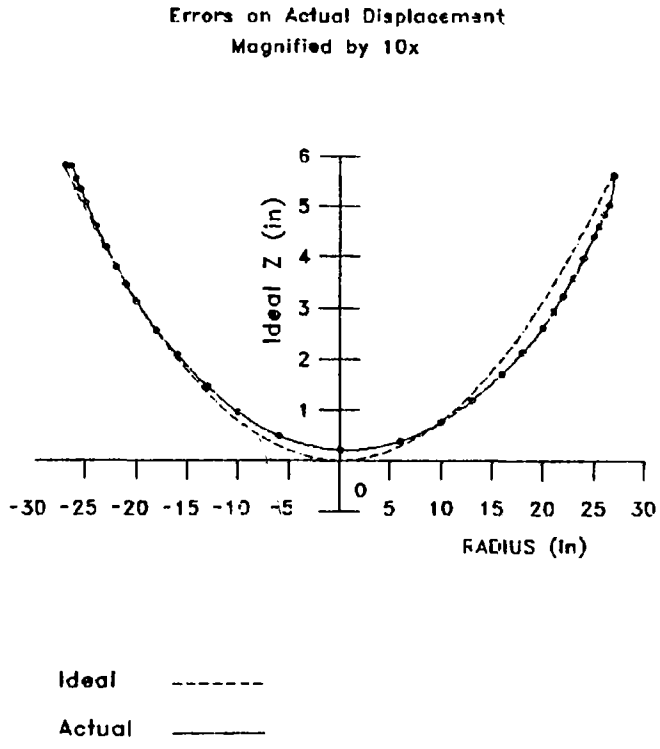

Figure A-45(a) Ideal and Actual Displacement vs. Radial Position

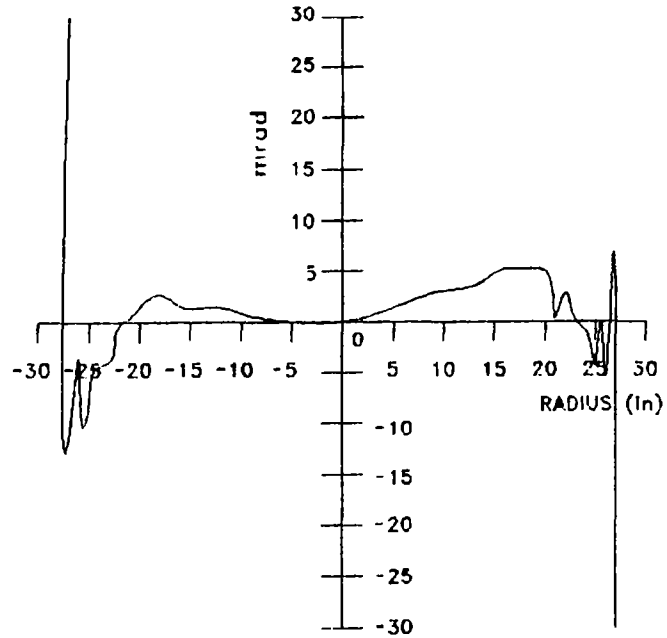

Figure A-45(b) Slope Error vs. Radial Position

Membrane: 20M1
Pdev: 4.335
Area: 96.330

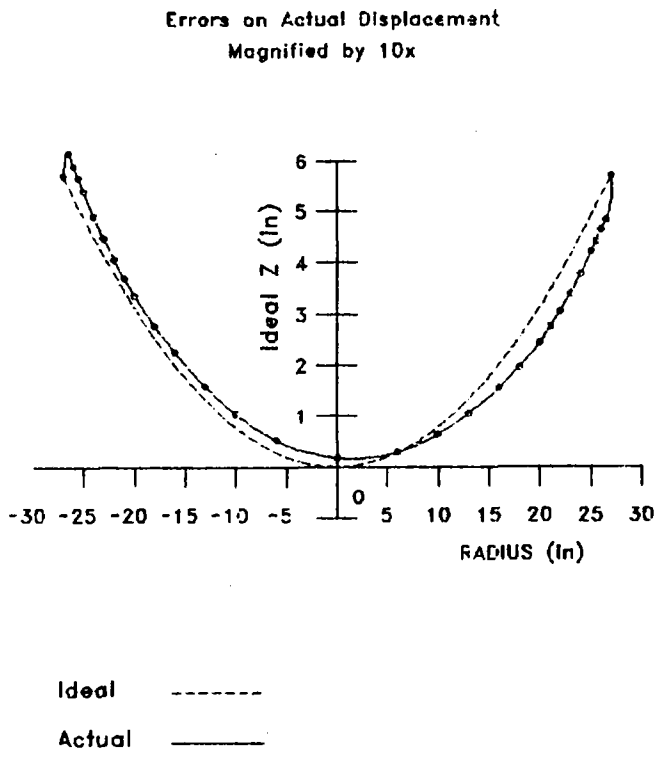

Figure A-46(a) Ideal and Actual Displacement vs. Radial Position

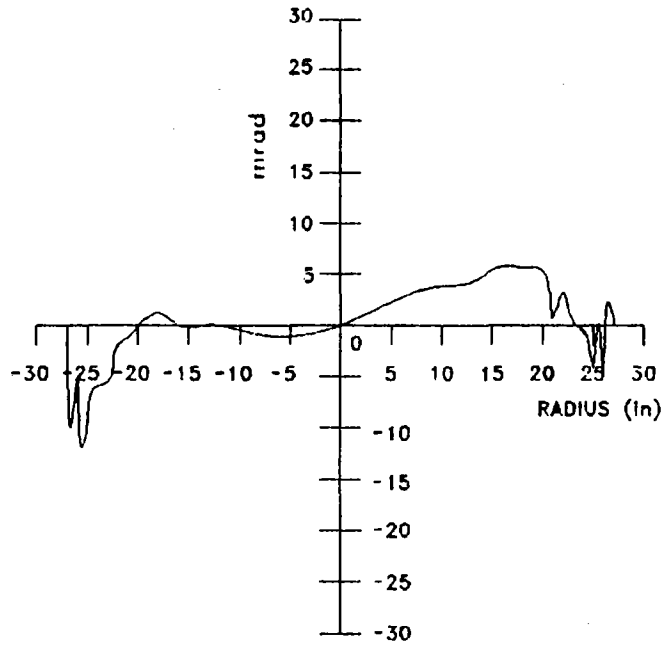

Figure A-46(b) Slope Error vs. Radial Position

Membrane: 21M1
Pdev: 9.845
Area: 100.000

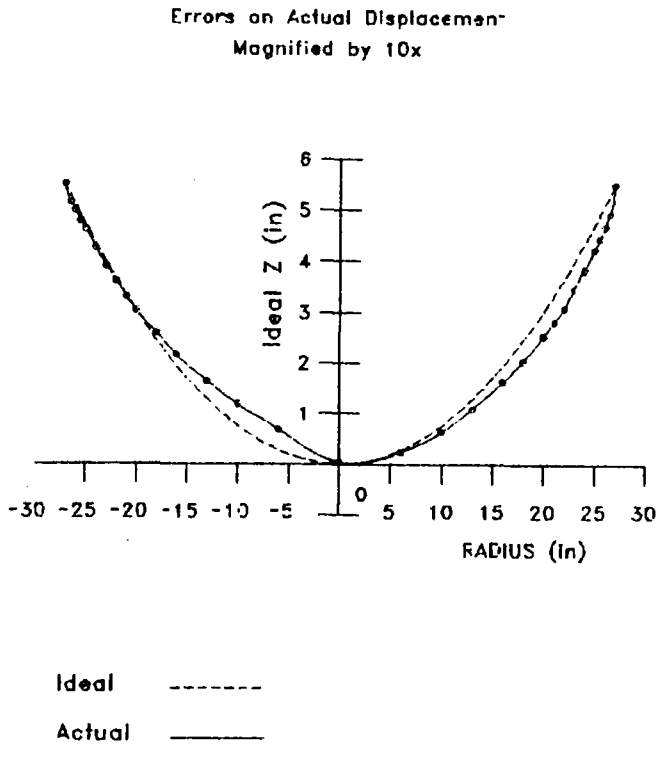

Figure A-47 (a) Ideal and Actual Displacemen- vs. Radial Position

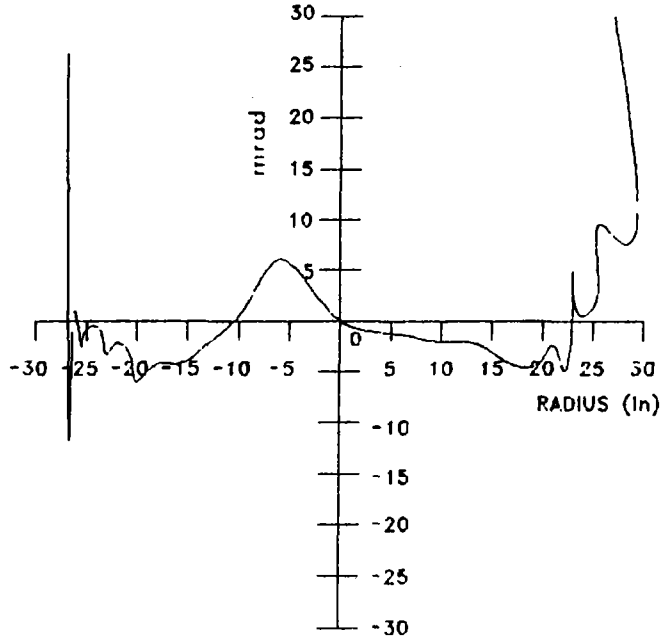

Figure A-47(b) Slope Error vs. Radial Position

Membrane: 21M1
Pdev: 3.625
Area: 96.330

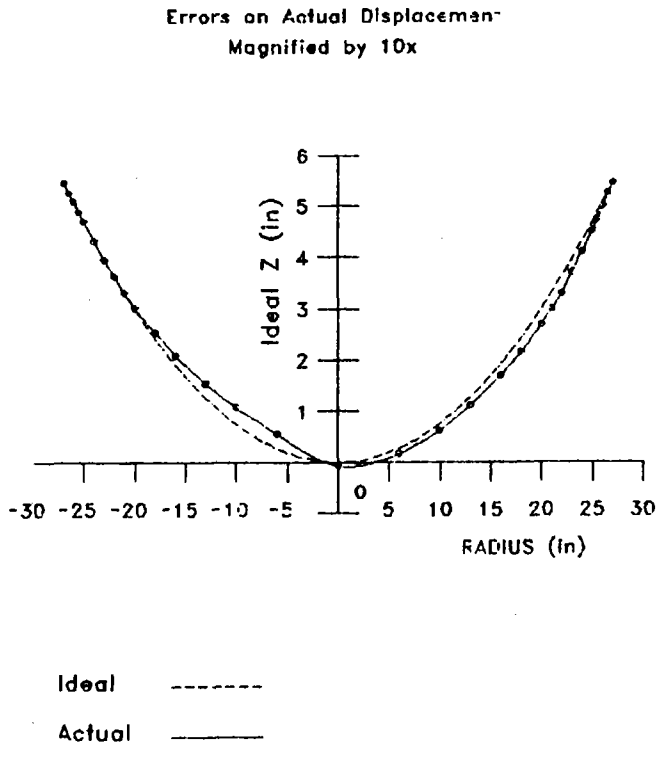

Figure A-48(a) Ideal and Actual Displacemen- vs. Radial Position

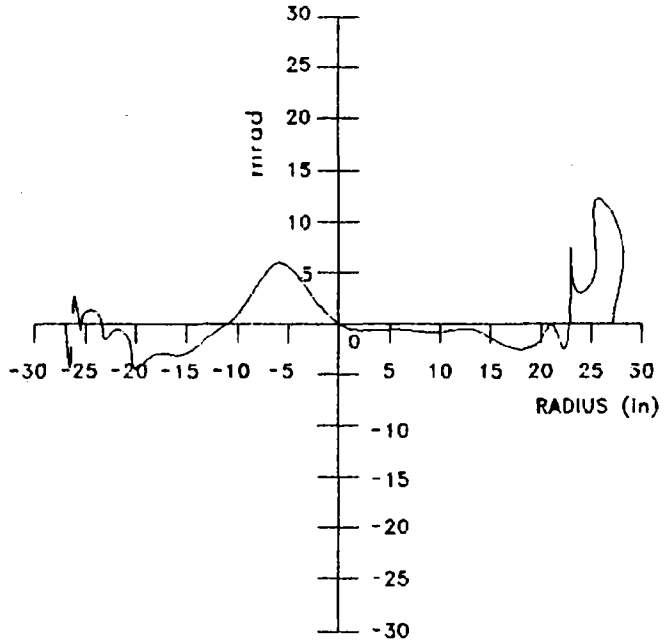

Figure A-48(b) Slope Error vs. Radial Position

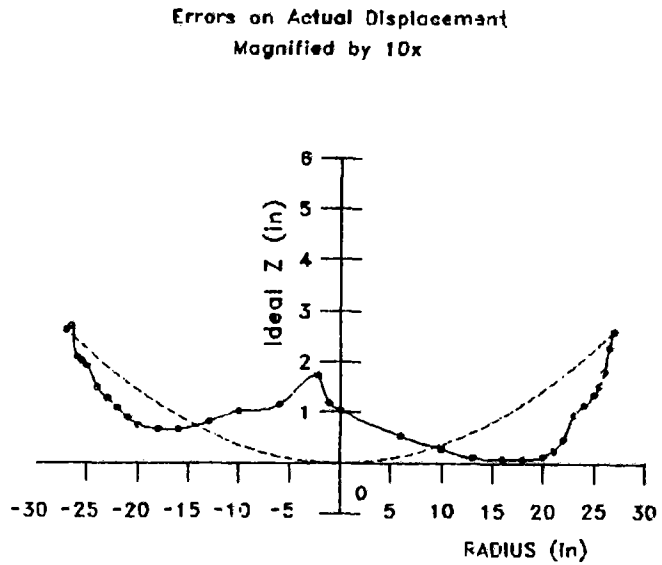

Figure A-49 (a) Ideal and Actual Displacement vs. Radial Position

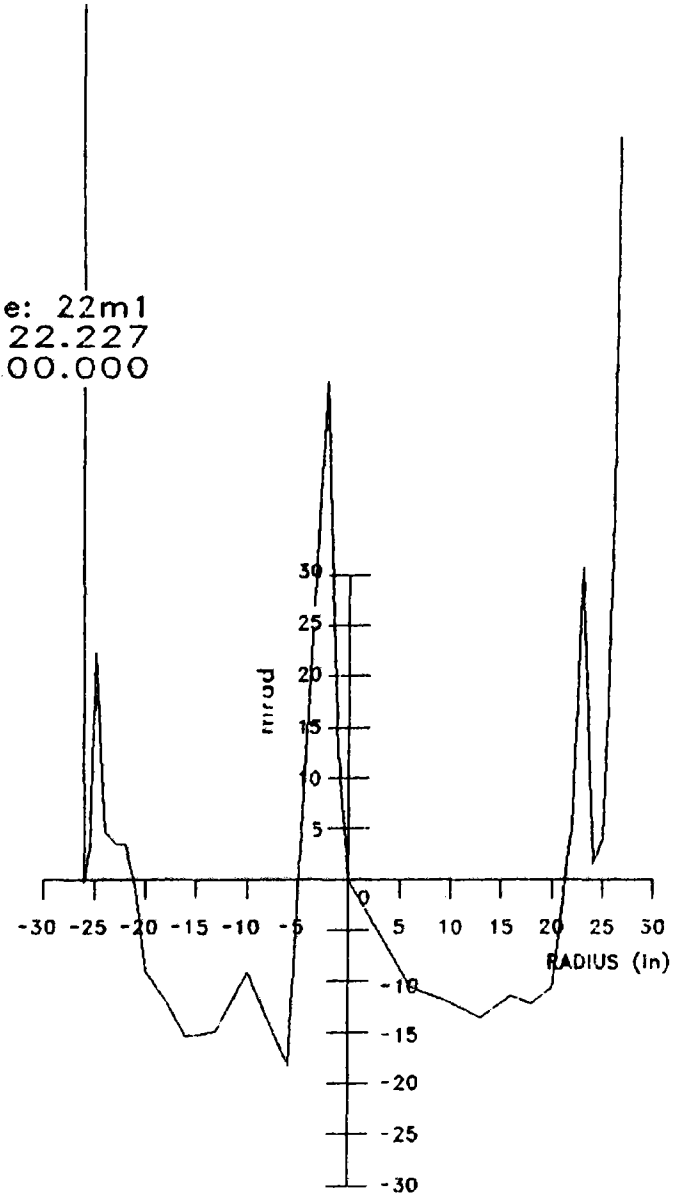

Figure A-49(b) Slope Error vs. Radial Position

Membrane: 23m1
Pdev: 15.376
Area: 100.000

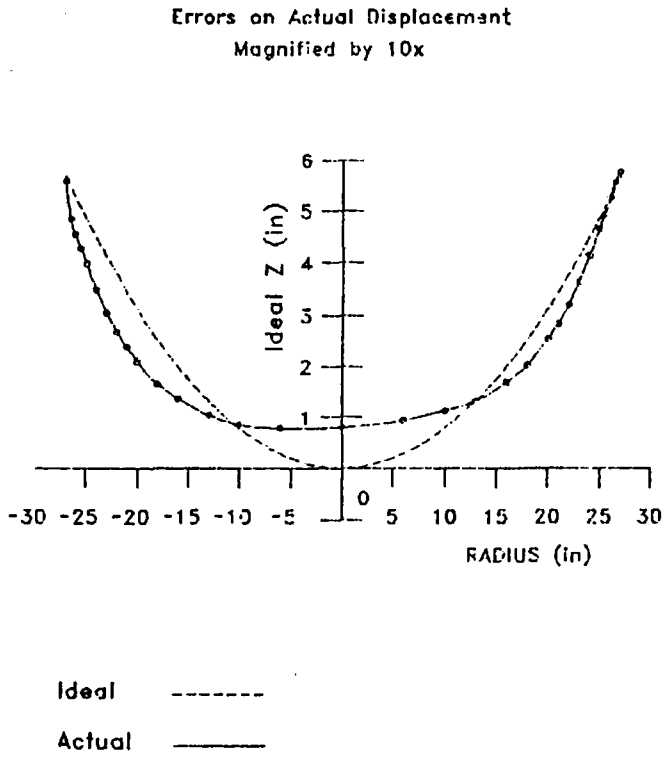

Figure A-50(a) Ideal and Actual Displacement vs. Radial Position

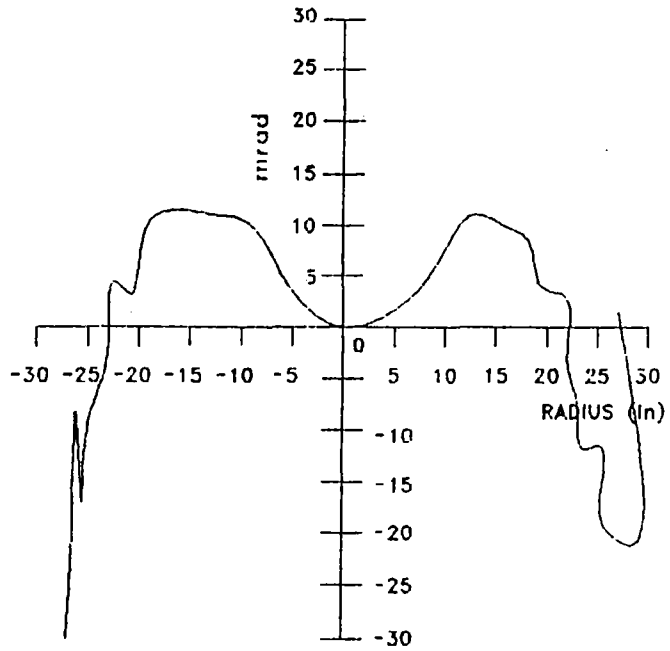

Figure A-50(b) Slope Error vs. Radial Position

Membrane: 23m2
Pdev: 18.186
Area: 100.000

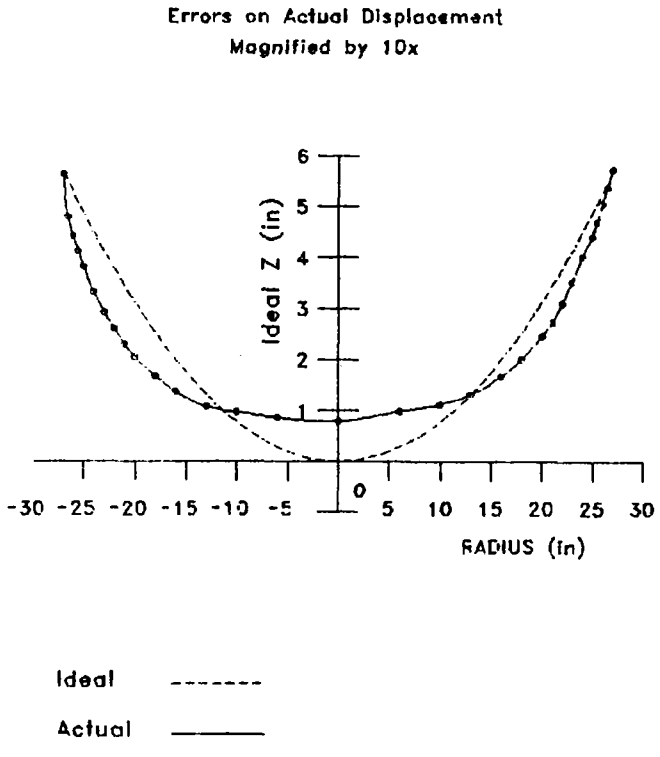

Figure A-51 (a) Ideal and Actual Displacement vs. Radial Position

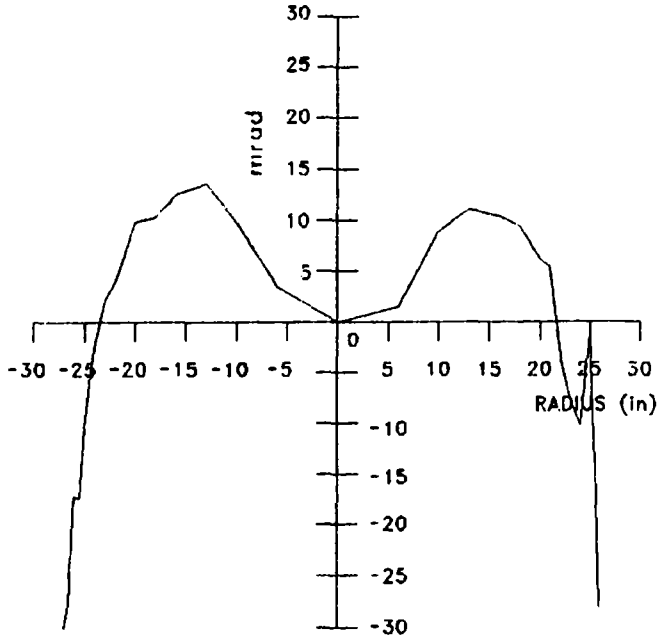

Figure A-51(b) Slope Error vs. Radial Position

Membrane: 23M2
Pdev: 11.390
Area: 96.310

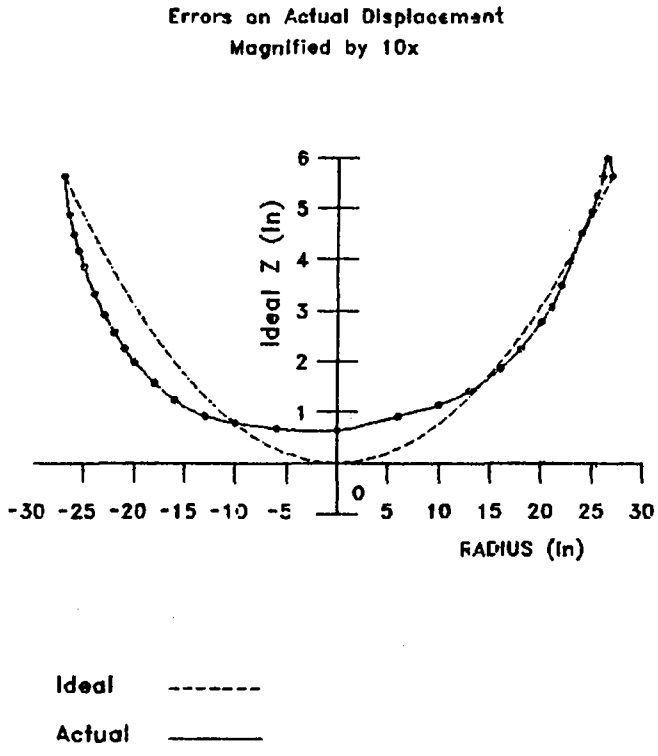

Figure A-52(a) Ideal and Actual Displacement vs. Radial Position

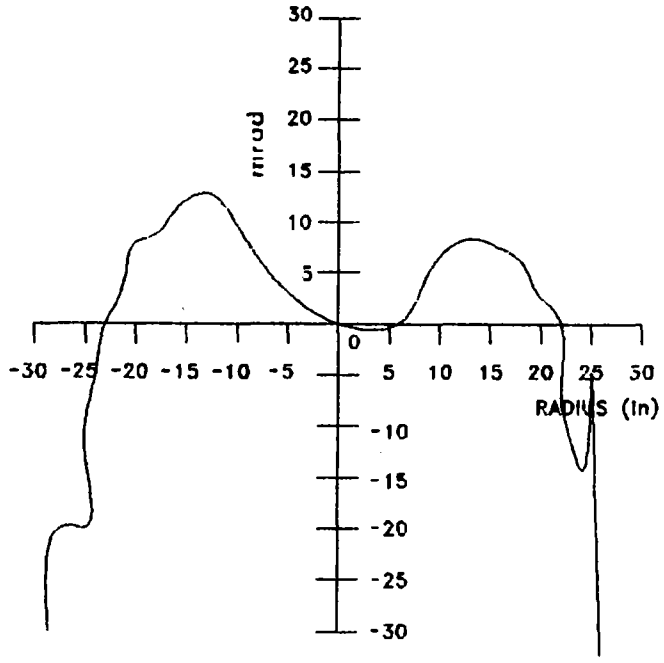

Figure A-52(b) Slope Error vs. Radial Position

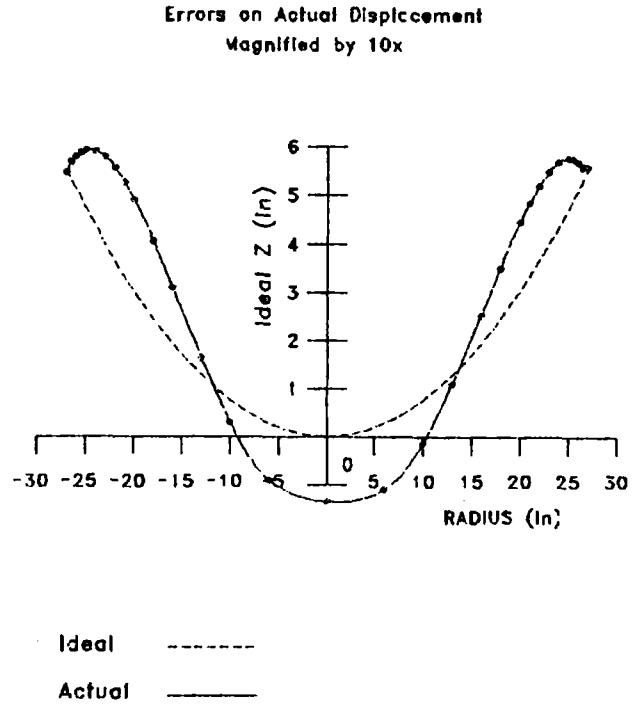

Figure A-53(a) Ideal and Actual Displacement vs. Radial Position

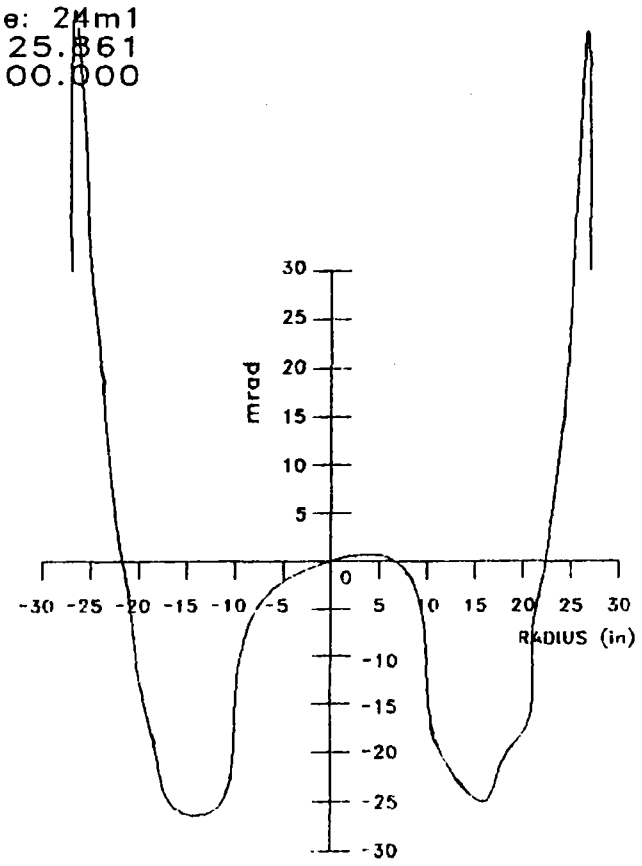

Figure A-53(b) Slope Error vs. Radial Position

Membrane: 24M2
Pdev: 4.176
Area: 100.000

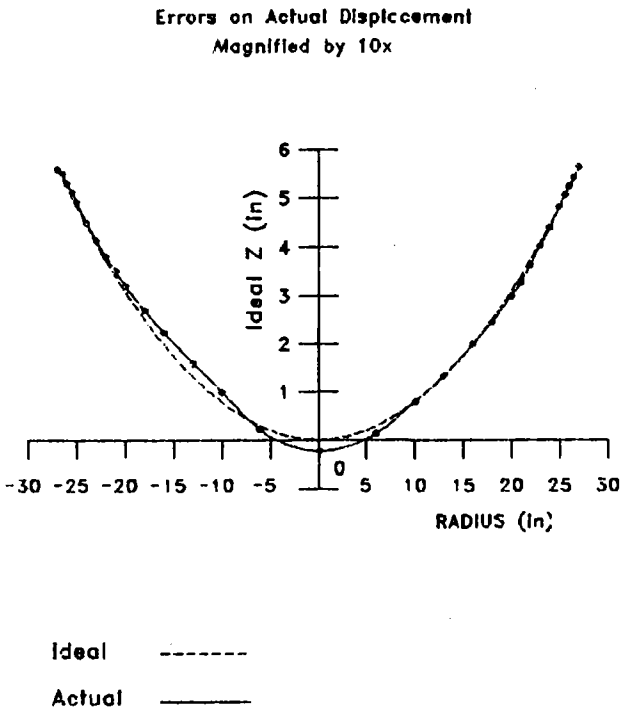

Figure A-54(a) Ideal and Actual Displacement vs. Radial Position

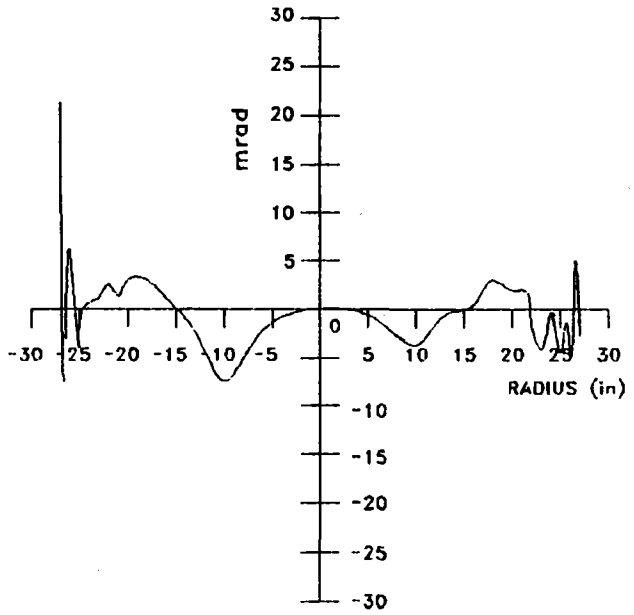

Figure A-54(b) Slope Error vs. Radial Position

Membrane: 24M2
Pdev: 3.088
Area: 96.380

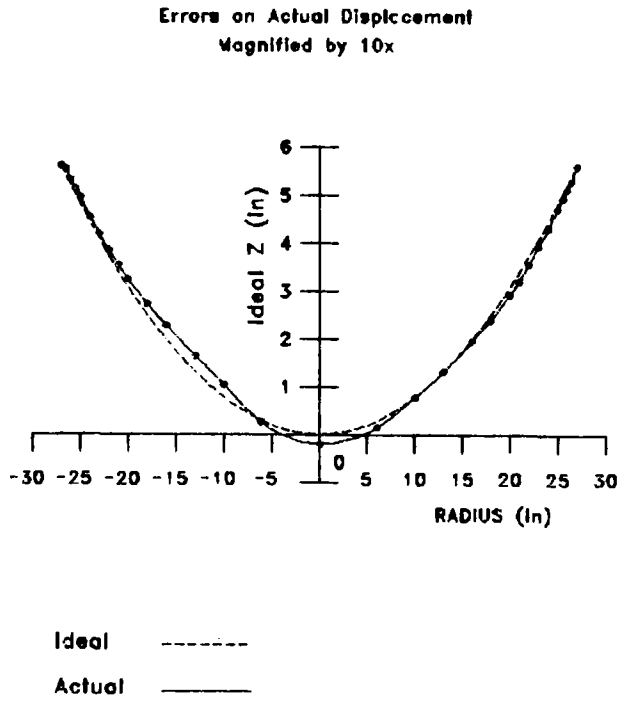

Figure A-55(a) Ideal and Actual Displacement vs. Radial Position

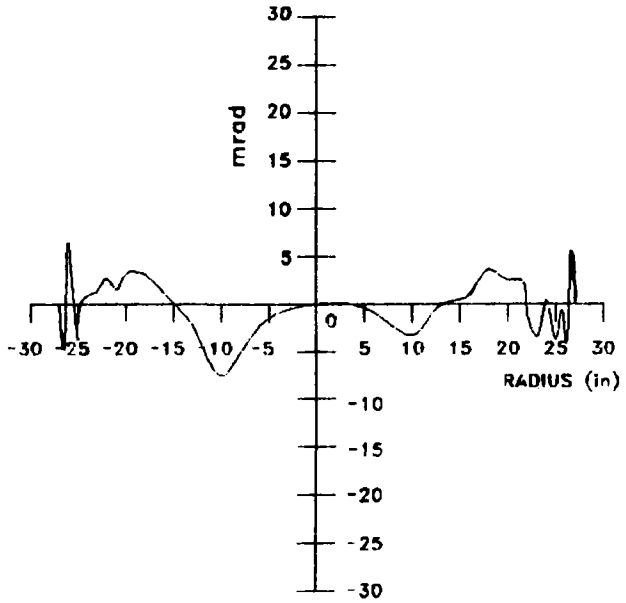

Figure A-55(b) Slope Error vs. Radial Position

Appendix B
Data on the Test-Scale Membrane

This section provides the original data and preliminary reductions for test-scale membranes. The test equipment, measurement equipment, and reduction process were defined in the main body of the text (Section 4.1).

The data are presented in the following format:

1. Header. The header describes membrane identifiers, filenames, forming processes, measurement processes, and comments made by the experimenter.

2. Radius. Radial position (inches) from vertex. Data are expressed in an r-z coordinate system. The r-axis origin is at the center of the ring plane. The z-axis is coincident with the optical axis; the origin is at the membrane vertex. The positive and negative signs are for notation purposes only. The positive radius is along the 0^{o}, or 90^{o} theta line, while the negative is along the 180^{o} or 270^{o} line, respectively.

3. Measured slope. Membrane slope (radians).

4. Ideal slope. The slope (radians) that corresponds to the surface normal on an ideal parabola at the referenced radial position.

5. Slope error. Slope error (mrad) is the difference in actual and ideal slope. The sign convention is positive for slopes that are too steep; negative when too shallow.

6. Effective area. The area (in^2) associated with the slope measurement. This value is used as an intermediate variable in determining the Pdev.

7. Pdev., Area Pdev., or the parabolic deviation, was the standard deviation of slope error between the ideal and measured parabolas. The ideal parabola was defined so that the mean slope error was zero. In some instances, Pdev was calculated over less than the full area. In other words, the outer data points may have been neglected. The area percentage indicates what fraction of the aperture was used for the data reduction.

The tabulated data have also been presented in a graphical format. The slope error for each membrane scan is shown in the accompanying figure. The ideal shape would have

no error. In other words, the abscissa represents the ideal parabola. Positive slope error indicates a shape that is too steep; negative is too shallow.

The data were generally splined before plotting to create a smooth curve between points. If specific slopes or displacements are required, the tabulated values should be used. The curves, on the other hand, provide a descriptive data presentation.

Following the standard data presentation are some figures illustrating the final membranes with alternated figures of merit. The first set of figures demonstrates the ratio of predicted-to-ideal beam image size at the target plane based upon slope measurements. This figure of merit was developed by C. Kutscher, at Solar Energy Research Institute, to incorporate the effects of slant range and cosine error, in addition to the area weight term. The second set of figures illustrates optical performance at different dispersions for a Gaussian sun-shape.

THIS SHEET INTENTIONALLY LEFT BLANK.

File Name : 1D.OUT Date : 05-06-1988
Data File : 1D.4MM

Membrane : 6 mil 1145-OT

Comments : FIRST SCAN AT F/D =.6
11/6/87
Target Height = 72.700 in.s
PASS: WE
SEAM: EW

Stabilization
Pressure : 1.1250 in.s H20

Area : 100.00 %
Pdev : 30.0959

DATA SET	RADIUS	MEASURED SLOPE	IDEAL SLOPE	SLOPE ERROR	EFFECTIVE AREA
1	-69.5580	-0.2959	-0.3449	-48.9769	1125.6300
2	-64.6177	-0.2950	-0.3221	-27.1562	1045.1300
3	-59.6729	-0.2910	-0.2990	-7.9821	964.6277
4	-54.7237	-0.2841	-0.2755	8.6690	884.1268
5	-49.6461	-0.2709	-0.2510	19.8313	803.6251
6	-44.6878	-0.2557	-0.2269	28.8149	723.1241
7	-39.7251	-0.2365	-0.2024	34.1328	642.6226
8	-34.7579	-0.2149	-0.1776	37.2631	562.1212
9	-29.7863	-0.1887	-0.1527	36.0354	481.6199
10	-24.8102	-0.1581	-0.1275	30.6580	401.1186
11	-19.8297	-0.1314	-0.1021	29.3167	320.6174
12	-14.8447	-0.0967	-0.0765	20.1688	240.1160
13	-9.9800	-0.0647	-0.0515	13.1779	159.6147
14	-5.2360	-0.0302	-0.0270	3.1860	79.1134
15	0.0120	0.0001	0.0001	0.0067	18.7613
16	5.1398	0.0297	0.0265	3.1276	79.1134
17	10.0219	0.0699	0.0517	18.1789	159.6147
18	14.9081	0.1019	0.0769	25.0915	240.1160
19	19.9241	0.1329	0.1026	30.3861	320.6174
20	24.8189	0.1635	0.1275	35.9571	401.1186
21	29.8437	0.1909	0.1529	37.9767	481.6199
22	34.7471	0.2148	0.1776	37.2593	562.1212
23	39.7807	0.2374	0.2027	34.7519	642.6226
24	44.8136	0.2546	0.2275	27.1087	723.1241
25	49.7350	0.2725	0.2515	21.0115	803.6251
26	54.7818	0.2822	0.2758	6.4426	884.1268
27	59.7067	0.2906	0.2991	-8.5220	964.6277
28	64.6359	0.2945	0.3222	-27.7319	1045.1300
29	69.6958	0.2959	0.3456	-49.6810	1125.6300

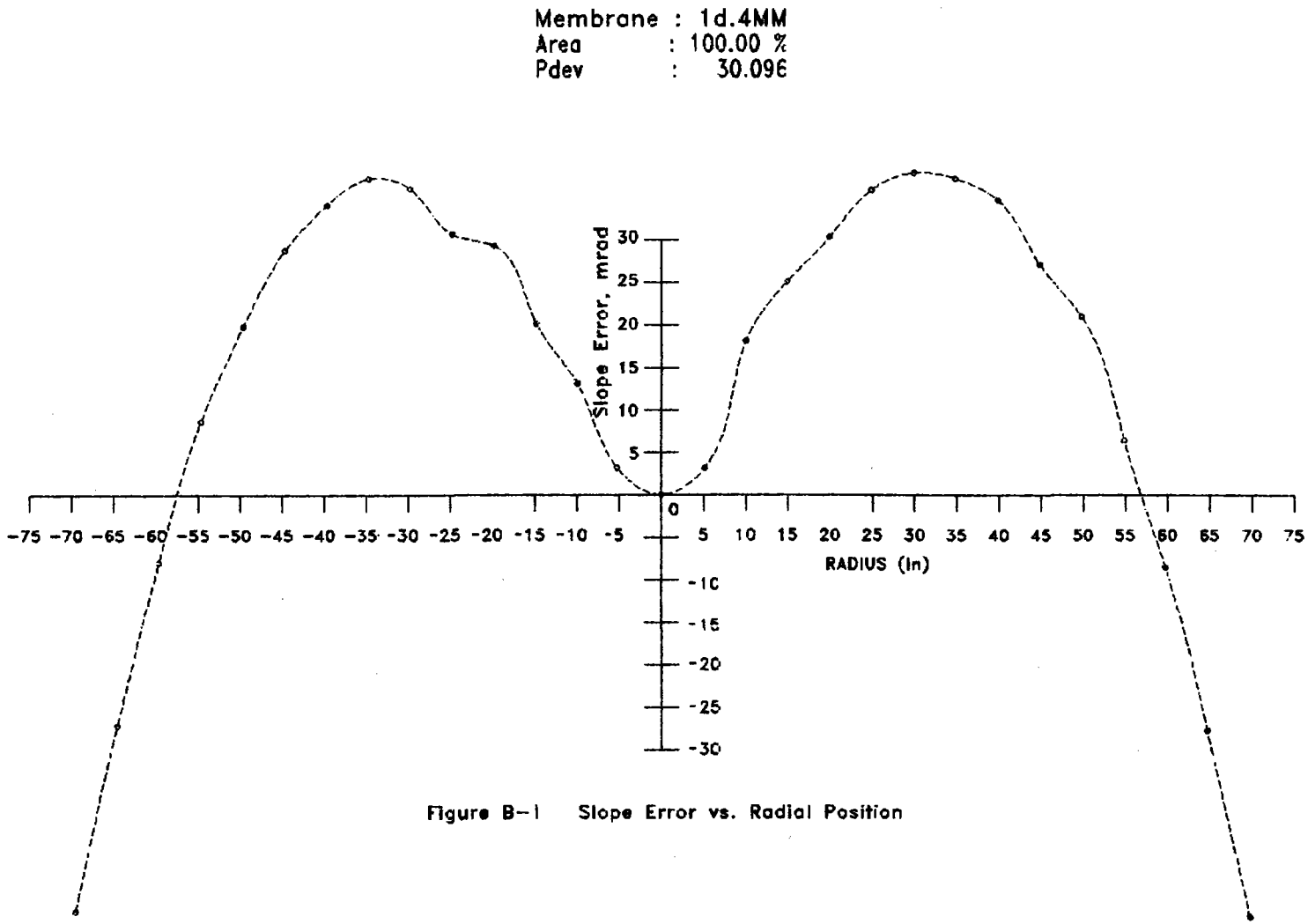

Figure B-1 Slope Error vs. Radial Position

File Name : 1I.OUT Date : 05-06-1988
Data File : 1I.4MM

Membrane : 6 mil 1145-OT

Comments : FIRST MEMB N TO S VACUUMED TO 10.5 REAL INCHES
11/9/87 TARGET RAISED TO H=79.79 FROM 72.7
Target Height = 79.790 in.s
PASS: NS
SEAM: EW

Stabilization
Pressure : 1.1250 in.s H20

Area : 100.00 %
Pdev : 5.9241

DATA SET	RADIUS	MEASURED SLOPE	IDEAL SLOPE	SLOPE ERROR	EFFECTIVE AREA
1	-68.8444	-0.3557	-0.3531	2.6082	1125.6300
2	-63.9034	-0.3317	-0.3296	2.0511	1045.1300
3	-58.9580	-0.3012	-0.3057	-4.5490	964.6277
4	-54.0081	-0.2732	-0.2814	-8.2198	884.1268
5	-48.9249	-0.2549	-0.2562	-1.2428	803.6251
6	-43.9660	-0.2290	-0.2312	-2.1965	723.1241
7	-39.0026	-0.2044	-0.2058	-1.4658	642.6226
8	-34.0348	-0.1771	-0.1802	-3.0969	562.1212
9	-29.0625	-0.1582	-0.1543	3.8287	481.6199
10	-24.0858	-0.1330	-0.1282	4.7674	401.1186
11	-19.1046	-0.1102	-0.1019	8.2769	320.6174
12	-14.1190	-0.0983	-0.0754	22.8229	240.1160
13	-9.2587	-0.0650	-0.0495	15.4821	159.6147
14	-4.5141	-0.0367	-0.0242	12.5024	79.1134
15	0.7346	0.0031	0.0039	-0.8294	18.7613
16	5.8681	0.0422	0.0314	10.8407	79.1134
17	10.7458	0.0713	0.0575	13.8049	159.6147
18	15.6377	0.1062	0.0835	22.7161	240.1160
19	20.6543	0.1171	0.1101	6.9564	320.6174
20	25.5447	0.1410	0.1359	5.0478	401.1186
21	30.5701	0.1681	0.1622	5.9234	481.6199
22	35.4792	0.1891	0.1877	1.3993	562.1212
23	40.5134	0.2141	0.2136	0.5602	642.6226
24	45.5521	0.2384	0.2392	-0.7908	723.1241
25	50.4640	0.2663	0.2639	2.4914	803.6251
26	55.5114	0.2815	0.2889	-7.3427	884.1268
27	60.4420	0.3111	0.3129	-1.7997	964.6277
28	65.3668	0.3361	0.3366	-0.5335	1045.1300
29	70.4274	0.3637	0.3605	3.1808	1125.6300

Membrane : 11.4MM
Area : 100.00 %
Pdev : 5.924

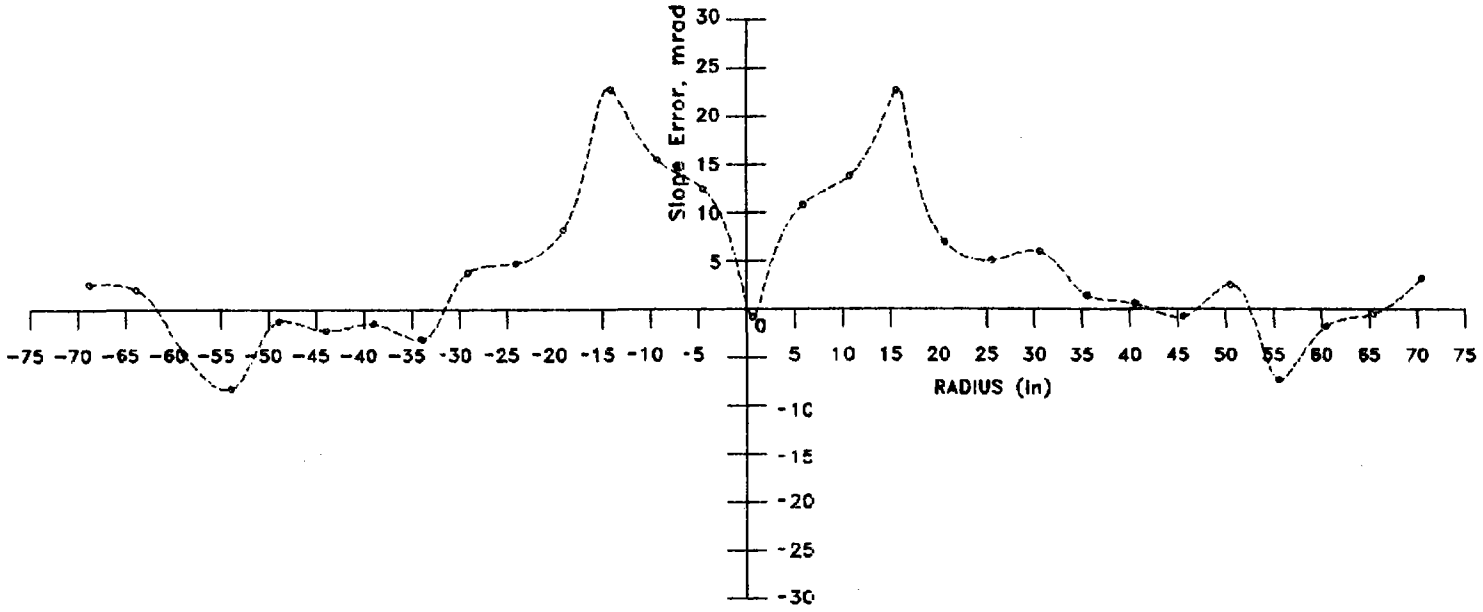

Figure B-2 Slope Error vs. Radial Position

File Name : 1J.OUT Date : 05-06-1988
Data File : 1J.4MM

Membrane : 6 mil 1145-OT

Comments : FIRST MEM W TO E SAME CONDITIONS AS 1I
11/9/87
Target Height = 79.790 in.s
PASS: EW
SEAM: EW

Stabilization
Pressure : 1.2500 in.s H20

Area : 100.00 %
Pdev : 5.5602

DATA SET	RADIUS	MEASURED SLOPE	IDEAL SLOPE	SLOPE ERROR	EFFECTIVE AREA
1	-69.6356	-0.3608	-0.3572	3.5858	1125.6300
2	-64.6340	-0.3343	-0.3334	0.8278	1045.1300
3	-59.6892	-0.3083	-0.3096	-1.3175	964.6277
4	-54.7400	-0.2822	-0.2853	-3.1880	884.1268
5	-49.7863	-0.2574	-0.2607	-3.3295	803.6251
6	-44.7657	-0.2325	-0.2355	-2.9330	723.1241
7	-39.8030	-0.2080	-0.2102	-2.1991	642.6226
8	-34.8359	-0.1846	-0.1846	0.0808	562.1212
9	-29.8644	-0.1618	-0.1587	3.1002	481.6199
10	-24.8884	-0.1385	-0.1326	5.9322	401.1186
11	-19.9079	-0.1208	-0.1063	14.5619	320.6174
12	-14.9858	-0.0958	-0.0801	15.6938	240.1160
13	-9.9965	-0.0651	-0.0535	11.5683	159.6147
14	-5.2145	-0.0385	-0.0279	10.5776	79.1134
15	-0.0165	-0.0010	-0.0001	-0.8853	18.7613
16	5.1864	0.0405	0.0278	12.6911	79.1134
17	10.0053	0.0685	0.0536	14.9665	159.6147
18	14.9548	0.0984	0.0800	18.3972	240.1160
19	19.9708	0.1219	0.1066	15.3140	320.6174
20	24.8707	0.1423	0.1325	9.7997	401.1186
21	29.8955	0.1645	0.1589	5.6635	481.6199
22	34.7939	0.1831	0.1843	-1.2913	562.1212
23	39.7066	0.2096	0.2097	-0.0471	642.6226
24	44.7446	0.2353	0.2353	-0.0174	723.1241
25	49.7870	0.2562	0.2607	-4.5859	803.6251
26	54.8338	0.2822	0.2858	-3.6042	884.1268
27	59.7537	0.3072	0.3099	-2.6980	964.6277
28	64.6880	0.3332	0.3337	-0.4758	1045.1300
29	69.6164	0.3595	0.3571	2.3698	1125.6300

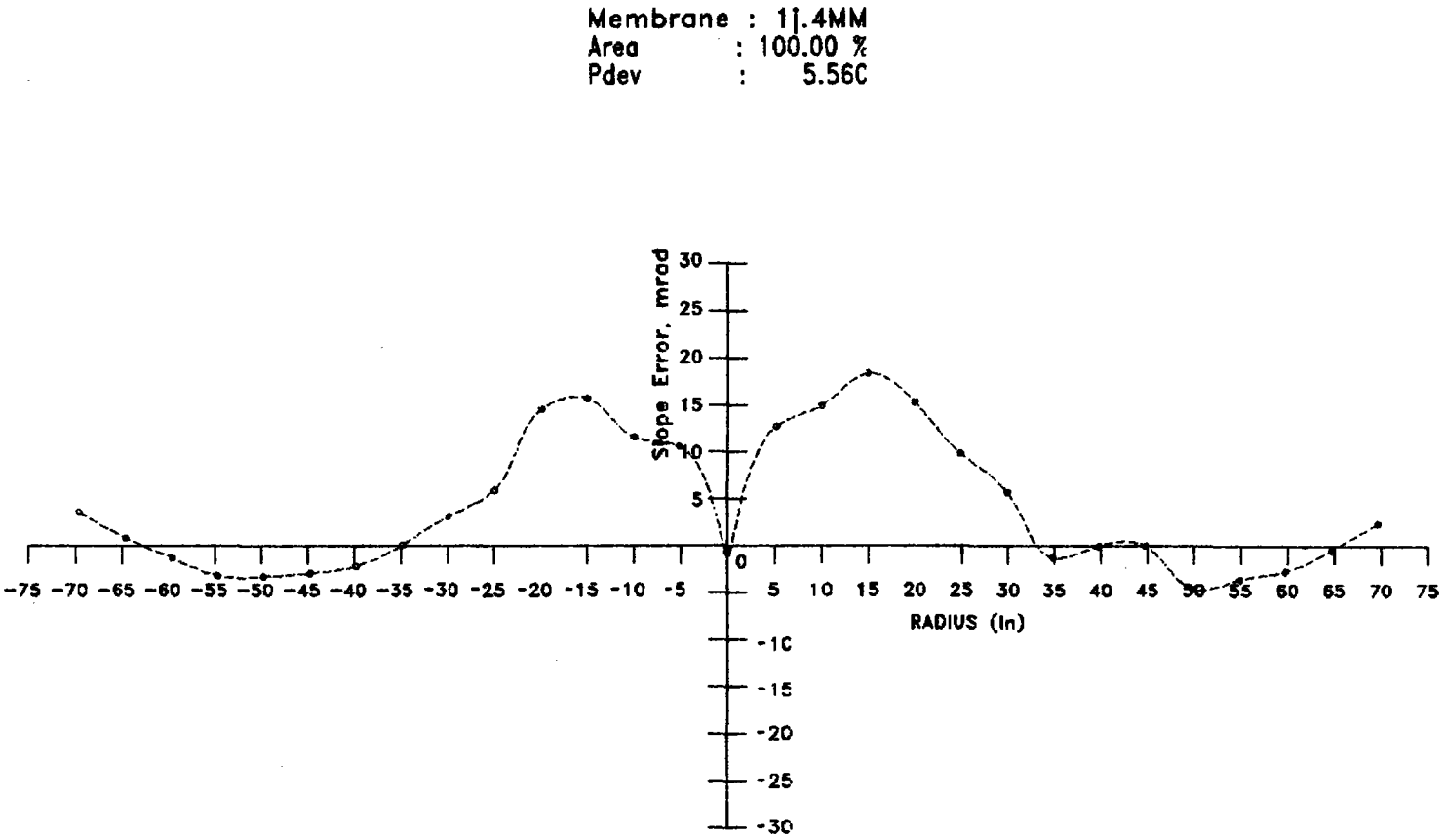

Figure B-3 Slope Error vs. Radial Position

File Name : 1N.OUT Date : 05-06-1988
Data File : 1N.4MM

Membrane : 6 mil 1145-OT

Comments : BUMPED AGAIN TO 5.25*2 IN WATER
11/10/87 STAB AT .375*2 WATER
Target Height = 79.790 in.s
PASS: WE
SEAM: WE

Stabilization
Pressure : 0.6250 in.s H20

Area : 100.00 %
Pdev : 5.6173

DATA SET	RADIUS	MEASURED SLOPE	IDEAL SLOPE	SLOPE ERROR	EFFECTIVE AREA
1	-69.6356	-0.3647	-0.3593	5.4204	1125.6300
2	-64.6340	-0.3376	-0.3354	2.1059	1045.1300
3	-59.6892	-0.3103	-0.3115	-1.2045	964.6277
4	-54.7400	-0.2840	-0.2871	-3.1118	884.1268
5	-49.7863	-0.2571	-0.2623	-5.2151	803.6251
6	-44.7657	-0.2322	-0.2369	-4.6765	723.1241
7	-39.8030	-0.2074	-0.2115	-4.0961	642.6226
8	-34.8359	-0.1838	-0.1857	-1.9708	562.1212
9	-29.8644	-0.1600	-0.1597	0.2729	481.6199
10	-24.8884	-0.1379	-0.1334	4.4923	401.1186
11	-19.9079	-0.1174	-0.1070	10.4410	320.6174
12	-14.9858	-0.0962	-0.0807	15.5613	240.1160
13	-9.9965	-0.0655	-0.0539	11.6410	159.6147
14	-5.1896	-0.0266	-0.0280	-1.3700	79.1134
15	-0.0045	-0.0009	-0.0000	-0.8530	18.7613
16	5.1864	0.0284	0.0280	0.4292	79.1134
17	10.0053	0.0683	0.0539	14.3980	159.6147
18	14.9548	0.0975	0.0805	16.9944	240.1160
19	19.9708	0.1188	0.1073	11.5204	320.6174
20	24.8656	0.1380	0.1333	4.6322	401.1186
21	29.8904	0.1612	0.1598	1.3240	481.6199
22	34.7939	0.1837	0.1855	-1.8383	562.1212
23	39.1980	0.2047	0.2084	-3.6372	642.6226
24	44.7395	0.2322	0.2368	-4.5536	723.1241
25	49.7189	0.2577	0.2620	-4.2822	803.6251
26	54.7657	0.2832	0.2872	-4.0314	884.1268
27	59.7537	0.3055	0.3118	-6.2648	964.6277
28	64.6829	0.3411	0.3357	5.3917	1045.1300
29	69.6164	0.3647	0.3592	5.5175	1125.6300

Membrane : 1n.4MM
Area : 100.00 %
Pdev : 5.617

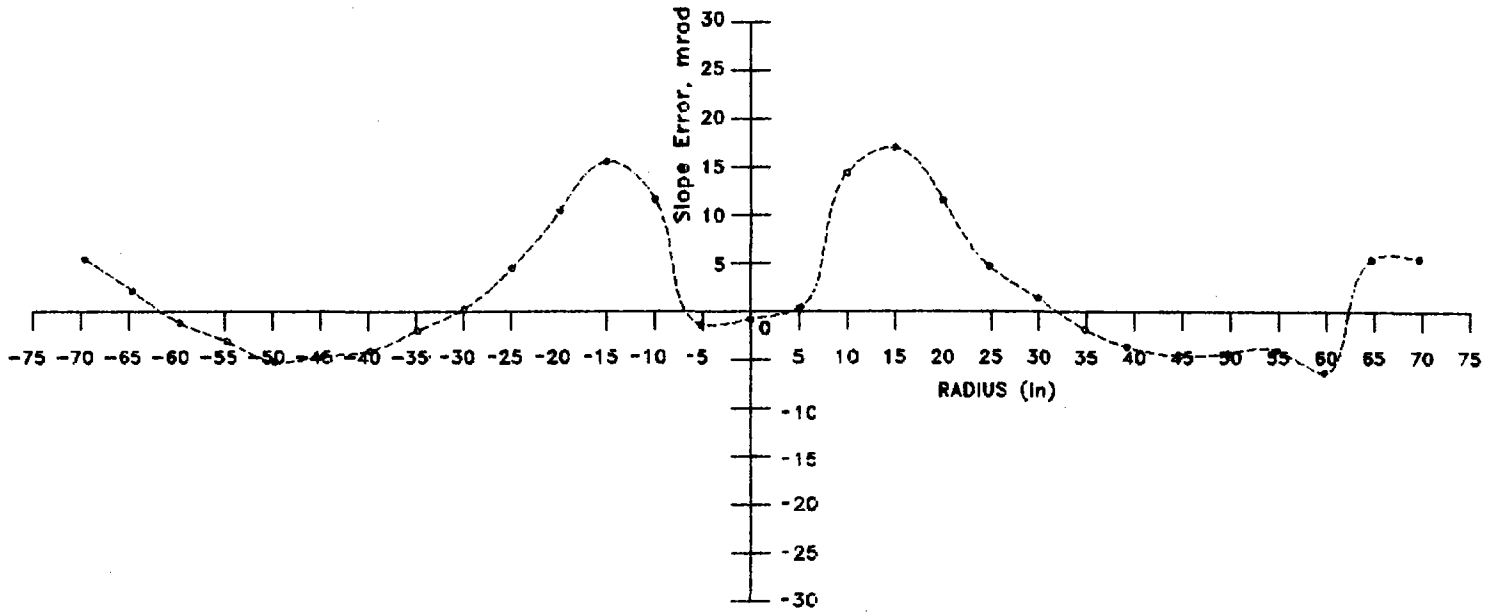

Figure B-4 Slope Error vs. Radial Position

File Name : 2F.OUT Date : 05-06-1988
Data File : 2F.4MM

Membrane : 6 mil 1145-OT

Comments : 100% OF AREA SAME COND AS 2E
.5*2 IN WATER STABAL 11/17/87
Target Height = 78.719 in.s
PASS: WE
SEAM: WE

Stabilization
Pressure : 20.2500 in.s H20

Area : 100.00 %
Pdev : 6.0660

DATA SET	RADIUS	MEASURED SLOPE	IDEAL SLOPE	SLOPE ERROR	EFFECTIVE AREA
1	-70.7159	-0.3669	-0.3666	0.3239	1125.6300
2	-65.6580	-0.3431	-0.3424	0.7158	1045.1300
3	-60.6053	-0.3158	-0.3179	-2.0332	964.6277
4	-55.5579	-0.2896	-0.2929	-3.3131	884.1268
5	-50.5059	-0.2634	-0.2676	-4.1817	803.6251
6	-45.4591	-0.2394	-0.2420	-2.5858	723.1241
7	-40.4077	-0.2151	-0.2159	-0.8689	642.6226
8	-35.3517	-0.1915	-0.1896	1.8606	562.1212
9	-30.3010	-0.1690	-0.1630	5.9600	481.6199
10	-25.2557	-0.1477	-0.1363	11.4814	401.1186
11	-20.2158	-0.1278	-0.1093	18.4508	320.6174
12	-15.1913	-0.1001	-0.0823	17.8368	240.1160
13	-10.1922	-0.0684	-0.0553	13.1562	159.6147
14	-5.3284	-0.0408	-0.0289	11.8471	79.1134
15	-0.0205	-0.0008	-0.0001	-0.6409	18.7613
16	5.2975	0.0393	0.0288	10.5708	79.1134
17	10.1496	0.0676	0.0550	12.5536	159.6147
18	15.1513	0.0990	0.0821	16.9216	240.1160
19	20.1876	0.1273	0.1092	18.1883	320.6174
20	25.2283	0.1461	0.1361	9.9716	401.1186
21	30.2735	0.1677	0.1629	4.7856	481.6199
22	35.3232	0.1902	0.1895	0.7133	562.1212
23	40.3774	0.2144	0.2158	-1.4018	642.6226
24	45.4260	0.2390	0.2418	-2.8223	723.1241
25	50.4791	0.2639	0.2675	-3.5972	803.6251
26	55.5367	0.2898	0.2928	-3.0134	884.1268
27	60.5886	0.3168	0.3178	-1.0177	964.6277
28	65.6450	0.3442	0.3423	1.8992	1045.1300
29	70.7058	0.3675	0.3665	1.0088	1125.6300

Membrane : 2f.4MM
Area : 100.00 %
Pdev : 6.148

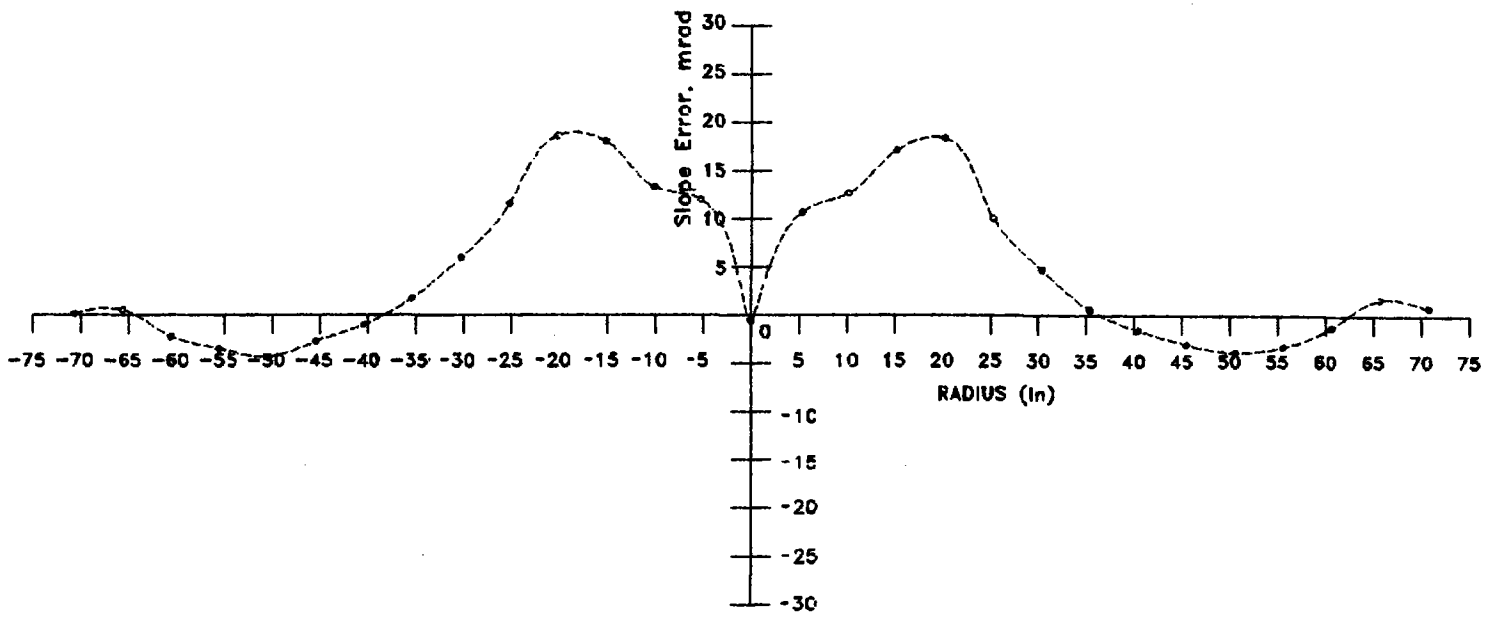

Figure B-5 Slope Error vs. Radial Position

File Name : 2G.OUT Date : 05-06-1988
Data File : 2G.4MM

Membrane : 6 mil 1145-OT

Comments : TRANSIL WRAP WITH 4*2 INCHES WATER WITH GRIT
NO GLASS MIRROR
Target Height = 78.719 in.s
PASS: WE
SEAM: WE

Stabilization
Pressure : 4.0000 in.s H20

Area : 100.00 %
Pdev : 6.6497

DATA SET	RADIUS	MEASURED SLOPE	IDEAL SLOPE	SLOPE ERROR	EFFECTIVE AREA
1	-70.7292	-0.3765	-0.3681	8.3755	1125.6300
2	-65.6664	-0.3431	-0.3438	-0.7365	1045.1300
3	-60.5989	-0.3157	-0.3191	-3.4239	964.6277
4	-55.5267	-0.2888	-0.2940	-5.1471	884.1268
5	-50.5118	-0.2623	-0.2688	-6.5037	803.6251
6	-45.4303	-0.2382	-0.2428	-4.5796	723.1241
7	-40.4062	-0.2143	-0.2169	-2.5035	642.6226
8	-35.3776	-0.1909	-0.1906	0.3106	562.1212
9	-30.2821	-0.1682	-0.1636	4.5114	481.6199
10	-25.2443	-0.1457	-0.1368	8.8857	401.1186
11	-20.2330	-0.1242	-0.1099	14.3518	320.6174
12	-15.1861	-0.0977	-0.0826	15.0968	240.1160
13	-10.1657	-0.0669	-0.0554	11.5024	159.6147
14	-5.2970	-0.0359	-0.0289	7.0084	79.1134
15	-0.0190	-0.0007	-0.0001	-0.5865	18.7613
16	5.2977	0.0347	0.0289	5.8351	79.1134
17	10.1486	0.0666	0.0553	11.3330	159.6147
18	15.1603	0.0968	0.0825	14.2830	240.1160
19	20.1765	0.1244	0.1096	14.8314	320.6174
20	25.2285	0.1457	0.1367	9.0380	401.1186
21	30.2851	0.1677	0.1637	4.0450	481.6199
22	35.3147	0.1913	0.1902	1.0586	562.1212
23	40.3487	0.2136	0.2166	-2.9412	642.6226
24	45.4502	0.2388	0.2429	-4.1649	723.1241
25	50.4933	0.2628	0.2687	-5.8314	803.6251
26	55.5407	0.2875	0.2941	-6.5750	884.1268
27	60.5927	0.3148	0.3191	-4.2845	964.6277
28	65.6490	0.3438	0.3437	0.0618	1045.1300
29	70.7099	0.3777	0.3680	9.7286	1125.6300

Membrane : 2G.4MM
Area : 100 %
Pdev : 6.65C

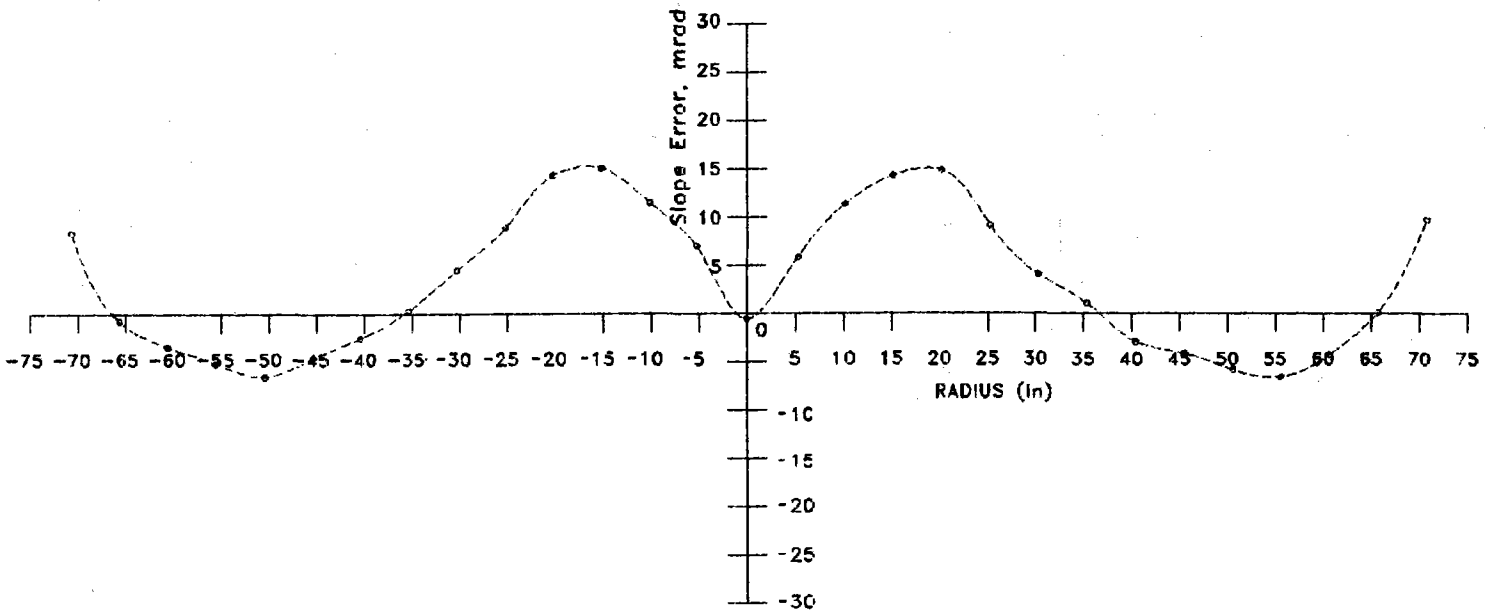

Figure B-6 Slope Error vs. Radial Position

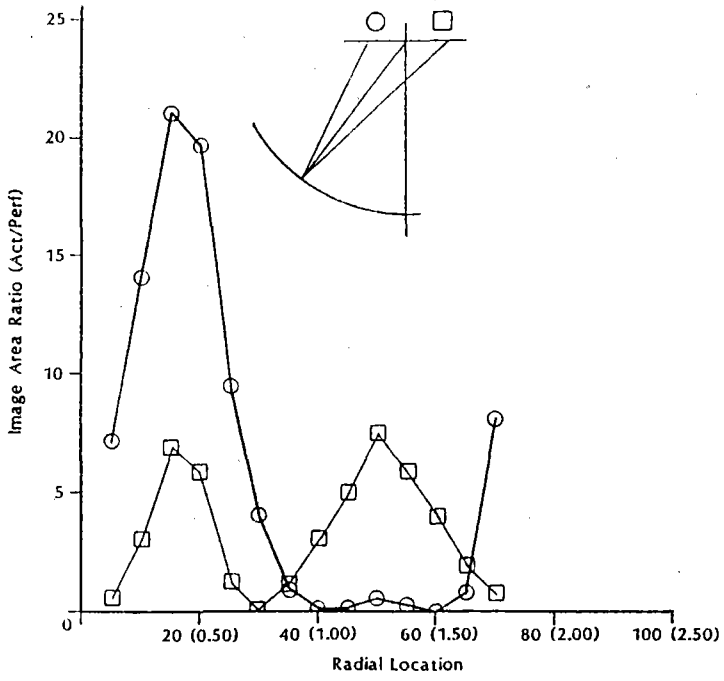

Figure B7. The Ratio of Predicted and Ideal Beam Size for the Test-Scale Membrane.

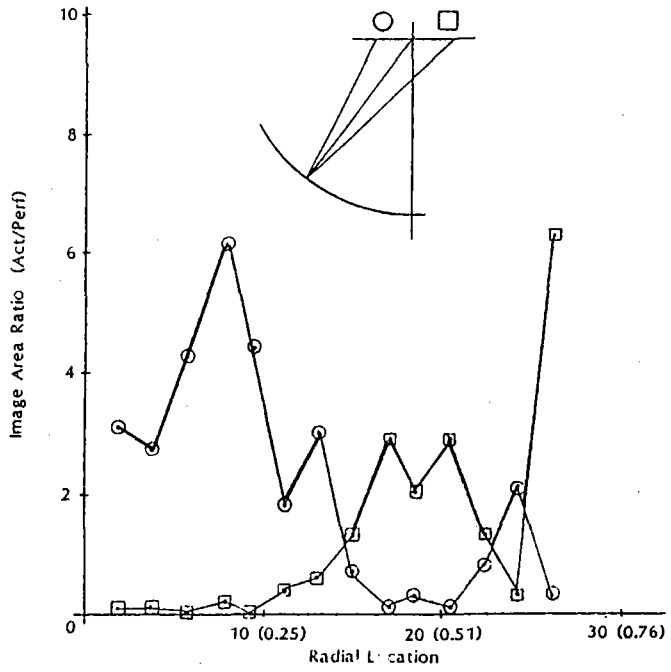

Figure B8. The Ratio of Predicted and Ideal Beam Size for the Bench-Scale Membrane.

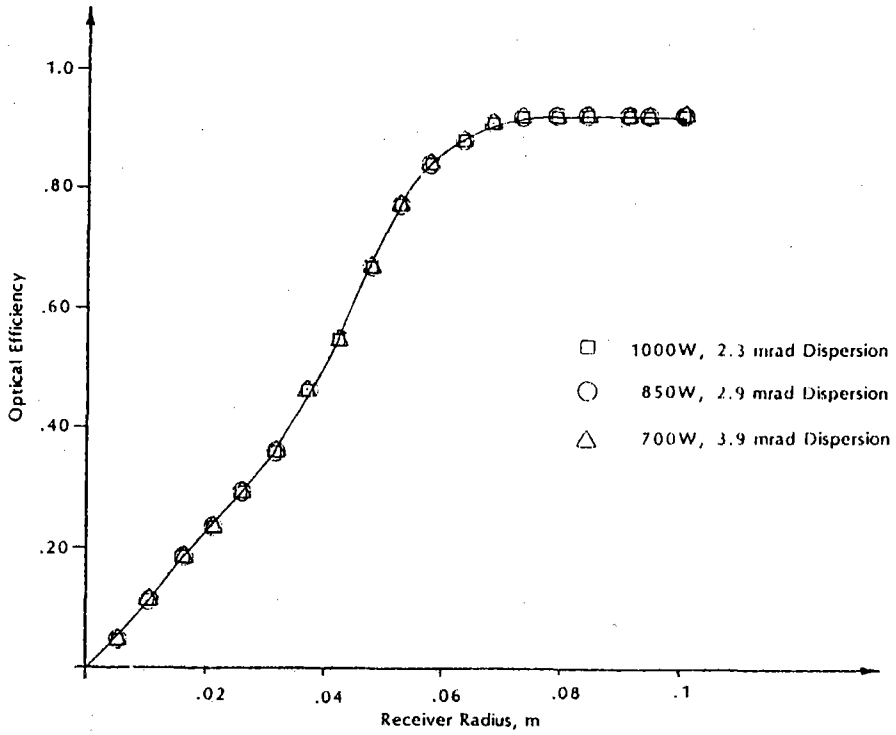

Figure B9. Optical Efficiency, Test-Scale Membrane, as a Function of Sun-Shape Dispersion.

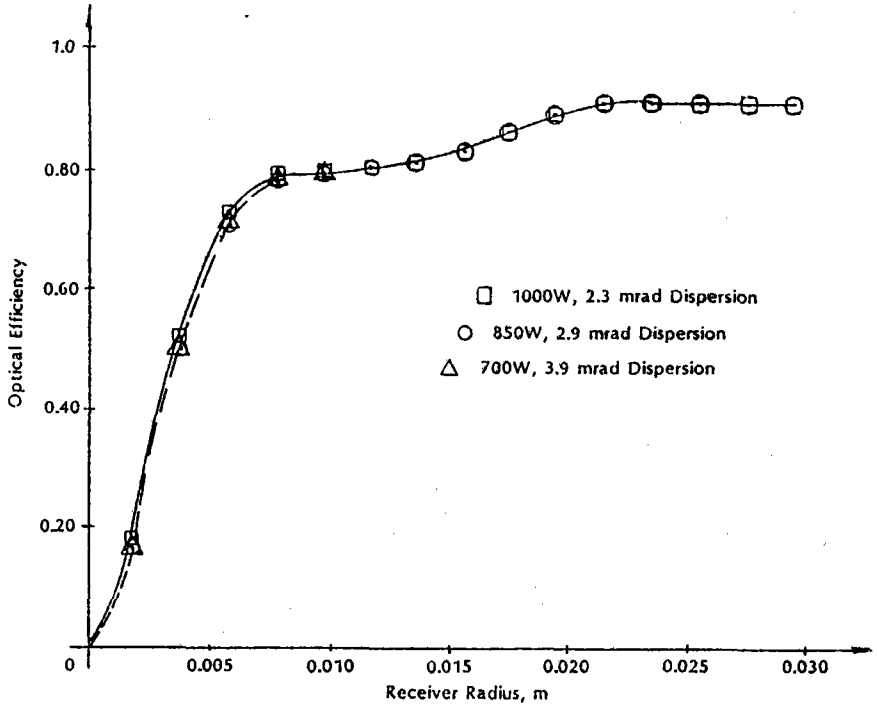

Figure B10. Optical Efficiency, Bench-Scale Membrane, as a Function of Sun-Shape Dispersion.

UNLIMITED RELEASE
INITIAL DISTRIBUTION

U.S. Department of Energy (5)
Forrestal Building
Code CE-314
1000 Independence Avenue, SW
Washington, DC 20585
Attn: H. Coleman
S. Gronich
M. Scheve
R. Shivers
T. Wilkins

U.S. Department of Energy (2)
Forrestal Building
Code CE-33
1000 Independence Avenue, SW
Washington, DC 20585
Attn: F. Morse
C. Carwile

U.S. Department of Energy (3)
Albuquerque Operations Office
P.O. Box 5400
Albuquerque, NM 87115
Attn: C. Garcia
G. Tennyson
N. Lackey

U.S. Department of Energy
San Francisco Operations Office
1333 Broadway
Oakland, CA 94612
Attn: R. Hughey

AAI Corporation
P. O. Box 6787
Baltimore, MD 21204

Acurex Corporation (2)
555 Clyde Avenue
Mountain View, CA 94039
Attn: J. Schaefer
H. Dehne

Advanced Thermal Systems
7600 East Arapahoe
Suite 319
Englewood, CO 80112
Attn: D. Gorman

Alpha Solarco
600 Vine Street
Cincinnati, OH 45202

Arizona Public Service Company
P.O. Box 21666
Phoenix, AZ 85036
Attn: J. McGuirk

Arizona Solar Energy Office
Dept. of Commerce
1700 W. Washington, 5th Floor
Phoenix, AZ 85007
Attn: F. Mancini

Australian National University
Department of Engineering Physics
P. O. Box 4
Canberra ACT 2600 AUSTRALIA
Attn: S. Kaneff

Barber-Nichols Engineering
6325 West 55th Avenue
Arvada, CO 80002
Attn: R. Barber

Battelle Pacific Northwest
Laboratory (2)
P.O. Box 999
Richland, WA 99352
Attn: T. A. Williams
D. Brown

BDM Coporation
1801 Randolph Street
Albuquerque, NM 87106
Attn: W. Schwinkendorf

Bechtel National, Inc.
50 Beale Street
50/15 D8
P. O. Box 3965
San Francisco, CA 94106
Attn: P. DeLaquil

Black & Veatch Consulting
Engineers
P.O. Box 8405
Kansas City, MO 64114
Attn: J. C. Grosskreutz

Tom Brumleve
1512 Northgate Road
Walnut Creek, CA 94598

California Energy Commission
1516 Ninth Street, M-S 43
Sacramento, CA 95814
Attn: A. Jenkins

California Polytechnic University
Dept. of Mechanical Engineering
Pomona, CA 91768
Attn: W. Stine

California Public Utilities Com.
Resource Branch, Room 5198
455 Golden Gate Avenue
San Francisco, CA 94102
Attn: T. Thompson

Cummins Engine Co.
MC 50179
P. O. Box 3005
Columbus, IN 47202
Attn: R. Kubo

DLR
Pfaffenwaldring 38-40
7000 Stuttgart 80 WEST GERMANY
Attn: R. Buck

DSET
P. O. Box 1850
Black Canyon Stage I
Phoenix, AZ 85029
Attn: G. Zerlaut

Electric Power Research
Institute (2)
P.O. Box 10412
Palo Alto, CA 94303
Attn: J. Bigger
E. DeMeo

Engineering Perspectives
20 19th Avenue
San Francisco, CA 94121
Attn: John Doyle

Energy Technology Engr. Center
Rockwell International Corp.
P. O. Box 1449
Canoga Park, CA 91304
Attn: W. Bigelow

ENTECH, Inc.
P. O. Box 612246
DFW Airport, TX 75261
Attn: R. Walters

Florida Solar Energy Center
300 State Road 401
Cape Canaveral, FL 32920
Attn: Library

Ford Aerospace
Ford Road
Newport Beach, CA 92663
Attn: R. Babbe

Foster Wheeler Solar Development
Corporation (2)
12 Peach Tree Hill Road
Livingston, NJ 07039
Attn: M. Garber
R. Zoschak

Garrett Turbine Engine Co.
111 South 34th Street
P. O. Box 5217
Phoenix, AZ 85010
Attn: E. Strain

Georgia Power (2)
7 Solar Circle
Shenandoah, GA 30265
Attn: E. Ney
R. Nelson

Harris Corporation (2)
Government and Aerospace
Systems Division
P. O. Box 9400
Melbourne, FL 32902
Attn: D. Ehresman
B. Valade

Industrial Solar Technologies
5775 West 52nd Avenue
Denver, CO 80212
Attn: R. Gee

Institute of Gas Technology
34245 State Street
Chicago, IL 60616
Attn: Library

ISEIR
951 Pershing Drive
Silver Spring, MD 20910
Attn: A. Frank

Jet Propulsion Laboratory
4800 Oak Grove Drive
Pasadena, CA 91109
Attn: M. Alper

LaJet Energy Company
P. O. Box 3599
Abilene, TX 79604
Attn: M. McGlaun

L'Garde, Inc. (2)
1555 Placentia Avenue
Newport Beach, CA 92663
Attn: M. Thomas
J. Williams

Lawrence Berkeley Laboratory
MS 90-2024
One Cyclotron Road
Berkeley, CA 94720
Attn: A. Hunt

Luz International (2)
924 Westwood Blvd.
Los Angeles, CA 90024
Attn: D. Kearney

3M-Energy Control Products (2)
207-1W 3M Center
St. Paul, MN 55144
Attn: B. Benson
J. Roche

McDonnell-Douglas Astronautics Company (3)
5301 Bolsa Avenue
Huntington Beach, CA 92647
Attn: R. Gervais
J. Rogan
D. Steinmeyer

Mechanical Technology, Inc. (2)
968 Albany Shaker Road
Latham, NY 12110
Attn: G. Dochat
J. Wagner

Meridian Corporation
4300 King Street
Alexandria, VA 22302
Attn: D. Kumar

NASA Lewis Research Center (4)
21000 Brook Park Road
Cleveland, OH 44135
Attn: R. Beremand 500-215
R. Evans 500-210
J. Savino 301-5
R. Corrigan 500-316

Nevada Power Co.
P. O. Box 230
Las Vegas, NV 89151
Attn: Mark Shank

Pacific Gas and Electric Company (2)
3400 Crow Canyon Road
San Ramon, CA 94526
Attn: G. Braun
J. Iannucci

Polydyne, Inc.
1900 S. Norfolk Street, Suite 209
San Mateo, CA 94403
Attn: P. Bos

Power Kinetics, Inc.
415 River Street
Troy, NY 12180
Attn: W. Rogers

Renewable Energy Institute
1001 Connecticut Ave. NW
Suite 719
Washington, DC 20036
Attn: K. Porter

Rockwell International
Rocketdyne Division
6633 Canoga Park Ave.
Canoga Park, CA 91304
Attn: T. Springer
W. Marlatt

San Diego Gas and Electric Company
P.O. Box 1831
San Diego, CA 92112
Attn: R. Figueroa

Sanders Associates
MER 15-2350
C. S. 2035
Nashua, NH 03061
Attn: B. Davis

SCE
P. O. Box 800
Rosemead, CA 91770
Attn: P. Skvarna

Schlaich, Bergermann & Partner
Hohenzollernstr. 1
D - 7000 Stuttgart 1
West Germany
Attn: W. Schiel

Sci-Tech International
Advanced Alternative Energy
Solutions
5673 W. Las Positas Boulevard
Suite 205
P.O. Box 5246
Pleasanton, CA 84566
Attn: U. Ortabasi

Science Applications International
Corporation (2)
10401 Roselle Street
San Diego, CA 92121
Attn: B. Butler
K. Beninga

Solar Energy Research Institute (5)
1617 Cole Boulevard
Golden, CO 80401
Attn: B. Gupta
L. M. Murphy
P. Schissel
R. Wood
A. Lewandowski

Solar Kinetics, Inc. (3)
P.O. Box 540636
Dallas, TX 75354-0636
Attn: J. A. Hutchison
D. White
P. Schertz

Solar Power Engineering Company
P.O. Box 91
Morrison, CO 80465
Attn: H. Wroton

Solar Steam
P. O. Box 32
Fox Island, WA 98333
Attn: D. Wood

Southern California Edison
P.O. Box 325
Daggett, CA 92327
Attn: C. Lopez

SRS Technologies
990 Explorer Blvd., NW
Huntsville, AL 35806
Attn: R. Bradford

Stearns Catalytic Corporation
P.O. Box 5888
Denver, CO 80217
Attn: T. E. Olson

Stirling Thermal Motors
2841 Boardwalk
Ann Arbor, MI 48104
Attn: B. Ziph

Sun Power, Inc.
6 Byard Street
Athens, OH 45701
Attn: W. Beale

Tom Tracey
6922 South Adams Way
Littleton, CO 80122

United Solar Tech, Inc.
3434 Martin Way
Olympia, WA 98506
Attn: R. Kelley

University of Arizona
Engineering Experimental Station
Harvil Bldg., Room 151-D
Tucson, AZ 85721
Attn: D. Osborne

University of Chicago
Enrico Fermi Institute
5640 Ellis Avenue
Chicago, IL 60637
Attn: J. O'Gallagher

University of Houston
Solar Energy Laboratory
4800 Calhoun
Houston, TX 77704
Attn: L. Vant-Hull

University of New Mexico
Dept. of Mechanical Engr.
Albuquerque, NM 87131
Attn: M. Wildin

University of Utah
Mechanical and Industrial
Engineering
Salt Lake City, UT 84112
Attn: B. Boehm

Eric Weber
302 Caribbean Lane
Phoenix, AZ 85022

WG Associates
6607 Stonebrook Circle
Dallas, TX 75240
Attn: V. Goldberg

☆ U.S. GOVERNMENT PRINTING OFFICE: 1989—673-049/81024

1840 R. E. Loehman
1846 D. H. Doughty
1846 C. S. Ashley
3141-1 S. A. Landenberger (5)
3151 W. I. Klein (3)
3154-1 C. L. Ward (8)
For DOE/OSTI
6000 D. L. Hartley
6200 V. L. Dugan
6210 B. W. Marshall
6220 D. G. Schueler
6221 E. C. Boes
6222 K. R. Boldt
6222 C. P. Cameron
6222 M. A. Quintana
6222 R. M. Houser
6222 J. V. Otts
6222 L. Yellowhorse
6223 G. J. Jones
6224 D. E. Arvizu
6224 A. R. Mahoney
6226 J. T. Holmes
6226 D. J. Alpert
6226 D. W. Cook
6226 J. D. Fish
6226 J. W. Grossman
6226 T. R. Mancini (20)
6226 J. E. Pacheco
6226 C. E. Tyner
6227 P. C. Klimas
6227 D. R. Adkins
6227 K. L. Linker
6227 R. B. Diver
7470 J. L. Ledman
7471 D. L. Stewart
7471 S. T. Reed
8524 J. A. Wackerly